UNIVERSITI TEKNOLOGI MARA

DEVELOPMENT OF PRINTED GRAPHENE-BASED NEAR FIELD COMMUNICATION (NFC) ANTENNA FOR TEMPERATURE MONITORING IN FOOD SAFETY APPLICATION

NAJWA BINTI MOHD FAUDZI

PhD

June 2026

UNIVERSITI TEKNOLOGI MARA

DEVELOPMENT OF PRINTED GRAPHENE-BASED NEAR FIELD COMMUNICATION (NFC) ANTENNA FOR TEMPERATURE MONITORING IN FOOD SAFETY APPLICATION

NAJWA BINTI MOHD FAUDZI

Thesis submitted in fulfilment
of the requirements for the degree of
Doctor of Philosophy
(Electrical Engineering)

Faculty of Electrical Engineering

June 2026

CONFIRMATION BY PANEL OF EXAMINERS

I certify that a Panel of Examiners has met on 19th January 2026 to conduct the final examination of Najwa Binti Mohd Faudzi on her Doctor of Philosophy thesis entitled "Development of Printed Graphene-Based Near Field Communication (NFC) Antenna for Temperature Monitoring in Food Safety Application" in accordance with Universiti Teknologi MARA Act 1976 (Akta 173). The Panel of Examiners recommends that the student be awarded the relevant degree. The Panel of Examiners was as follows:

Nor Salwa Damanhuri, PhD
Associate Professor
Faculty of Mechanical Engineering
Universiti Teknologi MARA
(Chairman)

Samihah Abdullah, PhD
Senior Lecturer
Faculty of Electrical Engineering
Universiti Teknologi MARA
(Internal Examiner)

Siti Zuraidah Ibrahim, PhD
Associate Professor
Faculty of Electronic Engineering Technology
Universiti Malaysia Perlis
(External Examiner)

PROFESSOR DR HJH ZURAEDA IBRAHIM
Dean
Institute of Postgraduates Studies
Universiti Teknologi MARA
Date : 4 June 2026

AUTHOR'S DECLARATION

I declare that the work in this thesis was carried out in accordance with the regulations of Universiti Teknologi MARA. It is original and is the results of my own work, unless otherwise indicated or acknowledged as referenced work. This thesis has not been submitted to any other academic institution or non-academic institution for any degree or qualification.

I, hereby, acknowledge that I have been supplied with the Academic Rules and Regulations for Post Graduate, Universiti Teknologi MARA, regulating the conduct of my study and research.

Name of Student	:	Najwa Binti Mohd Faudzi
Student I.D. No.	:	2020465728
Programme	:	Doctor of Philosophy (Electrical Engineering) - EE950
Faculty	:	Electrical Engineering
Thesis Title	:	Development of Printed Graphene-Based Near Field Communication (NFC) Antenna for Temperature Monitoring in Food Safety Application
Signature of Student	:	
Date	:	June 2026

ABSTRACT

Food safety across the supply chain requires reliable real-time temperature monitoring, particularly for perishable products that are sensitive to environmental variations. Near Field Communication (NFC) offers a promising battery-less solution for real-time monitoring. However, conventional metal-based NFC tag antennas, typically fabricated using copper, are prone to oxidation, generate toxic waste during etching, and are unsuitable for integration into food packaging. This research focuses on the development and experimental validation of a fully printed, battery-less NFC tag antenna using carbon-based conductive materials, specifically hybrid graphene-silver (HGS), for food temperature monitoring applications. The scope of the study includes material characterization, antenna design and optimization, systematic impedance tuning, robustness evaluation in terms of flexibility and sensitivity, as well as integration with a flexible temperature sensor circuit. Three conductive materials, namely silver conductor (SC), hybrid carbon-graphene (HCG), and HGS, were characterized in terms of conductivity, surface morphology, roughness, and thickness. Four antenna designs (D1, D2, D3, and D4) were developed and simulated at 13.56 MHz, with only the optimized D4-HGS design proceeding to full robustness and system-level validation. Impedance tuning was systematically implemented using Optenni Lab to achieve resonance and minimal insertion loss. The optimized D4-HGS antenna, inkjet-printed on PET, achieved low antenna resistance (<50 Ω), sufficient inductance (~1.21 μH), and a 20% size reduction compared to the reference D1 antenna design. The antenna maintained a minimum read range of 1.3 cm under bending at a maximum bending angle of 190.9°, with a 38% improvement in read range when encapsulated with PET shrink wrap under moist conditions. Performance degradation on metallic surfaces was mitigated using an amorphous magnetic sheet, enabling tag detection up to 1.5 cm when attached to a metal surface. The fully flexible graphene-based NFC tag achieved temperature accuracy within ±3°C across cold, room, and hot conditions and demonstrated high reliability through validation with various food products.

ACKNOWLEDGEMENT

In the name of Allah, the Most Gracious the Most Merciful.

Alhamdulillah, all praise to Allah swt, for His strength and blessings in enabling me to complete this thesis. This research has been accomplished with the help and support of many individuals and organizations. I would like to take this opportunity to express my deepest appreciation to all who have assisted me throughout this journey.

First and foremost, I would like to express my deepest gratitude and indebtedness to my supervisor, Dato' Prof. Ir Dr. Ahmad Rashidy Razali, for his invaluable support, constant encouragement, constructive suggestions and continuous guidance throughout the research. I would also like to extend my sincere gratitude to my co-supervisors, Prof. Dr. Asrulnizam Abd Manaf, Assoc. Prof. Ir. Dr. Nurul Huda Abd Rahman and Ir. Ts. Dr. Ahmad Azlan Ab Aziz, for their excellent guidance and continuous support during my study.

Special thanks and appreciation are extended to MIMOS Berhad, En. Khairu Anuar from CEDEC, and my colleagues at UiTM Cawangan Pulau Pinang and the Antenna Research Centre (ARC), who have provided great assistance throughout this research, particularly in the simulation and the measurement phases. I am also grateful to all those who have supported me, either directly or indirectly, for their constant encouragement, suggestions, and constructive comments.

Last but not least, my deepest appreciation goes to my beloved parents, husband, son, and family members for their love, concern, moral support, encouragement and understanding. Thank you to all those mentioned above for making this research a truly meaningful and rewarding experience for me.

TABLE OF CONTENTS

		Page
CONFIRMATION BY PANEL OF EXAMINERS		**ii**
AUTHOR'S DECLARATION		**iii**
ABSTRACT		**iv**
ACKNOWLEDGEMENT		**v**
TABLE OF CONTENTS		**vi**
LIST OF TABLES		**x**
LIST OF FIGURES		**xii**
LIST OF SYMBOLS		**xxii**
LIST OF ABBREVIATIONS		**xxiv**
CHAPTER 1: INTRODUCTION		**1**
1.1	Research Background	1
1.2	Problem Statement	2
1.3	Objectives	4
1.4	Scope of Work	4
1.5	Significance of Study	5
1.6	Thesis Organization	6
CHAPTER 2: LITERATURE REVIEW		**8**
2.1	Introduction	8
2.2	Overview of NFC System Technology	8
	2.2.1 NFC Components	9
	2.2.2 NFC Working Principle	10
	2.2.3 NFC Operation Mode	11
	2.2.4 Equivalent Circuit Model of NFC System	12
2.3	Conductive Materials	15
	2.3.1 NFC Antenna Conductive Materials and Fabrication Techniques	15
	2.3.2 Electrical and Structural Properties of Conductive Material	19
	2.3.2.1 Conductivity	19

2.3.2.2 Surface Morphology and Roughness 21
2.4 Design and Parameters of NFC Antenna 24
2.4.1 NFC Antenna Design 24
2.4.2 NFC Antenna Geometrical Configuration 27
2.4.3 NFC Antenna Parameters 30
2.4.3.1 Resonance Frequency and Antenna Tuning 31
2.4.3.2 Antenna Inductance, Resistance, and Q-factor 32
2.4.3.3 Read Range and Magnetic Field Strength 33
2.4.3.4 Power Transfer Efficiency 35
2.5 Robustness of NFC Antenna 36
2.6 Temperature Monitoring Application 41
2.7 Summary 45

CHAPTER 3: RESEARCH METHODOLOGY 47
3.1 Introduction 47
3.2 Flow of Research Work 48
3.3 Synthesis of HGS Conductive Materials 51
3.4 Characterization Process of Conductive Materials 52
3.4.1 Conductivity and Sheet Resistance Measurement 53
3.4.2 Surface Morphology Measurement Using SEM 54
3.4.3 Surface Roughness and Thickness Measurement 55
3.5 Antenna Design and Fabrication 58
3.5.1 Flow of Tag Antenna Design 58
3.5.2 NFC Tag Antenna Design 61
3.5.3 Simulation Software and Design Requirements 64
3.5.3.1 NFC Tag Antenna Design using CST Microwave Studio 64
3.5.3.2 Antenna Tuning Using Optenni Lab 65
3.5.4 Fabrication of Printed Flexible NFC Antenna 67
3.5.4.1 Direct Ink Writing (DIW) 68
3.5.4.2 Screen Printing 70
3.5.4.3 Inkjet Printing 71
3.6 Antenna Robustness Measurement 73
3.6.1 Flexibility Measurement 73

3.6.2 Sensitivity Measurement 74
3.7 Equivalent Circuit Model for On-Metal Tag 77
3.8 Measurement Standards and Procedures 82
3.8.1 Antenna Inductance and Resistance 82
3.8.2 Antenna Tuning and Resonant Frequency 83
3.8.3 Reading Range 85
3.9 Development of Temperature Monitoring System as NFC Application 86
3.9.1 Procedure of Fabrication for HGS NFC Tag Antenna with Temperature Sensor Circuit 87
3.9.2 Electrical Bonding and Mechanical Stability Limitations 92
3.9.3 Reliability Test of Temperature Monitoring 96
3.10 Summary 97

CHAPTER 4: RESULTS AND DISCUSSIONS 99
4.1 Introduction 99
4.2 Characterization of Printed Conductive Materials 100
4.2.1 Conductivity 100
4.2.2 Surface Morphology 103
4.2.3 Surface Roughness 104
4.2.4 Thickness 106
4.3 Printed Flexible NFC Tag Antenna Performance 108
4.3.1 Silver Conductive (SC) NFC Tag Antenna 108
4.3.1.1 Antenna Tuning and Verification 109
4.3.1.2 Simulation and Measurement Result Analysis 117
4.3.2 Hybrid Graphene-Silver (HGS) NFC Tag Antenna 125
4.3.2.1 Verification of Printed HGS-based Antenna 125
4.3.2.2 Simulation and Measurement Result Analysis 130
4.3.3 Hybrid Carbon-Graphene (HCG) NFC Tag Antenna 144
4.3.3.1 Verification of Printed HCG-based Antenna 144
4.3.3.2 Simulation and Measurement Result Analysis 146
4.3.4 Summary of Conductive Material Variation and Antenna Design 148
4.4 Robustness Analysis of NFC Tag Antenna 150
4.4.1 Flexibility of NFC Tag Antenna 150
4.4.2 Sensitivity of NFC Tag Antenna 158

4.4.2.1 Various Packaging Materials 158
4.4.2.2 Moisture 162
4.4.2.3 Temperature 172
4.4.3 On Metal HGS NFC Tag Antenna 173
4.4.3.1 Correlation Between Magnetic Sheet Parameters and Antenna Properties 174
4.4.3.2 Comparative Analysis of Magnetic Shielding *182*
4.5 NFC Tag Antenna for Temperature Monitoring of Food Packaging Application 190
4.5.1 Verification of Electrical Connectivity for Temperature Sensor Circuit 191
4.6 Enhancement of NFC Temperature Monitoring Application 194
4.6.1 Reliability Test Result of Temperature Monitoring System 200
4.6.2 Verification of Application for Temperature Monitoring of Food Packaging 204
4.7 Summary 207

CHAPTER 5: CONCLUSION AND FUTURE WORK **211**
5.1 Conclusion 211
5.2 Research Contributions 213
5.3 Future Work 214

REFERENCES **216**
APPENDICES **237**
AUTHOR'S PROFILE **245**

LIST OF TABLES

Tables	Title	Page
Table 2.1	The Fabrication Methods and the Limitations of Several Conductive Materials	18
Table 2.2	Summarization of Antenna Designs Characteristics and Findings/Gaps	27
Table 2.3	Summary Analysis of Literature Review Regarding Robustness of NFC Antenna	40
Table 2.4	Summarization of Temperature Monitoring Applications and Their Limitations	43
Table 2.5	Summary Analysis of Literature Review and the Proposed Solutions	46
Table 3.1	Specification of Antenna Designs	49
Table 3.2	Antenna Parameters	62
Table 3.3	SMD Components of Temperature Sensor Circuit	88
Table 3.4	Guideline and Procedures of NFC Tag and Circuit Fabrication	90
Table 4.1	Measurement Results of Resistivity, ρ and Conductivity, σ for the Printed Conductive Materials	100
Table 4.2	Measured Values of Roughness Parameters	106
Table 4.3	Measurement Results of Thickness for Printed Conductive Materials	107
Table 4.4	Summary of Conductive Material Parameters and Characteristics	108
Table 4.5	Analysis of Tuning Topologies with a Series Connection of $C_{int.}$	111
Table 4.6	Simulated and Measured Results for D1-SC and D2-SC Antennas	119
Table 4.7	Simulated and Measured Values of Ctun, Which Connected in Parallel to Cint	121

Table 4.8	Comparison of Antenna Electrical Properties for D3-HGS and D4-HGS with and without Chamfer	136
Table 4.9	Simulated and Measured Electrical Properties of D1-, D3- and D4-HGS	137
Table 4.10	Simulated and Measured Value of Ctun, Which Connected in Parallel to Cint	138
Table 4.11	Summary Results for D1-HGS, D3-HGS, and D4-HGS Antennas	144
Table 4.12	Simulated and Measured Results of La and Ra for D4-HGS Antenna	148
Table 4.13	Summary of Measurement Results for D1-D4 Tag Antennas with Varying Conductive Materials	150
Table 4.14	Electrical Properties of Various Packaging Materials	159
Table 4.15	Simulated and Measured Read Range for Antenna in Various Moist Conditions	171
Table 4.16	Variation of Thickness and Permeability for Ferrite, Amorphous, and Nanocrystalline Magnetic Sheets	175
Table 4.17	Properties of Magnetic Sheet	183
Table 4.18	The Simulated and Measured La and Ra for D4-HGS Antenna with Different Magnetic Sheets	185
Table 4.19	Electronic Components and Values Used for EC in ADS Simulation	187
Table 4.20	Simulated and Measured Tag Read Range with Various Magnetic Sheets	189
Table 4.21	Comparison of Properties and Performance for Various Magnetic Sheets	190
Table 4.22	Measured Resistance Between SMD Components and NFC Chip Ports	192
Table 4.23	Measured Voltage at Various Voltage Sources for PCB-based and D4-HGS Tag with Temperature Sensor Circuit	194
Table 4.24	Several Types of Food with Various Packaging Types and Storage Temperature	206
Table 4.25	Comparison of the Graphene-Based NFC Tag Antenna with the Proposed Tag	210

LIST OF FIGURES

Figures	Title	Page
Figure 2.1	Example of NFC (a) Readers and (b) Tags	10
Figure 2.2	Near Field Communication Working Principle [35]	11
Figure 2.3	NFC Reader and NFC Tag Equivalent Circuit Model [26]	13
Figure 2.4	Equivalent Circuit of NFC Tag Antenna with (a) The Increase of Dielectric Loss and (b) The Introduction of Silicon Coating [42]	14
Figure 2.5	Equivalent Circuit of Coil Inductor with the Existence of Conductive Plate and Shielding Material [43]	15
Figure 2.6	Fabricated NFC Antenna with Various Conductive Materials: (a) Etched Copper, (b) Copper Tape, (c) Printed Silver Ink and (d) Graphene Oxide [26][65][46][61]	17
Figure 2.7	Measurement of Electrical Conductivity Using the Two-Probe Method [70]	20
Figure 2.8	Measurement of Electrical Conductivity Using the Four-Probe Method Through (a) A Collinear Probe Array and (b) A Square Array	21
Figure 2.9	Height Parameters for Roughness Evaluation	23
Figure 2.10	Graphical Representation of (a) Sv, Sz, Sp (b) Sa and (c) Sq. The Grey Plane Indicates the Mean Value for the Measurement [74]	23
Figure 2.11	Serpentine-Shaped Coil of NFC Tag Antenna [76]	24
Figure 2.12	Multi-Layered Stack NFC Tag Antenna [79]	25
Figure 2.13	Basic Geometries of NFC Tag Antenna (a) Square Loop, (b) Circular Loop and (c) Planar Rectangular Loop [80][81][82]	26
Figure 2.14	Geometrical Parameters of the Coil Antenna [86][87]	28
Figure 2.15	Commercial Antenna Design for (a) NFC Tag and (b) Reader, Used as References [88] [89]	30
Figure 2.16	Magnetic Field Distribution of a Circular Antenna in Free Air [102]	35

Figure 2.17	Bending Evaluation of Flexible NFC Tag Antennas: (a) Textile NFC Antenna Bent at 150°, (b) Graphene-Based NFC Antenna at a Bending Radius of 2 cm, and (c) Resistance Response of Graphene-Paper Antennas Under Extensive Cyclic Bending Tests	37
Figure 2.18	Formation of Eddy Currents During on-Metal NFC Communication	38
Figure 2.19	Schematic Circuit Diagram of the Temperature Monitoring Circuit	44
Figure 3.1	Flow of Studies and Research Work	50
Figure 3.2	Block Diagram Illustration of Synthesis of AgNPs and rGO to Produce HGS Ink	52
Figure 3.3	Conductivity Measurement: (a) Using 4-Point Probe Loresta GX MCP-T700, (b) Measurement Conducted on Graphene Samples	54
Figure 3.4	Hitachi-Regulus 8200 Series Ultra High-Resolution-SEM	55
Figure 3.5	Samples Taken from the Printed Materials (Longitudinal Section) For Capturing the SEM Image	55
Figure 3.6	VHX Digital Microscopes and Display Unit	56
Figure 3.7	(a) 2D Captured Image from SC Printed Sample with Selected Area for Surface Roughness Measurement and (b) the Quantitative Data of Surface Roughness	56
Figure 3.8	Measurement of Thickness for the SC Printed Sample	57
Figure 3.9	NFC Tag Antenna Design Process	60
Figure 3.10	Proposed NFC Tag Antenna Designs (a) D1, (b) D2, (c) D3 and (d) D4	62
Figure 3.11	Flow of Antenna Design and Optimization Process	63
Figure 3.12	(a) Antenna Design Using CST Simulation Software (b) Schematic Diagram of NFC Antenna with Matching Circuit in CST Design Studio	65
Figure 3.13	Optenni Lab Software Interface	67
Figure 3.14	Voltera V-One PCB Printer	69
Figure 3.15	Different Layers of Printing for D2-SC Tag Antenna	69
Figure 3.16	Printing Process using DIW Technology	69

Figure 3.17	Fabricated D2 Tag Antenna Printed Using SC Material	70
Figure 3.18	Fabrication Process Using Screen Printing	71
Figure 3.19	PiXDRO LP50 (SuSS MicroTec) Inkjet Printer	71
Figure 3.20	Fabrication Process of Graphene-Based NFC Tag Antenna	73
Figure 3.21	(a) Simulation of Antenna Bending, (b) Cylinder Foam with Varying Radius, r in cm, and (c) Measurement Setup for S_{11} at Different Bending Angles Using VNA	74
Figure 3.22	Simulation of NFC Tag Antenna Attached to Food Packaging Material	75
Figure 3.23	D4-HGS is Connected to VNA Port and Attached to Different Materials: (a) Plastic (b) Carton Box (c) Glass and (d) Metal	76
Figure 3.24	(a)Water Layer Directly Attached to the Antenna and (b) Side View of the Antenna with the Water Layer	76
Figure 3.25	Different Amounts of Water Content: (a) 100 %, (b) 80%, (c) 50% and (d) 25%	77
Figure 3.26	Measurement Setup for La and Ra at Different Temperature Range	77
Figure 3.27	(a) The CST Simulation Design of NFC Tag Antenna on Free Space and (b) The ADS EC of NFC Tag Antenna	79
Figure 3.28	(a) The CST Simulation Design of NFC Tag Antenna with Magnetic Sheet and (b) the ADS EC of NFC Tag Antenna with Magnetic Sheet	80
Figure 3.29	CST Simulation Design of NFC Tag Antenna with Magnetic Sheet and Metal Plate	81
Figure 3.30	The ADS EC of NFC Tag Antenna with Magnetic Sheet and Metal Plate	81
Figure 3.31	(a) Vector Network Analyzer and (b) Standard Calibration Kit from Keysight	83
Figure 3.32	NFC Tag Antenna Connected to VNA for Impedance Measurement	83
Figure 3.33	Schematic Diagram NFC Tag Resonant Frequency Measurement [175]	84

Figure 3.34	(a) Conventional Coil Antenna Connected to VNA (b) NFC Tag Antenna in Close Proximity to the Conventional Coil Antenna	84
Figure 3.35	Measurement Setup for (a) Tag Reading Range and (b) Antenna Resonant Frequency	86
Figure 3.36	NFC Monitoring System Block Diagram	87
Figure 3.37	Flowchart of Data Transaction	87
Figure 3.38	PCB Layout of D4-HGS NFC Tag Antenna with Temperature Sensor Circuit Footprints in Altium Designer	88
Figure 3.39	Prototype of D4-HGS NFC Tag Antenna with Temperature Sensor Circuit	89
Figure 3.40	Flow Chart for the Development Process of NFC Monitoring System	92
Figure 3.41	Detached Trace Under Extremely High Temperature	93
Figure 3.42	(a) VQFN Package of the RF430FRL152H Chip, (b) Layout of HGS-Based Flexible Printed Circuitry, and (c) Dimensions of the RF430FRL152H Chip Pads [179]	94
Figure 3.43	(a) Short-Circuited Conductive Epoxy on the Chip Pads and (b) the Securely Bonded Other SMD Components on the Pads Using Conductive Epoxy	94
Figure 3.44	(a) Chip Layout Design with Through-Hole Vias, (b) Fabricated Flexible PCB, (c) Bonded Chip on the Flexible PCB, (d) Chip Layout Aligned with the HGS Printed Circuit and (e) Conductive Epoxy Applied Through the Vias	95
Figure 3.45	Measurement Setup in a Temperature-Controlled Environment	96
Figure 3.46	(a) Portable mini fridge (b) Temperature measurement of NFC tag using smartphone with temperature monitoring apps	97
Figure 4.1	The Effect of Conductivity to the Antenna Inductance, La and Antenna Resistance, Ra.	102
Figure 4.2	The Effect of Conductivity to the Antenna Q-Factor	102
Figure 4.3	SEM Image for (a) SC, (b) HCG, and (c) HGS Printed Samples	104

Figure 4.4	2D Image for (a) SC (b) HCG (c) HGS from VHX Digital Microscope	105
Figure 4.5	Unmatched S_{11} Result of D1-SC Antenna	110
Figure 4.6	Matched S_{11} Results with Several Generated Tuning Topologies	110
Figure 4.7	The S_{11} Results for All Tuning Topologies	112
Figure 4.8	PCSC Circuit Integrated with D1-SC Antenna in CST Software	113
Figure 4.9	Comparison of S_{11} Results from CST Studio Suite and Optenni Lab Software	114
Figure 4.10	Prototype of (a) D1-SC and (b) D2-SC Tag Antenna	115
Figure 4.11	The Labelled Line Numbers for (a) D1-SC and (b) D2-SC Tag Antenna Used for Resistance Measurement	115
Figure 4.12	Measured Resistance Reading Across the 24 lines for D1-SC Antenna	116
Figure 4.13	Measured Resistance Reading Across the 24 lines for D2-SC Antenna	117
Figure 4.14	Simulated Results of (a) La and (b) Ra for D1-SC and D2-SC tag Antennas	118
Figure 4.15	Measured Results of La and Ra for (a) D1-SC and (b) D2-SC Tag Antennas	118
Figure 4.16	Simulated PTE of D1-SC and D2-SC Antennas	120
Figure 4.17	Simulation and Measurement Result of S_{11} for (a) D1-SC and (b) D2-SC	121
Figure 4.18	Reading Range of D1-SC and D2-SC Antennas	123
Figure 4.19	Measured Result of Antenna Resonance Frequency and Tag Reading Range with Respect to Tuning Capacitance, C1, for (a) D1-SC and (b) D2-SC Antennas	124
Figure 4.20	Prototype of (a) D1-HGS, (b) D3- HGS and (b) D4- HGS Tag Antenna	126
Figure 4.21	The Labelled Line Numbers for (a) D1-HGS, (b) D3- HGS and (b) D4- HGS Tag Antenna Used for Resistance Measurement	127

Figure 4.22	Measured Resistance Reading Across the 24 lines for D1-HGS Antenna	128
Figure 4.23	Measured Resistance Reading Across the 24 lines for D3-HGS Antenna	129
Figure 4.24	Measured Resistance Reading Across the 16 lines for D4-HGS Antenna	130
Figure 4.25	Antenna Geometry and Resistance Comparison: (a) Geometric Layout of D1 Antenna, and (b) Comparison of Antenna Resistance (Ra) Versus Frequency for D1-SC and D1-HGS Antennas	131
Figure 4.26	Correlation Between Antenna Geometric Parameters and Electrical Performance: (a) Width with La and Ra, (b) Gap with La and Ra, (c) Width with Q-Factor, and (d) Gap with Q-factor	133
Figure 4.27	Comparison between D1-HGS and D3-HGS Antenna Designs: (a) D3-HGS Antenna Design (b) Ra Versus Frequency, (c) La Versus Frequency, and (d) Q-Factor Versus Frequency	134
Figure 4.28	Correlation Between the Number of Turns and (a) La and Ra, (b) Q-Factor, and (c) Final Antenna Design of D4-HGS	135
Figure 4.29	Chamfer Implemented in the Design of (a) D3-HGS and (b) D4-HGS	136
Figure 4.30	Measured and Simulated S11 for (a) D1-HGS, (b) D3-HGS and (c) D4-HGS Tag Antenna	139
Figure 4.31	Simulation of Power Transfer Efficiency (PTE) for All Antenna Designs	140
Figure 4.32	Simulation of Reading Range for All Antenna Designs	140
Figure 4.33	Measured Tag Reading Range Along with the Corresponding fres and Ctun Values for (a) D1-HGS, (b) D3-HGS and (c) D4-HGS Tag Antenna	143
Figure 4.34	D4-HCG Tag Antenna's (a) Prototype and (b) Labelled Line Numbers Used for Resistance Measurement	145
Figure 4.35	Measured Resistance Reading Across the 16 lines for D4-HCG Antenna	146

Figure 4.36	Simulated Antenna Resistance, Ra, for D4-HCG	147
Figure 4.37	Simulated Antenna Inductance, La, for D4-HCG	147
Figure 4.38	Simulation of S_{11} for (a) D2-SC (b) D4-HGS Antennas	152
Figure 4.39	Antenna Inductance for (a) D2-SC (b) D4-HGS Antennas	153
Figure 4.40	Simulation of Magnetic Field Distribution for (a) D2-SC and (b) D4-HGS During Bending	154
Figure 4.41	(a) Reader and Bending Tag During PTE Simulation and the Simulated PTE Results for (a) D2-SC and (b) D4-HGS Antennas	155
Figure 4.42	D2-SC Antenna Connected to VNA and Attached to Cylinder Foams with Different Radius: (a) 4.5 cm, (b) 3.5cm, (c) 2.5 cm, (d) 2 cm, and (e) 1.5 cm	156
Figure 4.43	Measurement of D2-SC for (a) S_{11} and (b) Reading Range with the Variation of Cylinder Radius, r	157
Figure 4.44	Measurement of D4-HGS for (a) S_{11} and (b) Reading Range with the Variation of Cylinder Radius, r	157
Figure 4.45	Simulation S_{11} for D4-HGS Attached on Different Packaging Materials	159
Figure 4.46	Simulated La for D4-HGS Attached on Different Packaging Materials	160
Figure 4.47	Simulated Tag Reading Range for D4-HGS Attached to Different Packaging Materials	161
Figure 4.48	D4-HGS Antenna Attached on Different Packaging Materials: (a) Plastic (b) Carton Box (c) Glass and (d) Metal	162
Figure 4.49	Measurement S_{11} for D4-HGS Attached on Different Packaging Materials	162
Figure 4.50	D4-HGS Tag Antenna in (a) Dry and (b) Wet Conditions	163
Figure 4.51	The Simulation Results of (a) S_{11} and (b) Antenna Inductance in Dry and Wet Conditions of the D4-HGS Antenna	164
Figure 4.52	The Simulated Tag Reading Range for D4-HGS in Dry and Wet Conditions	164
Figure 4.53	The Simulation Results of (a) Antenna Inductance and (b) S_{11} for D4-HGS with Variation of Water Content	166

Figure 4.54	The Simulated Tag Reading Range for D4-HGS with Variation of Water Content	167
Figure 4.55	(a) Top View and Side View of the PET Layer Introduced Between the Water Layer and Conductive Element (b) S11 Result of Dry and Wet Conditions of The Tag Antenna with the Existence of the PET Layer	168
Figure 4.56	Simulation of (a) La and (b) Reading Range for Dry and Wet Condition	169
Figure 4.57	Fabrication Equipment for Antenna Insulation: (a) Impulse Sealer, (b) PET Shrink Wrap and (c) Blower	170
Figure 4.58	D4-HGS Tag Antenna with PET Layer Covered	170
Figure 4.59	Fully Moist D4-HGS Tag Antenna Prototype	171
Figure 4.60	The Measured Result of (a) Antenna Resistance and (b) Antenna Inductance with Respect to the Temperature	173
Figure 4.61	(a) Front and (c) Side View of NFC Tag with Magnetic Sheet Affixed to a Metal Plate (200 mm x 200 mm)	175
Figure 4.62	Correlation Between the Thickness of Ferrite Sheets with (a) La and Ra (b) Read Range and (c) fres.	177
Figure 4.63	Correlation Between the Thickness of Amorphous and Nanocrystalline with (a)(b) Read Range (c)(d) La and Ra (e)(f) fres, Respectively	178
Figure 4.64	Correlation Between the Permeability of Ferrite Sheets with (a) La and Ra (b) Read Range and (c) fres.	180
Figure 4.65	Correlation Between The Permeability of Amorphous and Nanocrystalline with (a)(b) Read Range (c)(d) La and Ra (e)(f) fres, Respectively	182
Figure 4.66	Magnetic Sheets: (a) Ferrite (b) Amorphous and (c) Nanocrystalline	183
Figure 4.67	(a) Antenna Inductance and (b) S_{11} with Respect to the Frequency for Ferrite and Amorphous Sheet Configuration	184
Figure 4.68	Simulated S_{11} Result for D4-HGS Tag Antenna with Magnetic Sheets and Metal Plate Using CST Simulation	186

Figure 4.69	Simulated S_{11} Result for D4-HGS Tag Antenna with Magnetic Sheets and Metal Plate Using EC in ADS Simulation	186
Figure 4.70	Magnetic Field Strength as a Function of the Distance from the Tag Surface (z-axis) for Ferrite and Amorphous Sheet Configuration	188
Figure 4.71	D4-HGS Tag Antenna Attached to (a) Ferrite, (b) Amorphous, and (c) Nanocrystalline Magnetic Sheets	188
Figure 4.72	Schematic Diagram of RF430FRL152H Chip and Other Components	192
Figure 4.73	PCB-Based Tag Antenna with Temperature Sensor Circuit	194
Figure 4.74	(a) Interface of the Temperature Monitoring App Developed by Texas Instruments and (b) the Measurement Setup of Temperature Reading Verification	195
Figure 4.75	(a) Linear Regression Between Reference and App-Recorded Temperatures for the PCB-Based Antenna and (b) Mean Temperature Difference with STD	196
Figure 4.76	(a) Linear Regression Between Reference and App-Recorded Temperatures for the D4-HGS Antenna and (b) Mean Temperature Difference with STD	197
Figure 4.77	(a) Second Linear Regression Between Reference and App-Recorded Temperatures for the D4-HGS Antenna and (b) Mean Temperature Difference with STD	199
Figure 4.78	(a) Final Linear Regression Between Reference and App-Recorded Temperatures for the D4-HGS Antenna and (b) Mean Temperature Difference with STD	199
Figure 4.79	(a) The Interface of the Enhanced Mobile App and (b) the Flow of Temperature Reading Through the Enhanced Mobile App	200
Figure 4.80	Temperature Reading of NFC Tag Sensor and Reference Thermometer	202
Figure 4.81	Mean Temperature Difference with STD for Cold Condition	203
Figure 4.82	Mean Temperature Difference with STD for Room Condition	203
Figure 4.83	Mean Temperature Difference with STD For Hot Condition	204

Figure 4.84	NFC Tag Attached to Different Types of Foods: (a) Apple, (b) Yoghurt, (c) Peanut Butter Jar, (d) Bread, (e) Pizza, and (f) Lasagna	206
Figure 4.85	The Measured Tag Reading Range and Temperature for Various Types of Foods at Three Temperature Ranges - Cold, Room, and Hot Temperatures	207
Figure 4.86	D4-HGS NFC Tag with Temperature Sensing Circuit Incorporated with an Amorphous Sheet	207

LIST OF SYMBOLS

Symbols

R	Resistance
L	Inductance
C	Capacitance
Q-factor	Quality Factor
I	Current
V	Voltage
ρ	Resistivity
A	Cross sectional area
σ	Conductivity
S_p	Maximum peak height
S_v	Maximum peak depth
S_z	Total of S_p and S_v
S_a	Arithmetical mean height
S_q	Root mean square height
f_r	Resonance frequency
H	Magnetic field strength
S_{11}	Reflection coefficient
β	Material coefficient of thermistor

R_s	Sheet resistance
R_a	Antenna resistance
L_a	Antenna inductance
θ	Bending angle
ε_0	Permittivity of free space
μ'	Permeability of the magnetic material
μ''	Material loss
δ	Skin depth
T_g	Glass transition temperature
C_{int}	Internal capacitance
C_{tun}	Tuning capacitance

LIST OF ABBREVIATIONS

Abbreviations

2D	Two Dimensional
3D	Three Dimensional
ADC	Analogue-To-Digital Converter
ADS	Advanced Design System
AFM	Atomic Force Microscopy
CEDEC	Collaborative Microelectronic Design Excellence Centre
CST	Computer Simulation Technology
DIW	Direct Ink Writing
FR-4	Flame Retardant Grade 4
FSFS	Flexible Sintered Ferrite Sheet
GO	Graphene Oxide
HCG	Hybrid Carbon-Graphene
HF	High-Frequency
HGS	Hybrid Graphene-Silver
IC	Integrated Circuit
IEC	International Electrotechnical Commission
IoT	Internet of Thing
ISO	International Organization for Standardization
NFC	Near Field Communication

P2P	Peer-to-Peer
PCB	Printed Circuit Board
PDMS	Polydimethylsiloxane
PET	Polyethene Terephthalate
PGA	Programmable Gain Amplifier
PTE	Power Transfer Efficiency
PVA	Polyvinyl Alcohol
RCF	Resistivity Correction Factor
RFID	Radio Frequency Identification
rGO	Reduced Graphene Oxide
SC	Silver Conductor
SDG	Sustainable Development Goals
SEM	Scanning Electron Microscopy
SMD	Surface-Mount Device
STD	Standard Deviation
TPU	Thermoplastic Polyurethane
UHF	Ultra-High Frequency
VNA	Vector Network Analyzer
VQFN	Very thin Quad-Flat No-leads
WHO	World Health Organization

CHAPTER 1
INTRODUCTION

1.1 Research Background

Food safety is a critical global health issue as it is directly related to human health. In both developed or developing countries, foodborne disease surveillance has become an essential component of food safety systems. According to World Health Organization (WHO), foodborne disease causes 600 million people worldwide to fall ill every year, with 420,000 deaths, including 125,000 children under the age of five [1]. Eating food contaminated with bacteria, viruses, parasites, or chemical substances such as heavy metals is the key factor in foodborne illness.

Food spoilage can occur at any stage of the supply chain. One of the major factors contributing to food spoilage is improper storage conditions and temperature fluctuations during storage and transportation [2][3]. Temperature instability accelerates microbial growth, leading to physical and chemical degradation, including changes in texture, colour, and taste, which ultimately increase the risk of foodborne illnesses and food poisoning [4]. To address this issue, reliable real-time temperature monitoring systems are essential throughout the food supply chain to enable early detection of unsafe conditions, helping to maintain food quality, reduce wastage and minimize health risks in the food industry [5].

Existing temperature monitoring technologies, such as thermometer, optical temperature sensors, and infrared thermal imaging, rely on battery-powered electronic sensors, which pose multiple challenges, including limited lifespan, frequent replacements, high operational costs, and environmental hazards [6]. Batteries contain hazardous chemicals, such as lithium and mercury, which pose potential safety risks if they leak or come into contact with food packaging materials. Given these limitations, there is a strong need for a wireless and battery-free temperature monitoring system that can be seamlessly integrated into food packaging and enhance food safety in storage, distribution, and retail logistics.

Near Field Communication (NFC) technology has emerged as a promising solution, offering battery-less operation and real-time data retrieval [7][8]. NFC is a low-powered contactless communication technology that operates at 13.56 MHz. By

placing an NFC-enabled device (such as smartphone, tablet, or NFC reader) close to an NFC tag, the energy will be harvested and able to power up the chip together with other external electronics components including microcontrollers and sensors. The NFC tag, consisting of a coil antenna and a chip, plays a crucial role in the performance of the NFC communication system [9]. The selection of conductive materials and the geometrical design parameters of NFC tag antennas are crucial factors in developing efficient systems for food temperature monitoring applications.

Traditional NFC antennas rely on metal-based conductive materials such as silver, copper, or aluminum, which offer high conductivity and commercially available in the market [10][11][12]. However, these materials have limitations in flexibility, environmental stability, and sustainability [13]. Recent advancements in graphene-based conductive materials offer a promising alternative due to their lightweight, flexible, biocompatible and chemically inert properties [14][15][16]. However, the practical implementation of graphene-based NFC antennas remains a challenge due to limited research on the use of graphene-based materials for NFC tag antennas in temperature monitoring applications, where flexibility and sensitivity to the surface structure and environmental conditions are the main concern. Most previous studies on graphene antennas have focused on dipole-type antennas operating in the terahertz band [17], [18] or UHF-RFID operating at 860 – 960 MHz [19], [20], [21].

Therefore, this research aims to investigate the characteristics and feasibility of a newly developed graphene-based conductive materials for NFC tag antenna applications, particularly in temperature monitoring of food packaging. It addresses challenges related to antenna electrical properties, antenna design, flexibility, environmental sensitivity, fabrication limitations and integration into real-world food packaging environments.

1.2 Problem Statement

Traditionally, NFC tag antennas have been fabricated using metal-based conductive materials, such as copper, aluminium and silver, due to their high electrical conductivity, which contributes to efficient NFC tag performance. However, these materials present several challenges that limit their suitability for food safety monitoring applications. One major drawback is the oxidation of the metal-based materials. Copper, for instance, is highly conductive but prone to oxidation when

exposed to ambient conditions, forming a layer of copper oxide that reduces antenna efficiency and shortens its operational lifespan [22]. Additionally, the chemical etching processes involved in fabricating copper-based antennas generate toxic waste, raising serious environmental and health concerns, thus making it unsuitable for direct integration into food packaging [23]. An alternative to copper is the use of silver or aluminum-based conductive materials. However, these materials are mechanically brittle and prone to cracking under bending or flexing, which leads to degraded electrical properties [13][24]. Furthermore, printed silver inks require high-temperature sintering to achieve optimal conductivity, which limits compatibility with low-cost, flexible, and temperature-sensitive substrates commonly used in food packaging applications [25]. Given these limitations, graphene-based conductive inks have emerged as a promising alternative due to their flexibility, biocompatibility and resistance to oxidation [14]. However, there is limited research on graphene-based materials applied for NFC antenna design, which require further research to evaluate their performance, robustness, and compatibility in food safety monitoring application.

Food packaging comes in a variety of materials, such as plastic, carton boxes and aluminium foil, and in various forms, including square, rectangular, cylinder and irregular shapes, depending on the food type. Since the NFC tag will be attached to the food packaging, it is critical for the tag to be flexible enough to conform to different packaging surfaces, ensuring consistent functionality even when bent. Additionally, the storage and delivery conditions of food vary significantly depending on the type of foods. For example, fruits and vegetables stored at low temperatures in refrigerators are exposed to water vapor and condensation on their surface, which could affect NFC tag performance. Meanwhile, hot food deliveries, such as pizza, are exposed to high temperatures during transportation to maintain food quality. Therefore, it is essential to investigate the robustness of the NFC tag in terms of its sensitivity to moisture exposure, temperature variations, and different types of food packaging.

Conventional NFC tag antennas with integrated sensor circuits are typically fabricated on rigid printed circuit board (PCB-based), as proposed by [26][27]. The mounting of chips and surface-mount device (SMD) components can be easily performed using reflow soldering. However, PCB-based NFC tag antennas face challenges in adapting to curved structures, limiting their suitability for flexible packaging applications. To address this, the integration of NFC tags with flexible circuits, where both components are printed using graphene-based conductive

materials, has been proposed. Nevertheless, significant challenges remain, particularly in fabrication and achieving reliable performance for temperature monitoring applications, necessitating further investigation and enhancements to the NFC system.

1.3 Objectives

The objectives of this research are as follows:

a) To design and optimize an NFC tag antenna using various printed conductive materials, including silver conductor (SC), hybrid graphene-silver (HGS), and hybrid carbon-graphene (HCG).
b) To evaluate the robustness of graphene-based NFC tag antenna performance across various surface structures and environmental conditions.
c) To validate the graphene-based NFC tag with flexible circuit integration towards temperature monitoring application.

1.4 Scope of Work

The research focuses on evaluating the feasibility of graphene-based printed conductive materials for NFC tag antenna applications in temperature monitoring, with particular emphasis on the robustness of the tag antenna when attached to various structures and exposed to different environmental conditions.

A total of four antenna geometrical designs (D1–D4) were developed and evaluated using three conductive materials: silver conductor (SC), hybrid carbon-graphene (HCG) and hybrid graphene-silver (HGS). The scope of this study includes:

i. Characterization of printed conductive materials (SC, HGS, and HCG), through conductivity testing, surface morphology and roughness evaluation, and thickness measurement.
ii. Design, simulation and optimization of coil antennas for NFC tags operating at 13.56 MHz using CST Studio Suite.
iii. Fabrication of flexible NFC tag antennas using inkjet printing, screen printing and direct ink writing techniques.

iv. Systematic optimization of antenna tuning circuit configurations using Optenni Lab.
v. Investigation of mechanical flexibility and environmental sensitivity, including bending, moisture exposure, temperature variation, and metal interference.
vi. Comparative analysis of magnetic sheet materials to mitigate eddy current effects when the tag is attached to metallic surfaces.
vii. Enhancement of the NFC temperature monitoring application to ensure compatibility with graphene-based NFC tag antennas.
viii. Reliability validation of the flexible graphene-based NFC tag in real-world food packaging temperature monitoring scenarios.

Although four antenna geometries were initially designed and evaluated, only the D4-HGS configuration proceeded to full robustness and system-level validation. The other designs and material combinations were excluded based on preliminary electrical performance evaluation, including resistance, inductance, and read range, where D4-HGS demonstrated the most balanced performance and design stability. Other limitations in this research is regarding the long-term reliability, where long-term aging effects, mechanical fatigue under repeated bending cycles, and large-scale manufacturing scalability were not investigated in this study.

1.5 Significance of Study

This research will contribute to the development of an NFC system with energy harvesting capability as a method for temperature monitoring in the food supply chain. This approach addresses the limitations of previous methods, which are often power-consuming, bulky, and require batteries to operate, which needs to be carefully and strictly managed due to their hazardous substances and generally dangerous if ingested. Moreover, this research aligns with the United Nations' 3rd Sustainable Development Goals (SDG), which aims to ensure healthy lives and promote well-being for all.

The NFC system offers higher reliability, enhanced security and reduced device cost and complexity by eliminating the need for a dedicated reader. Peer-to-peer (P2P) communication can be established directly between NFC tags and NFC-enabled devices, such as smartphones, enabling seamless integration and usability. The main focus of this research is the development of an NFC tag antenna using graphene-based

conductive ink, which contributes to a cleaner and safer environment since graphene is chemically inert compared to other metal-based ink like silver, copper, and aluminium.

Additionally, the flexibility and sensitivity of the tag antenna are critical factors in achieving optimal NFC tag performance. Since the tag antenna will be attached to various food packaging structures and high possibility to be exposed to different environmental conditions, it is essential to evaluate its robustness and reliability. By testing antenna performance under temperature, moisture, and mechanical bending conditions, this research fills the identified research gap by providing the first systematic evaluation of printed graphene-based NFC antennas for food packaging applications.

Through proper investigation and the development of a flexible temperature sensor circuit, this research aims to optimize the performance of the NFC system, ensuring its effectiveness and reliability in real-world food monitoring applications while supporting the global effort toward safer, more sustainable, and battery-free smart packaging solutions.

1.6 Thesis Organization

This thesis comprises five chapters, which have been structured to discuss the work and findings of this study. The organization of the thesis is as follows:

Chapter 1 provides the background of the research and identifies the problems addressed in this study. This chapter also presents the research objectives, along with the scope and limitations of the research.

Chapter 2 gives an overview of the fundamental principles of the NFC system, including its working mechanism, standard protocols and key performance evaluation parameters for NFC tag antennas. Additionally, this chapter reviews previous studies on NFC tag antenna characteristics, focusing on design aspects, printed conductive materials and electrical properties. The literature review also covers various methods used to mitigate the eddy current effect and the basic principles of temperature monitoring sensors.

Chapter 3 outlines the research methodology, covering the characterization of conductive materials, followed by the antenna design process and tuning circuit optimization, using CST Studio Suite and Optenni Lab software, respectively. This chapter also details the fabrication methods and measurement techniques used for

evaluating the robustness and performance of the antenna. The final section describes the development of the temperature monitoring system, including fabrication procedures and associated limitations.

Chapter 4 presents the simulation and experimental results of NFC tag antennas printed using SC, HGS and HGS conductive materials. The performance of the NFC tag antenna is examined in terms of antenna electrical parameters, including antenna inductance, resistance, reflection coefficient, power transfer efficiency and tag reading range. Additionally, the flexibility and sensitivity of the graphene-based tag antenna are evaluated and a comparative analysis of magnetic sheet materials used to mitigate the eddy current effect are evaluated. Finally, the functionality and reliability of the fabricated graphene-based tag antenna integrated with the temperature monitoring circuit are verified, along with enhancements made to the temperature monitoring app.

Chapter 5 concludes the thesis by summarizing the research findings and presenting suggestions for future work. The contributions of this research are compiled in this chapter, along with recommendations for potential improvements and future developments.

CHAPTER 2
LITERATURE REVIEW

2.1 Introduction

In this chapter, previous works related to the research topic are discussed. The chapter begins with an overview of NFC technology, including the components involved in the NFC system, its working principle, and the modes of operation. Next, Section 2.3 presents a detailed review of the conductive materials used for NFC antennas, along with the electrical and structural properties involved in material characterization, including conductivity, surface morphology, and surface roughness. Section 2.4 reviews NFC tag antenna designs from previous studies and the antenna parameters used to evaluate performance. The robustness of the antenna, including its mechanical flexibility, sensitivity to metallic surfaces, moisture resistance, and thermal stability, is also discussed based on prior research. Finally, the application of NFC systems for temperature monitoring is reviewed to support further discussion. In this research, temperature monitoring is focused on food packaging, as it plays a critical role in preserving product quality and ensuring consumer safety. Issues related to packaging structure, material type, and exposure to environmental factors such as temperature variations and moisture have been carefully considered to ensure reliable and accurate temperature monitoring using the NFC system.

2.2 Overview of NFC System Technology

NFC technology has its roots in the late 1800s, when Thomas Edison conducted experiments with radio frequencies. In 1983, Charles Walton patented a new type of RFID technology, which laid the foundation for NFC. Subsequently, in 2002, Sony and NXP Semiconductors collaborated to pioneer a new form of NFC technology. The progress of NFC continued in 2004, when an official NFC Forum was established, with companies such as Sony, Philips, and Nokia dedicating efforts to integrating NFC into their production processes. Notably, in 2006, Nokia launched the first NFC-enabled phone, emphasizing the technology's application in information sharing, rather than merely being limited to a payment method. The year 2009 marked a significant

milestone, as the NFC Forum established peer-to-peer (P2P) standards, facilitating data transmission and reception between NFC-enabled phones. Following this development, between 2010 and 2016, a variety of applications emerged, including NFC-enabled Android phones, smart tags, secure transactions, and Felica cards. As technology progressed, NFC found diverse applications, extending its utility to various sensors and being extensively utilized in IoT, medical, and home applications by the year 2020. [28].

NFC is a short-range wireless communication technology operating at 13.56 MHz, used for contactless data exchange between devices close to each other [29] [30]. It operates effectively within a practical working distance of approximately 10 cm, making it ideal for short-range interactions. In terms of data transfer rates, NFC offers a typical range of 106 to 424 kbit/s, with a maximum rate of up to 848 kbit/s [31]. This technology has found its way into a wide array of devices, including smartphones, smart cards, and other handheld gadgets. Mobile phone manufacturers, banking institutions, medical and security departments have already harnessed NFC's potential to simplify content delivery, enable information sharing, and facilitate effortless transactions [28][32]. With billions of mobile phone users worldwide, NFC holds tremendous promise to revolutionize the payment ecosystem and beyond.

2.2.1 NFC Components

The fundamental elements of the NFC system comprise a reader and a tag, as illustrated in Figure 2.1. An NFC tag is composed of an antenna coil and a chip. The tag can function in either active or passive modes, depending on its power supply. Being passive devices, NFC tags operate without the need for external batteries, drawing their power from the electromagnetic field generated by the reader during communication. When the tag is placed in a magnetic field generated by the reader antenna, the tag antenna harvests energy for the tag's operation to communicate with the reader [5]. A strong signal (radio frequency waves) from the reader is required to activate the tag, and the returned signal from the tag is much lower than the emitted signal from the reader. Consequently, this tag’s reading range is smaller than that of the active tag [33]. However, due to its small size and low manufacturing cost, it is highly demanded in high-volume manufacturing.

The active tag has an on-board power supply, for example, a battery and a transmitter. It does not require a strong signal from the reader, unlike the passive tag, as its power supply can activate it. Once the power supply is activated, the tag will automatically transmit the data to the reader. In certain conditions, the active tag can also initiate communication with the reader or other tags. This tag is relatively expensive and is typically used to track high-value goods, such as vehicles. It can also be used in conjunction with an external sensor to monitor temperature, humidity, and other environmental conditions [34].



Figure 2.1 Example of NFC (a) Readers and (b) Tags

2.2.2 NFC Working Principle

The principle of magnetic induction, as described by Faraday, forms the foundation for near-field or inductive coupling between a reader and a tag. The reader generates a large alternating current through its reading coil, creating an alternating magnetic field in its vicinity. When a tag, incorporating a smaller coil, is placed within this magnetic field as illustrated in Figure 2.2, an alternating voltage is induced across it. By rectifying this voltage and coupling it to a capacitor, a reservoir of charge accumulates, providing power to the tag chip.

In near-field coupling, tags utilize load modulation to transmit data back to the reader. When the tag draws any current from its coil, it generates its minor magnetic field, which opposes the reader's field. Consequently, the reader's coil detects a slight increase in current flow through it. This current variation is proportional to the load applied to the tag's coil, a phenomenon referred to as load modulation. To meet specific requirements, such as the number of ID bits, data transfer rate, and error correction, various modulation encodings can be employed, thereby enhancing the reliability of the communication channel by reducing noise-induced errors [35].

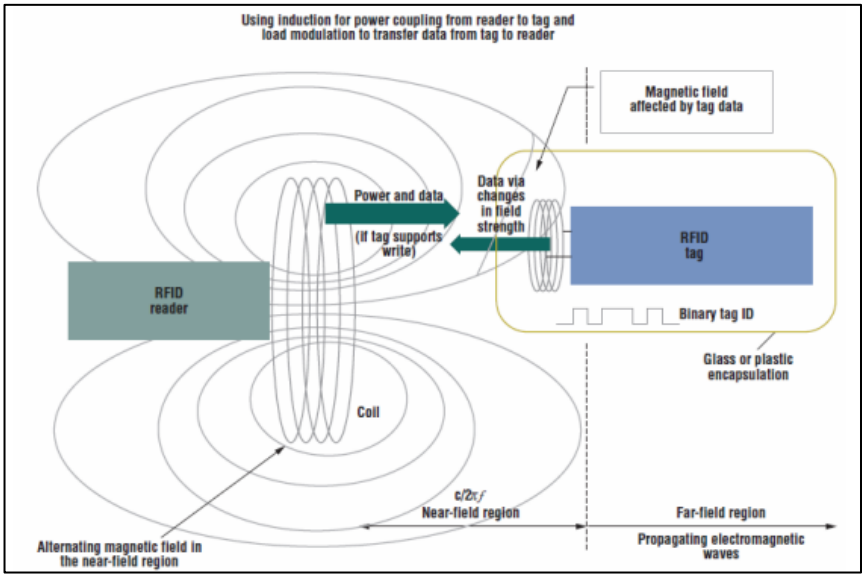


Figure 2.2 Near Field Communication Working Principle [35]

2.2.3 NFC Operation Mode

Three modes of operation are available in NFC devices, which are based on the ISO/IEC 18092, ISO/IEC 14443 and ISO/IEC 15693 standards [36][37][38], including read/write, card emulation, and peer-to-peer.

i) Reader/writer mode

The reader/writer mode in NFC is about the communication between an NFC-enabled mobile phone and an NFC tag, facilitating the process of either reading or writing data to these tags. Internally, it comprises two distinct modes: reader mode and writer mode. In reader mode, the initiator retrieves data from an NFC tag that already contains the requested information. Conversely, in writer mode, the mobile phone takes

on the role of the initiator, allowing data to be written onto the tag. An application example is a smart poster [39]. This mode is based on ISO/IEC 14443 or 15693.

ii) Peer to Peer mode

The peer-to-peer mode enables information exchange between two NFC-enabled mobile devices, allowing them to share various types of data, including contact records, text messages, and more. Data transmission occurs over a bidirectional half-duplex channel, meaning that when one device is transmitting, the other listens and then begins transmitting after the first device finishes. This mode has practical applications in scenarios such as sharing Bluetooth or Wi-Fi link setup parameters, conducting money exchanges between wallets, and exchanging data, including virtual business cards or digital photos [39]. This mode is based on ISO/IEC 18092.

iii) Card emulation mode

Card emulation mode enables an NFC-enabled mobile device to function as a contactless smartcard, facilitating contactless payments and ticketing without requiring modifications to the existing infrastructure. In this mode, the NFC-enabled mobile phone does not generate its radio frequency (RF) field; instead, the NFC reader generates the necessary field. Supported communication interfaces for the card emulation mode include ISO/IEC 14443 and 15693.

2.2.4 Equivalent Circuit Model of NFC System

Equivalent Circuit (EC) models use a lumped-element approach utilizing basic electrical components, including resistors (R), inductors (L), and capacitors (C), to describe the resonant and impedance characteristics of the system. Figure 2.3 illustrates a wireless power transfer model of an NFC system consisting of a reader and a tag [26]. NFC systems work through magnetic coupling between two coils, represented by the reader antenna and the tag antenna. The reader antenna is modelled as an inductance, L_1 and a series resistance, R_1, which accounts for energy losses. A matching network is included to match the reader antenna with the integrated circuit (IC) and to ensure resonance at the operating frequency of 13.56 MHz [40].

Similarly, the tag antenna is modelled by an inductance, L_2, in series with a resistance, R_2, representing its losses. A parasitic capacitance, C_p, which models unwanted capacitance from the antenna structure, is connected in parallel with L_2 and R_2. The impedance of the NFC chip is nonlinear and varies with the received power. It is modelled as a capacitor (C_{IC}) in parallel with a resistor (R_{IC}). A tuning circuit is placed between the antenna and the chip to ensure the circuit resonates at the desired frequency. This tuning circuit varies depending on the antenna characteristics and chip properties; one example is a parallel tuning capacitor, C_{tun} [26].

The efficiency of energy transfer between the reader and the tag depends on the coupling factor, k. This value ranges from 0 to 1 and indicates how effectively the magnetic field from the reader coil links with the tag coil [41]. A higher coupling coefficient results in more efficient energy transfer. It depends on the geometry of the antennas, the distance between the coils, and their alignment [40].

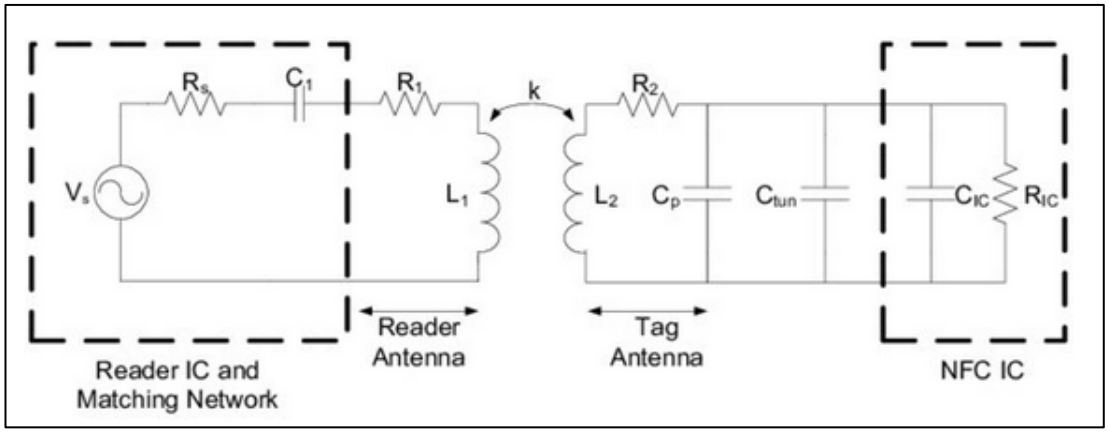


Figure 2.3 NFC Reader and NFC Tag Equivalent Circuit Model [26]

The EC of the tag antenna varies depending on the environment to which the antenna is exposed. For example, the implanted NFC tag antenna proposed by Boada et.al showed an increase in parasitic capacitance due to the high permittivity of the skin layer, which contributed to a shift in the tag's resonance frequency [42]. The increased dielectric losses of the skin layer were represented by a parallel resistance, R_p, added to the antenna's EC, as depicted in Figure 2.4 (a). The performance of the implanted antenna was further improved by encapsulating it with a silicon coating, which minimized resonance frequency detuning and increased the Q-factor. In the EC model, the integration of the silicon coating is represented by a capacitance, C_s, connected in series with the resistance R_p, as illustrated in Figure 2.4 (b).

The EC developed by Tounsi et al., as shown in Figure 2.5, illustrates the electrical interactions between the coil inductor (represented by Ls, Rs and Cs), the shielding material and the conductive plate. The shielding layer is modeled as a series connection of inductance, Lp and resistance, Rp1, which are in parallel with another resistance Rp2 to represent the eddy current and magnetic loss effects of the conductive plate [43]. A mutual inductance Msp is added between the spiral inductor and the shielding layer to model magnetic coupling. The proposed model effectively captures the physical effects of conductive and ferromagnetic plates on inductance, losses, and resonance behaviour. Additionally, parasitic capacitances, Cg, represent the capacitance between the inductor and the shielding plate, and C1 accounts for the capacitance between the inductor coil and the ground plane. These capacitors are symmetrically split on both sides of the inductor in the model.

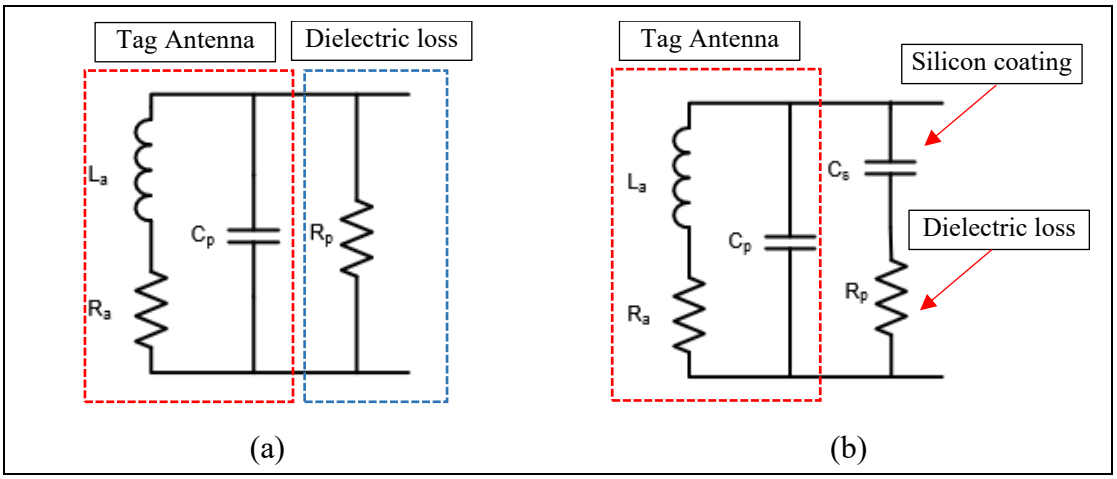


Figure 2.4 Equivalent Circuit of NFC Tag Antenna with (a) The Increase of Dielectric Loss and (b) The Introduction of Silicon Coating [42]

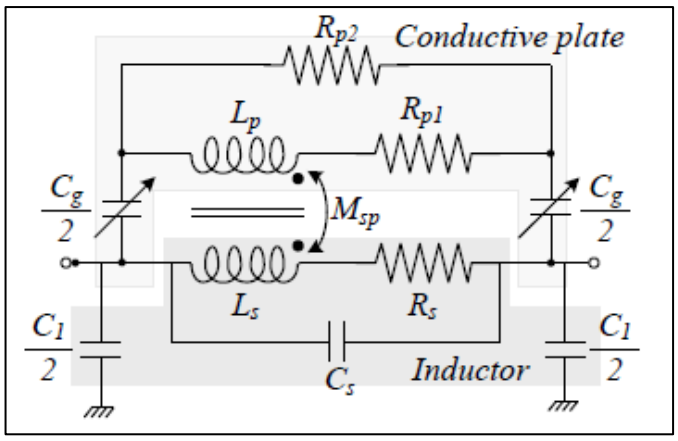


Figure 2.5 Equivalent Circuit of Coil Inductor with the Existence of Conductive Plate and Shielding Material [43]

2.3 Conductive Materials

Conductive materials play a fundamental role in the performance of NFC tag antennas, as their electrical, mechanical, and chemical properties directly impact antenna efficiency, conductivity, and durability. These materials enable efficient signal transmission and power transfer, ensuring reliable communication between the NFC tag and the reader. Conductive materials are available in various forms, including bulk metals and printed conductive inks.

2.3.1 NFC Antenna Conductive Materials and Fabrication Techniques

The most commonly used conductive materials for fabricating NFC tag antennas are metal-based materials such as silver, gold, copper, and aluminum. These materials are widely utilized due to their high conductivity and easy availability in the market [44][45]. Copper is typically used in the form of bulk metal and is often etched onto metal-plated laminates such as FR-4 and polyimide substrates. This process is relatively simple and cost-effective. However, the etching process generates a significant amount of metal salts and chemical waste products, which are environmentally hazardous [46]. Another form of copper material, such as copper tape and foil, is a more environmentally friendly alternative, as it can be directly adhered to flexible substrates, including paper, fabric, and polyethene terephthalate (PET) [47]. However, cutting copper tape into the coil geometry of an NFC antenna is quite challenging, which can result in inaccurate dimensions and affect performance.

Furthermore, another major drawback of copper material is its susceptibility to oxidation when exposed to ambient conditions, which degrades the performance of the NFC tag antenna, reduces electrical conductivity, and shortens the application's lifespan. One way to prevent oxidation is by applying a protective coating, but this increases the overall cost [48].

Meanwhile, silver materials are resistant to oxidation and are usually printed on flexible substrates, due to their high durability compared to other metal-based materials, such as aluminium. The fabrication method for silver material is typically achieved through inkjet printing or direct ink writing, which is more environmentally friendly and compatible with various stretchable and flexible substrates, such as Polyvinyl alcohol (PVA), photo paper, and PET [49][10][11]. The printing of NFC antennas using the inkjet printing method, which involves multiple stages including substrate preparation, material deposition, material sintering, cutting the substrate, and mounting the component, was discussed in [45]. In this process, silver nanoparticles were used as the conductive material, while PET was used as the substrate. However, high sintering temperatures are required to achieve the optimal conductivity, which limits the application of silver material to high-temperature-resistant substrates only [25]. Additionally, the mass production and raw materials costs are significantly higher for silver nanoparticles compared to other metal-based materials, such as copper and aluminum making them less suitable for low-cost applications.

Carbon-based materials have received significant attention from researchers as an alternative to metal-based materials due to their low cost, resistance to oxidation, chemical stability, and mechanical flexibility [14]. Carbon-based materials are those in which carbon atoms form covalent bonds with other carbon atoms or elements, resulting in various forms, such as carbon nanodiamonds, fullerenes, graphite, carbon nanotubes, and carbon nanofibers [50]. Among these forms, graphite is the most stable allotrope of carbon, with a single layer of graphite arranged in a two-dimensional honeycomb lattice known as graphene [51]. Initially, research on graphene-based antennas primarily focused on the terahertz band [52][53][54], and was mainly focusing on dipole-type antennas. However, since 2015, several studies have explored graphene-based antennas for much lower ranges, including ultra-high frequency (UHF) and microwave bands, as presented in [55][56][57]. The use of graphene in NFC antennas is also growing, but research on high-frequency (HF) graphene-based NFC antennas remains limited.

Different types of graphene materials have been used in NFC antennas, including graphene flakes [58][59], graphene oxide [13][60][61] and graphene paper [62] using various printing techniques such as screen printing, spray printing, and laser engraving. Other printing techniques, such as inkjet printing, have been used to print graphene-based materials on flexible substrates for electronic circuits and sensors [63][64], but they have not yet been implemented for NFC antenna printing. One of the main challenges with graphene-based materials is that the surface resistivity of single-layer graphene is higher than that of metal-based materials [57]. This contributes to high power loss, lower conductivity of the materials, and limits the efficiency of NFC antennas. Illustrations of some of the fabricated antennas are shown in Figure 2.6, while the fabrication methods and the limitations of the respective conductive materials are presented in Table 2.1.

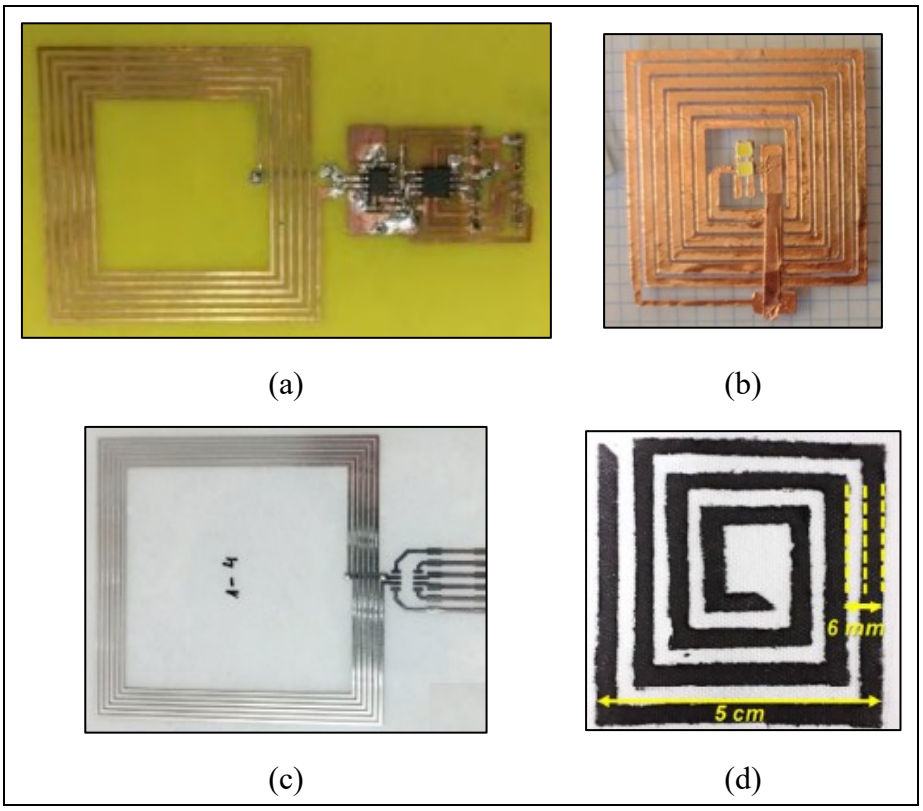


Figure 2.6 Fabricated NFC Antenna with Various Conductive Materials: (a) Etched Copper, (b) Copper Tape, (c) Printed Silver Ink and (d) Graphene Oxide [26][65][46][61]

Table 2.1
The Fabrication Methods and the Limitations of Several Conductive Materials

Conductive Materials		**Printing method**	**Limitations**	**Ref**
Metal-based	Copper	Etching	Susceptibility to oxidation and environmentally hazardous	[26]
	Copper tape	Manual cut and tape	Inaccurate dimension	[65]
	Silver ink	Inkjet printing	High sintering temperature and costly	[46]
Carbon-based	Graphene flakes	Screen printing	Low conductivity (~10^5) and low resolution	[58]
	Graphene paper	Robotic cutter plotter and laser engrave	Low conductivity (~10^5) and slow processing speed	[62]
	Graphene nano flakes	Screen printing	Low conductivity (~10^4) and low resolution	[59]
	Graphene oxide	Spray printing	Low resolution and rough edges	[61]

Several methods have been employed to enhance the conductivity of graphene-based materials, including the use of binders such as ethyl cellulose (EC) to prepare graphene ink [21]. However, this method is incompatible with heat-sensitive substrates, such as paper, PET, and textiles, as it requires high-temperature thermal annealing of up to 300 °C. Other methods suitable for low-temperature resistance substrates include graphene layer stacking [19] and rolling compression [22][23] techniques. However, achieving uniform compression and stacking poses challenges, as excessive compression and irregular stacking may lead to degradation of conductivity and graphene performance. One of the most promising methods for increasing conductivity is the incorporation of metallic nanoparticles with graphene [13], as it is compatible with a wide range of substrates and is mechanically more stable. However, careful material selection and processing techniques must be considered to avoid external resistance. Previously, hybrid graphene-based materials have mainly been applied in flexible electronics and sensors [13],[24],[25], and to date, no high-frequency (HF) antenna application has been demonstrated based on hybrid graphene-based materials.

2.3.2 Electrical and Structural Properties of Conductive Material

In developing the NFC tag antenna, it is crucial to study the electrical and structural properties of the conductive materials, including conductivity, surface morphology, surface roughness, and thickness, as these factors directly influence the antenna's electrical and mechanical performance. Conductivity determines the efficiency of signal transmission and power transfer, while surface morphology and roughness affect current distribution, impacting signal losses [66][67]. Thickness plays a crucial role in determining the antenna's resistance and flexibility, particularly for printed antennas [68].

2.3.2.1 Conductivity

Conductivity, σ is the ability of the material to conduct electric current. The SI units for conductivity is siemens per meter (S/m). The two-probe and four-probe methods can be used to measure the conductivity of conductive materials [69]. The two-probe method is the simplest way to measure conductivity, where current (I) is applied between two electrodes positioned on the materials, and the resultant voltage drop (V) across the same electrode is measured, as depicted in Figure 2.7[70]. Using Ohm's law, the resistance (R) of the sample is calculated using Equation (2.1). Conductivity is inversely proportional to the resistivity, ρ, as in Equation (2.2), where resistivity can be determined from resistivity Equation (2.3), with A indicates the cross-sectional area (w $\times$ t) and L is the probe spacing. However, a significant drawback of this method is that it includes contact resistance (R_c) at the interface between the probes and the sample, which can lead to measurement inaccuracies, especially for low-resistance or thin-film materials. Additionally, the two-probe method is susceptible to substrate interference, particularly when measuring printed conductive materials on flexible substrates. Despite these limitations, the two-probe method remains useful in measuring bulk materials with higher resistance, where contact resistance effects are negligible.

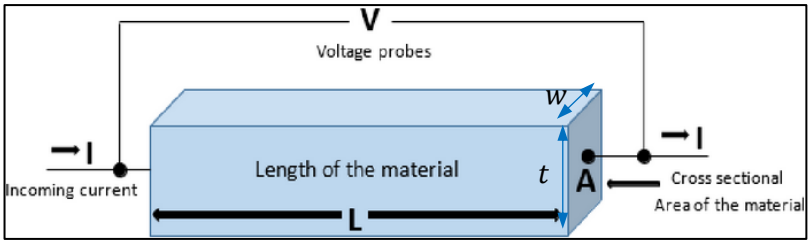


Figure 2.7 Measurement of Electrical Conductivity Using the Two-Probe Method [70]

$$R = \frac{V}{I} \tag{2.1}$$

$$\sigma = \frac{1}{\rho} \tag{2.2}$$

$$\rho = \frac{R \cdot A}{L} = \frac{R \cdot w \cdot t}{L} \tag{2.3}$$

The four-probe method involves injecting a known current (I) into the sample through the two outer probes and assessing the voltage drop (V) across the inner probes, as depicted in Figure 2.8 (a). The probes are arranged linearly on the sample's surface, establishing point connections. This configuration is known as a collinear probe array. The four-point probe configuration can also be arranged in a square array form, as depicted in Figure 2.8 (b), where the injected current flows through the upper probes, while the measured voltage drop occurs through the lower probes [71]. The four-probe technique yields a more precise resistivity measurement by isolating the voltage measurement from the current injection, thereby reducing the influence of contact and lead resistance. The sheet resistance of the thin film, R_s, can be determined using Equation (2.4), where RCF is the resistivity correction factor. RCF can vary depending on the sample shape, probe arrangement, and boundary conditions. The given RCF value in Equation (2.5) is specifically for an infinitely large thin film but changes for different geometries. The conductivity can be calculated using Equation (2.6), where t is the thickness of the conductive sample. This four-probe method is particularly advantageous for printed conductive materials and thin-film, as high contact resistance can distort results in the two-probe technique.

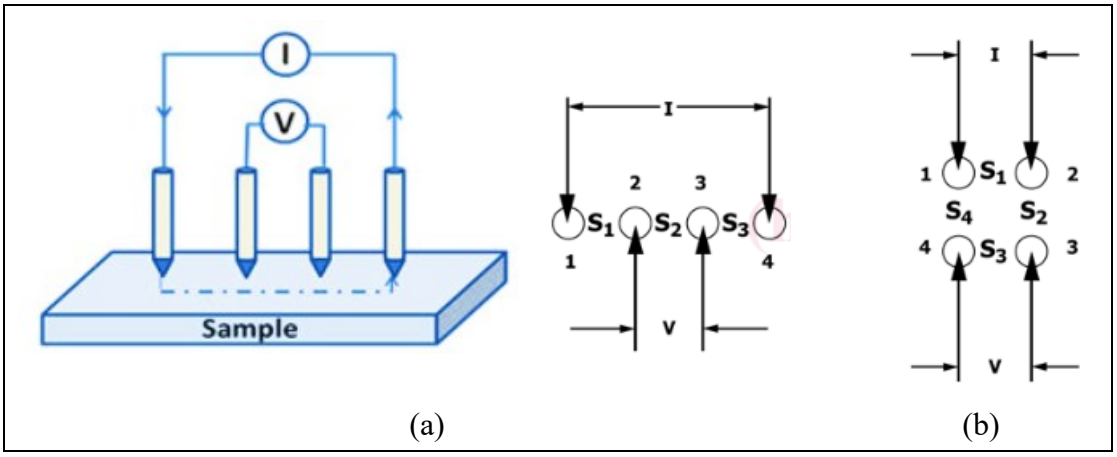


Figure 2.8 Measurement of Electrical Conductivity Using the Four-Probe Method Through (a) A Collinear Probe Array and (b) A Square Array

$$R_s = RCF \cdot \frac{V}{I} \tag{2.4}$$

$$RCF \approx \frac{\pi}{\ln 2} \tag{2.5}$$

$$\sigma = \frac{1}{R_s \cdot t} \tag{2.6}$$

Comparing the two methods, the two-probe method is advantageous due to its simplicity and ease of implementation, making it suitable for bulk conductive materials such as copper foils or thick silver films. However, for thin films, low-resistance printed materials, and flexible electronics, the four-probe method is preferred as it provides higher accuracy by eliminating contact resistance effects.

2.3.2.2 Surface Morphology and Roughness

Surface morphology refers to the structural features and texture of a material's surface, while surface roughness quantifies microscopic height variations across the surface. Observing surface morphology is crucial in printed conductive films, as the presence of voids, grain boundaries, or non-uniform deposition can lead to resistance variations and impact charge transport, electrical losses, and mechanical flexibility. Several characterization techniques are commonly used to analyze the surface morphology of conductive materials, including Atomic Force Microscopy (AFM) and

Scanning Electron Microscopy (SEM) [72]. These techniques help in understanding particle size, porosity, and the distribution of surface features. AFM is also capable of being used for roughness measurement and nanoscale imaging. Meanwhile, SEM is ideal for visualization of high-resolution surface morphology.

Surface roughness is measured by the deviations in the direction of the real surface's normal vector from its ideal form, where higher values indicate rougher surfaces and lower values indicate smoother surfaces. When a current is applied, a smooth surface with few irregularities may offer lower resistance, leading to higher conductivity. However, a rough surface may generate increased scattering of charge carriers, adding resistance to the flow of electricity [73]. Furthermore, at the microscopic level, surface morphology, such as peaks and valleys, influences the electron mean free path and consequent electrical behaviour of the plated material. According to physical principles, as electrons pass across a metallic surface, any surface imperfection can cause electron scattering, which impedes the flow of electrical current and thus affects conductivity measurements.

The unevenness can be evaluated using the height parameters (S_a, S_q, S_v, S_p and S_z) as depicted in Figure 2.9. Sa and Sq are the most widely used roughness parameters, as they provide stable results and are not significantly influenced by scratches, contamination, or measurement noise. Generally, lower values of Sa and Sq indicate smoother surfaces, contributing to better performance. Figure 2.10 shows the 3D views for S_a, S_q, S_v, S_p and S_z. The values of S_a, S_q, S_v, S_p and S_z can be calculated using Equations (2.7) to (2.11), with the peak height Z expressed as a function of the coordinates x and y [74].

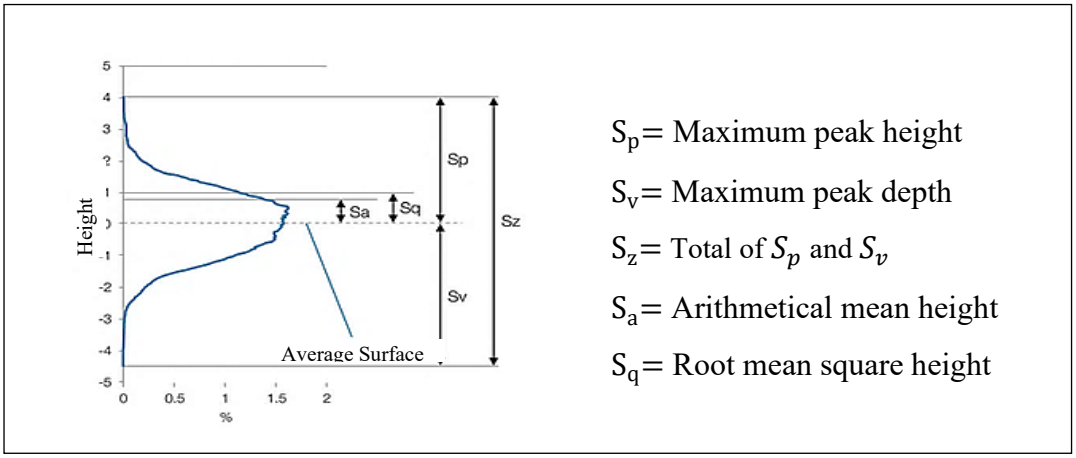


Figure 2.9 Height Parameters for Roughness Evaluation

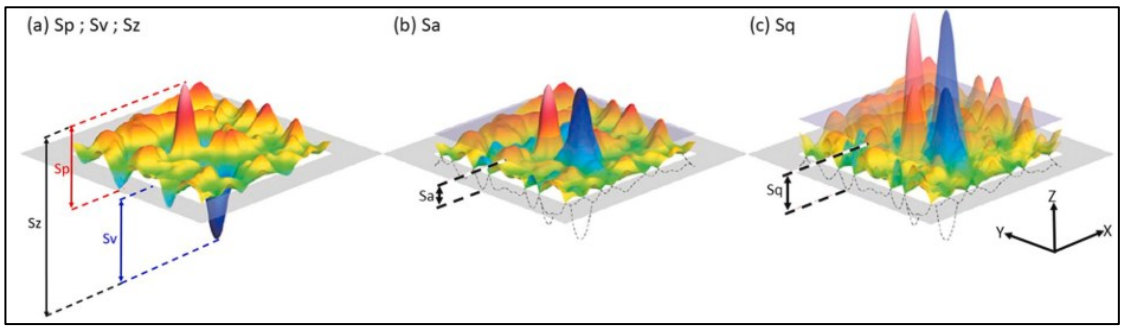


Figure 2.10 Graphical Representation of (a) S_v, S_z, S_p (b) S_a and (c) S_q. The Grey Plane Indicates the Mean Value for the Measurement [74]

$$S_a = \frac{1}{A}\iint |Z(x,y)|\,dx\,dy \tag{2.7}$$

$$S_q = \sqrt{\frac{1}{A}\iint Z^2(x,y)\,dx\,dy} \tag{2.8}$$

$$S_v = \left|\min\left(Z(x,y)\right)\right| \tag{2.9}$$

$$S_p = \left|\max\left(Z(x,y)\right)\right| \tag{2.10}$$

$$S_z = S_p + S_v \tag{2.11}$$

2.4 Design and Parameters of NFC Antenna

The NFC antenna is the most essential component in an NFC system, and its design, materials, and fabrication techniques have a significant impact on its performance. The design of the NFC tag antenna plays a crucial role in energy harvesting capability. The frequency of 13.56 MHz corresponds to a wavelength of approximately 22 meters, which limits the NFC tag antenna design to a coil shape. As a result, the maximum linear distance for effective communication is about 0.5% of the wavelength, which translates to approximately 10 cm [75].

2.4.1 NFC Antenna Design

Antenna design and geometry play an essential role in determining the inductive coupling efficiency and overall NFC performance. The NFC antenna must be in coil-shaped form to enable inductive coupling with the NFC reader, which also follows a similar design. However, the coil shape and geometry of an NFC tag antenna can vary based on design requirements and applications. In previous research, H. Jeong et al. implemented a serpentine-shaped coil, as depicted in Figure 2.11, to provide stretchability and flexibility, as the tag is designed to adhere to human skin [76]. The tag is 74 x 50 mm in dimension and is designed on a flexible substrate. Thermal release tape is used to laminate copper foil that has been cut with the intended circuit pattern. The "cut-and-paste" method eliminates the need for chemicals or stencils, making it a more cost-effective and faster alternative to chemical etching. However, a copper foil is prone to micro-cracking and fractures under repeated bending, stretching, or twisting, which can degrade NFC antenna performance [77][78].

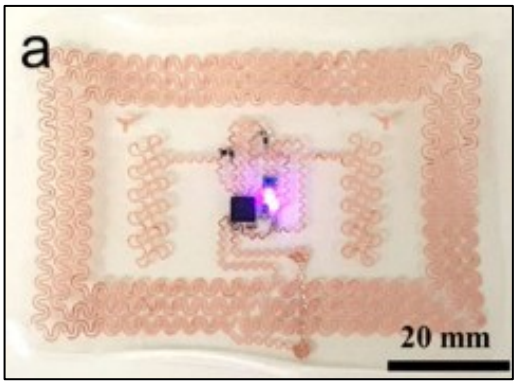


Figure 2.11 Serpentine-Shaped Coil of NFC Tag Antenna [76]

K. Hong et al. presented a stretchable, multi-layered stack antenna for smart wearable electronics as depicted in Figure 2.12, focusing on enhancing wireless reception performance without using conventional semiconductor processes [79]. The antenna, designed in a serpentine form for stretchability, was fabricated using PDMS and laser-patterned aluminium foil. It demonstrated reliable wireless power transfer for optoelectronic devices, such as LEDs and micro-heaters, even under 20% strain. The multi-layered design significantly improved antenna efficiency, achieving up to three times the power output compared to a single-layer antenna, while maintaining flexibility and conformability. This research eliminates the need for cleanroom-based fabrication, providing a low-cost and scalable approach for wearable NFC applications. However, alignment issues between layers may arise if the layers are not precisely positioned, potentially leading to poor contact, increased resistance, or open circuits.

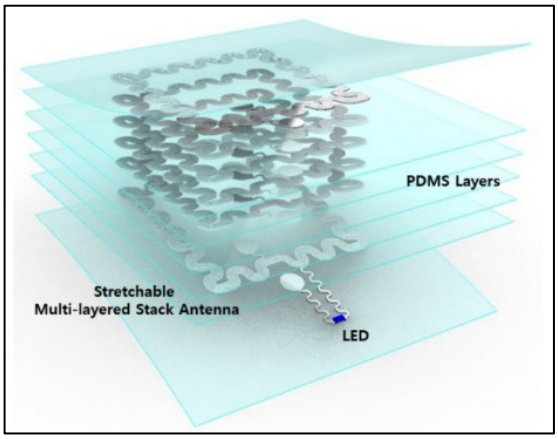


Figure 2.12 Multi-Layered Stack NFC Tag Antenna [79]

The design of an NFC tag antenna can also be simple, taking the form of a planar square loop, a circular flexible loop, or a planar rectangular coil, as shown in Figure 2.13. These basic shapes are commonly used in practice because their geometric analysis is relatively simple. However, fabrication complexity varies depending on the material used and its application. The square loop antenna, as proposed by Lazaro et al. in [80], is the simplest and easiest to manufacture, as it is a PCB-based antenna that can be etched onto an FR4 board. It is designed for battery-less colour sensing in food monitoring applications, but it lacks flexibility and is unsuitable for conformal structures. Meanwhile, the circular loop NFC antenna, made of a polymer material, was introduced by Kim et al.[81], It is flexible enough for biosensing applications, allowing it to adhere to human skin. However, it requires specialized fabrication techniques to

be integrated with a microfluidic sensor. The planar rectangular coil design, proposed by Awuah et al. in [82], utilizes geometrical optimization methods to achieve high trace width and pitch precision, thereby effectively maximizing power transfer efficiency. However, the use of bulk copper coils as conductors makes them more rigid and less suitable for flexible applications. Although bulk copper allows for thicker traces, improving the Q-factor, it comes at the cost of added weight, presenting a trade-off between efficiency and flexibility.

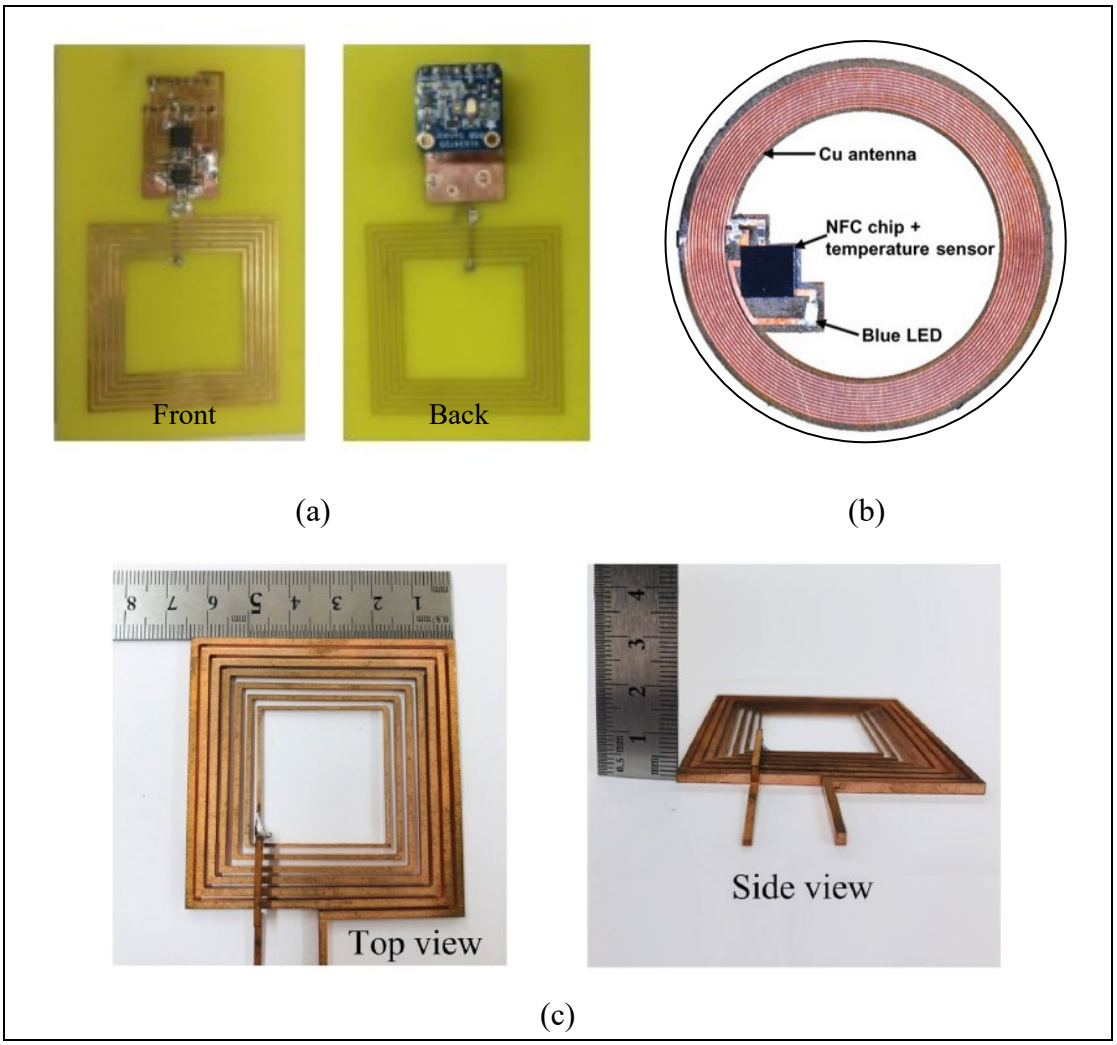


Figure 2.13 Basic Geometries of NFC Tag Antenna (a) Square Loop, (b) Circular Loop and (c) Planar Rectangular Loop [80][81][82]

Table 2.2 summarizes the key design characteristics, findings and gaps from previous researchers. Based on the findings, the basic shape of an NFC tag antenna is considered for implementation in the research due to its simplicity of design, which is suitable for antenna analysis and optimization. However, selecting a fabrication method

that is compatible with the chosen conductive materials, while remaining cost-effective and less complex, is a top priority in this study. By using a simple structure and minimizing fabrication complexity, uncertainties related to fabrication and human errors can be significantly reduced.

Table 2.2
Summarization of Antenna Designs Characteristics and Findings/Gaps

Ref	Material	Antenna Type	Size (cm^2) Read range	Application	Finding/Gap
[76]	Copper foil	Serpentine-shaped coil	74 x 50 3 cm	Skin temperature	Copper foil prone to micro-cracking and fractures under repeated bending, stretching, or twisting.
[79]	Aluminium foil	Serpentine multi-layer	1.6 x 1.6	Wearable device	Alignment issues between layers leading to poor contact, increased resistance, or open circuits.
[80]	FR-4 PCB	Planar square loop	50 X 50 2cm	Colour measurement	Lacks flexibility and is unsuitable for conformal structures
[81]	Copper	Circular loop	4 cm diameter	Skin temperature	Requires specialized fabrication techniques to be integrated with a microfluidic sensor
[82]	Bulk copper	Planar rectangular coil	6.3 x 6.6	Wireless power transfer	Bulk copper is rigid and less suitable for flexible applications

2.4.2 NFC Antenna Geometrical Configuration

The design of the NFC tag antenna is typically in a coil-shaped form to achieve a compact size suitable for operation at the high frequency (HF) band of 13.56 MHz. When designing the tag antenna, the geometrical parameters of the coil antenna, including the antenna length (a), width (b), number of turns (n), conductor width (w), and conductor gap (g), as shown in Figure 2.14, must be carefully determined. Proper selection of these parameters is essential to maximize the Q-factor, as well as the antenna inductance, L_a and antenna resistance, R_a.

According to D.Paret, the allowable value of the tag antenna inductance, L_a, should be in the range between approximately 300 nH and 10 µH, depending on the internal capacitance, C_{int} of the chip [83]. In selecting the values of w and g, the printing and ink specifications must also be considered to ensure accurate printing results and to prevent short circuits between the coils. For the tag antenna designed using SC material, the minimum values of w and g should be 0.25 mm and 0.7 mm, respectively [84]. Meanwhile, for HGS material, the minimum allowable w and g values are significantly smaller, at 0.2 mm and 0.3 mm, respectively, indicating more precise printing and manufacturing capabilities due to the fine structure of the HGS material. However, for HCG material, the minimum g should be 1 mm, while the minimum w is not specified in the datasheet [85].

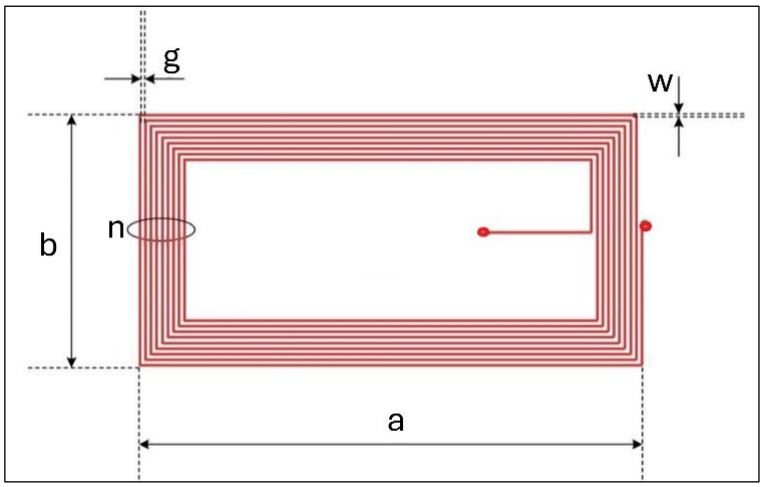


Figure 2.14 Geometrical Parameters of the Coil Antenna [86][87]

From the coil antenna geometrical parameter values, the antenna inductance, L_a, can be determined by using Equations (2.12) until (2.16). This equation combines the contributions of the coil's geometry (x_1, x_2,x_3,x_4) and the number of turns (n) to determine the inductance. The parameter E is the turn exponents, where the typical values for the printed antenna are between 1.7 and 1.8. The geometrical parameter (a,b,g,w,t,n) values of the coil antenna are adjusted to achieve the desired inductance, L_a while minimizing the resistance, R_a. This optimization ensures a high Q-factor, which is critical for efficient energy transfer in NFC applications.

$$L_a = \frac{\mu_0}{\pi}[x_1+x_2-x_3+x_4]\cdot n^E \tag{2.12}$$

where x_1,x_2,x_3,x_4 are intermediate variables given by:

$$x_1 = a_{avg}\cdot \ln\left[\frac{2\cdot a_{avg}\cdot b_{avg}}{d\cdot\left(a_{avg}+\sqrt{a_{avg}^2+b_{avg}^2}\right)}\right] \tag{2.13}$$

$$x_2 = b_{avg}\cdot \ln\left[\frac{2\cdot a_{avg}\cdot b_{avg}}{d\cdot\left(b_{avg}+\sqrt{a_{avg}^2+b_{avg}^2}\right)}\right] \tag{2.14}$$

$$x_3 = 2\cdot\left[a_{avg}+b_{avg}-\sqrt{a_{avg}^2+b_{avg}^2}\right] \tag{2.15}$$

$$x_4 = \frac{a_{avg}+b_{avg}}{4} \tag{2.16}$$

The term x_1 accounts for the contribution of the coil's average length (a_{avg}) to the inductance, considering the geometry of the coil and the conductor's effective diameter. The a_{avg} is calculated by subtracting the space occupied by the turns and gaps from the outer length (a) as described in Equation (2.17). Similarly, the term x_2 accounts for the contribution of the coil's average width (b_{avg}) to the inductance. The b_{avg} is calculated by adjusting the outer width (b), as described in Equation (2.18), following the same approach as for Equation (2.17).

The effective diameter (d) used in the calculation of x_1 and x_2 accounts for the conductor's cross-sectional area, as described in Equation (2.19). Meanwhile, the term x_3 adjusts the inductance calculation by accounting for the diagonal distance across the coil, ensuring that the whole geometry of the coil is considered. The last term, x_4, provides a linear correction factor based on the average length and width of the coil, ensuring that the inductance calculation accounts for the overall size of the coil.

$$a_{avg} = a\text{-}n\cdot(g+w) \tag{2.17}$$

$$b_{avg} = b\text{-}n\cdot(g+w) \tag{2.18}$$

$$d = \frac{2\cdot(t+w)}{\pi} \tag{2.19}$$

Square antennas in the range of 40–50 mm are widely used in industrial, retail, and asset-tracking environments due to their balanced trade-off between inductance, read range, and manufacturability. Commercial NFC tags utilizing ICODE SLIX2 (ISO 15693) and NTAG series chips frequently employ 50 × 50 mm^2 antenna layouts as depicted in Figure 2.15 (a), to achieve sufficient magnetic coupling and extended read range at 13.56 MHz [88]. PCB antennas with similar dimensions (50 × 50 mm^2) are also commonly used as reader antennas, as shown in Figure 2.15 (b) [89]. According to antenna design guidelines for HF RFID systems [83], larger loop dimensions, typically around 50 mm square, provide improved magnetic flux linkage and enhanced power transfer efficiency for passive tags operating in near-field conditions.

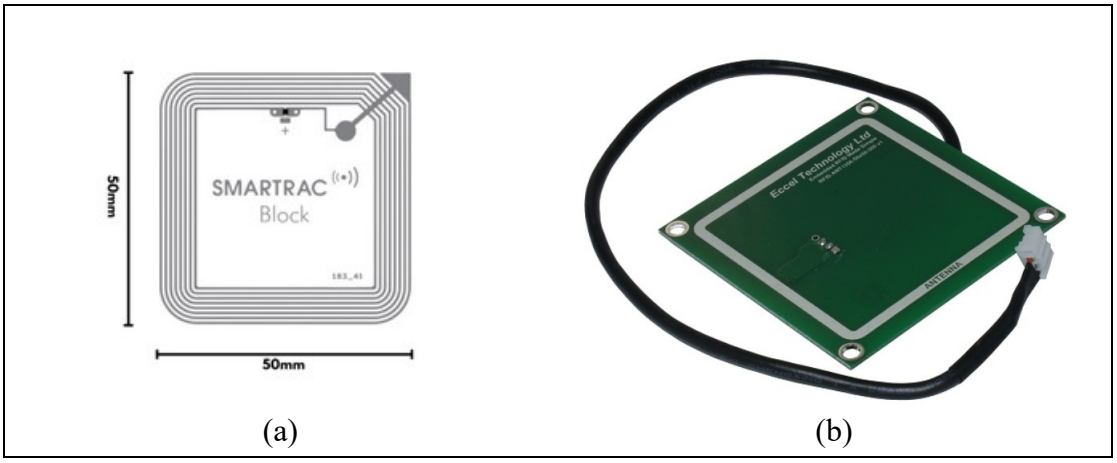


Figure 2.15 Commercial Antenna Design for (a) NFC Tag and (b) Reader, Used as References [88] [89]

2.4.3 NFC Antenna Parameters

In NFC antenna design, the main parameters to consider include resonance frequency, antenna tuning, antenna inductance, antenna resistance, Q-factor, power transfer efficiency, and read range. Since NFC antennas are significantly smaller than

the wavelength at 13.56 MHz (22 meters) or a half-wave dipole antenna (11 meters), their radiation efficiency is minimal, and typical antenna parameters, such as gain and radiation pattern, become irrelevant [90].

2.4.3.1 Resonance Frequency and Antenna Tuning

The resonance frequency (f_r) of the antenna is the frequency where the inductive and capacitive reactance of the antenna cancel each other out, thus behaving as purely resistive. The resonance frequency can be verified by measuring the S_{11} parameter connecting another loop antenna to a vector network analyser close to the tag. To achieve the resonance at 13.56 MHz, requiring precise tuning of antenna inductance (L_a) and capacitance (C), as referred to Equation (2.20).

$$f_r = \frac{1}{2\pi\sqrt{LC}} \tag{2.20}$$

Antenna tuning is crucial for ensuring the NFC tag antenna resonates efficiently at the desired operating frequency, hence achieving maximum coupling with the reader. A variety of tuning approaches can be employed, depending on the design constraints and application requirements. One of the methods is through capacitive tuning, where an external tuning capacitor (C_{tun}) is incorporated in parallel with the antenna coil to compensate for variations in the NFC chip capacitance (C_{chip}) and parasitic capacitance, ensuring resonance at the desired frequency [91][92]. The tuned frequency and the total capacitance, C_T, in the circuit is given by Equation (2.21) and (2.22), respectively.

$$f_r = \frac{1}{2\pi\sqrt{LC_T}} \tag{2.21}$$

$$C_T = C_{chip}+C_{tun}+C_{parasitic} \tag{2.22}$$

Another tuning method involves employing an L-C matching network, comprising series or parallel inductors and capacitors, to enhance impedance matching between the antenna and the NFC chip. This approach is especially advantageous in applications where optimising power transfer and reducing reflection losses are crucial

[93]. The impedance of the system is adjusted using Equation (2.23), where R and X are fine-tuned using external L and C components.

$$Z_{match} = R+jX \tag{2.23}$$

Another less common but effective method is inductive tuning, where the inductance of the antenna coil (L) is modified by adjusting the number of turns or incorporating a variable inductor. This technique enables dynamic tuning, making it suitable for applications that require adaptive resonance control. The tuned frequency and the total capacitance, L_T, in the circuit is given by Equation (2.24) and (2.25), respectively, where L_m indicates the mutual inductance [94].

$$f_r = \frac{1}{2\pi\sqrt{L_T C}} \tag{2.24}$$

$$L_T=L_a+L_{tun}+2L_m \tag{2.25}$$

Each of these tuning techniques has its advantages and trade-offs. Capacitive tuning is a cost-effective and straightforward method, but it can be affected by parasitic effects. L-C matching networks offer greater precision in tuning but require additional components, thereby increasing design complexity. Inductive tuning allows for dynamic adjustments but is rarely used in NFC applications due to the challenges in maintaining stable inductive coupling. Selecting the appropriate tuning method depends on the specific requirements of the NFC system, such as fabrication constraints, power efficiency, and antenna size limitations.

2.4.3.2 Antenna Inductance, Resistance, and Q-factor

The antenna inductance (L_a) is primarily determined by the number of turns in the loop, whereas the antenna resistance (R_a) depends on the diameter and total length of the loops. The most accurate method to measure L_a and R_a is by connecting the antenna coil to a vector network analyzer (VNA) and measuring the antenna impedance

(Z_a), as shown in Equation (2.26). It is recommended to measure L_a and R_a at 1 MHz to minimize the influence of parasitic capacitance [95].

Improving NFC antenna performance is typically achieved by increasing L_a and reducing R_a, resulting in a higher Q-factor, as described by Equation (2.27) [96]. A higher Q-factor implies that the device's stored energy is dissipated more slowly. In contrast, a lower Q-factor indicates increased energy losses, resulting in more power being wasted as heat rather than being utilised to generate a magnetic field [97]. Consequently, an NFC tag antenna with a higher Q-factor will have an extended reading range but a narrower bandwidth, since the Q-factor is inversely proportional to bandwidth, as depicted in Equation (2.28). However, an excessively high Q factor is undesirable for NFC tags, as it makes them more susceptible to detuning effects when placed near dielectric, conductive, or ferromagnetic materials. To enhance the performance of the tag antenna, it is essential to optimize the coil's inductance and resistance, aiming for a typical Q-factor of approximately 20 or less [98][99]. The coil inductance can be optimized by adjusting the coil's geometric parameters, such as the number of turns, N and the surface area, *A* as these parameters are directly proportional to the antenna inductance, as expressed in Equation (2.29), where H is the magnetic field strength and I is the induced current in the coil [100].

$$Z_a = R_a + j\omega \cdot L_a \tag{2.26}$$

$$Q = \frac{\omega \cdot L_a}{R_a} \tag{2.27}$$

$$Q = \frac{f_{res}}{BW} \tag{2.28}$$

$$L_a = \frac{N \cdot \mu \cdot H \cdot A}{I} \tag{2.29}$$

2.4.3.3 Read Range and Magnetic Field Strength

The read range is an important performance parameter for an NFC tag, as it indicates the maximum distance at which the tag can communicate successfully with an NFC reader [101]. It directly correlates with the magnitude of the magnetic field,

also known as magnetic field strength, H, generated by the reader antenna. According to the NFC standard, a passive NFC tag requires a minimum magnetic field strength (H_{min}) of approximately 1.5 A/m at its position to activate and power its internal circuits [102]. Thus, the NFC read range (d) can be defined as the maximum distance from the reader antenna at which the magnetic field strength remains above this minimum threshold. The typical reading range for NFC tag is between 1 to 5 cm when detected using smart phone [103]. According to the Biot-Savart law, the relationship between H and d for a circular loop antenna is expressed in Equation (2.30), where I is the current flowing through the antenna coil, N represents the number of turns, r denotes the loop's radius, and d signifies the distance from the coil's centre. Additionally, for a rectangular loop antenna with dimensions a and b, the magnetic field strength at distance d is represented by Equation (2.31) [83][104].

$$H = \frac{I \cdot N \cdot r^2}{2\sqrt{\left(r^2+d^2\right)^3}} \tag{2.30}$$

$$H = \frac{I \cdot N \cdot a \cdot b}{4\pi\sqrt{\left(\frac{a}{2}\right)^2+\left(\frac{b}{2}\right)^2+d^3}} \cdot \left(\frac{1}{\left(\frac{a}{2}\right)^2+d^2} + \frac{1}{\left(\frac{b}{2}\right)^2+d^2} \right) \tag{2.31}$$

Equations (2.30) and (2.31) show that as the read range increases, the magnetic field strength decreases, following an inverse-cube law beyond the coil radius. Consequently, the maximum read range is limited by the minimum magnetic field strength required to activate and power the NFC tag. This theoretical correlation between magnetic field strength and read range is illustrated in Figure 2.16, where the read range of a circular antenna, which is approximately 7.5 cm, is derived from the intersection with the minimum field strength line (1.5 A/m) [102]. Therefore, optimizing antenna design parameters, such as inductance, coil radius, number of turns, and Q-factor, is crucial for enhancing the NFC read range by increasing the generated magnetic field strength at greater distances.

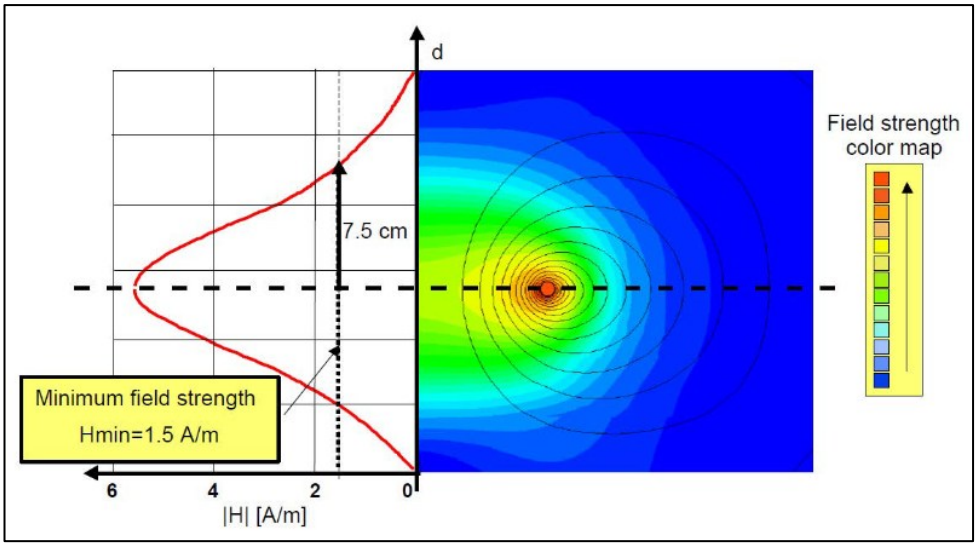


Figure 2.16 Magnetic Field Distribution of a Circular Antenna in Free Air [102]

2.4.3.4 Power Transfer Efficiency

The power transfer efficiency (PTE) of an NFC antenna represents the effectiveness of energy transmission between the reader and the tag antenna, significantly affecting the overall performance of the NFC system. This efficiency is commonly evaluated using S-parameters, specifically the transmission parameter S_{21}, which indicates the magnitude of the signal transferred from the transmitting (reader) coil to the receiving (tag) coil [105]. The PTE is directly correlated with the magnitude of S_{21}, as expressed in Equation (2.32).

$$PTE = |S_{21}|^2 \tag{2.32}$$

At resonance, the antenna system achieves optimal impedance matching, resulting in maximal energy transfer. Deviations from the resonant frequency cause a significant reduction in efficiency due to impedance mismatch and related signal reflections. Therefore, it is essential to precisely tune the antenna circuit to achieve resonance at the desired NFC frequency, thus optimizing the $|S_{21}|^2$ value and consequently enhancing the PTE [40]. Optimizing this parameter is crucial because increased efficiency directly contributes to an extended read range and more reliable NFC communication, particularly in passive NFC systems that depend entirely on the reader's power for operation [106].

2.5 Robustness of NFC Antenna

The robustness of NFC antennas is particularly crucial for temperature-monitoring applications in food packaging, where reliable antenna operation is essential for accurate and consistent sensing and data transmission throughout the supply chain. NFC tags integrated into food packaging are frequently exposed to challenging environmental conditions, including significant temperature fluctuations, moisture from condensation, mechanical bending during handling, and potential interference from metallic packaging materials. Such factors may degrade antenna performance, leading to unreliable readings or complete system failure, ultimately compromising food safety monitoring and quality assurance processes. Therefore, it is essential to thoroughly evaluate and optimize antenna robustness parameters, such as mechanical flexibility, sensitivity to metallic surfaces, moisture resistance, and thermal stability, to ensure sustained and accurate performance of NFC-based temperature monitoring systems for food packaging applications.

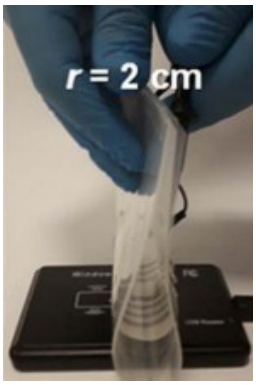
Mechanical flexibility refers to the antenna's ability to maintain stable electrical and performance characteristics when subjected to bending, folding, or twisting. Other mechanical stresses, such as stretchability and tensile strength, are also typically included in the robustness analysis for flexible antennas [3]. However, for an NFC tag antenna intended to be attached to food packaging, only the bending element will be analysed, as food packaging surfaces typically experience minimal stretching or tensile forces during standard storage and transportation. This contrasts with antennas used directly on the human body, which require stretchability analysis due to continuous movement and deformation [107][108]. In practice, food packages usually undergo bending or slight deformation during handling, stacking, and transit, making bending tests the most relevant mechanical robustness assessment for ensuring reliable antenna performance.

Several researchers have examined the mechanical flexibility of NFC antennas through bending analyses [61][62][109]. Jiang et al. analyzed textile-integrated NFC antennas subjected to bending angles of up to 150° as depicted in Figure 2.17 (a), noting shifts in resonant frequencies and reductions in inductance, but confirming continued antenna functionality despite mechanical deformation [109]. Meanwhile, Ozek et al. reported that graphene-based RFID antennas printed onto textile substrates maintained operational stability under bending conditions down to a radius of 2 cm as depicted in

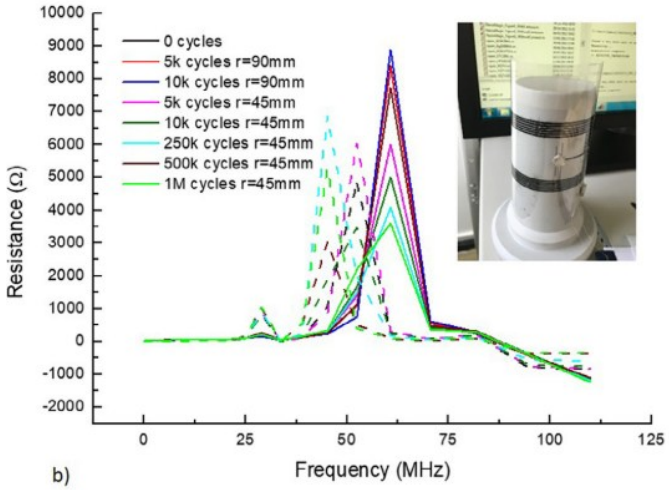
Figure 2.17 (b), although induced voltage levels were significantly decreased at higher bending angles [61]. Similarly, Scidà et al. studied graphene-paper antennas under extensive bending fatigue tests (up to one million cycles) as depicted in Figure 2.17 (c), observing minimal changes in electrical properties (at lower frequency of 1 MHz) compared to commercial metallic antennas, thus highlighting superior fatigue resistance and mechanical stability [62]. Therefore, the flexibility performance of tag antennas is influenced by several factors, including antenna geometry, substrate type, and the choice of conductive materials[109]. Further mechanical flexibility investigations are required for newly proposed conductive materials for NFC antenna applications, such as hybrid graphene-metal-based materials.



(a)



(b)



(c)

Figure 2.17 Bending Evaluation of Flexible NFC Tag Antennas: (a) Textile NFC Antenna Bent at 150°, (b) Graphene-Based NFC Antenna at a Bending Radius of 2 cm, and (c) Resistance Response of Graphene-Paper Antennas Under Extensive Cyclic Bending Tests

In addition to mechanical flexibility, analyzing the robustness of NFC tag antennas when attached to different types of packaging materials is also crucial. Previous studies have shown that the performance of NFC antennas can be significantly compromised when placed near metallic surfaces due to electromagnetic interference caused by induced eddy currents in the metal, as depicted in Figure 2.18[110][111]. These eddy currents generate their own magnetic field (secondary field), which oppose the primary magnetic field and significantly dampens the overall magnetic flux. Consequently, the coil inductance is reduced, and the resonant frequency shifts upward, thereby decreasing the read range.

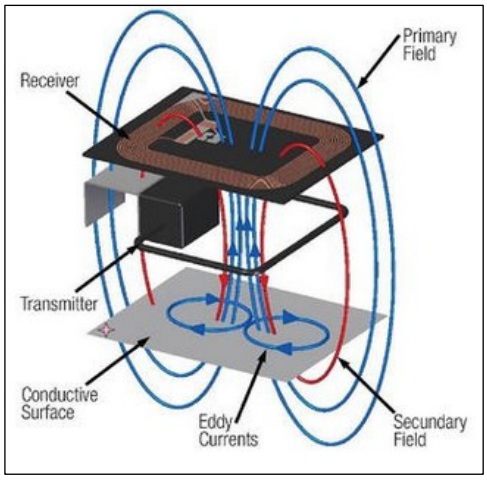


Figure 2.18 Formation of Eddy Currents During on-Metal NFC Communication

Commonly proposed methods to mitigate this effect include integrating ferrite sheets [112][113] to isolate antennas from metal surfaces magnetically, adaptive impedance matching circuits [114] to compensate for resonance shifts, and booster antenna configurations [115][116] to enhance magnetic coupling efficiency. However, adaptive impedance matching circuits and booster antennas typically introduce additional complexity and reduced flexibility, as these solutions are generally designed for stationary or static setups [110]. The use of ferrite sheets is more favourable due to their relatively simple configuration. However, ferrite materials typically exhibit rigidity and brittleness, which can potentially lead to mechanical failure under repeated bending [117]. These characteristics limit their applicability in flexible or conformal packaging scenarios where mechanical flexibility is crucial. Other types of magnetic sheets, such as amorphous and nanocrystalline materials, also provide effective shielding due to their high magnetic permeability [118][119]. However, their

application in high-frequency scenarios, such as NFC, is less explored in the existing literature.

Several studies have investigated the impact of moisture exposure on RFID and NFC tag antennas, highlighting the significance of environmental conditions on antenna reliability. Toni Björninen et al. demonstrated that moisture absorption significantly affects the electrical characteristics of paper-based HF RFID tags, leading to increased leakage currents and changes in distributed capacitance, which consequently shift the resonance frequency and reduce the antenna sensitivity [120]. Similarly, Toivonen et al. investigated the effects of moisture and repeated washing on UHF RFID tags with embroidery. Their findings highlighted that moisture temporarily degraded the antenna's performance due to increased substrate permittivity and dielectric losses, which caused antenna detuning and reduced radiation efficiency [121]. However, once dried, the antenna recovered its original performance, indicating that moisture exposure alone did not cause permanent damage to the antenna or integrated circuits. Conversely, repeated washing cycles caused permanent degradation of the antenna's performance, attributed to the dissolution and physical degradation of conductive embroidery threads, leading to a progressive reduction in the read range. The study concluded that protective coatings, such as polydimethylsiloxane (PDMS), thermoplastic polyurethane (TPU), or polymer-ceramic composites, are necessary to maintain stable operation [121][122].

Meanwhile, previous studies addressing the effects of temperature variation on antenna performance have mainly focused on antennas operating in the ultra-high frequency (UHF) and microwave frequency ranges [123][124][125]. Kim et al. described how elevated temperatures significantly altered RFID system performance by reducing the read range and reliability due to increased thermal noise and impedance mismatches [126]. Additionally, elevated temperatures were also reported to affect the impedance and radiation efficiency of RFID tags [124]. Maurya et al. observed that rising temperatures affected the dielectric properties of microstrip patch antennas, notably reducing resonant frequencies and altering antenna impedance and efficiency, which consequently degraded antenna performance at higher temperatures [115]. However, limited research exists specifically addressing temperature effects on NFC antennas operating at 13.56 MHz. Although several studies have utilized NFC antennas in temperature-monitoring applications, the impact of temperature on antenna performance has not been thoroughly analyzed. Table 2.3 summarizes the findings the research gap from previous literature regarding the robustness analysis.

Table 2.3
Summary Analysis of Literature Review Regarding Robustness of NFC Antenna

Topic	Analysis of literature review	Research Gap
Mechanical Flexibility	• Bending of NFC antennas causes changes in resonant frequency and inductance, but the antenna can remain functional. • Flexible substrates like textile and paper enable operation under bending conditions. • Antenna flexibility depends on geometry, substrate type, and conductive material used.	• Limited analysis on hybrid graphene-metal-based NFC antennas. • Only bending analysis is relevant for food packaging; stretchability is not applicable.
Metal surface interference	• Placement on metal degrades performance due to eddy currents, reducing inductance and shifting resonance frequency. • Ferrite sheets, impedance matching circuits, and booster antennas are proposed solutions. • Ferrite offers a simple solution but lacks flexibility.	• Ferrite sheets are brittle and unsuitable for flexible packaging. • Amorphous and nanocrystalline materials offer potential but remain underexplored for flexible NFC integration.
Moisture exposure	• Moisture increases substrate permittivity and dielectric losses, detuning the antenna and reducing read range. • Performance may recover after drying, but repeated exposure can cause permanent damage. • Protective coatings like PDMS and TPU help mitigate these effects.	• Lack of evaluation on NFC tag reliability under intermittent or repeated moisture exposure, especially in food packaging conditions.
Temperature variation	• Elevated temperatures cause impedance mismatch, detuning, and reduced radiation efficiency. • Performance degradation is more studied at UHF than NFC frequencies. • Thermal effects change dielectric properties and impact antenna efficiency.	• Effects of temperature variation on NFC antennas operating at 13.56 MHz remain insufficiently investigated. • Requires dedicated study for temperature-monitoring applications.

2.6 Temperature Monitoring Application

Temperature monitoring is crucial in all sectors, including health, food safety, pharmaceuticals, and agriculture, for ensuring product integrity, regulatory compliance, operational efficiency, and the overall safety and quality of goods throughout production, storage, transportation, and distribution. [127]. The traditional approach to monitoring temperature includes the use of digital thermometers, temperature data loggers, thermocouples, and infrared thermal imaging [128][129][64]. These methods can provide quick temperature readings and are easy to use due to their handheld and compact size. However, their major limitations are that they are battery-reliant and unable to provide real-time wireless monitoring without manual intervention. The IoT-based temperature monitoring systems have also been proposed by several researchers in [120] [121] [122], which utilize internet connectivity and cloud-based storage to provide continuous, real-time temperature data that is remotely accessible via connected devices. However, it also requires a continuous power supply or batteries to operate. The use of batteries in the system not only requires regular maintenance but also contains hazardous chemicals, which pose potential safety risks if they leak or come into contact with food or food packaging.

Recent advancements in wireless communication technologies, specifically RFID, have been leveraged to enhance temperature monitoring capability. Passive UHF-RFID temperature sensors have attracted considerable research interest due to their batteryless operation and wireless data transmission capability. The UHF-RFID temperature monitoring has been implemented for human body applications [130][131], in poultry egg incubators [132], and also for environmental applications [133]. However, the UHF-RFID system also still faces several limitations, including the requirement for dedicated readers and infrastructure to read the temperature, as well as the design complexity, which necessitates precise impedance matching to specific chip types, thereby limiting its generalizability across different use cases. Due to this, the attention of researchers has shifted to high-frequency (HF) RFID, also known as NFC, which only requires an NFC-enabled smartphone to read the temperature from the tag.

Several researchers have already implemented NFC in temperature monitoring systems, as proposed by [134][135][59][3]. Maskey et al. developed a wireless time–temperature history (TTH) food label using a roll-to-roll printed NFC antenna and

thermistor, integrated with a silicon chip and printed battery [134]. This system provided real-time monitoring and traceability by linking NFC data with a cloud-based microbial growth model, enabling accurate food safety feedback. Despite its functional advantage, it relied on a hybrid structure and printed battery, which introduced cost, complexity, and limited sustainability for disposable applications. Similarly, the NFC-enabled dual-channel printed sensor tag for monitoring both temperature and ethylene gas, proposed by Choi et al., also utilized screen-printed sensors and a silver-epoxy integrated PCB [135]. Another study by Escobedo et al., proposed a battery-less NFC tag incorporating flexible strain and temperature sensors using conductive polymers such as PEDOT:PSS. This design demonstrated complete structural flexibility, as all components, including the antenna and circuitry, were printed on a flexible PCB using ultraviolet etching [3]. However, the use of copper as a conductive material presents durability issues, as it easily oxidizes when exposed to air or humidity, forming copper oxide that significantly reduces its conductivity.

In contrast, graphene-based materials, as proposed by Pan et al. [59], offer greater robustness in temperature monitoring systems due to their non-oxidized nature and mechanical flexibility. Nevertheless, these materials face limitations in the circuit printing process, such as poor adhesion and lower resolution in fine-line features, which require the graphene-based antenna to be hybridized with a PCB circuit, similar to the hybrid integration approach seen in [134] and [135]. The comparison of the temperature monitoring applications from previous studies is presented in Table 2.4. The comparison highlights the limitations of battery-dependent and hybrid structures and emphasizes the need for a fully printed, battery-less, and flexible NFC tag antenna for food packaging applications, which aligns with the research objective described in Section 1.3.

Table 2.4
Summarization of Temperature Monitoring Applications and Their Limitations

Ref / System	Reader Requirement	Antenna Material	Flexibility	Limitations
Digital thermometer/ Logger [128][129]	Manual reading	N/A	Rigid	Battery reliant and no real-time monitoring
IoT-based monitoring [120][121][122]	Dedicated gateway	N/A	Rigid	Requires continuous power supply and battery for operation
Passive UHF-RFID [130] – [133]	Dedicated RFID reader	Copper	Semi-flexible	Reader dependency, design complexity
NFC TTH label [134]	NFC smartphone	Roll-to-roll printed antenna	Flexible	Hybrid structure, battery dependency
NFC dual sensor [135]	NFC smartphone	Silver + PCB	Semi-flexible	PCB integration, higher cost
NFC flexible sensor [3]	NFC smartphone	Copper (etched)	Flexible	Copper oxidation issue
Graphene NFC [59]	NFC smartphone	Graphene	Flexible	Requires hybrid PCB integration

The temperature sensor integrated with the NFC tag comes in various forms, such as thermistors [136][137], conductive polymers [3] and carbon materials, including carbon nanotubes and graphene [138][139], as well as on-chip temperature sensors [140]. In this research, a 100 kΩ NTC thermistor has been used as the temperature sensor, integrated with the RF430FRL152H chip from Texas Instruments. The NTC thermistor was selected due to its high sensitivity, fast response time, compact size, and cost-effectiveness, making it well-suited for low-power, passive NFC systems.

Figure 2.19 depicts the schematic circuit diagram of the RF430FRL152H chip from Texas Instruments together with the 100 kΩ NTC thermistor (R_T), NFC antenna and other tuning and resistive components [141]. The antenna is connected to the chip via the ANT1 and ANT2 pins, which indicate the RF analogue front-end. The connection between the sensors and the RF430FRL152H transponder was established via a resistive sensor bias interface, utilizing an inbuilt 14-bit sigma-delta analogue-to-digital converter (ADC) and a programmable gain amplifier (PGA). The NTC thermistor (R_T), which act as temperature sensor, is connected to the ADC2 pin and

grounded to the virtual ground of the sensor reference potential (SVSS). A reference resistor (R_{ref}), with the same value as the thermistor (100 kΩ), is connected to ADC1 and SVSS to achieve more accurate temperature measurement. The chip typically applies an output current of approximately 2.4 µA to both ADC1 and ADC2 pins in accordance with the specification [142]. Other tuning capacitance and resistance has been connected to the chip pins as suggested in the datasheet [143].

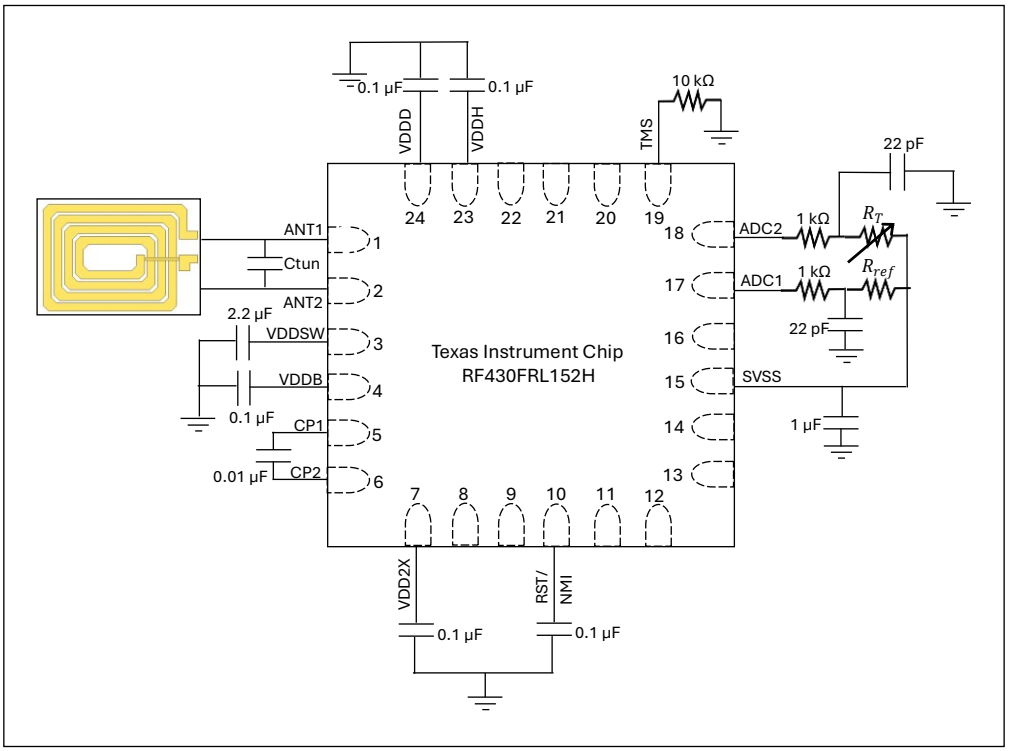


Figure 2.19 Schematic Circuit Diagram of the Temperature Monitoring Circuit

The general equation for the temperature change of a thermistor in Equation (2.33) is used to calculate the measured temperature, T, in relation to the resistance of the thermistor, R_T [64]. Here, R_T represents the resistance value of the sensor at the sensing temperature T , R_{ref} denotes the reference resistance at the reference temperature T_0, and β represents the material coefficient of the NTC thermistor. The values for T_0 and β used in the calculations are 25 ºC (298.15 K) and 3950, respectively, as referenced in the datasheet attached in Appendix 1. The R_T value can be calculated using Equation (2.35), where the gain of the PGA (G_{PGA}) was set to 2 to improve the resolution of the measurement, as recommended by [142], and the ADC1 and ADC2 data are the values that are stored in memory by the ADC.

$$R_T = R_{ref} e^{(\frac{\beta}{T} - \frac{\beta}{T_0})} \tag{2.33}$$

$$T = \frac{\beta * \log e}{\log\left(\frac{R_T}{R_0 * e^{\frac{\beta}{T_0}}}\right)} \tag{2.34}$$

$$R_T = \frac{V_{temp}}{V_{ref}} * R_{ref} \tag{2.35}$$

$$V_{ref} = \frac{\frac{ADC1data}{2^{14}-1} * 0.9V}{G_{PGA}} \; ; V_{temp} = \frac{\frac{ADC2data}{2^{14}-1} * 0.9V}{G_{PGA}} \tag{2.36}$$

2.7 Summary

This chapter presents a comprehensive literature review of existing works on NFC system technology, focusing specifically on NFC tag antenna components, including the conductive materials used, antenna designs, and robustness analysis. Metal-based materials, such as copper and aluminium are widely used for NFC tag antennas. However, they face sustainability and robustness challenges, as they are prone to oxidation when exposed to ambient conditions and are susceptible to cracking under mechanical bending. Therefore, this research proposes a hybrid metal- and carbon-based material, and its characterization is performed in comparison to conventional metal-based and carbon-based materials. Issues related to the sensitivity of NFC tag antennas to metallic surfaces, moisture, and temperature variations are also highlighted. Table 2.5 summarizes existing works on NFC antennas and identifies the research gaps that form the basis and motivation for this study.

Table 2.5
Summary Analysis of Literature Review and the Proposed Solutions

Topic	Analysis of Literature Review	Research Gap / Our Proposal
NFC Antenna conductive material	• Metal-based inks, such as copper and silver, are commonly used as conductive materials, but they have several issues with oxidation, brittleness, and sustainability.	• Explore hybrid carbon-metal (e.g., hybrid graphene-silver) materials to improve flexibility and environmental safety.
Antenna design	• Designs include rectangular, circular, and serpentine coils. • Optimization of geometry improves inductive coupling.	• Propose optimized design with low resistance and sufficient inductance using printed graphene-based materials.
Robustness of NFC antenna	• Environmental factors (bending, metal, moisture, temperature) affect antenna performance. • Commonly used magnetic shielding (ferrite sheet) offers limited flexibility.	• Investigate alternative magnetic sheets (e.g., amorphous) and validate antenna performance under various stress conditions.
Temperature monitoring application	• Conventional systems use battery-powered sensors, which require regular maintenance and are hazardous in case of leakage. • A partially flexible NFC tag has several limitations in terms of fabrication and mechanical flexibility.	• Develop a battery-less, printed NFC tag integrated with a flexible temperature sensor circuit.

CHAPTER 3
RESEARCH METHODOLOGY

3.1 Introduction

This chapter discusses the processes and procedures required to achieve several objectives, starting with the design of an NFC tag antenna using printed metal-based and carbon-based conductive materials, which offer high conductivity and environmental stability, respectively. The design process involves a preliminary study of the conductive material's characteristics, including material conductivity, surface morphology, surface roughness, and thickness. Accurate characterization ensures optimal material selection and design adjustments, as these factors directly impact antenna performance, including reading range and power transfer efficiency. In designing the NFC tag antenna, integrating an external tuning at the antenna's port is one of the critical design requirements to ensure that the antenna resonates at the required operating frequency of 13.56 MHz. Optenni Lab software was used to determine the optimum topology and configuration of the lumped elements required for antenna tuning. These configurations were then integrated into the coil antenna design in CST simulation software. This represents a key contribution of this study, as previous studies have not emphasized the validation of the tuning circuit for NFC tag antennas using Optenni Lab software.

Next, the evaluation process of the antenna robustness, which highlights the second objective of the study, is discussed. Since the antenna's application focuses on temperature measurement for food packaging, various forms and materials of food packaging, as well as the impact of exposure to moisture and temperature fluctuations, have been considered when evaluating the antenna's performance. Further evaluation was carried out for the tag antenna attached to metal surfaces, as this significantly impacts antenna performance. The final part of this chapter discusses the development process of the temperature monitoring system as an NFC application, highlighting the third objective of the study. The procedures and guidelines for fabricating the tag antenna with the temperature sensor circuit, both printed using hybrid graphene silver (HGS) conductive material, are discussed, and the limitations encountered during fabrication are also highlighted.

3.2 Flow of Research Work

The flow chart in Figure 3.1 illustrates the overall flow of studies and research work for developing a printed hybrid graphene-metal-based NFC tag antenna optimized for temperature monitoring in food packaging applications. Stage 1 begins with a comprehensive literature review to identify gaps in existing technologies and to conceptualize the NFC tag antenna design. In Stage 2, printed conductive materials, categorized as metal-based, carbon-based and hybrid graphene-metal-based, namely Silver Conductor (SC), Hybrid Carbon Graphene (HCG) and Hybrid Graphene Silver (HGS), are characterized through measurements of conductivity, surface morphology, surface roughness and thickness. Based on these material characteristics, the NFC tag antenna was designed, simulated and fabricated to meet the specifications listed in Table 3.1 [83][96]. Four antenna designs, namely Design 1 (D1), Design 2 (D2), Design 3 (D3) and Design 4 (D4), were analyzed using the respective conductive materials.
In Stage 3, the flexibility of the printed D2 and D4 antennas, made from SC and HGS materials, respectively, was analyzed based on their S_{11} parameter, power transfer efficiency (PTE) and tag reading range. These parameters were selected as they are critical indicators of NFC antenna performance under bending conditions. Specifically, S_{11} represents impedance matching quality, PTE reflects power transmission efficiency from the reader to the tag, and the tag reading range determines the practical communication distance [62][105]. Further robustness analysis was conducted on D4-HGS to evaluate the sensitivity of the tag when attached to various packaging materials and exposed to moisture and temperature fluctuations. Due to performance issues of the tag antenna on metallic surfaces, various magnetic shielding materials, including ferrite, amorphous, and nanocrystalline, were characterized and incorporated into the D4-HGS tag antenna to ensure it met the minimum detection requirement of a 1 cm reading range [103][144].

In stage 4, a flexible temperature sensor circuit was developed and integrated with the D4-HGS design, enabling precise temperature monitoring. Finally, the performance and reliability of the integrated system were validated under real-world conditions, demonstrating its suitability for food packaging applications. The system was tested across various temperature ranges, including cold, room temperature, and hot, to meet the requirements of a maximum temperature deviation of 2 °C from the reference thermometer and a minimum reading range of 1 cm.

Table 3.1
Specification of Antenna Designs

Item	Symbol	Specification	Justification
Resonant Frequency	f_r	13.56 MHz	Standard HF NFC operating frequency defined by ISO/IEC 14443 & ISO/IEC 15693; ensures compatibility with commercial NFC readers [30].
Antenna Inductance	L_a	300 nH ≤ L_a ≤3.8 μH	Matches impedance requirements of common NFC ICs (e.g., TI RF430FRL, NXP SLIX2) and allows resonance tuning with external/on-chip capacitors.
Antenna Resistance	R_a	≤ 50 Ω	Maintains high Q-factor and low ohmic loss for efficient power transfer and adequate read range.
Q-factor	Q	> 0.75	For the graphene-based tag antenna, the typical Q-factor value need to be more than 0.75 for stable operation.
Power Transfer Efficiency	PTE	≥ 40 %	Provides enough harvested energy for passive chip activation and operation.
Read Range	r	≥ 1 cm	Allows practical user interaction and ensures stable NFC communication with a sufficient magnetic field strength (≥ 1.5 A/m).

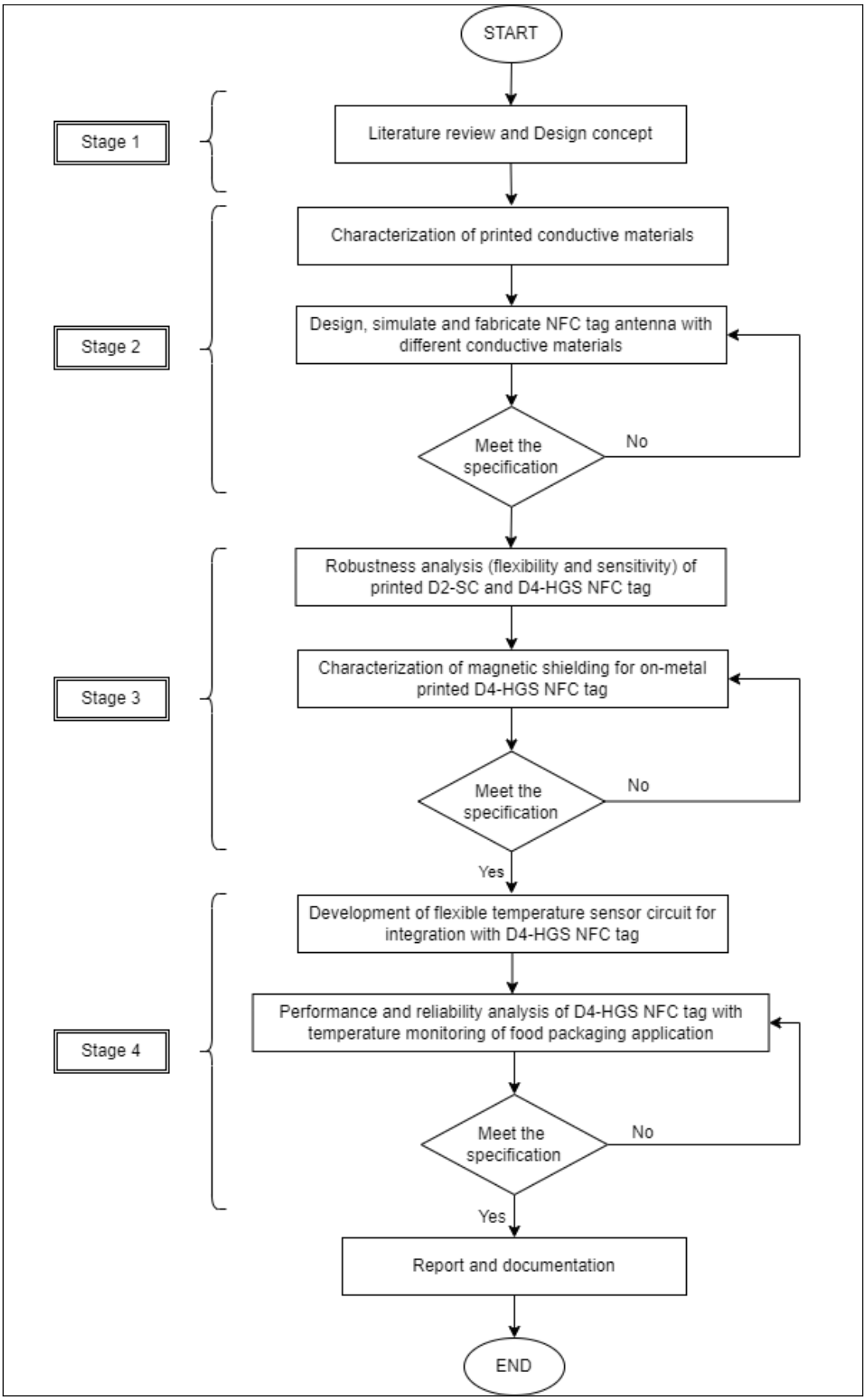


Figure 3.1 Flow of Studies and Research Work

3.3 Synthesis of HGS Conductive Materials

In this study, printed conductive materials, namely SC, HCG, and HGS, were investigated to evaluate their suitability based on their ability to fulfil the specified electrical, mechanical, and environmental performance criteria, as discussed in the previous section. Both SC and HCG are commercial inks from Volterra and Dycotec, respectively, which are available in the market. SC is a metal-based conductive material that serves as a benchmark in this study, providing a reference for performance evaluation. Meanwhile, HCG is a carbon-based conductive material that has been included in this study due to its superior mechanical flexibility and environmental stability. The inclusion of both materials broadens the scope of the study to encompass a broader range of conductive material classes, enabling a comprehensive evaluation of how different material types perform in the context of NFC tag antennas.

HGS is a customized conductive ink synthesized by MIMOS Berhad [145]. MIMOS Berhad provided the HGS ink for further evaluation and application in NFC systems, as MIMOS Berhad faces limitations in technology and techniques for verifying and applying the newly developed ink for NFC antennas. HGS combines the high conductivity of silver with the flexibility and robustness of graphene. Its synthesis process, tailored to ensure optimal particle dispersion and formulation, enhances its applicability in NFC tag antenna designs. The synthesis process of HGS material is as illustrated in Figure 3.2.

The HGS conductive ink was formulated by MIMOS Berhad through a chemical reduction method involving a hybrid combination of reduced graphene oxide (rGO) and silver nanoparticles (AgNPs) [146]. rGO is produced when further reductive exfoliation treatment is applied to graphene oxide (GO) from Graphenea, USA, which was utilized as the precursor for synthesizing graphene. By having fewer oxygen functional groups, rGO produces greater electrical conductivity and carrier mobility than GO as much of its original graphene structure is restored [138][147]. The combined solution of 50% rGO and 50% silver nitrate ($AgNO_3$), along with the reducing and encapsulating agent, was allowed to undergo incubation to facilitate the formation of AgNPs through the reduction of silver ions and to attach the AgNPs to the rGO surface. Subsequently, the resulting black composite, collected after centrifugation, was crushed into a fine powder, and deionized water was added to create the HGS colloid. The colloid was then converted into HGS inkjet printable ink with a

proprietary water-based formulation, which is called Mi-GraphPrInk (MIMOS Berhad, Malaysia) with <10% solid content, pH ~6.8 and viscosity of ~2.39 cP.

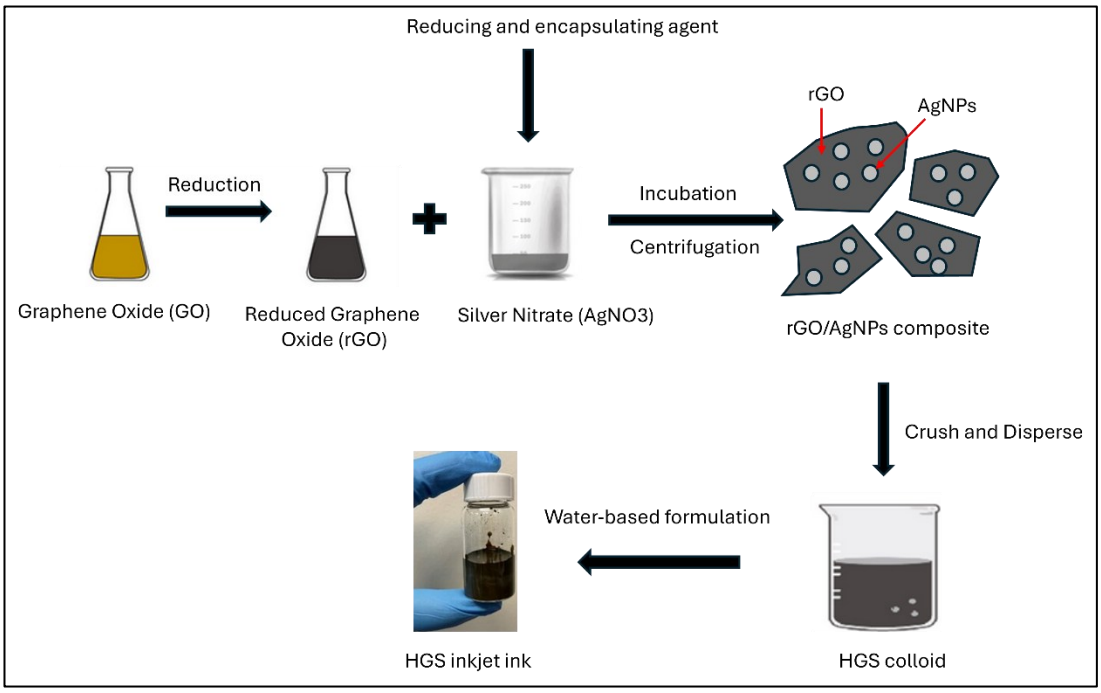


Figure 3.2 Block Diagram Illustration of Synthesis of AgNPs and rGO to Produce HGS Ink

3.4 Characterization Process of Conductive Materials

This section describes the experimental characterization procedures used to evaluate the electrical and surface properties of the printed conductive materials. The process follows a linear measurement sequence without conditional parameter optimization. The characterization of the conductive materials is a preliminary measurement conducted before the antenna design process. This characterization process is crucial because it ensures the selected materials meet the performance requirements for efficient antenna operation. Based on previous research, the characteristics of each conductive material have been analyzed in terms of conductivity and sheet resistance, as these properties directly influence the performance and efficiency of the antenna [148] [149]. Materials with low conductivity and high sheet resistance may increase ohmic losses, degrading signal strength, reducing the reading range, and affecting power transfer efficiency.

The surface morphology and surface roughness of the printed conductive materials have also been examined through Scanning Electron Microscope (SEM) and a digital microscope, respectively, to verify the suitability of the materials for NFC tag antenna applications. The connection and dispersion of particles can be observed by analyzing the surface morphology and roughness along with the texture and structural patterns on the material's surface [150]. This information is essential for understanding how surface features impact the electrical and mechanical properties of the antenna. Excessive roughness can cause non-uniform current paths and resistive losses, reducing antenna performance and detuning the resonant frequency.

In antenna design, the thickness of the conductive material is crucial as it influences both mechanical integrity and electrical performance [151]. Hence, the thickness of the conductive materials was measured using a digital microscope. If the conductive layer is too thin, it can lead to increased electrical resistance due to the skin effect, effectively reducing the cross-sectional area available for current flow. This increased resistance can result in significant power losses, thereby diminishing the antenna's efficiency [152]. In contrast, excessively thick conductive materials can make the antenna bulkier and may interfere with the antenna's resonance characteristics. This comprehensive characterization ensures that the conductive materials are optimized for their intended application, thereby enhancing the overall performance and reliability of the NFC tag antenna.

3.4.1 Conductivity and Sheet Resistance Measurement

The conductivity of the printed materials was measured using a 4-Point Probe Loresta GX MCP-T700, manufactured by Mitsubishi Chemical Analytech Co., Ltd., as illustrated in Figure 3.3(a). This instrument provides precise and reliable resistance measurements, which are essential for accurately calculating the material's conductivity. High conductivity is essential to minimise antenna series resistance and maintain efficient magnetic coupling. The setup includes a probe, equipped with a four-square array of aligned metallic pins, to make electrical contact with the sample, and a display unit, which records and displays the measured resistance values [153].

Four square samples of the printed materials, each measuring 1 cm x 1 cm, were printed on a flexible PET substrate. The sample was set to 1 cm^2 to ensure it fits well with the probe and is large enough for the current to spread uniformly between the outer

probes, avoiding edge effects that can distort the resistivity reading. The 4-point probe was carefully positioned on the sample, ensuring consistent contact with the printed material, as shown in Figure 3.3 (b). Proper alignment and gentle pressure were maintained to avoid damage to the sample material. The sheet resistance, R_s of each square was measured four times to ensure accuracy and reproducibility. The conductivity, σ, of the material was automatically calculated using Equation (2.5), as discussed in Section 2.4 and displayed in the Display Unit. The results were averaged across multiple measurements for each sample to obtain a representative value of conductivity, and these values are presented in Chapter 4.

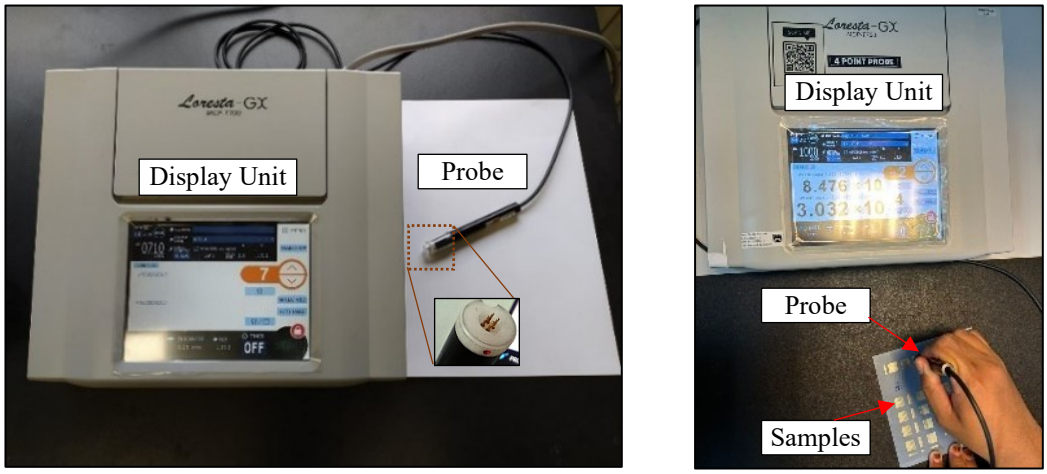


Figure 3.3 Conductivity Measurement: (a) Using 4-Point Probe Loresta GX MCP-T700, (b) Measurement Conducted on Graphene Samples

3.4.2 Surface Morphology Measurement Using SEM

Surface morphology measurement was conducted to observe the particle distribution, which influence conductive path formation and overall electrical behaviour. SEM is an electron microscope used to examine the surface morphology of materials by interacting a high-energy beam of electrons with the sample surface. The SEM images of printed SC, HCG and HGS were examined using Hitachi-Regulus 8200 Series Ultra High-Resolution SEM at the Centre for Global Archaeological Research, Universiti Sains Malaysia, as depicted in Figure 3.4. The sample size of 2 cm x 1 cm for each material, as shown in Figure 3.5, was used for imaging. The sample was securely mounted on the SEM sample holder using carbon tape. The sample holder was

then carefully loaded into the SEM chamber. The accelerating voltage was set to 5 kV, and the magnification was adjusted until a clear image was obtained.

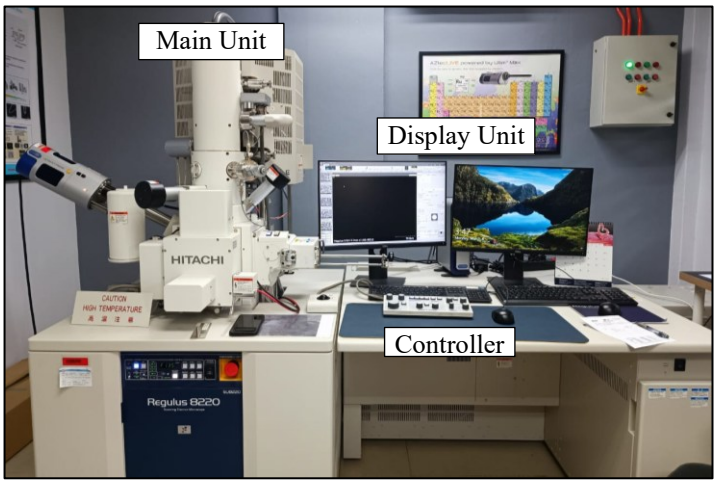


Figure 3.4 Hitachi-Regulus 8200 Series Ultra High-Resolution-SEM

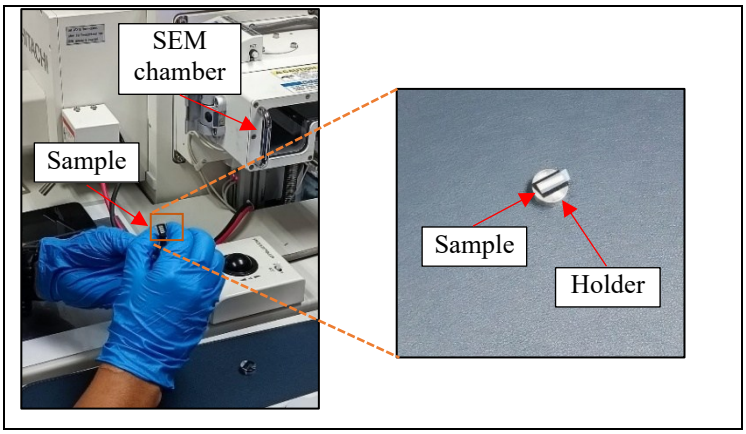


Figure 3.5 Samples Taken from the Printed Materials (Longitudinal Section) For Capturing the SEM Image

3.4.3 Surface Roughness and Thickness Measurement

Surface roughness was monitored using VHX Digital Microscope, as shown in Figure 3.6. Samples of the printed conductive material were prepared and mounted on a stable platform to ensure consistent imaging. The movement of the objective lenses were handled with care to avoid mechanical damage to the samples. The appropriate magnification level was selected to capture high-resolution images of the surface, allowing for precise visualisation of microstructural details. Multiple areas of each sample were scanned and imaged to capture any variations in surface roughness. The

microscope's built-in software was used to generate 2D profiles of the surface, providing quantitative data including S_a, S_q, S_v, S_p and S_z as discussed in Section 2.3.2.2 previously. Figure 3.7 shows a sample image captured by the microscope, along with the corresponding quantitative data.

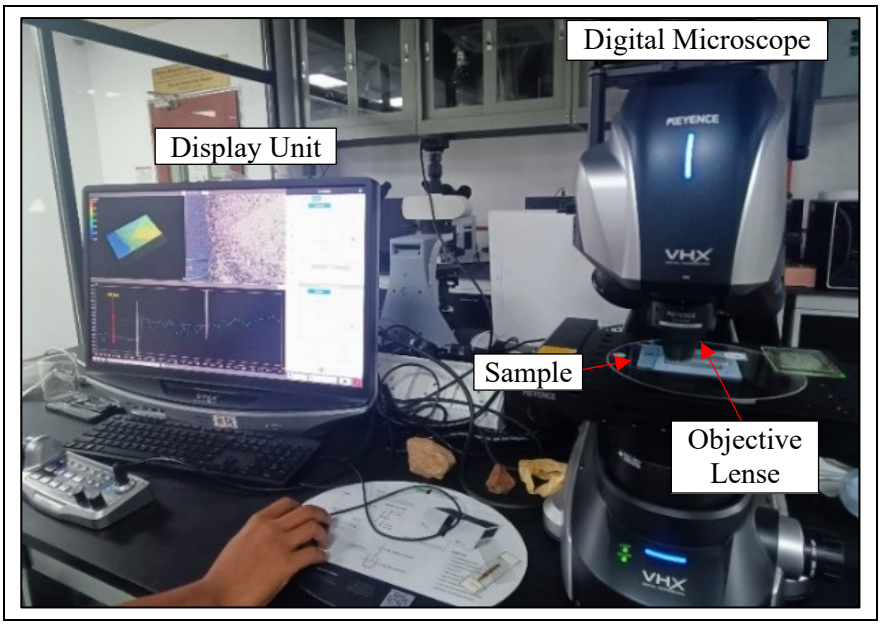


Figure 3.6 VHX Digital Microscopes and Display Unit

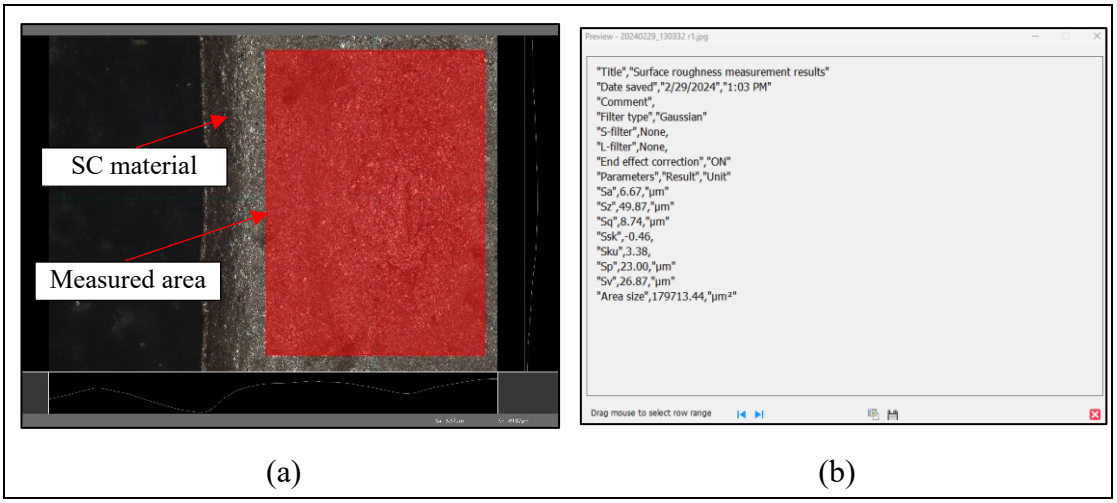


Figure 3.7 (a) 2D Captured Image from SC Printed Sample with Selected Area for Surface Roughness Measurement and (b) the Quantitative Data of Surface Roughness

The thickness of the materials was also measured using a VHX Digital Microscope, which captures high-resolution 3D and cross-sectional views of the printed sample on a PET substrate. This method offers a precise and non-destructive approach

to measuring material thickness by analyzing its height profile. The 3D view image, as illustrated in Figure 3.8, displays variations in height across the sample, allowing for a clear distinction between the PET substrate and the conductive material (i.e., SC material). The top-view image provides a detailed visual representation of the printed SC material on the substrate, with the intended regions for thickness measurement marked.

A cross-sectional view is generated to display the vertical height profile of the sample. The profile highlights the constant height of the PET substrate and the highest peak of the SC material, enabling precise thickness measurement. The PET substrate serves as a baseline reference for the height measurement, as its surface is identified as having a consistent, flat profile, allowing for accurate differentiation between the substrate and the SC material. The thickness of the SC material is determined by calculating the difference between the highest peak of the SC material and the constant height of the PET substrate. Multiple measurements were taken at different locations on the sample to ensure consistency, and the average thickness was determined. The measured thickness is presented in Chapter 4.

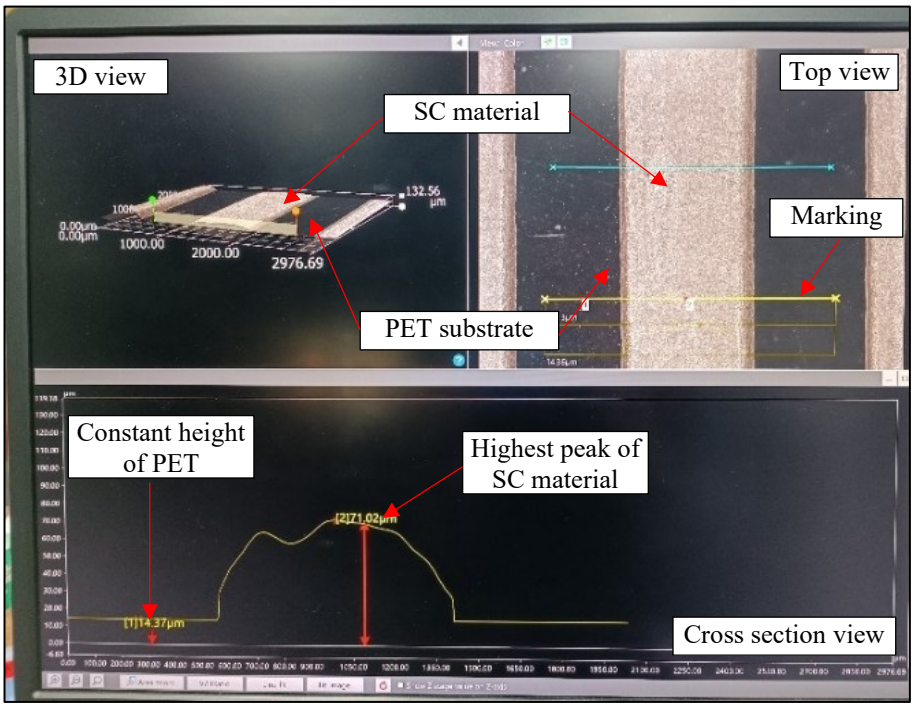


Figure 3.8 Measurement of Thickness for the SC Printed Sample

3.5 Antenna Design and Fabrication

In this subsection, the process of designing an antenna using printed conductive materials is explained. Four coil antenna designs were developed using metal-based, carbon-based, and hybrid graphene- and metal-based materials, referred to as SC, HCG and HGS materials, respectively. The NFC antenna simulation utilized two software tools: CST Studio Suite for antenna design and analysis, and Optenni Lab for antenna tuning and optimization. Meanwhile, the fabrication of the printed antenna involved three different printing techniques depending on the conductive materials used. These techniques include Direct Ink Writing (DIW), screen printing, and inkjet printing.

3.5.1 Flow of Tag Antenna Design

The process of designing the NFC tag antenna involves a complex integration process that demands careful consideration of electrical, material, and geometric parameters [154][155]. In this context, the term complex integration refers to the complex interaction between the tag antenna, the NFC chip, and the external tuning circuit, all of which must be carefully designed to achieve optimal performance at the operating frequency of 13.56 MHz. Several key steps, as illustrated in Figure 3.9, must be followed when designing an NFC tag antenna to ensure its effectiveness. The design process begins with defining the application-specific requirements, which requires the fundamental design constraints. In this research, the tag is intended for food temperature monitoring and will be attached to various packaging materials and structures. Consequently, the tag must be compact, flexible, and robust, ensuring reliable operation across various environmental conditions when affixed to different surfaces.

The next crucial step is selecting the material for the antenna's conductive layer, which significantly influences its electrical properties, performance stability, and compatibility with food-grade applications. Since the tag will be attached to food packaging, biocompatible conductive materials are highly recommended to mitigate potential health risks or contamination issues. These materials ensure that the antenna is safe for close proximity to food products, minimizing the possibility of harmful substances leaching into the packaging. Beyond biocompatibility, the electrical characteristics of the conductive material, particularly conductivity, thickness, and

surface roughness, must be carefully evaluated to reduce resistive losses and maintain optimal power transfer efficiency.

On the other hand, the selection of substrate is less critical than that of the conductive material, as it has a relatively smaller impact on antenna performance at high-frequency operation (13.56 MHz). Nevertheless, the substrate must be chosen based on its flexibility, mechanical strength, and ability to withstand higher temperatures, to ensure its compatibility over a wide temperature range. In this study, PET was selected as the substrate due to its lightweight nature, flexibility, and robustness, making it suitable for attachment on food packaging [156][157].

After selecting suitable materials, the next essential step is choosing the appropriate NFC chip, which must align with the functional requirements of the tag, whether it is designed for read-only or read-write operations. In this study, RF430FRL152H chip from Texas Instruments was selected. This chip is chosen for its integration efficiency and the inclusion of an embedded low-power microcontroller, enabling direct connection with sensors [184]. The selected NFC chip supports both read and write operations, but for a temperature monitoring application, only reading is primarily utilized to ensure energy efficiency. Other chip parameters that need to be considered is the chip's internal capacitance (C_{int}), as it directly influences the resonant frequency of the antenna and determines the necessary inductance for achieving proper impedance matching [92].

After determining the NFC chip specifications (chip type and internal capacitance), the antenna's coil geometry is carefully designed using CST Studio Suite to meet the required inductance. To ensure that the antenna resonates at the required operating frequency, an external tuning circuit is integrated between the antenna port and the NFC chip. The Optenni Lab software is used to initially verify the optimum tuning circuit configurations. The selection of tuning circuit topology is crucial as it directly influences the impedance matching and overall energy transfer efficiency of the NFC system [158].

Following the design and tuning stages, the NFC tag antenna is fabricated and extensively measured. Any discrepancies between simulated and measured results must be identified and rectified through optimization, such as adjustments to the external tuning circuit to precisely match the target resonant frequency. Finally, the functional validation of the NFC tag is conducted using an NFC-enabled smartphone, confirming its detection capability under real-world operating conditions.

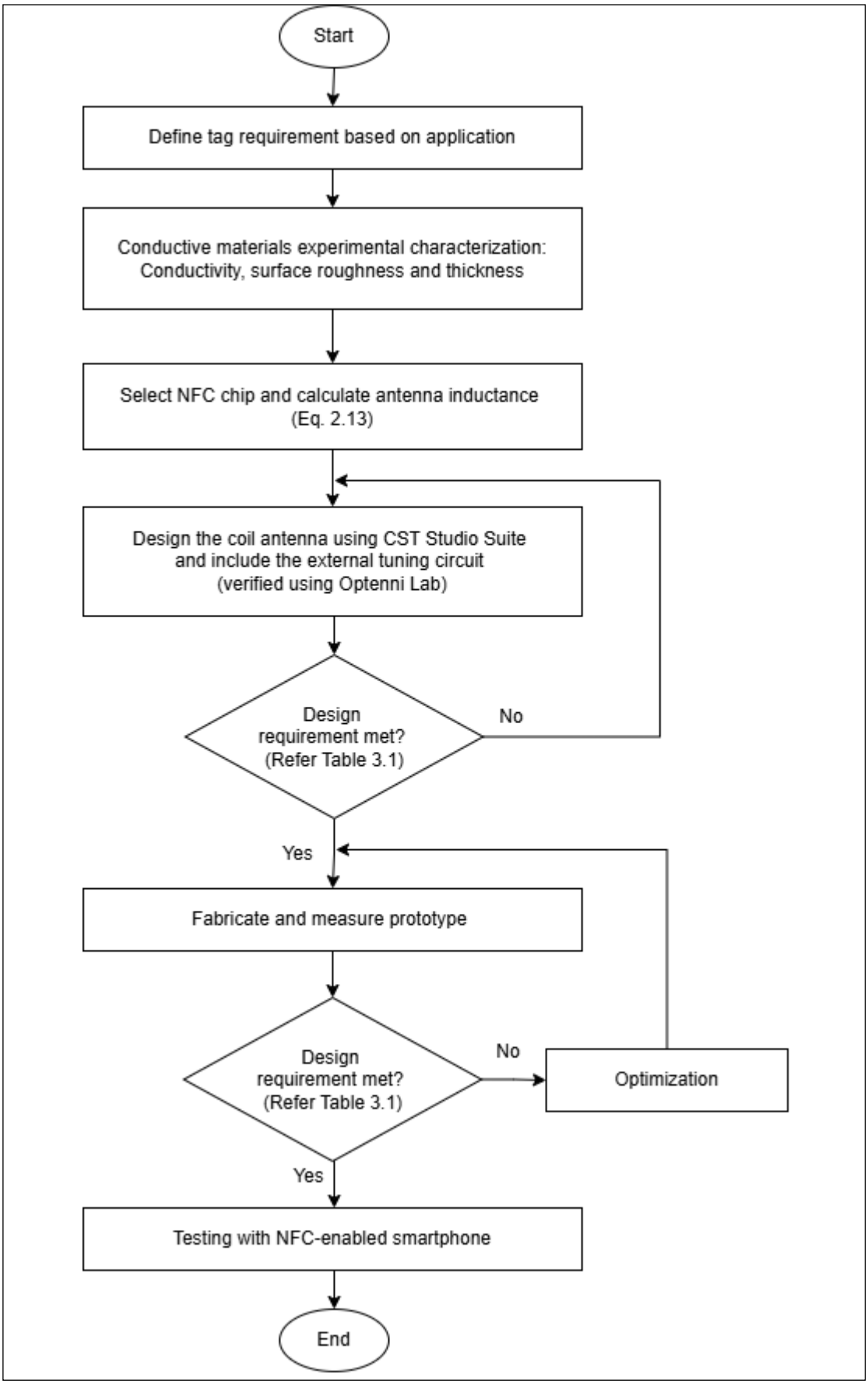


Figure 3.9 NFC Tag Antenna Design Process

3.5.2 NFC Tag Antenna Design

Four antenna designs with variations in size and geometrical parameter values have been proposed in this research for use with SC, HGS, and HCG conductive materials. The proposed Design 1 (D1), Design 2 (D2), Design 3 (D3), and Design 4 (D4) tag antennas are illustrated in Figure 3.10. The flow of the antenna design and optimization process is presented in the flow chart in Figure 3.11.

Design 1 was used as the reference antenna design, as its dimensions are based on a commercially used antenna, as elaborated in Section 2.4.2. Design 1 and Design 2 were printed using SC material, while for HGS material, Design 1, Design 3, and Design 4 were sequentially designed and analyzed. Additionally, Design 4 was printed using HCG material. However, the results for D4-HCG were not promising and has been discussed further in Section 3.5.4.2. The optimization process is further discussed in Section 4.3.2.2. Table 3.2 summarizes the dimensions and geometrical parameters of the developed antennas. The antennas were designed to be printed on a PET substrate with an electrical permittivity of 3.2 and a thickness of 0.12 mm, chosen for its excellent mechanical strength and flexible characteristics. A conductive bridge is required to connect the inner and outer loops of the coil antenna, allowing for a complete loop to be formed. The antenna geometrical analysis is discussed further in Chapter 4.

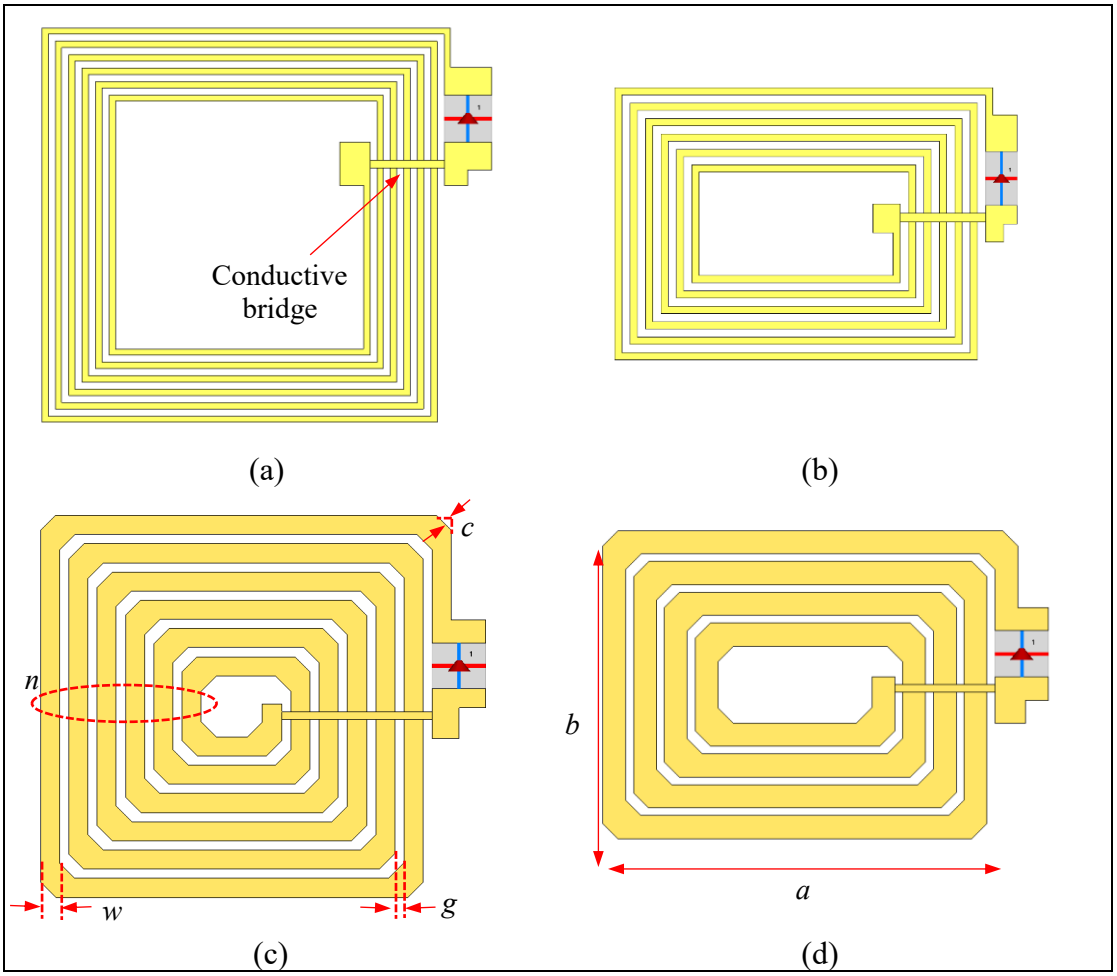


Figure 3.10 Proposed NFC Tag Antenna Designs (a) D1, (b) D2, (c) D3 and (d) D4

Table 3.2
Antenna Parameters

Antenna Design	**Design 1**	**Design 2**	**Design 3**	**Design 4**
Dimension, $a * b$ (mm^2)	50 x 50	40 x 30	50 x 50	50 x 40
Conductor width, w (mm)	0.8	0.8	2.5	3
Gap between conductors, g (mm)	0.9	0.9	1	1
Number of turns, n	6	6	6	4
Chamfer width, c (mm)	-	-	2	2

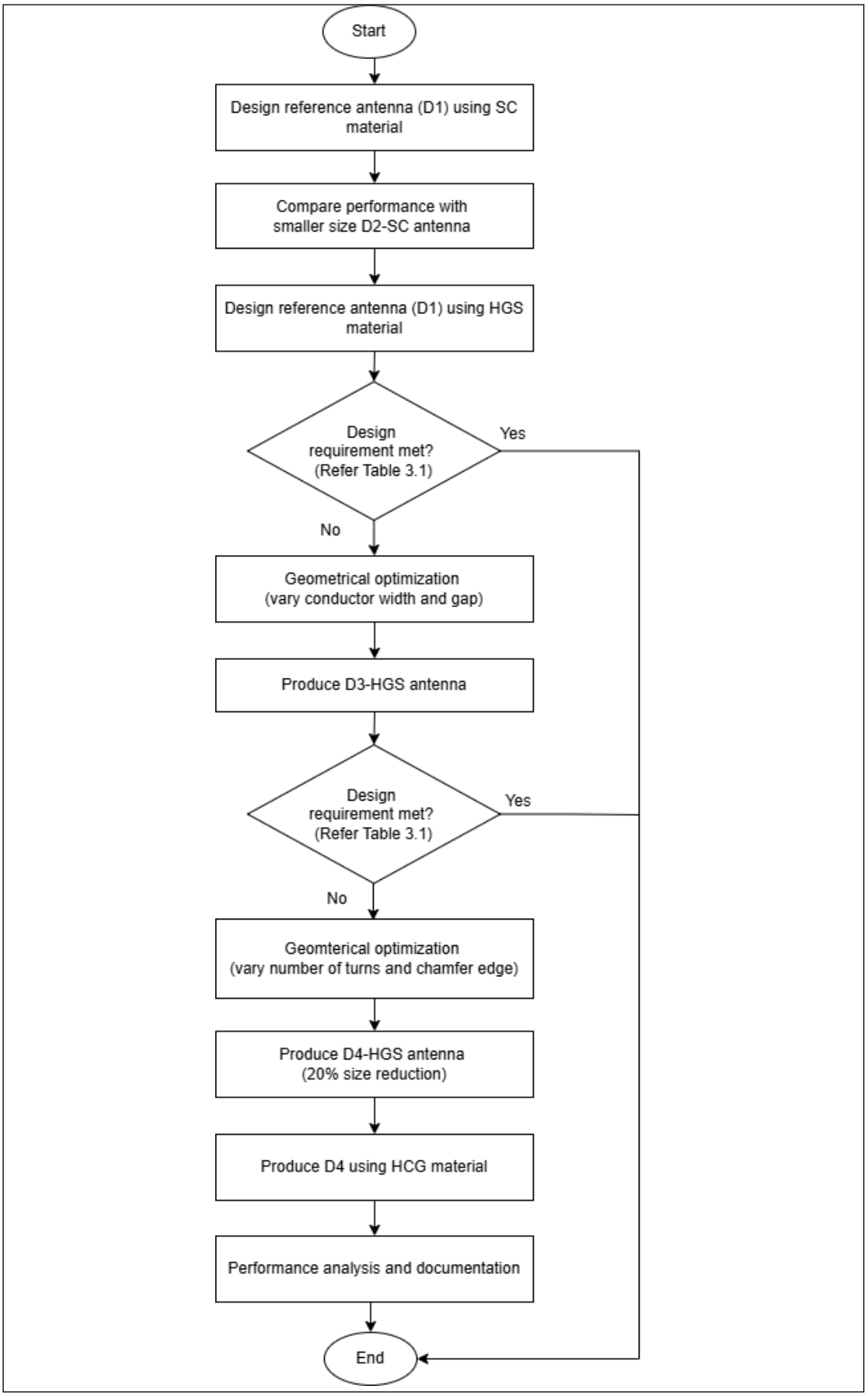


Figure 3.11 Flow of Antenna Design and Optimization Process

3.5.3 Simulation Software and Design Requirements

The design and optimization of the NFC tag antenna require accurate electromagnetic modelling and systematic impedance matching to ensure efficient operation at 13.56 MHz. In this study, two simulation tools were employed, which are CST Microwave Studio and Optenni Lab. CST Microwave Studio was used for full-wave electromagnetic simulation to extract antenna parameters and analyse field behaviour. Meanwhile, Optenni Lab was utilized for systematic tuning network optimization to achieve resonance and proper matching with the NFC chip.

3.5.3.1 NFC Tag Antenna Design using CST Microwave Studio

Computer Simulation Technology (CST) Studio Suite is a professional 3D electromagnetic software used for designing and analysing electromagnetic components and systems. CST Microwave Studio (MWS), a module within the CST Studio Suite, is tailored for analysing and addressing HF electromagnetic challenges. It can also be used to design and analyse a variety of High Frequency (HF) devices, such as antennas, couplers, resonators, and filters. In this research, the frequency-domain solver was utilized to design and simulate the NFC tag antenna, as it provides highly accurate results for specific frequencies.

This design process involved creating a coil antenna with a conductor bridge to connect the outer and inner loops of the antenna, as illustrated in Figure 3.12(a). A discrete port is used as the feeding point source for the antenna, representing an NFC chip. Between the port and the antenna, a matching circuit, consisting of the internal capacitance of the NFC chip, C_{int}, and an external tuning circuit is integrated, as illustrated in Figure 3.12 (b). This external tuning circuit plays a critical role in ensuring the antenna achieves resonance at 13.56 MHz by compensating for variations in the antenna's inductance and the chip's internal capacitance. However, CST Studio Suite has limitations when it comes to verifying the performance of the external tuning circuit across multiple iterations and configurations. While CST can accurately simulate the electromagnetic behaviour of the antenna, it is not specifically optimized for the iterative design and optimization of external matching and tuning circuits. To address this limitation, Optenni Lab software is proposed for use in the external tuning process.

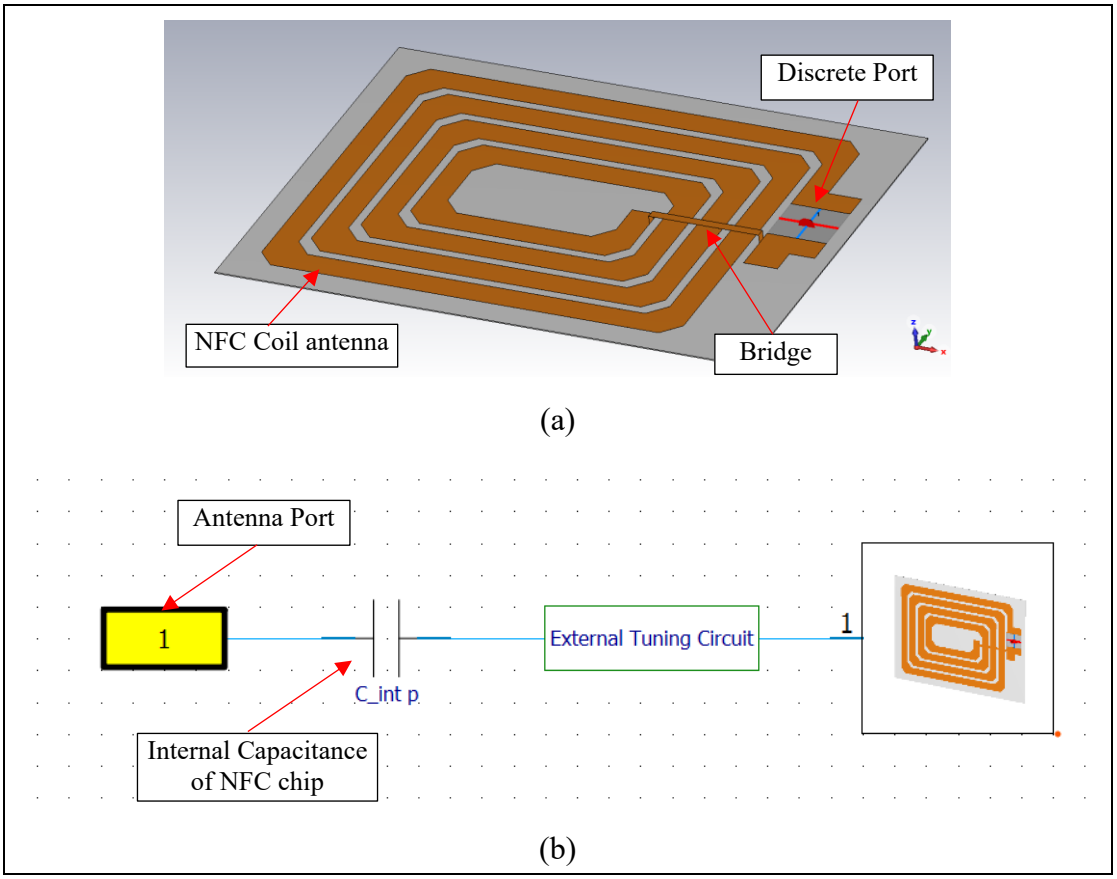


Figure 3.12 (a) Antenna Design Using CST Simulation Software (b) Schematic Diagram of NFC Antenna with Matching Circuit in CST Design Studio

3.5.3.2 Antenna Tuning Using Optenni Lab

Optenni Lab is a specialized software designed for the automatic design and optimization of matching networks. It allows for rapid iteration, providing insights into the optimal tuning circuit configurations for achieving the desired impedance matching and resonance frequency. For NFC applications, the goal is to optimize the antenna system for operation at 13.56 MHz, ensuring efficient power transfer and robust performance. Optenni Lab can be used for initial verification to obtain the optimum tuning circuit configurations before they are integrated with the antenna design in CST software. Figure 3.13 illustrates the interface of the Optenni Lab software.

Initially, the antenna is simulated in CST Studio Suite using a frequency domain solver, as it is capable of handling fine meshing more efficiently for compact structures of NFC antennas without requiring very large time steps. The original unmatched impedance data obtained from the CST simulation is exported as an .S1p file (Touchstone format). This file contains the antenna's impedance response, which was

then imported into Optenni Lab. The specific frequency band relevant to the research, in this case, the NFC band, is selected for tuning to achieve the required resonant frequency of 13.56 MHz. Optenni Lab analyzes the imported impedance data to identify the degree of mismatch between the antenna's impedance and the desired load impedance (typically 50 Ω for most NFC chips).

Based on the impedance data, Optenni Lab proposes multiple matching circuit topologies using combinations of capacitors and inductors in series or parallel configurations. The number of iterations and the complexity of the topologies depend on the user-defined number of components and configuration options. It is recommended to start with a smaller number of components (i.e. 2 to 3 components) to simplify the topology and reduce potential losses. An example of topology variation is illustrated in the red-dashed box in Figure 3.13. The proposed topologies are reviewed, and the one that best meets the following criteria is selected:

i. Compatibility with the NFC chip's internal capacitance (C_{int}).
ii. Minimal insertion loss.
iii. Alignment with the target resonant frequency of 13.56 MHz.

Optenni Lab highlights the performance of each topology in terms of impedance matching, reflection coefficient (S_{11}), and efficiency. One of the tips when selecting a topology is to choose the simplest topology that achieves the desired performance, thereby minimising implementation complexity. Once the optimal topology is selected, it is exported back to CST Studio Suite in the form of a matching network schematic, which is then integrated with the antenna design for further simulation and validation. The equation representing the coil antenna and the tuning circuit with respect to the resonant frequency is then developed. By combining CST Studio Suite for antenna design and Optenni Lab for tuning circuit optimization, a more comprehensive design workflow can be achieved, ensuring that the NFC tag antenna meets its performance requirements while minimizing manual trial-and-error in the tuning process.

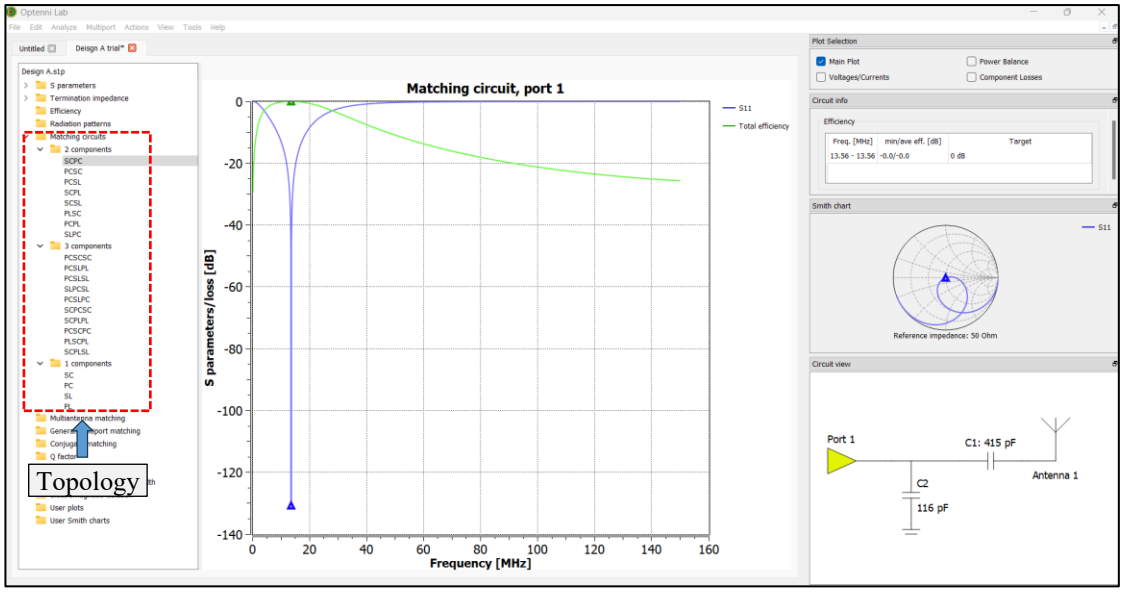


Figure 3.13 Optenni Lab Software Interface

3.5.4 Fabrication of Printed Flexible NFC Antenna

The traditional fabrication method of NFC antennas is through chemical etching. This technique wastes a significant amount of raw materials and generate chemical waste during the etching process [159]. Nowadays, the most commonly used printing methods for flexible antennas are screen printing and inkjet printing [23]. In comparison to the previous etching method used for metal-based ink fabrication, these methods are more environmentally friendly, simpler, and require a reduced number of processing stages. Other methods, such as direct ink writing (DIW), are also emerging as alternatives for fabricating flexible NFC antennas. The choice of fabrication method for different inks (SC, HCG, and HGS) is primarily determined by the specific physical and functional properties of each ink.

SC inks are often highly viscous, making them suitable for extrusion-based techniques, such as DIW. DIW enables the precise deposition of highly conductive traces with consistent thickness, which is essential for maintaining the desired electrical properties of SC-based antennas [160]. In contrast, HGS inks typically have lower viscosity than SC inks, making them compatible with the inkjet printing process. Lower viscosity is essential for inkjet printing, as the ink must flow easily through micro-sized nozzles without clogging [161]. Meanwhile, screen printing is well-suited for inks like HCG, which require thicker, robust layers to achieve the desired conductivity. The high viscosity of HCG also allows for precise deposition through the mesh screen,

preventing smudging. The detailed processes of each printing method are described in the following subsection.

3.5.4.1 Direct Ink Writing (DIW)

Direct ink writing (DIW) requires the nozzle to move relative to the substrate to draw and fill in the pattern feature by feature. Basically, the nozzle moves like a pencil over paper, depositing the pattern onto the substrate one trace at a time. This technique offers greater material efficiency, as ink is deposited only where needed, further reducing waste. However, the printing duration is longer compared to screen and inkjet printing [162]. This printing excels in low-volume prototyping and applications that require high customization.

The Voltera V-One PCB printer, shown in Figure 3.14, is a type of DIW technology used to print the antenna pattern with SC ink on a PET substrate. The fabrication process was conducted at the Collaborative Microelectronic Design Excellence Centre (CEDEC), USM. The antenna was printed in three layers, as illustrated in Figure 3.15, adapted from a previous technique [163]. The first layer formed the coil, the second layer served as the insulator, and the third layer acted as the bridge, connecting the inner and outer coils of the antenna. Connecting the inner and outer coils ensured the formation of a loop antenna, which achieved the required inductive performance. The square labels in each layer must be properly aligned during the printing process to ensure that each layer is connected in the desired location.

The printing process is illustrated in Figure 3.16. The first and third layers were printed using SC ink from Voltera, while the insulator layer was printed using UV-curing solder mask ink from Mechanic [84]. To ensure that the first layer functions correctly before proceeding to the second layer, a verification process was carried out. This process involved measuring the resistance of each line of the coil antenna, along with performing a continuity test using a multimeter. A resistance of less than 50 Ω is generally acceptable for functional printed conductive lines in antennas or circuits, ensuring proper current flow without significant losses [164]. If the measured resistance is within this range, it is considered stable, indicating that the lines of the coil are well-connected. However, if the resistance falls outside the acceptable range, it indicates issues such as breaks, inconsistencies in the printed lines or very low conductivity of the material. In such cases, the coil antenna layer must be reprinted, and the verification

process repeated until the measured resistance is within the acceptable range. The verification results for D1-SC and D2-SC are presented in Chapter 4. The fabricated D2-SC tag antenna is illustrated in Figure 3.17.



Figure 3.14 Voltera V-One PCB Printer

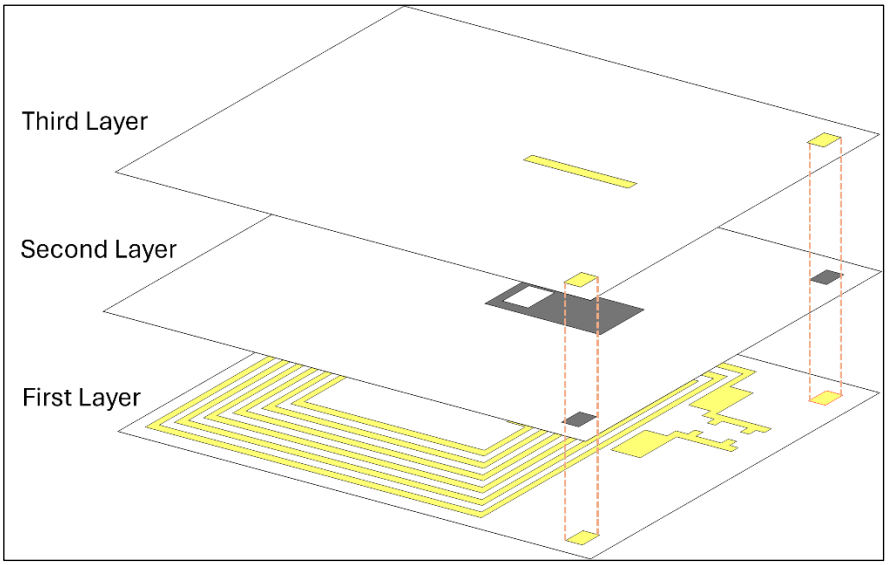


Figure 3.15 Different Layers of Printing for D2-SC Tag Antenna

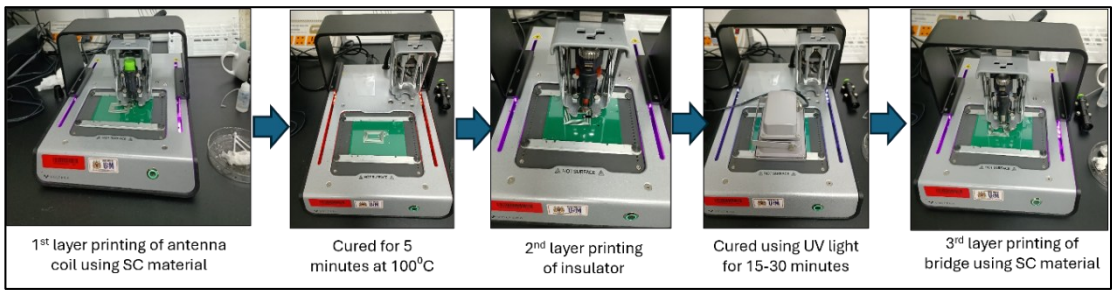


Figure 3.16 Printing Process using DIW Technology

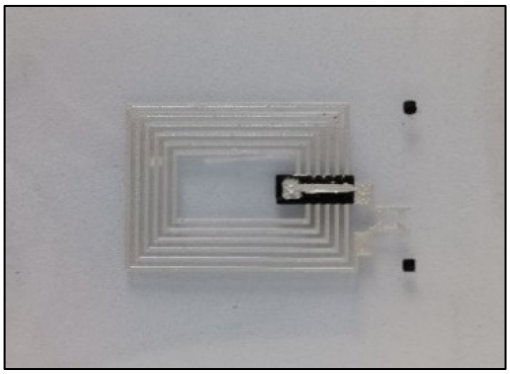


Figure 3.17 Fabricated D2 Tag Antenna Printed Using SC Material

3.5.4.2 Screen Printing

Screen printing, also known as silk screening or silkscreen printing, is a process of transferring a stencilled design onto a surface using a mesh screen, ink, and a squeegee (a rubber blade) [45]. It is a popular technique due to several advantages, the most compelling being its cost-effectiveness, as high volumes of items can be printed in a short time [165]. In this study, the screen-printing technique was used to print the HCG conductive ink onto a PET substrate. The basic process involves creating a stencil on a mesh screen, as illustrated in Figure 3.18(a). The PET substrate is placed flat beneath the stencil, and the conductive ink is applied at the top of the screen. A squeegee, angled at 45◦, as shown in Figure 3.18 (b), pulls the ink across the screen, forcing it through the stencil to imprint the design on the surface below. The fabricated antenna is subsequently dried on a hot plate at 110°C for 10 minutes, as illustrated in Figure 3.18 (c), to enhance the adhesion between the ink and the substrate.

To ensure the printed coil antenna was well-connected, a verification process similar to that used for antennas printed with DIW was conducted. This process involved measuring the resistance of each line of the coil antenna and performing a continuity test using a multimeter. However, during the continuity test, no beep sound was detected, and the measured resistance was significantly higher than the acceptable range ($< 50\ \Omega$) for a stable connection. This issue is probably due to the lower conductivity of the HCG ink (~10^2 S/m), which inherently results in higher resistance compared to materials with higher conductivity, such as silver-based inks (~10^5 to ~10^6 S/m). The verification results for D4-HCG are presented in Chapter 4.

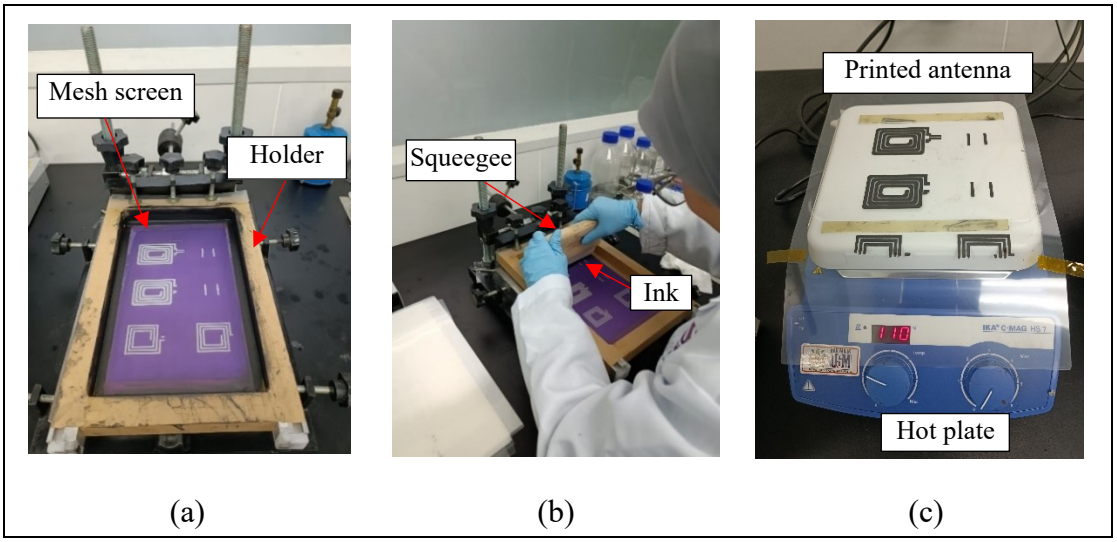


Figure 3.18 Fabrication Process Using Screen Printing

3.5.4.3 Inkjet Printing

Inkjet printing is a non-contact method that deposits ink on a substrate without using a mask. Through the inkjet printing method, the specified design is directly transferred to the substrate, thus minimize the electrical device production costs, as the material can be inserted on demand [166]. Moreover, multiple thin conductive layers with low edge roughness can be printed using ink-jet printing technology [167]. The NFC tag antenna using HGS conductive materials was fabricated at MIMOS Berhad using an inkjet printing technology with PiXDRO LP50 (SuSS MicroTec), as shown in Figure 3.19. It is a drop-on-demand (DOD) printer that utilises piezoelectric inkjet technology, with droplets ejected only when needed.

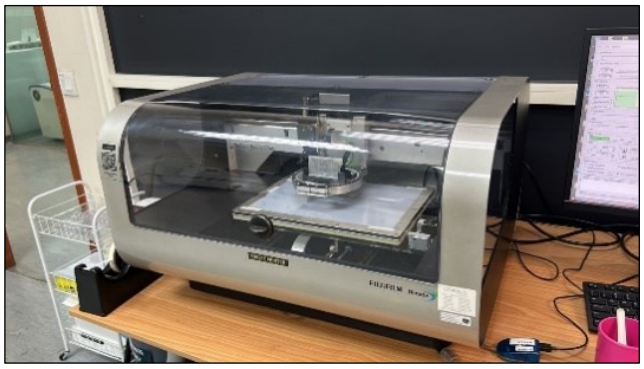


Figure 3.19 PiXDRO LP50 (SuSS MicroTec) Inkjet Printer

Figure 3.20 illustrates the inkjet printing process of the NFC tag antenna using HGS conductive ink. During the inkjet printing stage, the ink is dispensed from a nozzle in the form of micro-droplets and deposited onto the substrate surface. The platen temperature of the printer can be adjusted between 28 °C and 60 °C to control the spreading and evaporation of the droplets. For this fabrication, the platen temperature was fixed at 40 °C to minimize ink spreading and achieve uniform line definition. The thickness of the printed layer is controllable within the range of 1 μm to 5 μm, depending on the number of printing passes. To ensure flexibility, the antenna design, including the bridge structure used to electrically connects the inner and outer antenna coils, was directly printed on a flexible PET substrate. After printing, the antenna was cured at 40°C for 30 minutes to evaporate the solvent and improve adhesion between the ink and the substrate.

A verification process was also conducted to ensure that the printed coil antenna was well-connected. This involved measuring the resistance of each line of the coil antenna and performing a continuity test using a multimeter. If the measured resistance was within the acceptable range ($<50\ \Omega$), it is considered stable, indicating that the lines of the coil are well-connected. However, if the resistance fell outside the acceptable range, it indicated issues such as breaks or inconsistencies in the printed lines. In such cases, the coil antenna layer was reprinted, and the verification process was repeated until the resistance was within the acceptable range. The verification results for D1-HGS, D3-HGS, and D4-HGS are presented in Chapter 4.

After the verification process, the antenna coil and bridge were bonded using conductive epoxy (CW2400). The conductive epoxy was cured at room temperature (25°C) for 4 hours, with maximum bond strength achieved after 24 hours.

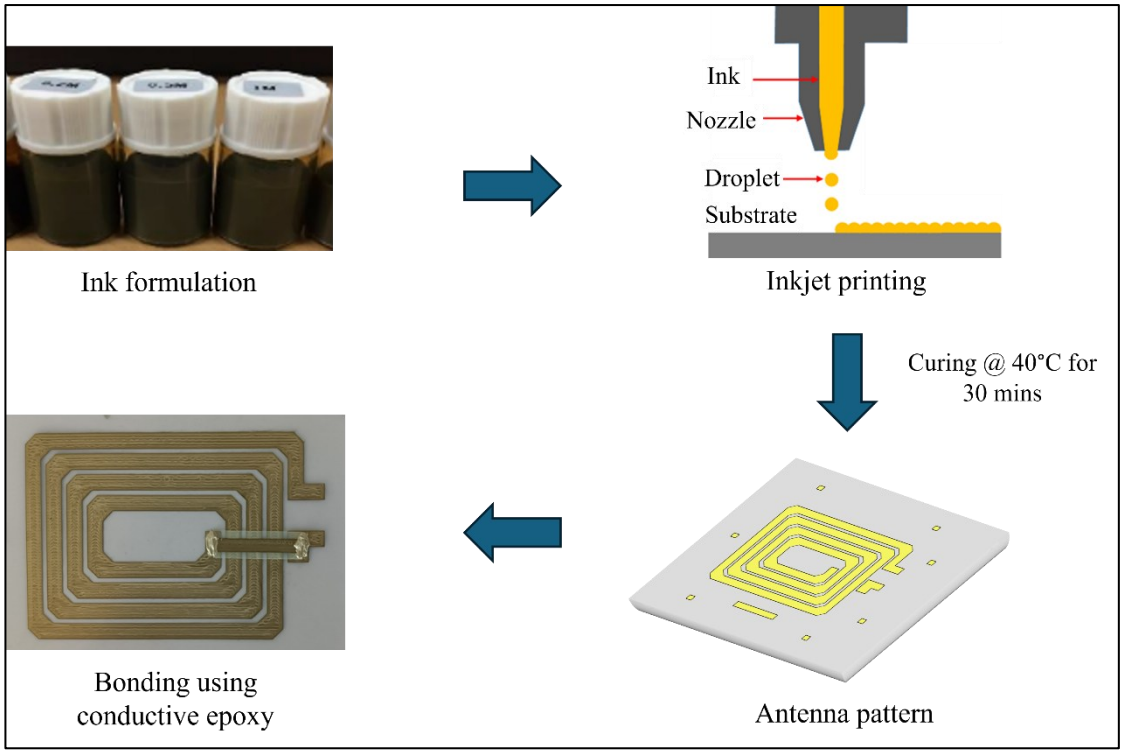


Figure 3.20 Fabrication Process of Graphene-Based NFC Tag Antenna

3.6 Antenna Robustness Measurement

The robustness of an NFC antenna is a critical parameter that determines its reliability and functionality in real-world applications [111]. In food packaging, where the antenna is exposed to varying mechanical stresses and environmental conditions, ensuring its robustness becomes even more significant [168]. A robust NFC antenna must maintain consistent performance despite being subjected to bending or folding during handling and use. It should also remain unaffected by different packaging materials and environmental factors such as temperature fluctuations and exposure to moisture.

3.6.1 Flexibility Measurement

Food packaging materials often come in various forms, such as pouches, boxes, or curved surfaces, requiring the NFC tag to conform without compromising performance. Flexibility analysis is crucial to ensure that the NFC tag can accommodate the diverse shapes of food packaging and remain functional under bending and folding during application, transportation, and handling [3][169]. The flexibility of the tag

antenna has been assessed by varying the bending radius. Bending radius of 1.5 cm to 4.5 cm were selected to replicate typical curvatures encountered in food packaging such as bottles, cups, and flexible pouches. In the simulation, the antenna is bent on a cylindrical foam with a dielectric constant, ε_r, of 1, at different angles by varying the cylindrical bending radius, r, as shown in Figure 3.21 (a). The relationship between the bending radius and angle can be determined using the arc length, s formula in Equation (3.1) , where the bending angle, θ, is inversely proportional to the radius of the cylinder, r. Thus, an increase in radius (1.5 cm to 4.5 cm) results in a decrease in the bending angle (190.9º to 63.7º). To verify the simulation results, the tag was measured at different bending angles by attaching it to various sizes of cylindrical foam, as shown in Figure 3.21 (b), and connecting the tag antenna to the VNA and tuning capacitors, as depicted in Figure 3.21 (c), to observe shifts in the resonant frequency.

$$s = \theta \cdot r \approx \frac{s}{r} = \theta \tag{3.1}$$

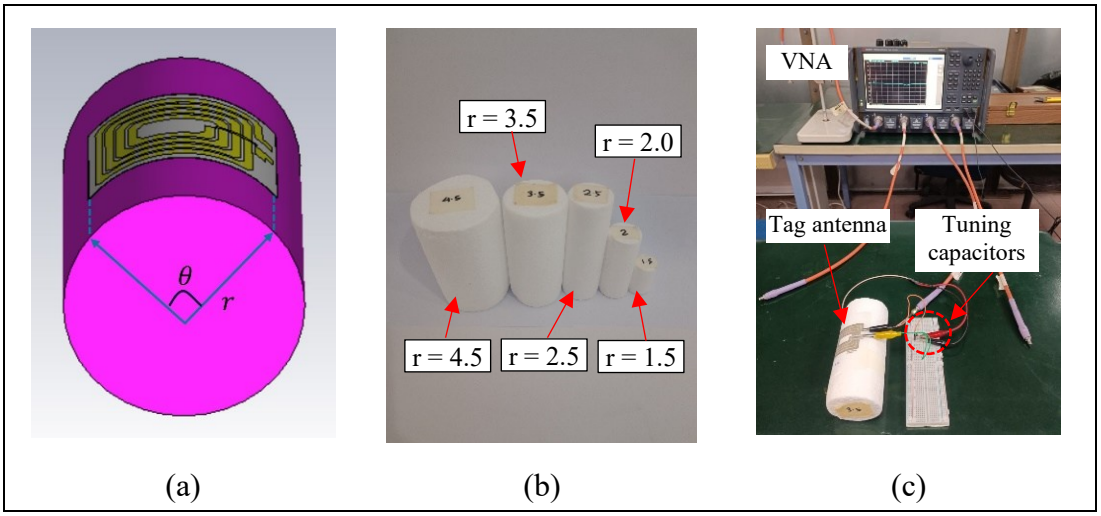


Figure 3.21 (a) Simulation of Antenna Bending, (b) Cylinder Foam with Varying Radius, r in cm, and (c) Measurement Setup for S_{11} at Different Bending Angles Using VNA

3.6.2 Sensitivity Measurement

Sensitivity analysis is crucial for ensuring the NFC tag operates reliably across various packaging types and environmental factors, such as moisture and temperature variations, which are common in food storage and handling. In this context, sensitivity

refers to the degree to which external environmental factors influence the performance of the NFC antenna, particularly its impedance matching, resonant frequency, and read range [3][170]. Testing the performance of the NFC tag antenna on commonly used food packaging materials, such as plastic (PE/PS), carton boxes, glass, and aluminium foil, is essential for determining its practical usage and reliability in real-world applications. Each of these materials interacts differently with the magnetic field of the antenna, which can affect crucial factors such as resonance frequency, electrical properties (including antenna inductance and resistance), and reading range [101]. Aluminum foil and other metals, in particular, present unique challenges due to their conductive nature, which can significantly interfere with the operation of the NFC antenna. Therefore, simulations and measurements of the tag antenna attached to these materials, as depicted in Figure 3.22 and Figure 3.23, were conducted to examine the effects on antenna performance.

Further analysis focused on tag antennas attached to metallic surfaces, with a detailed investigation into the use of different types of magnetic sheets, including ferrite, amorphous, and nanocrystalline, to mitigate the effects of eddy currents generated on the metallic surfaces. Correlations were established between the properties of magnetic sheets, such as permeability and thickness, and their ability to reduce metallic interference. The equivalent circuit modelling was also conducted for the tag antenna with the magnetic sheet and metallic surface to predict the performance output by analysing the interaction of key electrical components, such as resistance, inductance, and capacitance, under varying conditions. The equivalent circuit model is further discussed in Section 3.7.

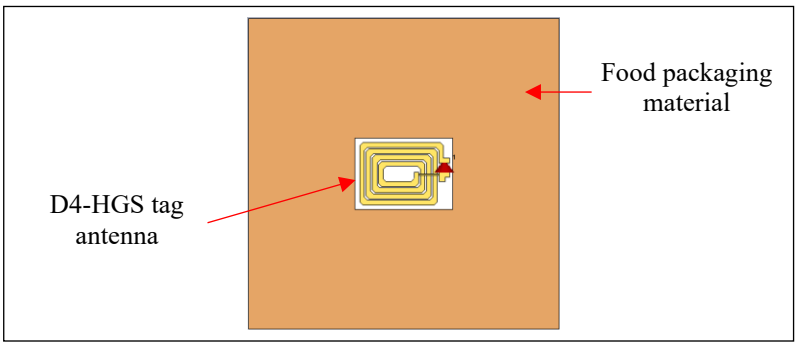


Figure 3.22 Simulation of NFC Tag Antenna Attached to Food Packaging Material

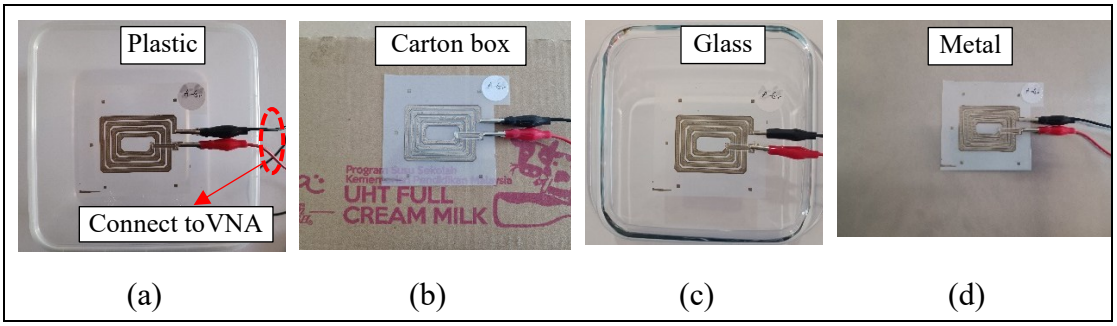


Figure 3.23 D4-HGS is Connected to VNA Port and Attached to Different Materials: (a) Plastic (b) Carton Box (c) Glass and (d) Metal

The sensitivity of the NFC tag to a moist environment was investigated through simulations by exposing the tag antenna to a water element, as depicted in Figure 3.24. A water layer with a permittivity of 80 was introduced directly to the conductive layer of the tag antenna. The water amount was varied from 25%, 50%, 80% and 100 % (fully moist), corresponding to different water layer sizes of 30 x 20 mm², 40 x 30 mm², 50 x 40 mm² and 60 x 40 mm², respectively, as illustrated in Figure 3.25, to observe its correlation with antenna performance in terms of S_{11}, inductance and reading range. By introducing water layers with different coverage areas, the analysis simulates scenarios that mimic condensation, spills, or high-humidity storage conditions often encountered in food packaging environments. The reading range of the tag antenna in wet conditions was also measured and compared with that in dry conditions.

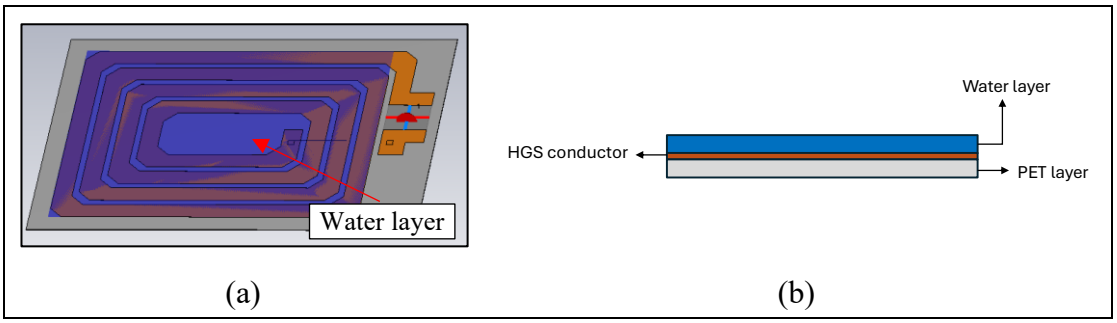


Figure 3.24 (a)Water Layer Directly Attached to the Antenna and (b) Side View of the Antenna with the Water Layer

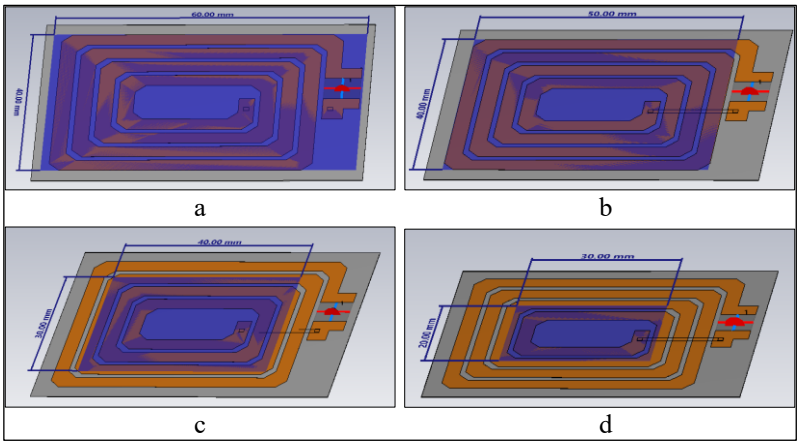


Figure 3.25 Different Amounts of Water Content: (a) 100 %, (b) 80%, (c) 50% and (d) 25%

Temperature fluctuations are common in food storage and handling, such as during refrigeration, transportation, or shelf placement, and these changes may affect the performance of the antenna, which requires further investigation [3][134]. Using a hotplate, the antenna, which is connected to the LCR meter, as shown in Figure 3.26, was exposed to temperatures ranging from 25°C to 65°C. A digital thermocouple thermometer, also connected to the hotplate, was used as a reference to ensure accurate temperature delivery to the tag antenna. The antenna's characteristics, in terms of resistance and inductance, were observed concerning temperature changes.

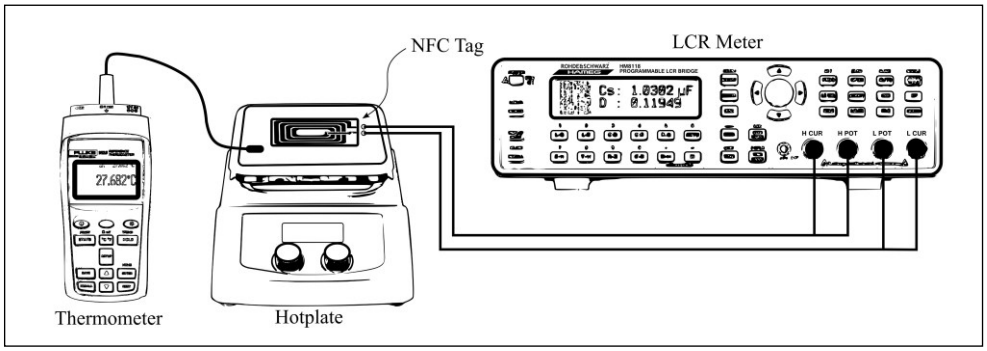


Figure 3.26 Measurement Setup for La and Ra at Different Temperature Range

3.7 Equivalent Circuit Model for On-Metal Tag

The equivalent circuit (EC) of the NFC tag antenna with the magnetic sheet and metal plate was modelled using the Advanced Design System (ADS) simulator software to observe and verify its response in terms of the reflection coefficient, which was subsequently compared to CST simulation results. This modelling approach provides a

deeper understanding of the electrical behaviour of the antenna structure in a metallic environment and the influence of the magnetic sheet on its electrical characteristics. This circuit modelling is beneficial for predicting the impedance matching and resonance behaviour of the NFC tag antenna before real measurements are conducted. The electrical components, including a resistor (R), an inductor (L), and a capacitor (C), are connected in parallel and series topologies, representing the antenna structure that incorporates a magnetic sheet and a metal plate. The development of EC was carried out in several steps: initially, the EC of the NFC tag antenna alone was created, followed by the addition of the magnetic sheet, and finally, the inclusion of the metal plate to complete the EC model.

The EC of the NFC tag antenna can be represented by a series inductor, L_a, and a resistor, R_a, connected in parallel with a capacitor, C_a as depicted in Figure 3.27 [171]. L_a is primarily related to the number of coil turns, while R_a depends on the diameter and length of the antenna conductor. C_a is influenced by the gap between the coil (g) and the overall antenna geometry, including the dielectric material. The value of L_a is mainly determined by the antenna's geometry and can be calculated using Equation (2.12), as discussed in Section 3.5.2. Meanwhile, R_a and C_a can be calculated using Equation (3.2) and (3.3), respectively, where ρ is the resistivity of the conductor material, n is the number of turn, l_{avg} is the average turn length of the conductor, A is the cross-sectional area of the conductor, l_t is the total length of overlapping turns, ε_r is the relative permittivity of the material between the turns and ε_0 is the permittivity of free space (8.85×10^{-12} F/m) [172].

$$R_a = \rho \cdot n \cdot \frac{l_{avg}}{A} \tag{3.2}$$

$$C_a = \varepsilon_r \cdot \varepsilon_0 \frac{l_t}{g} \tag{3.3}$$

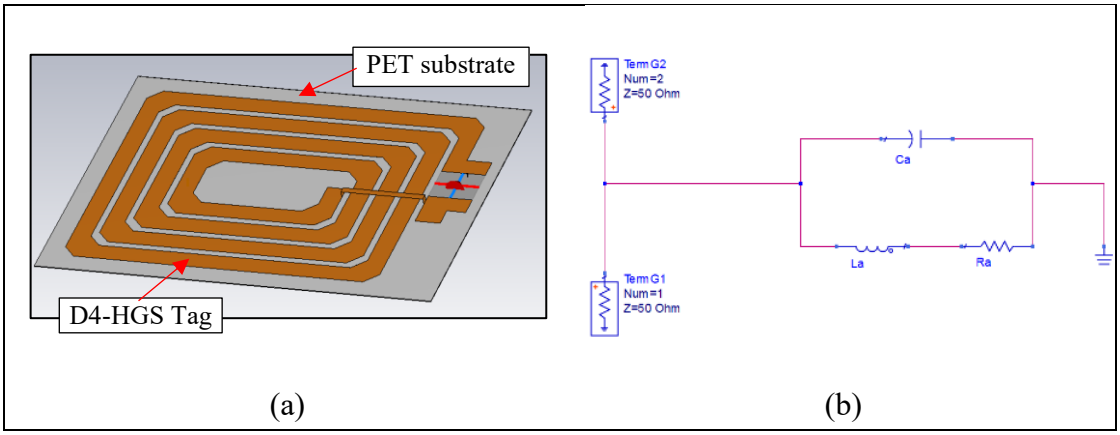


Figure 3.27 (a) The CST Simulation Design of NFC Tag Antenna on Free Space and (b) The ADS EC of NFC Tag Antenna

Next, a magnetic sheet is introduced at the back of the NFC tag antenna, as depicted in Figure 3.28. The electrical properties of the magnetic sheet are represented by an inductance, L_{mag}, and self-capacitance, C_{mag}, connected in parallel, as shown in Figure 3.28. L_{mag} represents the inductive energy storage based on the material's geometry and permeability, while C_{mag} arises from the sheet's ability to store electric charge due to its dielectric properties and thickness, calculated using Equations (3.4) and (3.5), respectively. Additionally, coupling capacitance (C_{couple}) and mutual inductance, M arise due to the close proximity and magnetic interaction between the antenna conductor and the magnetic sheet, calculated using Equation (3.5) and (3.6), respectively [105][173]. The parameter μ_r represents the relative permeability of the magnetic material, μ_0 is the permeability of free space ($4\pi \times 10^{-7}$ H/m), $t_{mag/PET}$ and $A_{mag/PET}$ are the thickness and cross sectional area of magnetic sheet or PET substrate, respectively, and k is the coupling coefficient ($0 \leq k \leq 1$).

$$L_{mag} = \frac{\mu_r \cdot \mu_0 \cdot A_{mag}}{t_{mag}} \tag{3.4}$$

$$C_{mag/couple} = \frac{\varepsilon_r \cdot \varepsilon_0 \cdot A_{mag/PET}}{t_{mag/PET}} \tag{3.5}$$

$$M = k\sqrt{L_a \cdot L_{mag}} \tag{3.6}$$

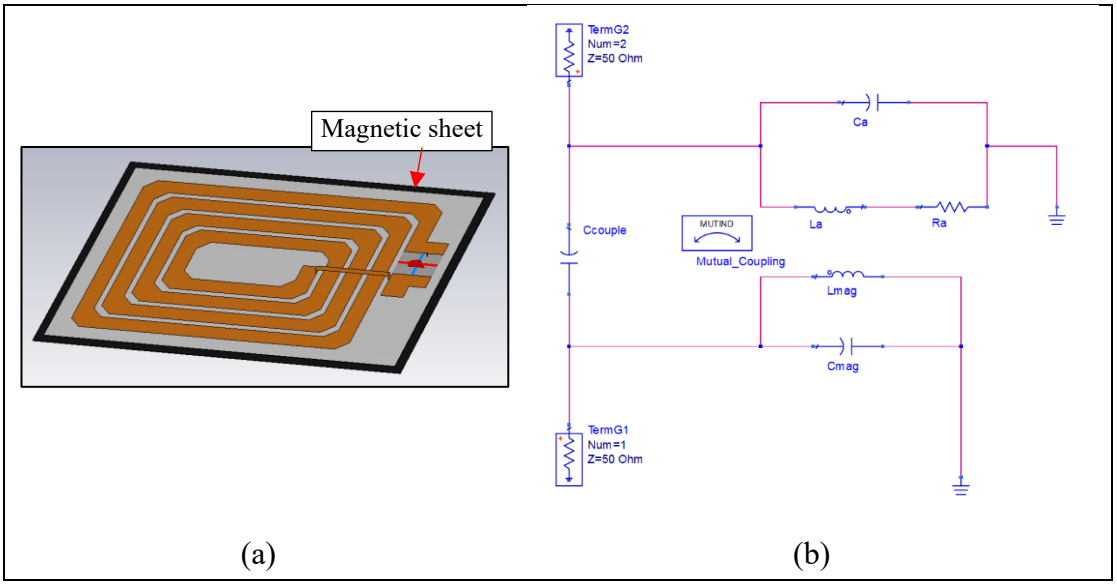


Figure 3.28 (a) The CST Simulation Design of NFC Tag Antenna with Magnetic Sheet and (b) the ADS EC of NFC Tag Antenna with Magnetic Sheet

When the tag antenna with the magnetic sheet is attached on the metal plate as shown in Figure 3.29, eddy currents are induced in the metal plate, contributing additional resistance components: the resistance of eddy currents (R_{eddy}) and resistance of the metal plate (R_{met}). In the EC, the R_{eddy} and R_{met} are represented in series with the tag antenna as shown in Figure 3.30, reflecting the combined resistive losses due to eddy currents and the metal plate. The inclusion of these components in the EC provides a more accurate representation of the system's overall impedance and helps predict the antenna's performance in metallic environments.

Additionally, the self-capacitance of the metal sheet, C_{met}, also has been included in parallel to the L_{mag} and C_{mag}. The value for R_{eddy} can be calculated using Equation (3.7), where σ is the conductivity of the metal plate and δ is the skin depth (Equation (3.8)). The skin depth determines how deeply electromagnetic waves penetrate the metal plate, which depends on the permeability of the magnetic material, μ. Meanwhile, the calculation of C_{met} can refer to previous Equation (3.5), while the value for R_{met} can be calculated using Equation (3.9), where L, W and t refer to the length, width and thickness of the metal plate, respectively [174].

$$R_{eddy} = \frac{1}{\sigma \cdot \delta \cdot A} \tag{3.7}$$

$$\delta = \sqrt{\frac{2}{\sigma \cdot \mu \cdot 2\pi \cdot f}} \tag{3.8}$$

$$R_{met} = \frac{\rho \cdot L}{t \cdot W} \tag{3.9}$$

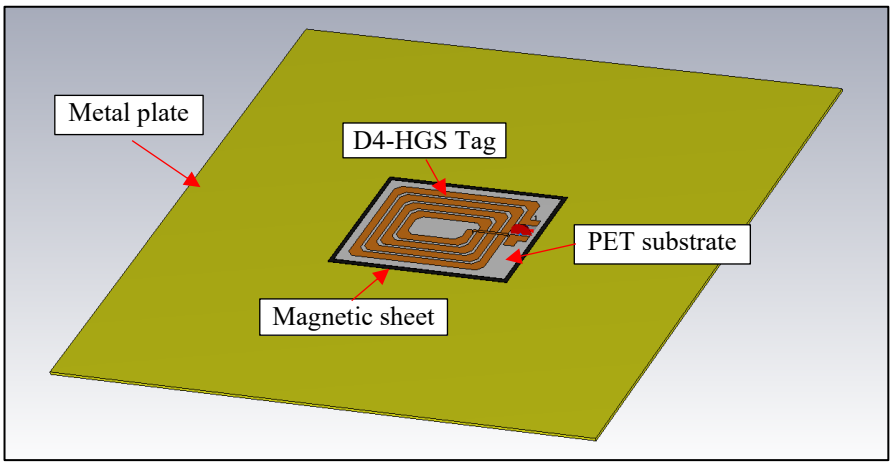


Figure 3.29 CST Simulation Design of NFC Tag Antenna with Magnetic Sheet and Metal Plate

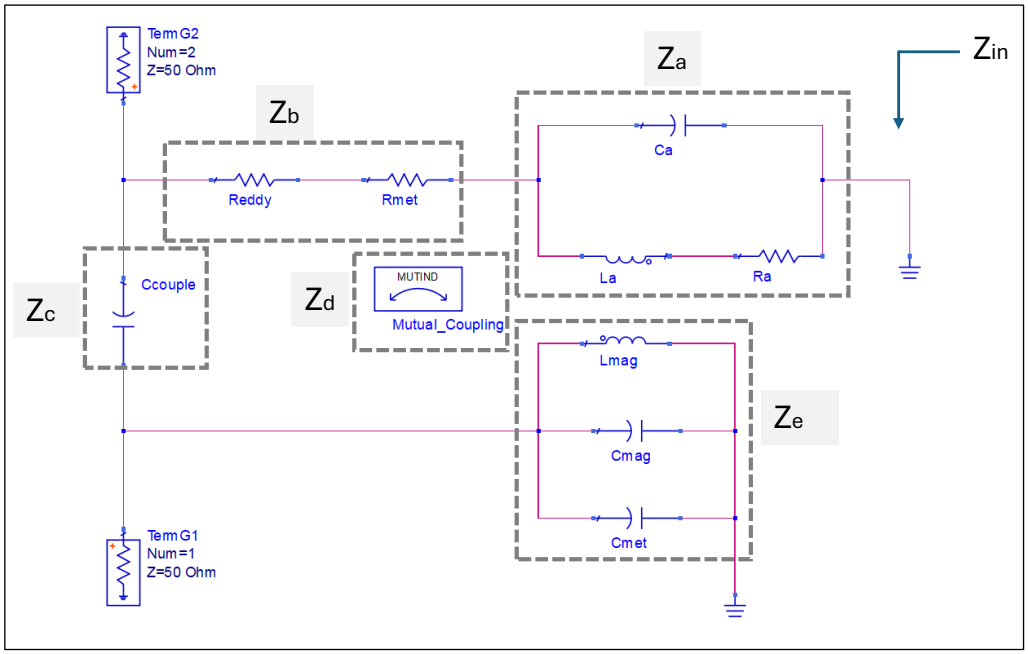


Figure 3.30 The ADS EC of NFC Tag Antenna with Magnetic Sheet and Metal Plate

The total impedance of the tag antenna with the magnetic sheet and metal plate can be calculated using the π-topology formulation, where the series combination of Z_a,

Z_b, Z_c and Z_d, representing the impedance of the antenna, metal plate, coupling capacitance, and mutual inductance, respectively, are connected in parallel with Z_e, representing the impedance of the magnetic sheet. The total impedance, Z_{total} can be calculated as in Equations (3.10) - (3.15). This equivalent circuit modeling approach provides a predictive framework for evaluating the performance of NFC tag antennas when attached to metallic packaging with magnetic shielding layers.

$$Z_{total} = \frac{(Z_a+Z_b+Z_c+Z_d)\|Z_e}{Z_a+Z_b+Z_c+Z_d+Z_e} \tag{3.10}$$

$$Z_a = \frac{R_a+j\omega L_a}{j\omega R_a C_a - \omega^2 L_a C_a+1} \tag{3.11}$$

$$Z_b = R_{met}+R_{eddy} \tag{3.12}$$

$$Z_c = \frac{1}{j\omega C_{couple}} \tag{3.13}$$

$$Z_d = j\omega M,\ M = k\sqrt{L_a L_{mag}} \tag{3.14}$$

$$Z_e = \frac{j\omega L_{mag}}{1 - \omega^2 L(C_{met}+C_{mag})} \tag{3.15}$$

3.8 Measurement Standards and Procedures

To evaluate and validate the performance of the simulated antenna, measurements of the antenna's electrical properties, including inductance, resistance, tuning, and resonant frequency, as well as the tag's reading range, were conducted. The measurement setup used for all tests is discussed in the following subsection.

3.8.1 Antenna Inductance and Resistance

The measurement of antenna inductance and resistance has been carried out using a Keysight N5232B PNA-L Vector Network Analyzer (VNA) as depicted in Figure 3.31 (a). To start the measurement, the VNA must be calibrated first, so that systematic errors from the measurement can be removed. A calibration kit provided by Keysight consists of short, open and matched standards, as shown in Figure 3.31 (b).

These calibration standards will be sequentially connected to the cable at the calibrated point to perform the calibration process. After the VNA is successfully calibrated, the impedance of the antenna can then be measured by connecting the antenna port, where the chip is intended to be connected, to the VNA port, as illustrated in Figure 3.32. Using VNA, the antenna impedance, resistance, inductance and resonant frequency can be measured and the results can be displayed in the form of a Smith chart and return loss graph. The measurement results can be saved in a Touchstone file as well as in Excel format.

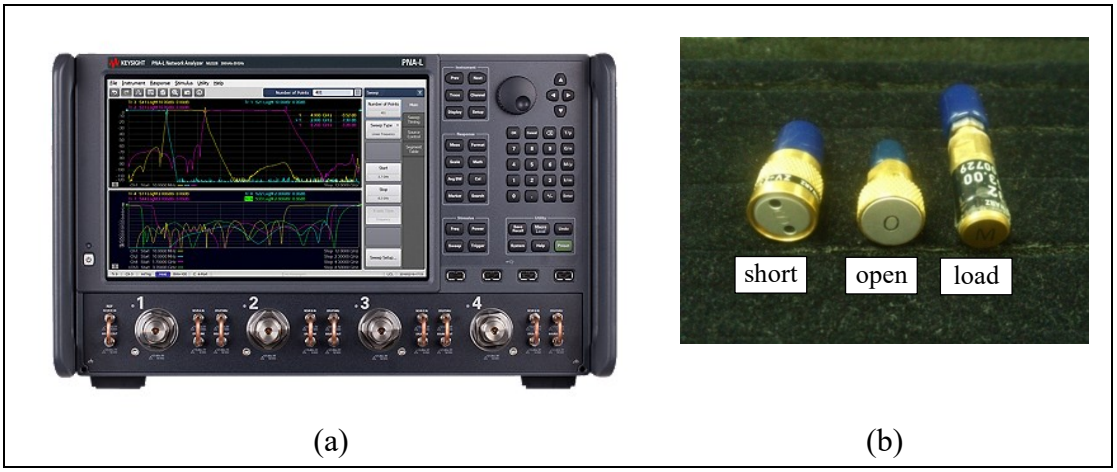


Figure 3.31 (a) Vector Network Analyzer and (b) Standard Calibration Kit from Keysight

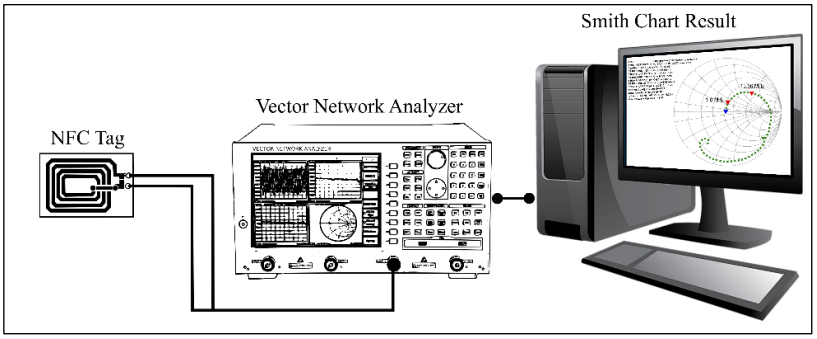


Figure 3.32 NFC Tag Antenna Connected to VNA for Impedance Measurement

3.8.2 Antenna Tuning and Resonant Frequency

The operating frequency of the NFC reader is 13.56 MHz. Meanwhile, for the tag antenna, the recommended resonance frequency falls within the range of 13.56 MHz to 16 MHz to minimize the interference with nearby tags [111] [104]. The method used

to determine the resonant frequency of the NFC tag antenna is through inductive coupling with a secondary coil antenna (with a resonant frequency above 50 MHz) connected to the VNA, as illustrated in the schematic diagram in Figure 3.33 [175]. The measurement setup is as shown in Figure 3.34 (a), where the secondary coil antenna made of a copper layer and FR-4 substrate is connected to the VNA. To measure the resonant frequency of the printed NFC tag antenna, it is then brought into close proximity with the secondary coil antenna, resulting in mutual coupling as depicted in Figure 3.34 (b). When this coupling occurs, a peak resonant frequency is displayed on the VNA, indicating the NFC tag antenna's resonant frequency. The tuning capacitors connected to the printed NFC tag antenna were adjusted until the required operating frequency is achieved.

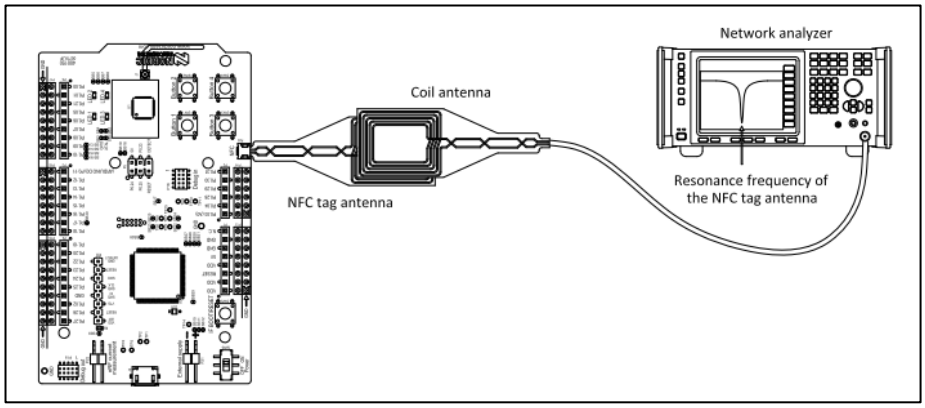


Figure 3.33 Schematic Diagram NFC Tag Resonant Frequency Measurement [175]

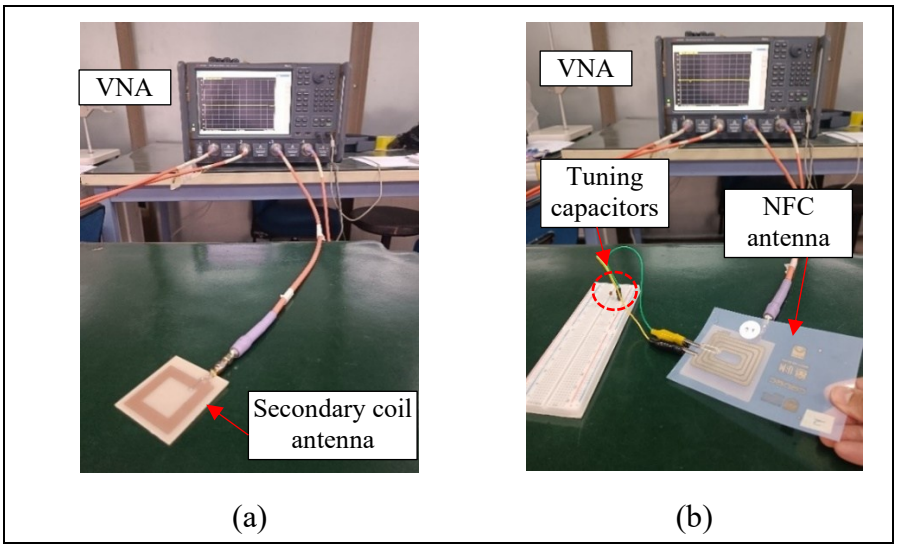


Figure 3.34 (a) Conventional Coil Antenna Connected to VNA (b) NFC Tag Antenna in Close Proximity to the Conventional Coil Antenna

3.8.3 Reading Range

The tag reading range refers to the distance between the tag and the reader within which communication can be successfully established. It is a standard method used by researchers to evaluate the performance of NFC tag antennas and has been adopted in this study as well [176][177][178]. The NFC tag reading range can be measured using either a smartphone with NFC functionality enabled or a dedicated NFC reader. For this research, a Xiaomi 11 smartphone was used as the reader. A testing setup was required to ensure that the smartphone antenna remained perpendicular to the tag antenna during reading range measurements. To achieve this, the smartphone was affixed to an adjustable-height platform placed on a table, as illustrated in Figure 3.35 (a).

Meanwhile, the tag antenna was connected to the Texas Instrument Evaluation Board (RF430FRL152HEVM), as shown in Figure 3.35 (b), to test the system using the RF430FRL152H chip available on the board. This chip will later be integrated into the printed flexible circuit. To measure the tag reading range, the smartphone was initially brought close to the tag until detection occurred. The distance between the tag and the reader was then incrementally increased until the tag could no longer be detected. The maximum distance was then measured using a vernier calliper. Additionally, the tuning capacitance connected on a breadboard between the antenna port and the RF430FRL152HEVM board was adjusted to determine the maximum achievable reading range for the tag antenna.

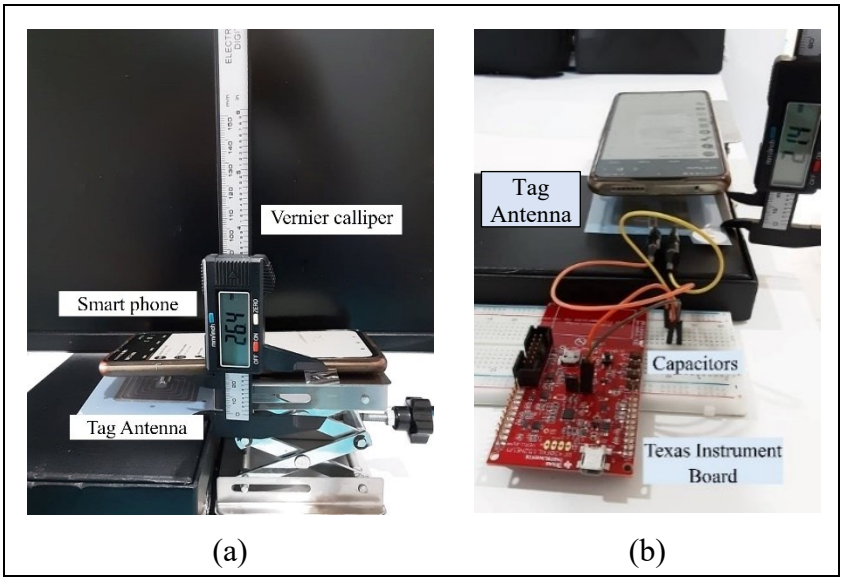


Figure 3.35 Measurement Setup for (a) Tag Reading Range and (b) Antenna Resonant Frequency

3.9 Development of Temperature Monitoring System as NFC Application

The NFC tag antenna can be integrated with a microcontroller and sensors to function as a monitoring system. In this study, a temperature sensor is utilized to monitor the temperature of food packaging, ensuring that food quality remains within safe and optimal conditions throughout storage and transportation. Figure 3.36 illustrates the block diagram of the temperature monitoring system, which comprises a reader (such as an NFC-enabled smartphone), an NFC tag that incorporates a temperature sensor, and a communication method that operates through magnetic induction. A suitable mobile application is also required to monitor the temperature detected by the sensor when the tag is activated.

The flow of data transactions between the smartphone and NFC tag is illustrated in Figure 3.37. The process begins when the NFC-enabled smartphone is brought close to the NFC tag, initiating coupling and activating the tag. Once the NFC chip is activated, the microcontroller collects data from the sensor and transmits it to the NFC interface. Simultaneously, the app on the smartphone waits for incoming data, reads and processed the sensor information transmitted by the tag, and displays the processed data on the app's graphical user interface (GUI) for the user to interpret.

The following subtopics describe the fabrication procedure for the D4-HGS tag antenna with temperature sensor circuit, including detailed guidelines for printing and integrating surface-mount NFC sensor integrated circuits (ICs) onto HGS-printed

traces. This study proposes, for the first time, a practical guideline for the integration of SMD circuits with hybrid graphene silver (HGS) inks, providing valuable reference for future researchers and manufacturers. Additionally, the challenges encountered during the fabrication of the graphene-based NFC tag with a temperature monitoring circuit, as well as the methods used to conduct reliability testing, are also discussed in the following subtopics.

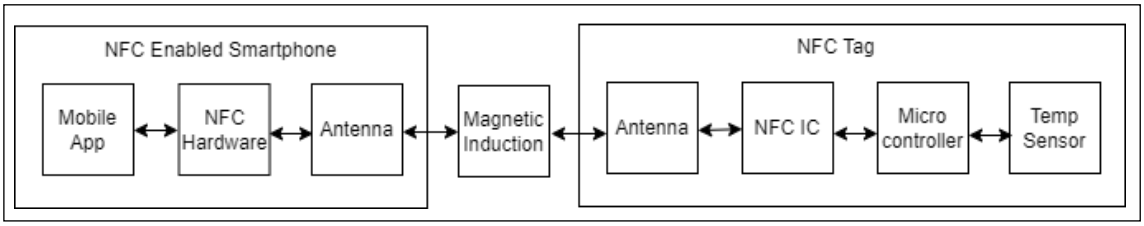


Figure 3.36 NFC Monitoring System Block Diagram

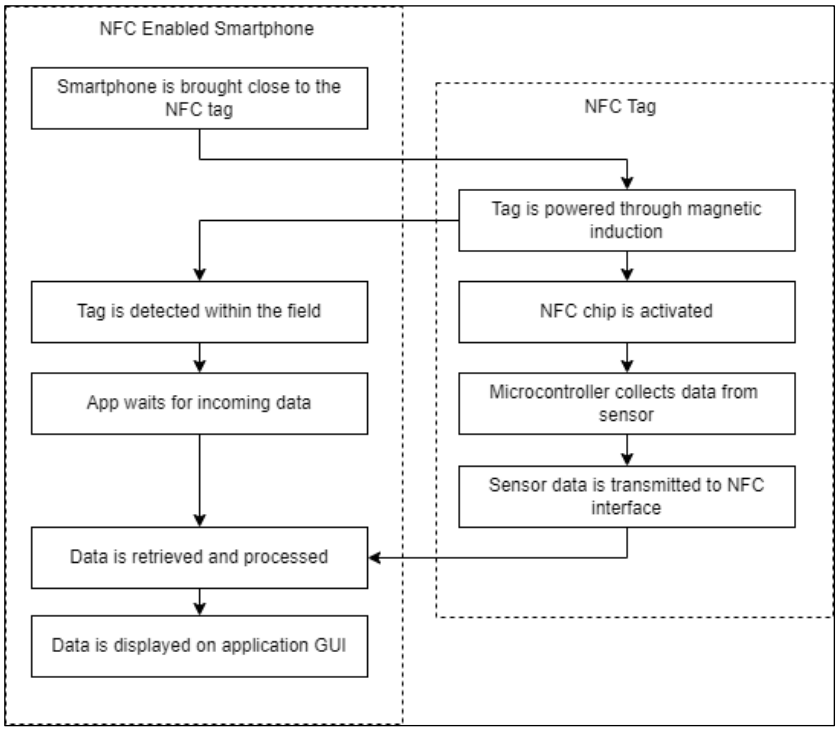


Figure 3.37 Flowchart of Data Transaction

3.9.1 Procedure of Fabrication for HGS NFC Tag Antenna with Temperature Sensor Circuit

This section outlines the summary procedure for fabricating an NFC tag antenna and temperature sensor circuit using HGS conductive material, incorporating necessary

guidelines to ensure precision and functionality. The primary challenge in the fabrication process lies in depositing the RF430FRL152H chip onto the printed circuit, which is made of HGS conductive material. Since this conductive material has not been previously used for printed circuit fabrication, where SMD components and the VQFN (Very thin Quad-Flat No-leads) package of the RF430FRL152H chip must be attached, a comprehensive fabrication guideline has been proposed. This guideline is particularly beneficial for other researchers intending to use the material with similar characteristics.

Figure 3.38 shows the PCB layout of a D4-HGS NFC tag antenna with temperature sensor circuit footprints, created using Altium Designer. The footprints were designed for 0603- and 1206-packaged size of the SMD components to simplify the deposition process of SMD components onto the HGS-printed circuit. Table 3.3 presents the list of SMD components involved in the temperature sensor circuit with reference from RF430FRL152H datasheet [179][143].

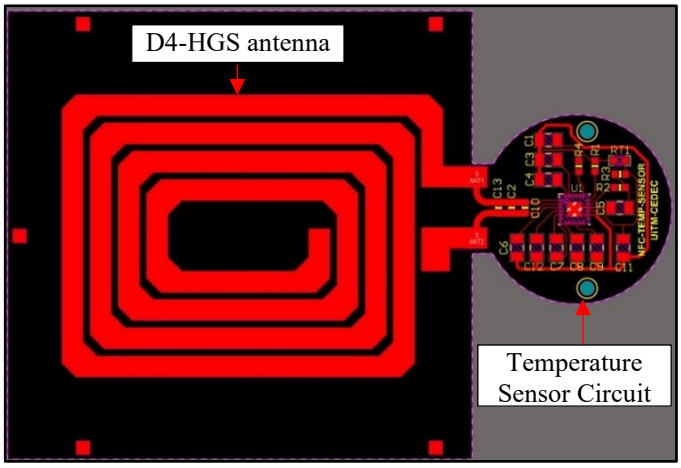


Figure 3.38 PCB Layout of D4-HGS NFC Tag Antenna with Temperature Sensor Circuit Footprints in Altium Designer

Table 3.3
SMD Components of Temperature Sensor Circuit

Name	Value	Description
U1	NA	RF430FRL152H Texas Instrument Chip
C7	10 nF	Charge pump capacitor
C9	0.1 µF	Decoupling capacitor at RST

Name	Value	Description
C6	2.2 µF	Decoupling capacitor at power supply (VDDSW)
C3	0.1 µF	Decoupling capacitor at power supply (VDD)
C4	0.1 µF	Decoupling capacitor at power supply (VDDH)
C8	0.1 µF	Decoupling capacitor at power supply (VDD2X)
C12	0.1 µF	Decoupling capacitor at power supply (VDDB)
C11	1 µF	Bypass capacitor between SVSS and VSS
C2, C10, C13	2 pF – 200 pF	External tuning capacitors
RT1	100 kΩ	NTC Thermistor
R1, R2	1 kΩ	Voltage divider
R3	100 kΩ	Reference resistance
R4	10 kΩ	External host controller

Figure 3.39 shows the prototype of the fabricated D4-HGS NFC tag antenna with a temperature sensor circuit. As shown in the figure, the RF430FRL152H chip was successfully deposited onto the printed graphene-based circuit using the double-layer chip connection method, which is further discussed in Section 3.9.2. Table 3.4 summarizes the guideline and procedures involved in the fabrication process.

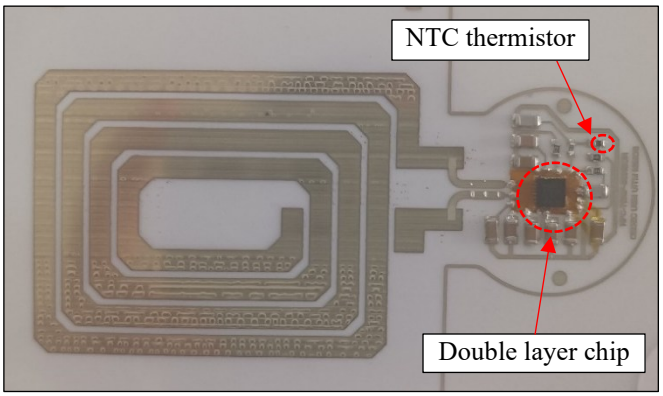


Figure 3.39 Prototype of D4-HGS NFC Tag Antenna with Temperature Sensor Circuit

Table 3.4
Guideline and Procedures of NFC Tag and Circuit Fabrication

Step		Procedures	Materials/ Equipment	Key Notes/ Precautions
1.	Antenna design	Design the NFC antenna by considering the HCG material properties, such as conductivity and thickness.	CST Simulation software	Ensure the design meets the electrical properties requirement and NFC chip specifications (Cin = 35 pF).
2.	Circuit design	Design the circuit layout using 0603-packaged resistors and NTC thermistor, and 1206-packaged capacitors to simplify connections.	Altium Designer software	Ensure component spacing and trace width meet PiXDRO LP50 printer specifications, with a minimum gap of 0.3 mm and trace width of 0.2 mm, to prevent bridging or misalignment.
3.	Substrate preparation	Clean the PET substrate using isopropyl alcohol to remove dust and contaminants.	PET substrate. isopropyl alcohol	Ensure the substrate is completely dry before printing.
4.	Deposition of HGS Conductive Pattern	Deposit the HGS ink onto the PET substrate according to the predefined design, then cure at 40°C for 30 minutes.	HGS ink, PET substrate, PiXDRO LP50 printer, multimeter	Inspect the printed pattern for defects such as breaks or uneven thickness. Ensure all traces are properly connected and verify the absence of short circuits.
5.	Stencil fabrication and epoxy application	Fabricate a stencil using an aluminium plate and apply conductive epoxy through the stencil to all the designated circuit pads, except for the NFC chip.	Stencil, CW2400 Conductive Epoxy	Mix equal amounts (1:1) by weight or volume of the CW2400 Conductive Epoxy Part A and Part B for 2 minutes. Use the mixture within 8 minutes. Avoid excess and overapplication of epoxy to prevent short circuits.
6.	Sensor and SMD component integration	Place the temperature sensor (NTC Thermistor), resistor, and capacitor SMD components onto the epoxy-coated pads.	100 kΩ NTC Thermistor, SMD Components	Ensure proper alignment and contact of components with the epoxy. Leave the assembly to cure at room temperature for 24 hours to achieve a strong bond.
7.	Fabrication of a flexible chip circuit	Design a flexible chip circuit with through-hole vias using Altium Designer and fabricate it on a flexible PCB, utilising copper as the conductor and polyimide as the substrate.	Altium Designer software, Flexible PCB	Inspect the fabricated flexible circuit to verify the quality and functionality of the vias and traces.
8.	NFC Chip soldering	Apply solder paste evenly to the chip pads and carefully align the NFC chip with the pads. Then, place the assembly in an	RF430FRL152H chip, XG-Z40 Mechanic solder paste, T-962A infrared IC	Ensure that each pin is correctly assigned to its corresponding pad. After removing the assembly from the heater, allow it to cool at

Step		Procedures	Materials/ Equipment	Key Notes/ Precautions
		infrared IC heater for 7 minutes at 200°C.	heater, microscope, multimeter,	room temperature for 5 minutes, and then inspect the soldered joints using a microscope and a multimeter.
9.	Integration of the assembled chip	Connect the assembled chip to the HGS printed circuit design using conductive epoxy and leave it at room temperature for 24 hours to achieve a strong bond.	CW2400 Silver Conductive Epoxy, multimeter	Verify the connections for continuity using a multimeter to ensure all traces are properly connected and free of short circuits.
10.	Functional testing	Test the NFC tag functionality using an NFC-enabled smartphone. Use a Vector Network Analyzer (VNA) to measure the antenna's resonance frequency.	NFC-enabled smartphone. Vector Network Analyzer (VNA), SMD capacitors	Ensure the resonant frequency aligns with the desired operating frequency. If necessary, adjust the matching network by adding external capacitors in parallel with the antenna port.
11.	Temperature monitoring and calibration	Test the sensor's temperature response by exposing it to a controlled temperature range (20–60°C) and comparing the results with those of a calibrated thermometer.	NFC-enabled smartphone, thermometer	Make any necessary calibration adjustments to ensure the system operates within the desired tolerance range.

The flow of the fabrication process for the NFC tag antenna and temperature sensor circuit is summarize in the flowchart illustrated in Figure 3.40. The fabrication process begins with the completion of the antenna and circuit design. The fabrication of the antenna and circuit runs in parallel with the preparation of the stencil and flexible chip circuit. Once the conductive epoxy is applied to the circuit pads using the stencil, all components are placed onto the designated pads. Finally, the functionality of the developed NFC tag, integrated with the temperature sensor, is tested for performance evaluation.

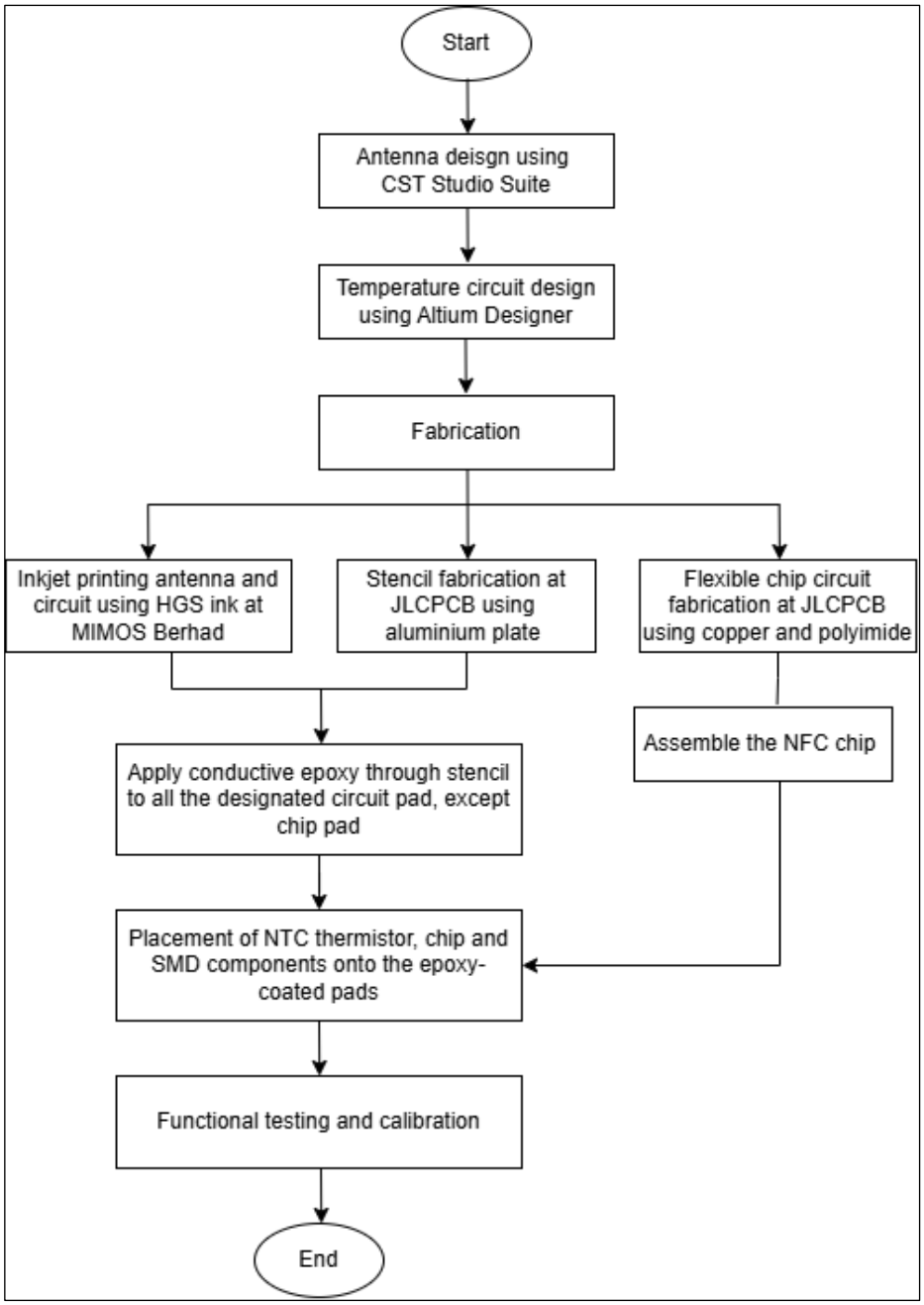


Figure 3.40 Flow Chart for the Development Process of NFC Monitoring System

3.9.2 Electrical Bonding and Mechanical Stability Limitations

The printed flexible graphene-based tag antenna with the integrated circuit faces some challenges in mounting the components, particularly the NFC chip (RF430FRL152H), onto the printed layout. This occurs due to limitations of the HGS conductive material and the PET substrate, which cannot withstand high temperatures due to low glass transition temperatures (T_g) (~150ºC for HGS and 80ºC for PET) [180][16]. This makes them unsuitable for use in the oven for electrical bonding of the

chip and other SMD components, as is typically done with copper-etched tags on standard PCBs. The traces of the printed HGS material tend to detach under extremely high temperatures, as shown in Figure 3.41, and the PET crumples when exposed to such conditions.

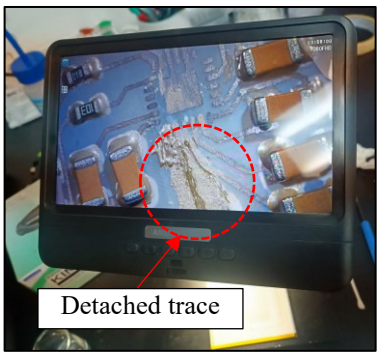


Figure 3.41 Detached Trace Under Extremely High Temperature

Another challenge is the small pin size and VQFN (Very Thin Quad-Flat No-Leads) package of the RF430FRL152H chip as shown in Figure 3.42 (a), which has never been mounted on graphene-based flexible printed circuitry, as illustrated in Figure 3.42 (b), due to the lower temperature resistance of the PET substrate. To date, no literature has discussed methods for electrically bonding VQFN-type chips to printed flexible circuitry, particularly for graphene-based tags. The layout of the RF430FRL152H chips, as shown in Figure 3.42 (c), reveals very small gaps between consecutive pins, which is only 0.26 mm, while the pad for each pin is also very small at 0.24 mm [179]. Manually applying silver conductive epoxy within such small gaps is highly challenging. Even with the aid of a stencil, the conductive epoxy tends to connect across pads, as shown in Figure 3.43 (a), leading to short circuits. In contrast, other small SMD components, such as 0603-packaged resistors and 1206-packaged capacitors, can be easily bonded using conductive epoxy, as depicted in Figure 3.43 (b), since the gap between their pads is significantly larger, approximately 1.5 to 3.5 mm.

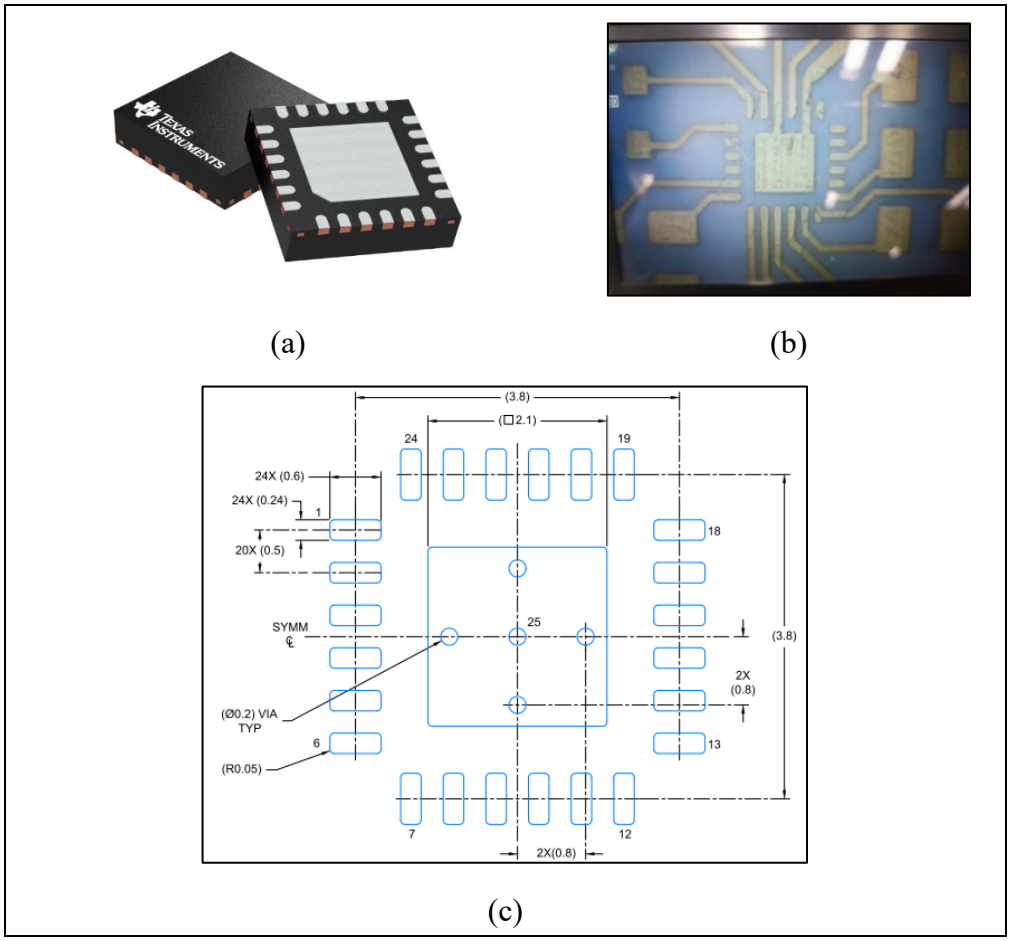


Figure 3.42 (a) VQFN Package of the RF430FRL152H Chip, (b) Layout of HGS-Based Flexible Printed Circuitry, and (c) Dimensions of the RF430FRL152H Chip Pads [179]

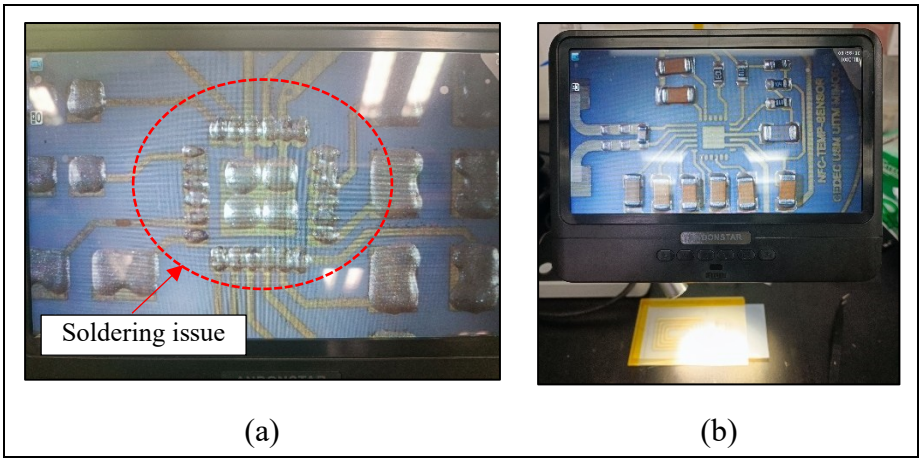


Figure 3.43 (a) Short-Circuited Conductive Epoxy on the Chip Pads and (b) the Securely Bonded Other SMD Components on the Pads Using Conductive Epoxy

To address this issue, a double-layer chip connection is proposed for mounting the RF430FRL152H chip on the printed layout. The chip layout is separately designed

using Altium Designer, as shown in Figure 3.44 (a), where each traces connected to the chip's pad is equipped with through-hole vias at the end of the traces. These vias serve as connectors between the first layer, which is the printed graphene-based circuitry, and the second layer, which is the separated chip layout. The chip layout is printed on a flexible PCB made of copper and polyimide, as shown in Figure 3.44 (b). Since both the polyimide substrate and copper traces can withstand high temperatures (over 200 °C), the RF430FRL152H chip can be securely bonded using solder paste and cured in an infrared IC heater for approximately 7 minutes at 200 °C. Figure 3.44 (c) demonstrates the strong bonding of the chip on the printed chip layout. The chip layout with the mounted RF430FRL152H chip is then properly aligned on the printed graphene-based circuitry, and conductive epoxy is applied to each of the vias, as shown in Figure 3.44 (d), to connect the chip layer to the printed circuit. The circuit is then left to dry at room temperature for one day to ensure stronger bonding.

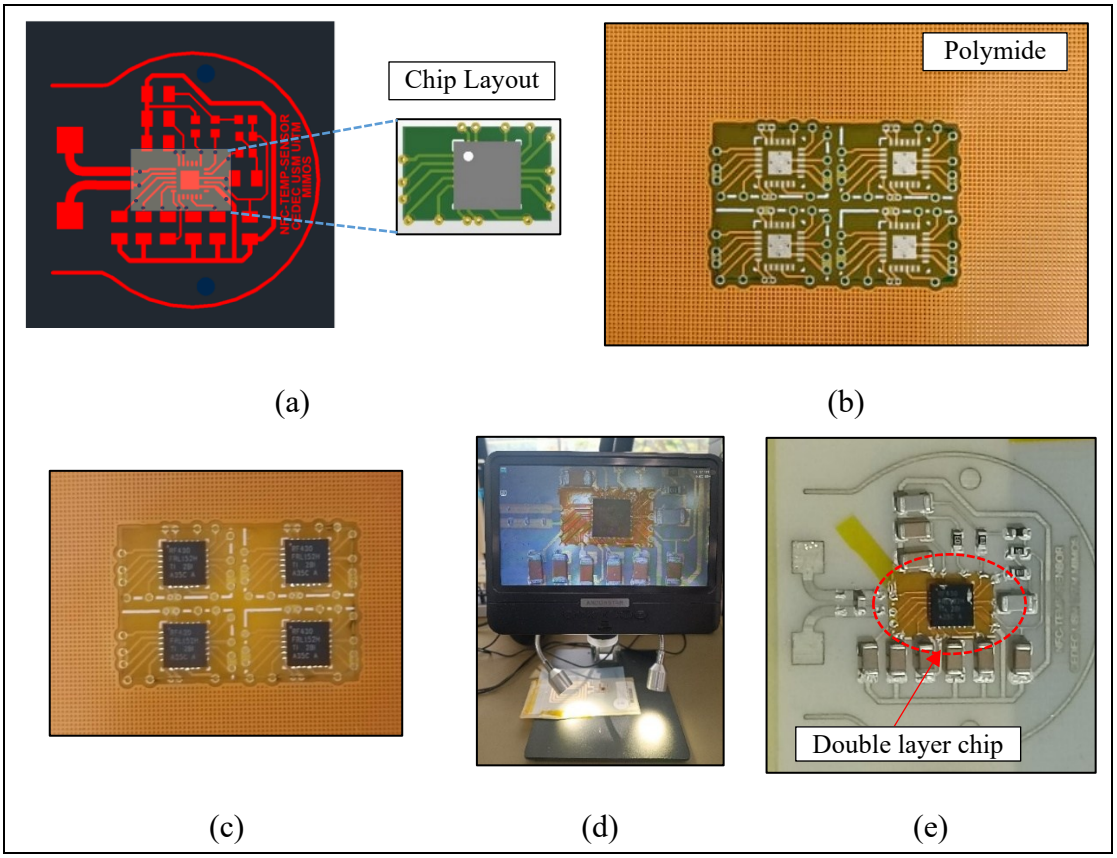


Figure 3.44 (a) Chip Layout Design with Through-Hole Vias, (b) Fabricated Flexible PCB, (c) Bonded Chip on the Flexible PCB, (d) Chip Layout Aligned with the HGS Printed Circuit and (e) Conductive Epoxy Applied Through the Vias

3.9.3 Reliability Test of Temperature Monitoring

Reliability testing is crucial when evaluating a temperature monitoring system utilising NFC technology to ensure that the system consistently delivers accurate and reliable results under varying conditions. Determining the mean and standard deviation (STD) is crucial for assessing reliability and consistency in the measurement system [181][182].

To perform this data analysis, the measurement setup shown in Figure 3.45 is required, which incorporates a temperature-controlled environment, a reference thermometer, alongside an NFC tag and NFC reader, to conduct the reliability test. Temperature measurements were performed inside a portable mini fridge with dual cooling and warming functionality, as depicted in Figure 3.46 (a). The temperature range was set to cold (3-5°C), medium (20-25°C), and hot (55-60°C), covering typical storage and transportation requirements for food products.

A fridge thermometer was included inside the portable mini fridge as a reference to ensure accurate temperature readings. At each level, sufficient time was allowed for temperature stabilization before measurements began. The temperature of the NFC tag was then measured using an NFC-enabled smartphone, the Xiaomi 11T, equipped with NFC temperature monitoring apps, as shown in Figure 3.46 (b). Measurements were conducted for 30 minutes at each temperature level, with readings recorded every 5 minutes. Corresponding temperature values from the reference thermometer were also recorded for comparison. The entire process was repeated for three different fabricated NFC tags.

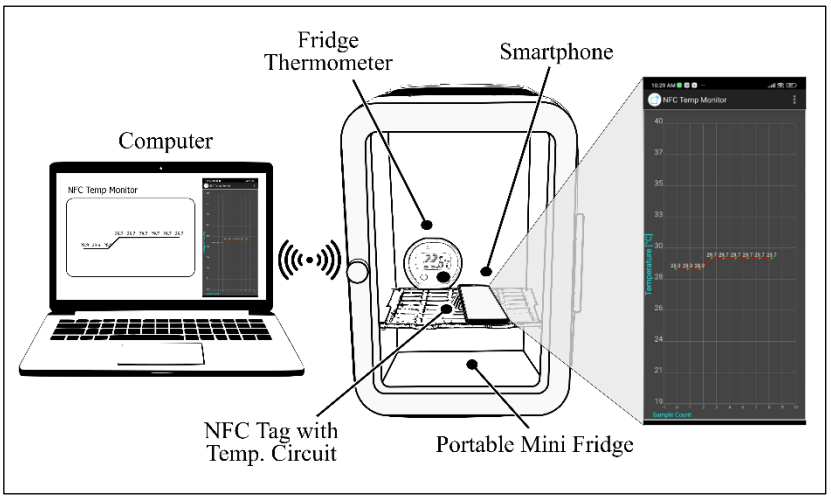


Figure 3.45 Measurement Setup in a Temperature-Controlled Environment

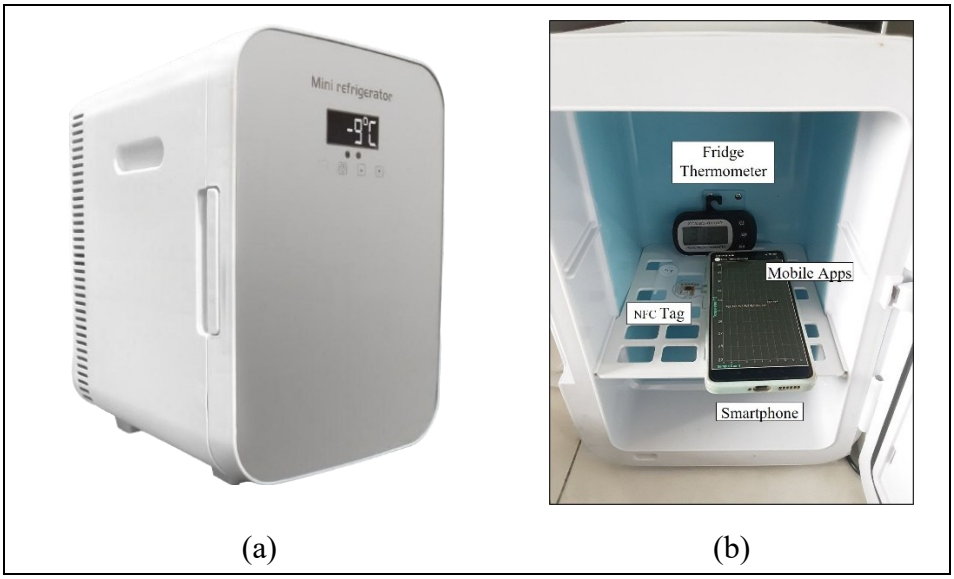


Figure 3.46 (a) Portable mini fridge (b) Temperature measurement of NFC tag using smartphone with temperature monitoring apps

For each temperature level, the mean, $\bar{x}$ and standard deviation (STD) of the recorded readings were calculated using Equations (3.16) and (3.17), respectively, where x_i represents an individual reading and n is the total number of readings.

$$\bar{x}=\frac{1}{n}\sum_{i=1}^{n} x_i \tag{3.16}$$

$$STD=\sqrt{\frac{\sum(x_i-\bar{x})^2}{n}} \tag{3.17}$$

3.10 Summary

In this chapter, the research methodology is presented, covering five major components: characterization of conductive materials, NFC tag antenna design and fabrication methods, robustness evaluation methods, measurement procedures, and the development process of an NFC tag antenna integrated with a temperature sensor circuit. In this research, three conductive materials, categorized as metal-based, carbon-based, and hybrid graphene-metal-based, referred to as SC, HCG, and HGS, were characterized in terms of conductivity, surface morphology, roughness, and thickness for the initial verification of NFC tag antenna design, addressing the first objective of

the study. These conductive materials were subsequently used in four NFC tag antenna designs, namely D1, D2, D3 and D4, which were designed and tuned using CST Studio Suite and Optenni Lab, respectively. The use of Optenni Lab for antenna tuning contributes to a more precise and faster tuning process, as the matching configuration could be easily generated from various lumped elements topologies.

The antennas were fabricated using suitable printing methods for each material, including screen printing, inkjet printing, and direct ink writing. Verification was conducted at each stage of the printing process to ensure the reliability of the fabrication method. The methodology for achieving the second objective, which involves evaluating the robustness of the NFC tag antenna, including its flexibility and sensitivity to different packaging materials, a moist environment, and temperature variations, is also discussed in this chapter. Additionally, the proposed equivalent circuit for the on-metal NFC tag antenna with magnetic shielding is highlighted as a key contribution.

Finally, the development process of the temperature monitoring system application, integrated with the D4-HGS tag antenna, is thoroughly discussed. The procedures and guidelines for developing the flexible HGS NFC tag antenna with a temperature sensor circuit are emphasized as one of the study's significant contributions. Challenges in integrating the VQFN type of NFC chip onto the printed HGS circuit are also addressed, with a proposed double-layer chip solution. The results and analysis of the simulated and measured antennas, as well as the reliability testing of the developed temperature monitoring application, are detailed further in Chapter 4.

CHAPTER 4
RESULTS AND DISCUSSIONS

4.1 Introduction

This chapter focuses on the performance analysis of the printed NFC tag antenna, specifically evaluating antenna inductance, resistance, Q-factor, resonant frequency, power transfer efficiency, and reading range using different types of conductive materials, including Silver Conductor (SC), Hybrid Carbon Graphene (HCG), and Hybrid Graphene Silver (HGS). As these materials exhibit variations in conductivity, surface morphology, roughness, and thickness, which influence antenna impedance and efficiency, a preliminary study on their characteristics is presented at the beginning of the chapter. The measured conductivity and thickness values from this characterization process were then applied to the antenna designs discussed in Section 4.3, where both simulated and measured results are analyzed.

Since material and antenna geometry affect the antenna's electrical performance, a tuning process is required to ensure that the resonance frequency aligns with the NFC operating standard. The tuning process using Optenni Lab is demonstrated with the SC material, which serves as a benchmark due to its commercial availability and widespread use in printed antennas, making it a reliable reference for comparison. The optimum tuning topology, which offers good impedance matching with minimal reflected power, precise resonance at 13.56 MHz, and low complexity with a reduced component count, is then applied to the HGS material.

Section 4.4 evaluates the selected tag antenna designs, D2-SC and D4-HGS, under bending conditions. Furthermore, the sensitivity of D4-HGS, referring to the extent to which NFC antenna performance is affected by external conditions such as moisture, various packaging materials, and temperature variation, is assessed. Proposed solutions to mitigate the antenna's sensitivity to moisture and metal surfaces are also discussed and evaluated. As for the HCG material, further robustness testing has not been conducted due to its unsatisfactory performance in free air conditions.

Finally, in the last section, the NFC tag antenna integrated with a temperature monitoring circuit is evaluated, and the system's reliability, referring to the consistency

of antenna performance under varying conditions, is assessed and compared to other commercial temperature monitoring systems.

4.2 Characterization of Printed Conductive Materials

4.2.1 Conductivity

The conductivity of the SC, HCG, and HGS printed samples was measured using the method described in section 3.4.1 of Chapter 3. Four sets of measurements were conducted for each conductive material, and the mean values of resistivity, ρ and conductivity, σ were calculated. As presented in Table 4.1, the mean conductivity value measured for the SC material from Voltera (0.55×10^6 S/m) is relatively close to the manufacturer's datasheet value of 9.76×10^6 S/m (Appendix 2). Since the measurement results are relatively consistent with the datasheet values, the measurement technique is considered reliable for determining the resistivity and conductivity of other conductive materials. Thus, further measurements were conducted on the off-the-shelf HCG material from Dycotec and the proposed HGS conductive materials from MIMOS Berhad. The results show that HCG's mean resistivity and conductivity values are 1.84×10^{-3} Ωm and 5.84×10^2 S/m, respectively, with the conductivity value being one order lower than stated in the datasheet. Meanwhile, the mean resistivity and conductivity values for HGS are 2.63×10^{-7} Ωm and 3.95×10^6 S/m, respectively, representing the highest conductivity among the materials tested.

Table 4.1
Measurement Results of Resistivity, ρ and Conductivity, σ for the Printed Conductive Materials

Cond. Materials	Symbol (unit)	Data Sheet	Number of Measurements				Mean Value
			1	2	3	4	
SC	ρ (Ωm)	σ = 9.76 x 10^6 S/m	1.65 x 10^{-6}	1.81 x 10^{-6}	1.89 x 10^{-6}	2 x 10^{-6}	1.84 x 10^{-6}
	σ (S/m)		0.61 x 10^6	0.55 x 10^6	0.54 x 10^6	0.51 x 10^6	0.55 x 10^6
HCG	ρ (Ωm)	σ = 2 x 10^3 S/m	2.07 x 10^{-3}	1.61 x 10^{-3}	1.66 x 10^{-3}	1.71 x 10^{-3}	1.84 x 10^{-3}
	σ (S/m)		4.85 x 10^2	6.48 x 10^2	6.16 x 10^2	5.86 x 10^2	5.84 x 10^2
HGS	ρ (Ωm)	NA	2.67 x 10^{-7}	2.59 x 10^{-7}	2.45 x 10^{-7}	2.82 x 10^{-7}	2.63 x 10^{-7}
	σ (S/m)		3.85 x 10^6	3.92 x 10^6	4.37 x 10^6	3.67 x 10^6	3.95 x 10^6

To demonstrate the effect of conductivity, σ, on coil antenna performance, the fundamental principles of coil antenna were studied in relation to the conductivity values of various printed conductive materials. A reference Design 1 coil antenna, as described in Section 3.5.2 of Chapter 3, was simulated and analysed in terms of its electrical properties, specifically antenna inductance, L_a and antenna resistance, R_a. These properties are closely related to the Q-factor of the antenna, as indicated by Equation (2.27), which is one of the factors that determines the performance of the coil antenna [97]. The thickness of the conductive material was set to 50 μm, as specified in the SC thickness in the datasheet in Appendix 2, and printed on a PET substrate with an electrical permittivity of 3.2 and a thickness of 0.12 mm.

Figure 4.1 illustrates the effects of different conductivity values, ranging from 10 S/m to 10^7 S/m, on the electrical properties of the coil antenna. Based on the graph, for a sample with a conductivity higher than ~10^4 S/m, the L_a values remain consistent, at approximately 2.65 μH. However, as the conductivity decreases, the L_a value is significantly affected, even degrading to negative L_a values. This indicates that at very low conductivity levels, the coil antenna can no longer function as an inductor, preventing inductive coupling with the reader. A similar trend is observed with antenna resistance, R_a, where lower conductivity results in significantly higher R_a values. Conversely, R_a gradually decreases as the conductivity increases, reinforcing the importance of highly conductive materials in maintaining optimal antenna performance. The effect on the Q-factor is depicted in Figure 4.2, which shows that a very low Q-factor is achieved at low conductivity values. Consequently, more power is lost as heat rather than being used to generate a magnetic field at a low Q-factor value [97].

From the measured conductivity values of the three materials in Table 4.1, the SC and HGS materials fall within the acceptable conductivity range, which is ~10^5 to ~10^6 S/m, comparable to the other reported graphene- and silver-based inks [58][62] [183]. Thus, these materials are predicted to function effectively as NFC tag antennas, depending on the antenna designs. However, the HCG material exhibits a very low conductivity value, ~10^2 S/m, outside the acceptable range for efficient coil antenna performance. Further investigation is conducted in the next section to validate the compatibility of these materials for NFC tag antenna applications.

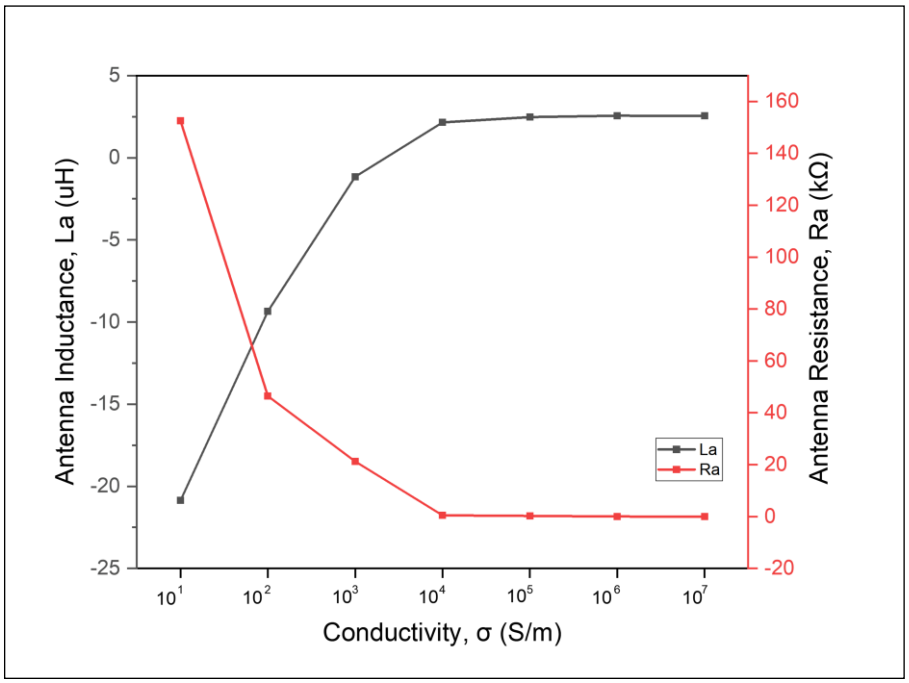


Figure 4.1 The Effect of Conductivity to the Antenna Inductance, L_a and Antenna Resistance, R_a.

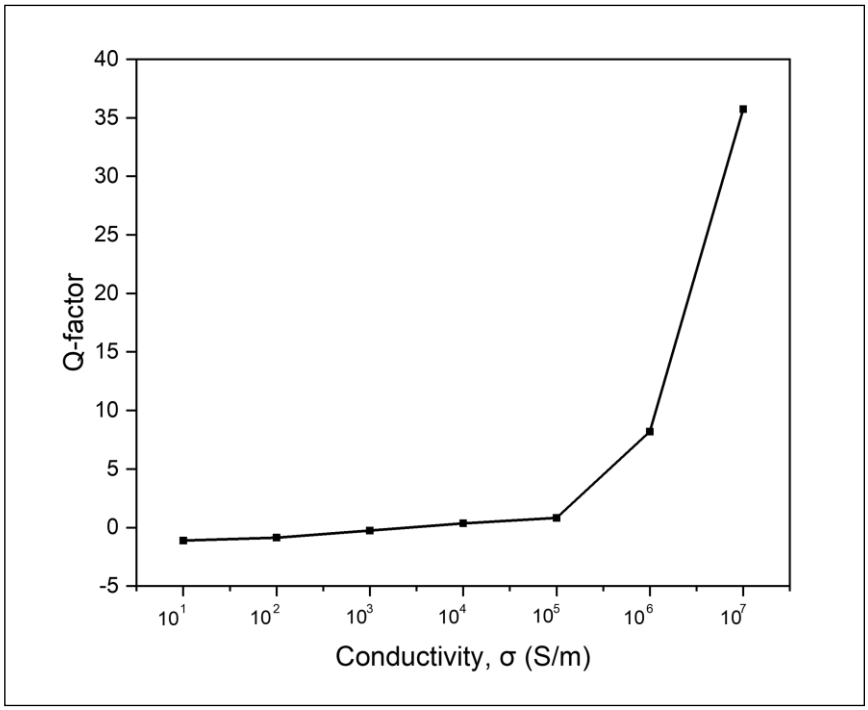


Figure 4.2 The Effect of Conductivity to the Antenna Q-Factor

4.2.2 Surface Morphology

Surface morphology analysis provides critical insight into the structural characteristics and particle distribution of printed conductive materials, which influence the formation of conductive paths and overall electrical behaviour. Figure 4.3 (a) – (c) show the observed images with a 1 μm magnifier for SC, HCG, and HGS materials, respectively. For the SC material (Figure 4.3 (a)), the structure appears to consist of large, irregularly shaped silver particles of varying sizes. A relatively dense silver particles is beneficial for conductivity as it helps to form a conductive network across the material. However, a few small gaps between particles may disrupt the continuity of the conductive pathways, resulting in increased resistance. However, because the majority of the material appears densely packed, these gaps likely have a minimal effect on overall conductivity.

For the HCG material, the SEM image illustrated in Figure 4.3 (b) reveals a rough and irregular surface structure with clusters of particles and some interconnected networks. This structure indicates a porous morphology with multiple contact points between the graphene and carbon particles, where some graphene flakes cover the carbon. Some of the interconnected networks may enhance the pathway for electron flow, which is beneficial for conductivity. However, large gaps and poorly connected areas could impede conductivity, as they might create discontinuities in the conductive pathway. This could be one of the reasons for the lower conductivity value of HCG compared to other materials, in addition to the well-known lower conductivity of carbon.

Meanwhile, for the HGS material shown in Figure 4.3 (c), the surface exhibits a dense structure of rGO with small AgNPs dispersed throughout it. The incorporation of rGO in the composite helps form a continuous network that facilitates electron transport, especially when connected to the AgNPs. The graphene-silver hybridization creates a synergistic network that enhances conductivity by combining the high electrical conductivity of silver with the conductive properties of graphene, making it particularly beneficial for applications that require both flexibility and conductivity. Additionally, it can be observed that only minimal gaps exist between the particles, which helps to reduce overall resistance. Therefore, the HGS material is expected to perform better than SC and HCG due to its optimized hybrid structure.

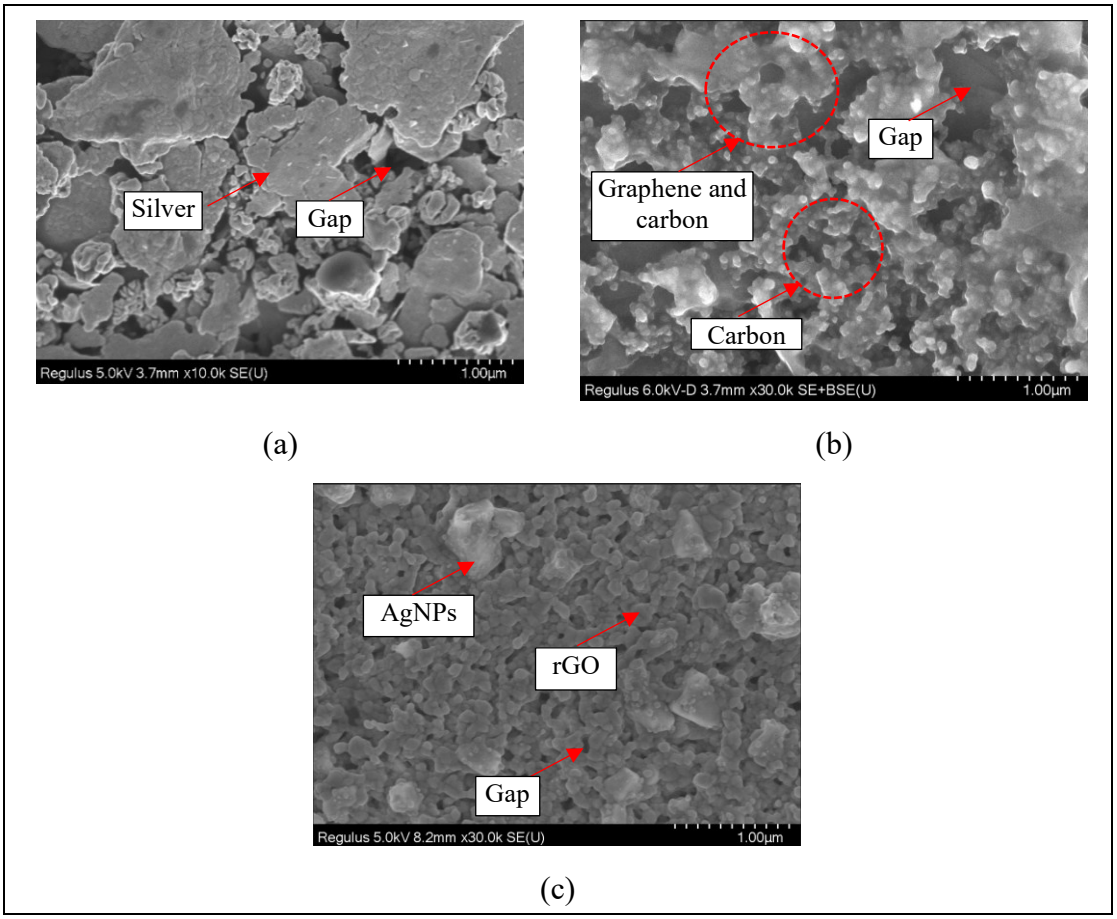


Figure 4.3 SEM Image for (a) SC, (b) HCG, and (c) HGS Printed Samples

4.2.3 Surface Roughness

The microscope images of the printed SC, HCG, and HGS materials are shown in Figure 4.4 (a), (b), and (c), respectively. Among the three, the surface of HGS appears the smoothest, followed by HCG, with SC being the roughest. This observation is supported by the measured values of the roughness parameters (S_a, S_q, S_v, S_p and S_z) for each material, as presented in Table 4.2. The calculation methods for these parameters were discussed in Section 2.4.2 of Chapter 2.

The results indicate that SC has a relatively rough surface compared to HGS and HCG due to its higher values of all roughness parameters. A rougher surface can result in higher resistance because the irregularities disrupt the contact between silver particles, leading to increased resistance of the material. Additionally, the larger peak heights (S_p) and deeper valleys (S_v) may contribute to inconsistent electron flow, potentially reducing the efficiency of signal transmission and reception due to greater power dissipation. In contrast, HGS exhibits the lowest values for all roughness

parameters, with S_a (arithmetical mean height) and S_q (root mean square height) are measured at 0.05 µm, indicating an exceptionally smooth surface. This smoothness minimizes resistance and promotes efficient current flow, which may contribute to an increase in conductivity [184]. Furthermore, a smoother surface facilitates stronger adhesion between layers, contributing to the durability and stability of the printed NFC tag antenna.

For HCG, its surface roughness falls between SC and HGS. However, its conductivity remains lower, despite having better surface roughness than SC. This is because surface roughness is not the primary determinant of high conductivity. The intrinsic properties of carbon, which inherently have lower electrical conductivity compared to silver, are the main reason for the lower conductivity of HCG. Even with improved surface morphology, HCG exhibits reduced conductivity because the carbon-based material limits the formation of highly efficient conductive pathways. This emphasizes that while surface roughness can influence conductivity to some extent, the material's intrinsic electrical properties are the dominant factor in determining overall performance.

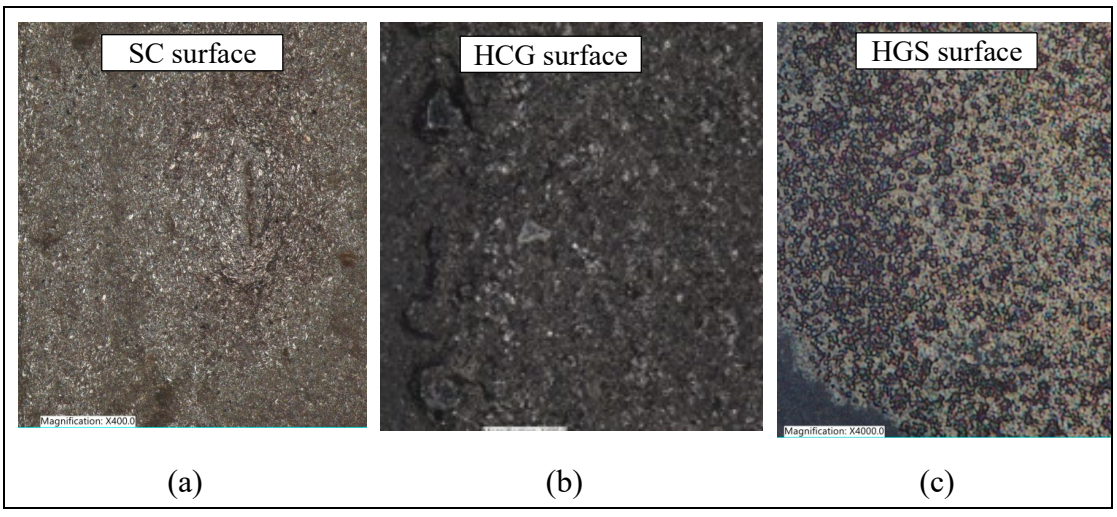


Figure 4.4 2D Image for (a) SC (b) HCG (c) HGS from VHX Digital Microscope

Table 4.2
Measured Values of Roughness Parameters

Parameters	SC	HCG	HGS
S_a (µm)	6.63	2.9	0.05
S_q (µm)	8.69	3.38	0.05
S_y (µm)	26.81	8.22	0.18
S_p (µm)	23.02	8.41	0.15
S_z (µm)	49.83	16.63	0.34

4.2.4 Thickness

The thickness of the conductive material affects the performance of the antenna as it is inversely proportional to the antenna resistance [185]. A larger thickness will ease the current flow by reducing resistance, which in turn enhances the antenna's conductivity and efficiency. For this reason, the actual thickness of the conductive material should be measured and included in the simulation to obtain the optimum performance of the antenna. Table 4.3 presents the measured thickness for all printed conductive materials, where measurements were conducted at four different places, and the mean values were calculated.

The measured thicknesses for SC and HCG show a slight deviation from the typical print thickness stated in the datasheet, which is 50 µm for SC and 10-12 µm for HCG, respectively. This deviation can be attributed to the fabrication methods used to print the antenna, where DIW and screen-printing techniques were employed for SC and HCG materials, respectively. In DIW printing, the ink is dispensed in a controlled manner, but variations in nozzle pressure, ink viscosity, or layer deposition precision can lead to thickness inconsistencies. Similarly, in screen printing, factors such as squeegee pressure, ink spreading, and the number of ink layers deposited on the mesh screen can contribute to variations in the printed layer thickness. Meanwhile, for HGS, the measured thickness aligns with expectations, as printing with the inkjet printer was conducted in a single layer, where one layer corresponds to an expected thickness of 1 µm. However, the lower thickness of the printed conductive material may contribute to higher antenna resistance, as the cross-sectional area of the printed conductors is inversely proportional to the antenna resistance, as described in Equation (2.3).

Table 4.3
Measurement Results of Thickness for Printed Conductive Materials

Conductive materials	Symbol (unit)	Number of Measurements				Mean value
		1	2	3	4	
SC	tc (μm)	81.28	79.64	84.36	76.22	80.38
HCG	tc (μm)	38.42	33.87	30.48	28.79	32.89
HGS	tc (μm)	0.52	1.75	0.65	1.24	1.04

Table 4.4 summarizes the characteristics of all the printed conductive materials. Overall, HGS offers a combination of high measured conductivity (3.95×10^6 S/m) and the thinnest printed layer among the materials, providing advantages in terms of flexibility and lightweight design. Its low curing temperature (40°C for 30 minutes) makes it ideal for use with low-temperature-resistance substrates, such as PET. Additionally, its precise printing capabilities (minimum print gap of 0.3 mm and print width of 0.2 mm) make it well-suited for NFC coil antenna designs and printed flexible electronics circuits.

Meanwhile, the fabricated SC material exhibits conductivity slightly lower than HGS. However, the high thickness of the printed layer (~80 μm) may contribute to nearly the same performance as HGS, as the increased thickness reduces resistance. Nevertheless, the larger minimum print gap of SC material makes it less suitable for NFC coil antennas with small gaps between the coils and for dense electronic circuit connections. The rough surface of the printed SC material may also contribute to higher resistance due to inconsistent electron flow.

In contrast, HCG material exhibits the lowest measured conductivity (5.84×10^2 S/m), indicating significantly lower electrical performance compared to SC and HGS. However, its moderate thickness, ~30 μm, and moderate curing requirements (140°C for 30 minutes) suggest that it is suitable for applications that prioritize mechanical durability over electrical conductivity. With a minimum print gap of 1 mm, it is less precise than HGS and SC but is suitable for broader, less complex designs.

Table 4.4
Summary of Conductive Material Parameters and Characteristics

Parameter	**Silver Conductor (SC)**	**Hybrid Graphene Silver (HGS)**	**Hybrid Carbon Graphene (HCG)**
Ink Name	Voltera Conductor 2 (Model: 1000388)	Mi-GraphPrInk	DM-GRA-9100S
Thickness [µm] (measure)	80.38	1	32.89
Conductivity [S/m] (measure)	0.55×10^6	3.95×10^6	5.84×10^2
Curing (Temp - duration)	210 ºC – 30 mins	40 ºC – 30 mins	140 ºC – 30 mins
Surface Roughness – Arithmetic mean height, S_a	6.63 (rough)	0.05 (smooth)	2.9 (medium rough)
Min print gap, width [mm]	0.7, 0.25	0.3, 0.2	1, NA

4.3 Printed Flexible NFC Tag Antenna Performance

The performance of the NFC tag antenna printed using SC, HCG and HGS conductive materials was analyzed based on several parameters, including antenna inductance, L_a, antenna resistance, R_a, resonant frequency, external tuning, power transfer efficiency, and tag reading range. These selected parameters directly influence the ability of NFC tags to communicate with readers effectively and are widely accepted in NFC antenna evaluation studies [95][105][177][186]. Since the SC material is readily available on the market, it was used as a reference for analysing the performance of the printed antenna. Once reliable results were obtained with the SC material, the same method was applied to HGS and HCG.

4.3.1 Silver Conductive (SC) NFC Tag Antenna

The characteristics of the SC material were summarized previously in Table 4.4 in Section 4.2 , where the measured conductivity and thickness of the SC material were 0.55×10^6 S/m and 80 µm, respectively. These values were used in the CST simulation software to simulate the Design 1 (D1-SC) and Design 2 (D2-SC) tag antennas, as described in Section 3.5.2 of Chapter 3. The square shape of the Design 1 tag antenna was chosen for its higher inductance value and relatively simple design compared to circular or hexagonal antennas of the same size, making it easier to manufacture.

Meanwhile, the rectangular shape of the Design 2 tag antenna offers greater design flexibility, as its length and width can be adjusted independently.

4.3.1.1 Antenna Tuning and Verification

In this study, an ISO/IEC 15693 compliant chip from Texas Instruments, the RF430FRL152H, with an internal capacitance, C_{int}, of 35 pF, was selected for integration with the antenna. This chip is chosen for its integration efficiency and the inclusion of an embedded low-power microcontroller, enabling direct connection with sensors [187]. According to Equation (2.20), the inductance should be 3.94 µH to match the internal capacitance of 35 pF at the operating frequency of 13.56 MHz. However, achieving this inductance value would result in a very large tag antenna size, approximately 76 mm × 50 mm, as per Equation (2.12). Since the tag antenna is intended for attachment to food packaging, its size need to be small enough to fit the packaging dimensions. Consequently, two smaller tag antenna designs, Design 1 and Design 2, with overall dimensions of 50 × 50 mm^2 and 40 × 30 mm^2, respectively, were developed for further investigation using the SC material.

The reduction in antenna size, however, led to a degradation in antenna inductance to 2.56 µH and 1.28 µH for Design 1 and Design 2, respectively, as inductance is proportional to the loop area and the number of turns, as stated in Equation (2.29) in Section 2.4 of Chapter 2. To ensure the antenna resonates at the required operating frequency of 13.56 MHz, an external tuning circuit is necessary. This circuit is integrated between the antenna port and the chip, as discussed in Section 3.5.3.1 of Chapter 3. Optenni Lab software was used to determine the optimal tuning circuit configuration before integrating it with the coil antenna design in the CST simulation.

Design 1 was used as a reference to determine the optimum tuning circuit configuration in Optenni Lab software. The unmatched S_{11} result from the CST simulation, depicted in Figure 4.5, was imported into Optenni Lab for the tuning process. The number of components (capacitors and inductors) used to create the topologies was limited to a range of two to four components to simplify the circuit. Several topologies with matched S_{11} results were generated, as shown in Figure 4.6. Since C_{int} of the RF430FRL152H chip is specified as 35 pF, the tuning topology must include a series connection of C_{int} in the configuration. Therefore, the selection of the optimum tuning topology was constrained to topologies with a series connection of

capacitance (SC) close to the antenna port, as listed in Table 4.5. Each of the topologies were analyzed based on several criteria, including resonant frequency matching and S_{11} performance as illustrated in Figure 4.7, component complexity and power loss.

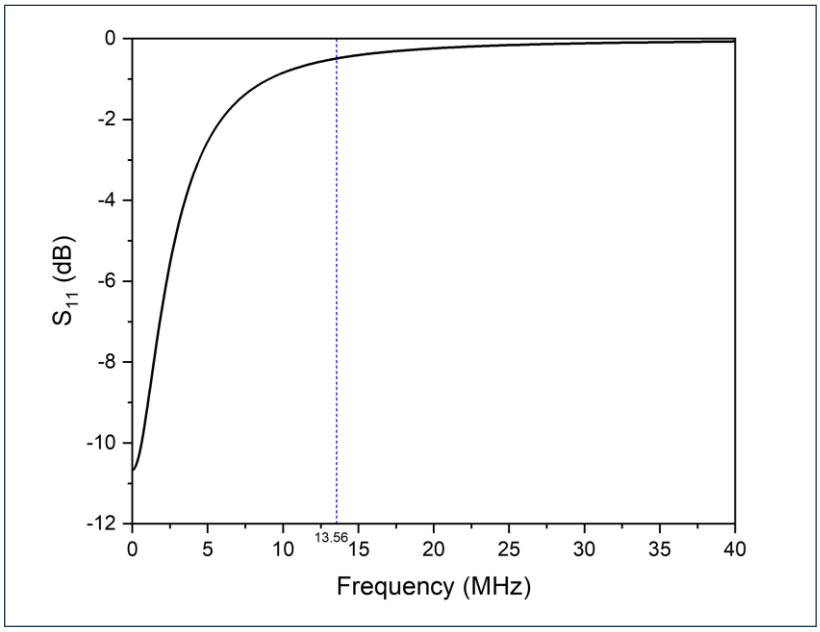


Figure 4.5 Unmatched S_{11} Result of D1-SC Antenna

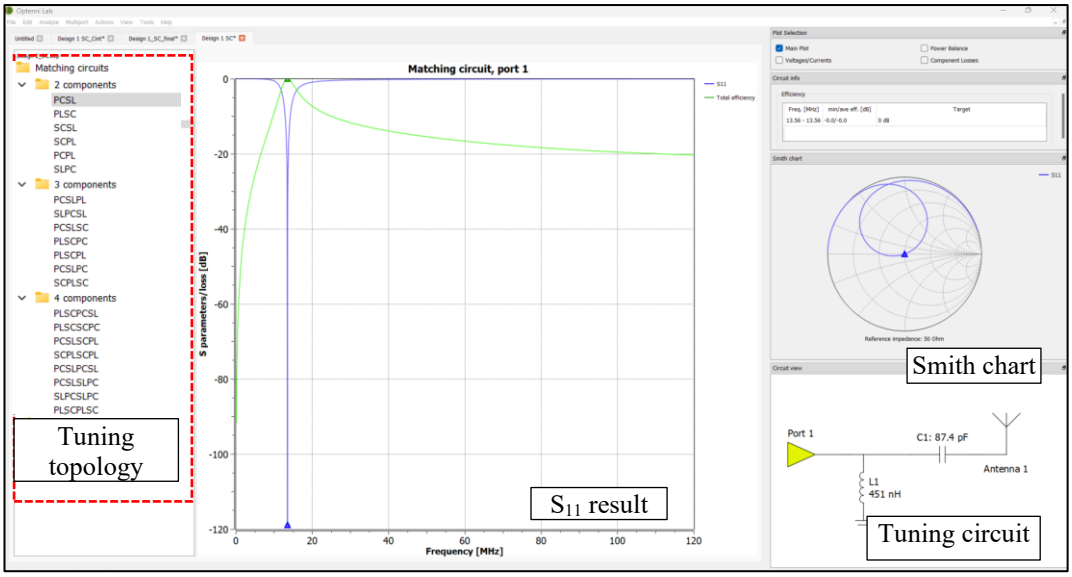
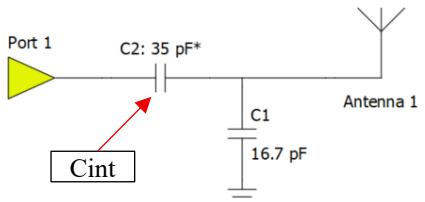
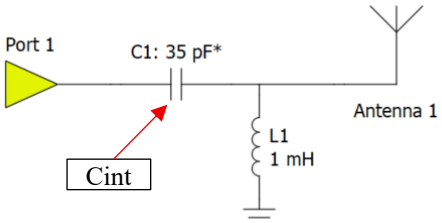
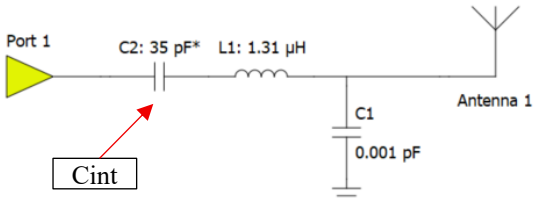
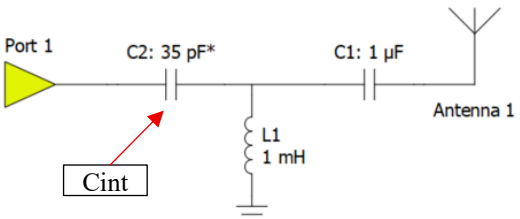
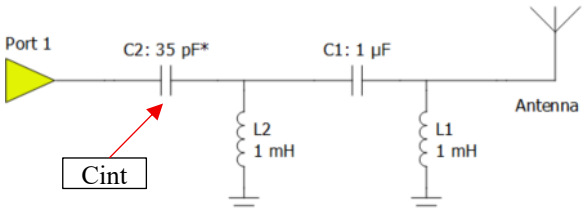


Figure 4.6 Matched S_{11} Results with Several Generated Tuning Topologies

Table 4.5
Analysis of Tuning Topologies with a Series Connection of C_{int}.

Tuning Topology	Tuning Circuit	Analysis
PCSC (Parallel C1, Series C2)		This topology exhibits adequate resonance matching at the operating frequency of 13.56 MHz, as shown in Figure 4.7. It has low component complexity, which minimizes parasitic effects and power losses. However, it has limited flexibility in impedance tuning due to the fewer number of components.
PLSC (Parallel L1, Series C1)		This topology features a simple configuration consisting of one capacitor and one inductor. However, the resonance is slightly higher (~3 MHz) than the required operating frequency of 13.56 MHz. This is due to the limited capacitance value at the chip's internal capacitor, which prevents the circuit from matching effectively with the inductive coil antenna.
PCSLSC (Parallel C1, Series L1, Series C2)		This topology effectively matches the resonant frequency. However, complexity increases due to the additional inductor (L_1) and the lower value of the capacitor (C_1). The higher number of components may also increase power loss and present practical challenges.
SCPLSC (Series C1, Parallel L1, Series C2)		Similar to PLSC, the resonance of this topology is slightly higher (~3 MHz) than the required operating frequency of 13.56 MHz. Therefore, this topology is not suitable for tuning NFC tag antennas.

Tuning Topology	Tuning Circuit	Analysis
PLSCPLSC (Parallel L1, Series C1, Parallel L2, Series C2)		This topology adds a second inductor (L_2) to the circuit for advanced tuning capabilities. It exhibits the lowest S11 value at a resonance frequency of 13.56 MHz, indicating the best impedance matching. However, the complexity increases with the addition of two inductors with high values (1 mH). Higher inductance values may introduce higher series resistance, which contributes to power loss.

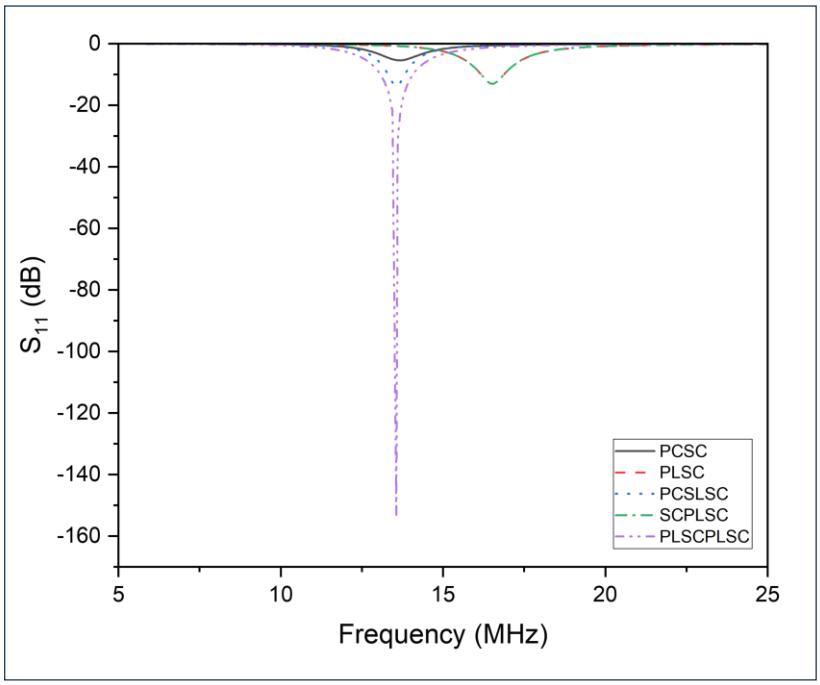


Figure 4.7 The S_{11} Results for All Tuning Topologies

By considering all the analyzed criteria, a simpler PCSC topology, which uses minimal components, is identified as the most optimal for integration with the coil antenna, as all requirements listed in Section 3.5.3.2 are fulfilled. This selection is supported by its advantages, including lower power loss, ease of integration, and practicality in maintaining overall antenna performance. Additionally, the PCSC topology minimizes parasitic effects and reduces the complexity of the tuning circuit, making it more reliable and cost-effective for real-world applications. While more

complex topologies, such as PLSCPLSC, may offer slightly better impedance matching, the trade-offs in terms of increased component count, higher parasitic losses, and power consumption make PCSC a more balanced and efficient choice for NFC tag antenna designs.

The PCSC circuit was then transferred to CST software to be connected with the Design 1 antenna, as shown in Figure 4.8. The obtained S_{11} result was compared with the result from Optenni, as depicted in Figure 4.9. The comparison indicates that the result from Optenni aligns well with the CST result when using the same tuning topology circuit. A slight difference in the S_{11} value and the resonant frequency might be due to discrepancies in the simulation environments of the two software tools. Optenni simplifies the antenna model as a lumped network, while CST accounts for the full electromagnetic interactions and physical dimensions of the coil antenna. Despite these differences, the close agreement between the results confirms the reliability of the PCSC tuning topology for achieving impedance matching and optimal performance at the target frequency of 13.56 MHz.

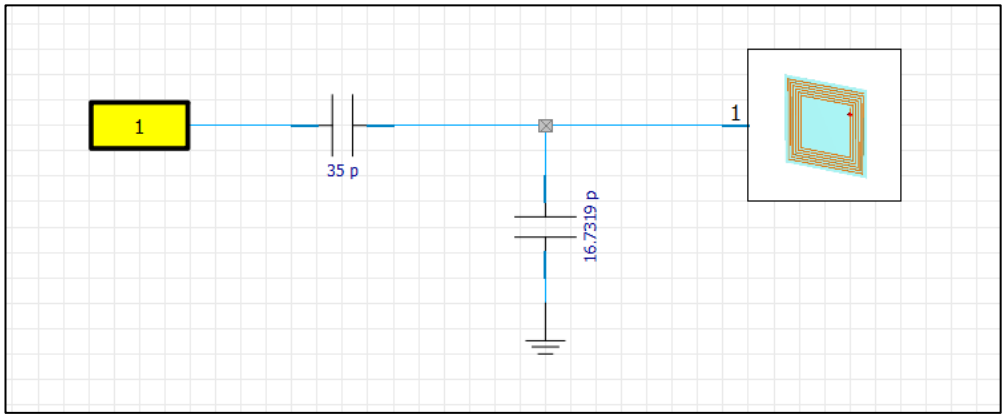


Figure 4.8 PCSC Circuit Integrated with D1-SC Antenna in CST Software

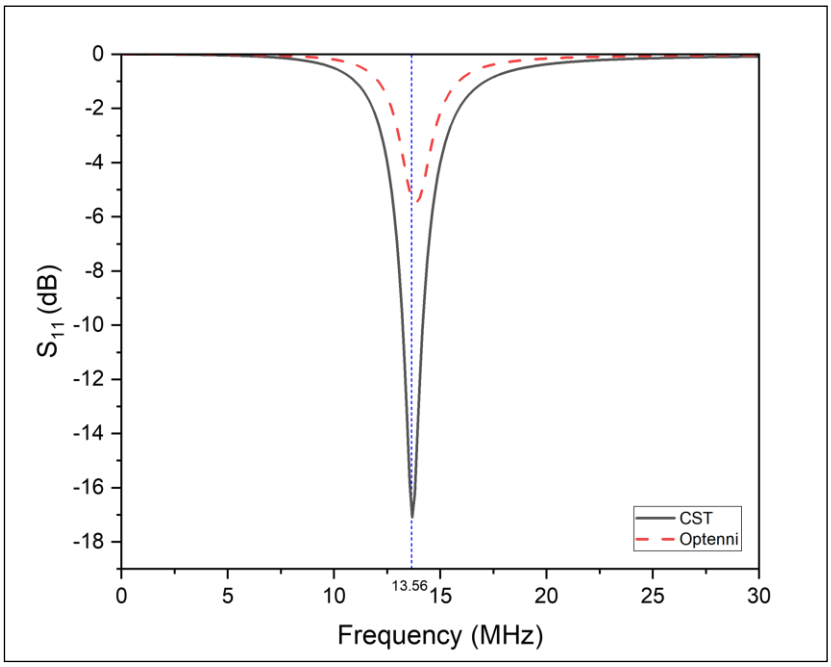


Figure 4.9 Comparison of S_{11} Results from CST Studio Suite and Optenni Lab Software

Figure 4.10 (a) and (b) illustrate the prototypes of D1-SC and D2-SC tag antennas, printed using the DIW method as described in Section 3.5.4.1 of Chapter 3. The antenna was printed in three layers, where the first layer formed the coil, the second layer served as the insulator, and the third layer acted as the bridge, connecting the inner and outer coils of the antenna. The verification process has been conducted at the first layer of the coils to ensure that all printed lines are well-connected. The resistance for each line, labelled as line 1 until line 24, as illustrated in Figure 4.11 (a) and (b) for D1-SC and D2-SC, respectively, was measured.

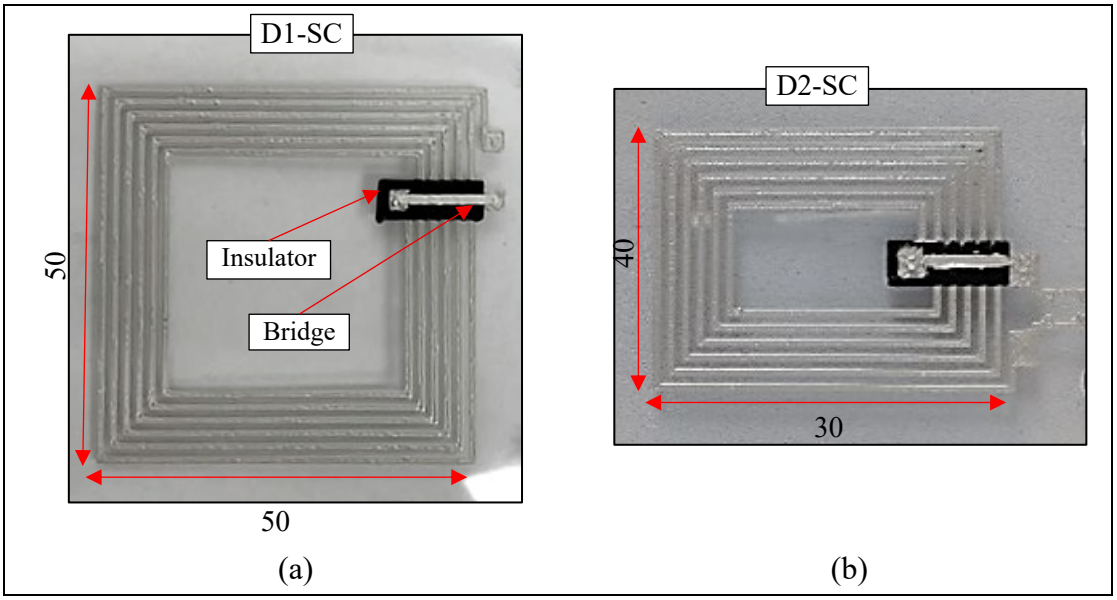


Figure 4.10 Prototype of (a) D1-SC and (b) D2-SC Tag Antenna

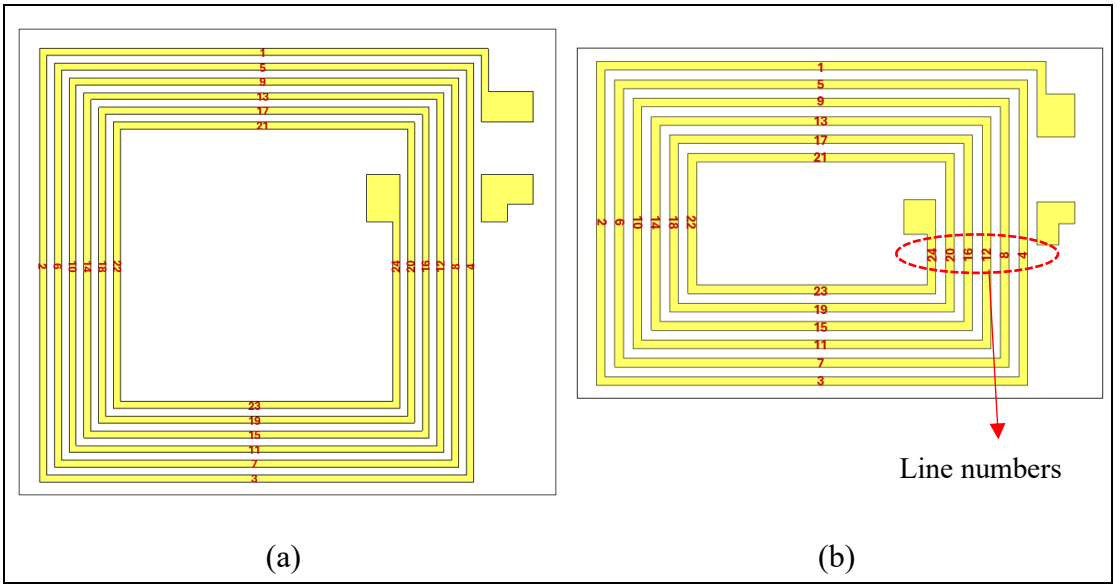


Figure 4.11 The Labelled Line Numbers for (a) D1-SC and (b) D2-SC Tag Antenna Used for Resistance Measurement

Figure 4.12 shows the results of the analysis for the verification of line continuity in the first layer of the D1-SC coil antenna. The resistance readings across the 24 lines show a mean value of 23.54 Ω with a standard deviation (STD) of 2.15 Ω, indicating moderate variability. Most data points fall within the range of 21.44 Ω (mean - STD) to 25.64 Ω (mean + STD), reflecting a reasonable degree of stability in the printed lines. However, there are some outliers, such as Lines 4 and 12, where the resistance peaks at 29 Ω and 28 Ω, respectively. These irregularities may be due to

inconsistencies in the thickness of the printed SC material on the PET substrate, which contribute to slight deviations in resistance measurements. Nevertheless, the measured values fall within the acceptable range for functional conductive lines, which is less than 50 Ω [164].

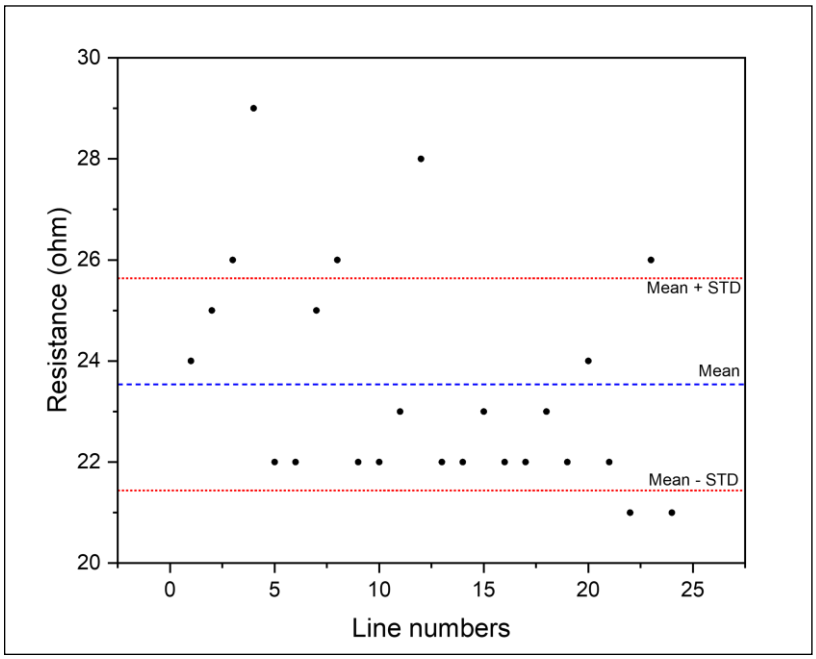


Figure 4.12 Measured Resistance Reading Across the 24 lines for D1-SC Antenna

Figure 4.13 shows the results analysis for the verification of the line continuity for the first layer of the D2-SC coil antenna. The resistance readings exhibit a mean value of 20.83 Ω with a very small STD of 0.38 Ω, indicating minimal variability and high stability across the 24 lines. Most resistance values consistently align with 21.0 Ω, with only a slight drop to 20.0 Ω observed in lines 20 to 23. Despite the minor variations, the measured values are well within the acceptable threshold for functional lines, ensuring the design's reliability and performance.

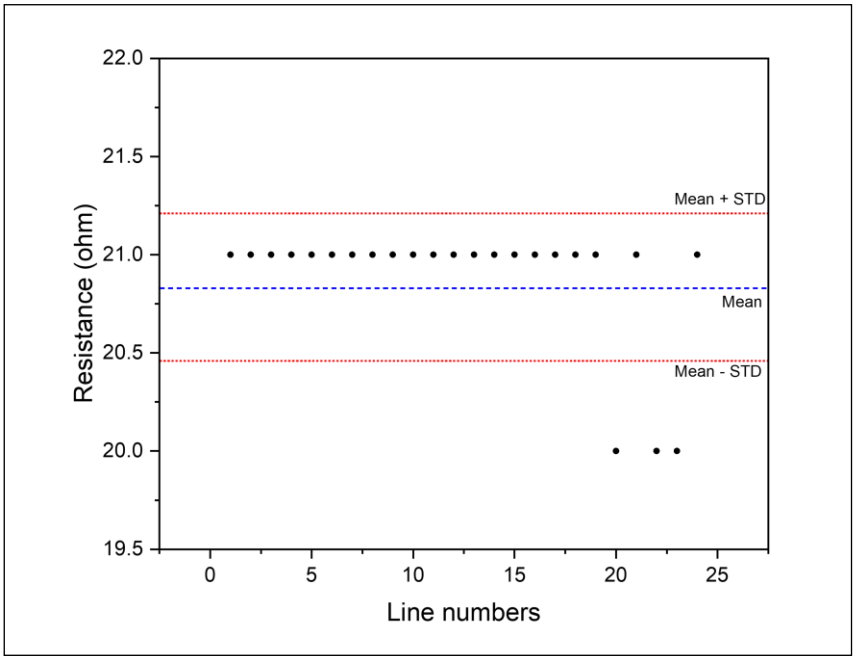


Figure 4.13 Measured Resistance Reading Across the 24 lines for D2-SC Antenna

4.3.1.2 Simulation and Measurement Result Analysis

The electrical properties of the D1-SC and D2-SC antennas, including antenna inductance, L_a, antenna resistance, R_a, and Q-factor, were evaluated through both simulation and measurement. Figure 4.14 (a) and (b) illustrate the simulated L_a and R_a values, respectively, for both antenna designs across different frequencies. The L_a and R_a values were specifically observed at the lower frequency of 1 MHz to minimize the influence of parasitic capacitance [95]. Meanwhile, the Q-factor was calculated using Equation (2.27) based on the L_a and R_a values at the operating frequency of 13.56 MHz. Similarly, the measured L_a and R_a values, as shown in Figure 4.15 (a) and (b), were obtained using VNA as discussed in Section 3.8.1 of Chapter 3. The measured results were compared with the simulation data and summarized in Table 4.6.

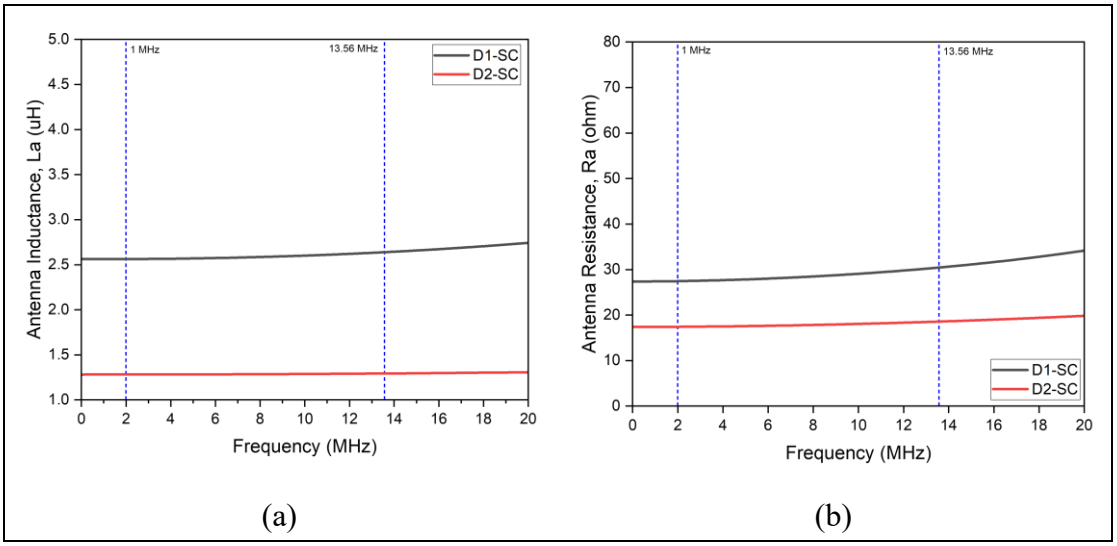


Figure 4.14 Simulated Results of (a) L_a and (b) R_a for D1-SC and D2-SC tag Antennas

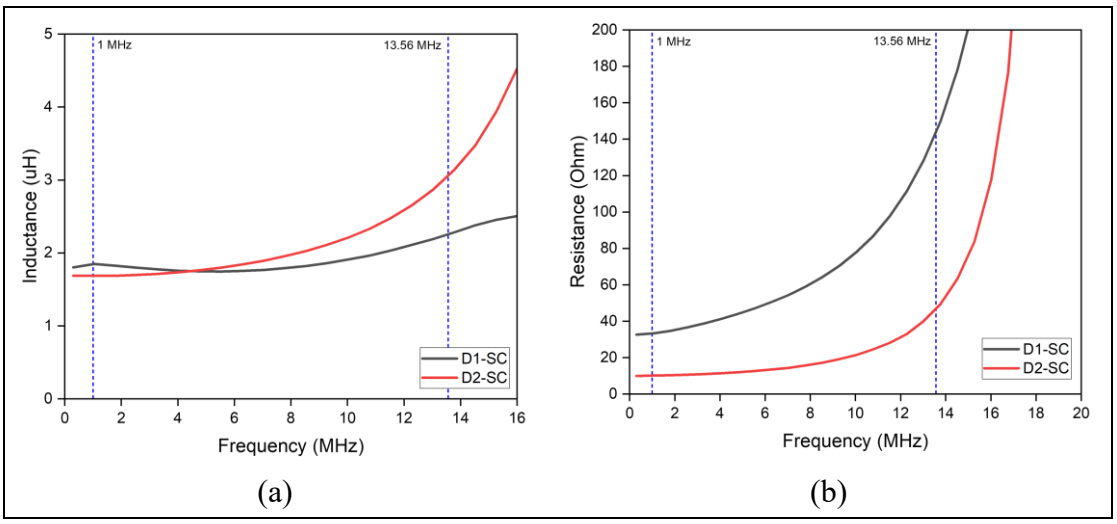


Figure 4.15 Measured Results of L_a and R_a for (a) D1-SC and (b) D2-SC Tag Antennas

Table 4.6
Simulated and Measured Results for D1-SC and D2-SC Antennas

Parameter	**D1-SC**		**D2-SC**	
	Simulation	**Measurement**	**Simulation**	**Measurement**
Antenna Inductance, L_a (μH) @ 1 MHz	2.56	1.85	1.28	1.69
Antenna Resistance, R_a (Ω) @ 1 MHz	27.39	33.36	17.39	10.22
Antenna Impedance, Z_{ant} (Ω) @ 13.56 MHz	30.44 + j224.83	143.3 + j191.92	18.56 + j110.16	46.76 + j259.97
Q-factor @ 13.56 MHz	7.39	1.34	5.93	5.56
PTE (%)	66.5	-	62.8	-

The simulated and measured results for both antenna designs exhibit good agreement, with very slight differences in L_a values at 1 MHz. These findings demonstrate that the SC material is printed with sufficient precision, where the physical implementation closely matches the simulated geometry, including trace width, spacing, and overall coil layout. However, the measured R_a values show slight variation compared to the simulation results for both antenna designs. This discrepancy is likely due to limitations in accurately modeling the thickness of the SC material in the simulation environment. Variations in the thickness of the printed SC layer due to the manufacturing process can lead to higher or lower resistance in certain areas of the antenna, which contribute to the difference in the measured results of R_a compared to the simulation.

D1-SC exhibits higher L_a and R_a values compared to D2-SC, primarily due to its larger surface area and longer conductive traces, as described in Equation (2.29). Since the amount of magnetic flux (Φ) passing through a given surface is proportional to the antenna inductance, a higher inductance value results in a stronger induced magnetic field. This, in turn, enhances the power transfer efficiency (PTE) of D1-SC as compared to D2-SC by approximately 4%, as illustrated in the simulated result of PTE in Figure 4.16. Moreover, the larger surface area of D1-SC provides better coupling with the magnetic field generated by the reader, reducing energy losses and improving power transfer.

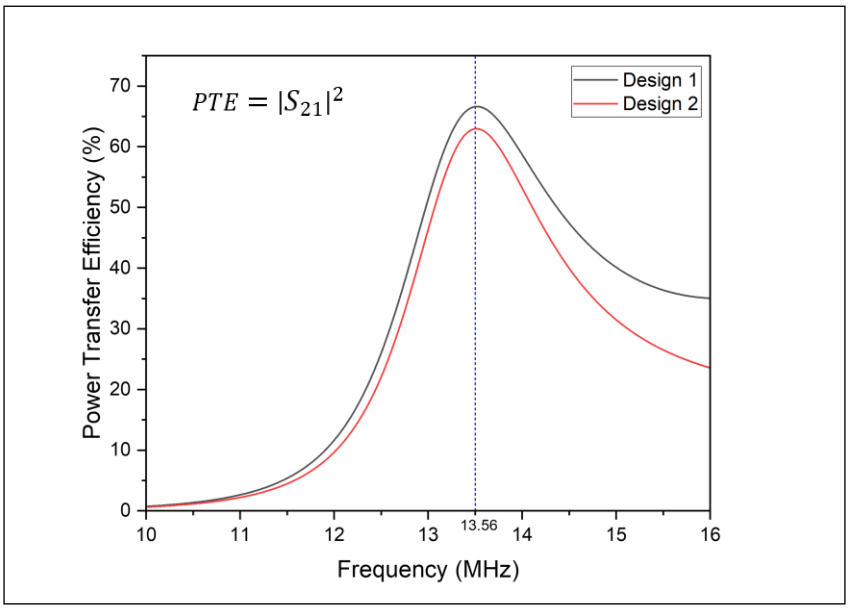


Figure 4.16 Simulated PTE of D1-SC and D2-SC Antennas

Figure 4.17 (a) and (b) show the simulated and measured S_{11} results for D1-SC and D2-SC antenna designs, respectively, with the integration of the PCSC tuning circuit at the antenna port, as previously shown in Figure 4.8. The capacitance values used to tune the antennas, C_{tun}, to resonate at 13.56 MHz are listed in Table 4.7. The capacitance values for the measurements were selected based on commercially available components. The results indicate that the simulated and measured resonant frequencies align closely for both antenna designs, demonstrating good agreement between the simulation and measurement. This agreement validates the accuracy of the simulated tuning topology, as the tuning capacitance values used in the simulation successfully resonated the antennas very close to 13.56 MHz in the measurement. The matching of the S_{11} curves further confirms that the PCSC tuning circuit was modelled effectively in the simulation.

In comparison to other types of antennas, the S_{11} value for the NFC antenna does not necessarily need to be below -10 dB because the tag antenna does not radiate power. It operates based on inductive coupling with the reader antenna, which also resonates at the same operating frequency of 13.56 MHz. Therefore, the critical factor for successful communication is ensuring that the tag antenna resonates within the frequency range of the reader antenna to establish the coupling [188].

The broader bandwidth observed in the measured results of the D1-SC antenna, compared to the simulation, may be attributed to fabrication imperfections such as uneven layer thickness and surface roughness. These factors could introduce additional

resistance and reduce the Q-factor as presented in Table 4.6, resulting in a wider resonance. In contrast, the simulated and measured S_{11} responses for D2-SC show good agreement, suggesting that this design is less sensitive to variations in real-world implementation. This robustness could be attributed to its smaller inductance and dimensions, which minimize the potential for additional losses or parasitic effects.

Table 4.7
Simulated and Measured Values of C_{tun}, Which Connected in Parallel to C_{int}

Antenna Design	**Simulation**		**Measurement**	
	C_{tun}	C_{int}	C_{tun}	C_{int}
D1-SC	18.2 pF	35 pF	20 pF	35 pF
D2-SC	74.5 pF	35 pF	77 pF	35 pF

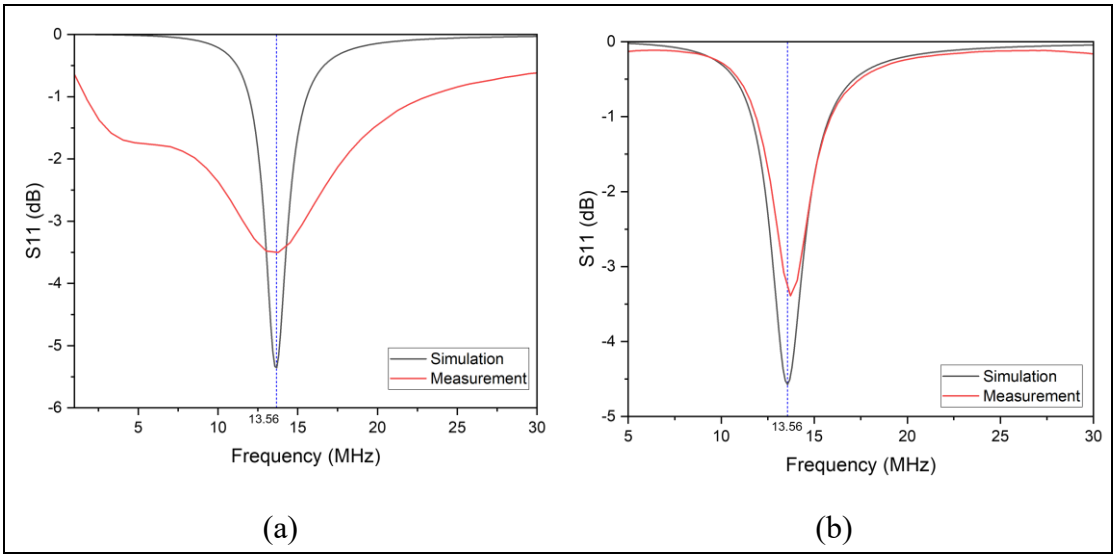


Figure 4.17 Simulation and Measurement Result of S_{11} for (a) D1-SC and (b) D2-SC

The tag reading range is determined in the CST simulation from the magnetic field strength curve, as shown previously in Figure 3.35. The distance at 1.5 A/m of magnetic field strength is considered the maximum reading distance, as 1.5 A/m is the standard value for the minimum field strength required to activate the chip [102][171]. According to the graph, the D1-SC and D2-SC antennas achieve a maximum reading range of approximately 5.17 cm and 4.16 cm, respectively. The longer reading range of the D1-SC antenna aligns with the higher power transfer efficiency achieved previously, as more efficient power transfer results in a stronger induced current in the

NFC chip, ensuring sufficient energy is available to activate the chip at greater distances.

The simulated tag reading range was verified through measurements using the experimental setup discussed in Section 3.8.2 and 3.8.3. The graphs in Figure 4.19 (a) and (b) illustrate the relationship between the tag reading range and the antenna resonance frequency as a function of the tuning capacitance, C_{tun}, for D1-SC and D2-SC antennas, respectively. The graphs show that increasing the C_{tun} value decreases the resonance frequency, and the maximum detection distance is achieved when the tag's resonance frequency falls within the recommended range of 13.56 MHz to 16 MHz [111]. For the D1-SC tag antenna, the maximum reading range is 3.3 cm, achieved with a C_{tun} value of 20 pF at a resonant frequency of 14 MHz. Meanwhile, for the D2-SC antenna, the maximum distance is 2.2 cm, obtained with a C_{tun} values of approximately 77 pF at a resonance frequency of 13.6 MHz.

The measured tag reading range for D1-SC and D2-SC decreased by approximately 1.8 cm and 1.9 cm, respectively, compared to the simulated reading range. This discrepancy is likely due to several factors, including the presence of parasitic elements during the reading range measurement. These elements can include external components, such as cables and connectors used to connect the antenna to the capacitors and the board, which introduce additional capacitance and resistance into the system. Furthermore, the coupling between the reader's magnetic field and the tag antenna during measurement was influenced by several factors, including the size mismatches between the reader antenna and the tag, as well as the orientation and alignment of the reader and the tag antennas, which contributed to the reduction in the measured tag reading range [189][190]. However, the achieved tag reading range remained within the acceptable range for NFC tag operation, ranging from 1 cm to 5 cm when using a smartphone as a reader [103].

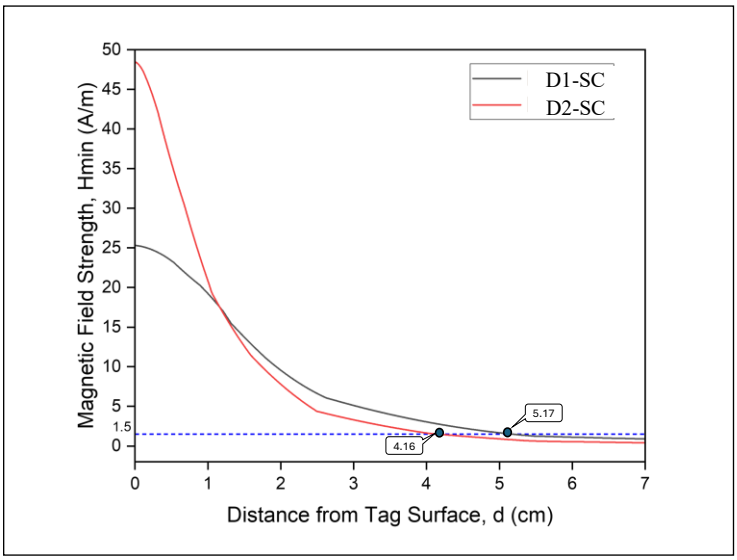


Figure 4.18 Reading Range of D1-SC and D2-SC Antennas

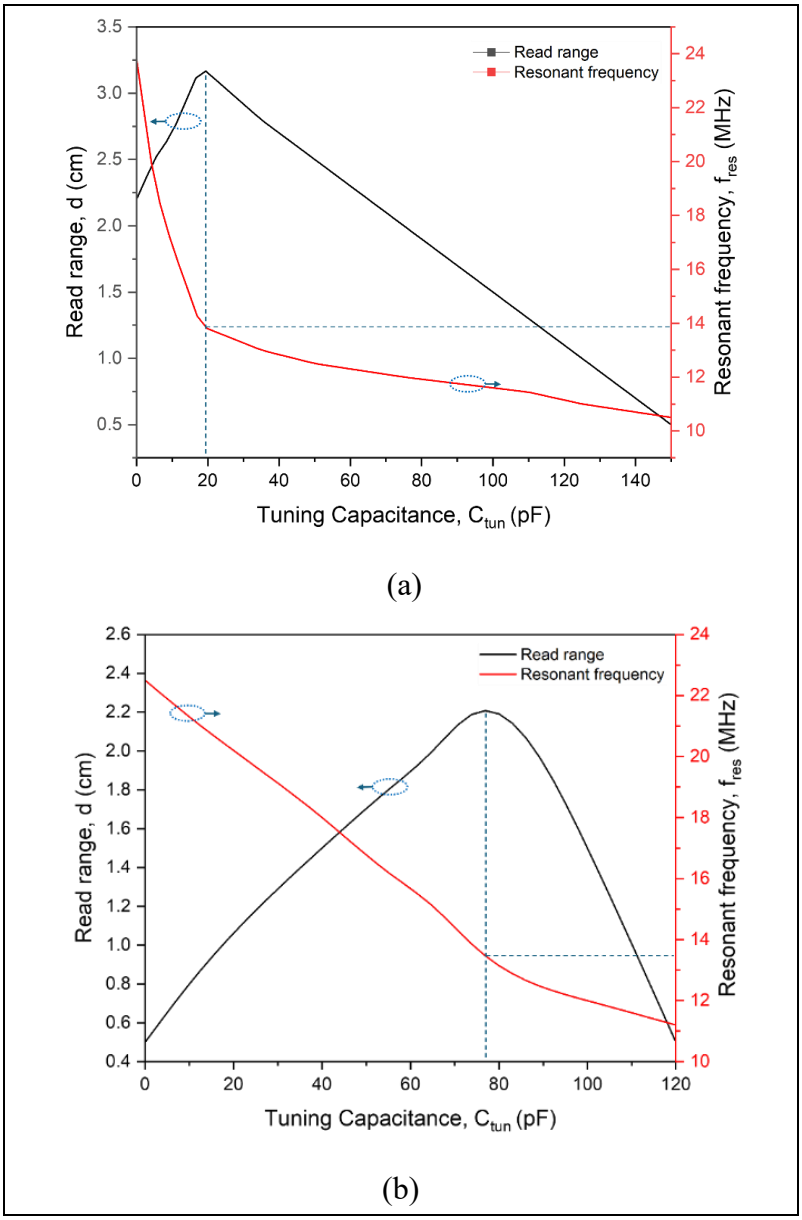


Figure 4.19 Measured Result of Antenna Resonance Frequency and Tag Reading Range with Respect to Tuning Capacitance, C_1, for (a) D1-SC and (b) D2-SC Antennas

In summary, both D1-SC and D2-SC antennas demonstrate good performance in terms of electrical properties, resonant matching, and tag reading range, thereby fulfilling the fundamental requirements for effective NFC tag antenna operation. These results confirm the suitability and compatibility of the SC material for NFC applications, providing a valuable performance benchmark for subsequent studies on HCG and HGS conductive materials.

However, despite its advantageous electrical characteristics, the SC material exhibits several limitations that hinder its practical implementation in food-related

applications. The SC consists mainly of bulk silver particles, making it more prone to silver ion leaching, especially under humid or reactive conditions [24]. This poses a potential health hazard in food-contact applications and creates regulatory issues related to adherence to food safety requirements. Additionally, the use of high-purity silver significantly increases production costs, making SC less economically feasible for disposable or large-scale packaging applications.

Due to these limitations, the study proceeds to investigate alternative materials such as HCG and HGS, which offer the potential for lower cost, improved mechanical flexibility, and safer integration with food packaging. For further flexibility analysis in the upcoming section, the D2-SC antenna is selected due to its smaller size and more stable S_{11} performance, which is an important factor in maintaining antenna functionality during bending. This selection also highlights the potential of D2-SC for applications that require compact and flexible NFC tag designs, while setting the stage for assessing whether HCG and HGS can offer enhanced material suitability without compromising performance.

4.3.2 Hybrid Graphene-Silver (HGS) NFC Tag Antenna

For the HGS material, the measured conductivity value is slightly higher than that of the SC material, which is 3.95×10^6 S/m, as summarized previously in Table 4.4 in Section 4.2. The low thickness of printed HGS conductive materials, which is only 1 μm, offers benefits in terms of flexibility, lightweight, and ease of printing for the NFC tag [9]. However, the tag antenna may suffer from a very high value of antenna resistance due to its lower cross-sectional area, which will limit the flow of current along the coil. The high value of antenna resistance will contribute to a very low Q-factor, which is proportional to the power transfer efficiency and tag reading range [191].

4.3.2.1 Verification of Printed HGS-based Antenna

Three antenna designs, as described in Section 3.5.2 of Chapter 3, were simulated and fabricated using HGS conductive material for further analysis. The first antenna design, denoted as D1-HGS, is similar to the Design 1 antenna as being used by SC material (D1-SC) in Section 4.3.1. The second and third antenna designs are

denoted as D3-HGS and D4-HGS, respectively. Figure 4.20 (a), (b), and (c) show the prototypes for D1-HGS, D3-HGS, and D4-HGS tag antennas, respectively, printed using the inkjet printing method as described in Section 3.5.4.3 of Chapter 3.

The coil antenna design and the bridge, which connects the inner coil and the outer coil of the antenna, were printed separately. Before they were bonded using the conductive epoxy, a verification process was conducted for the coil antenna to ensure that all the printed lines were well-connected. The resistance for each line, labelled as line 1 through line 24 for D1-HGS and D3-HGS, and line 1 through line 16 for D4-HGS, as illustrated in Figure 4.21(a), (b), and (c), respectively, was measured and statistically analyzed.

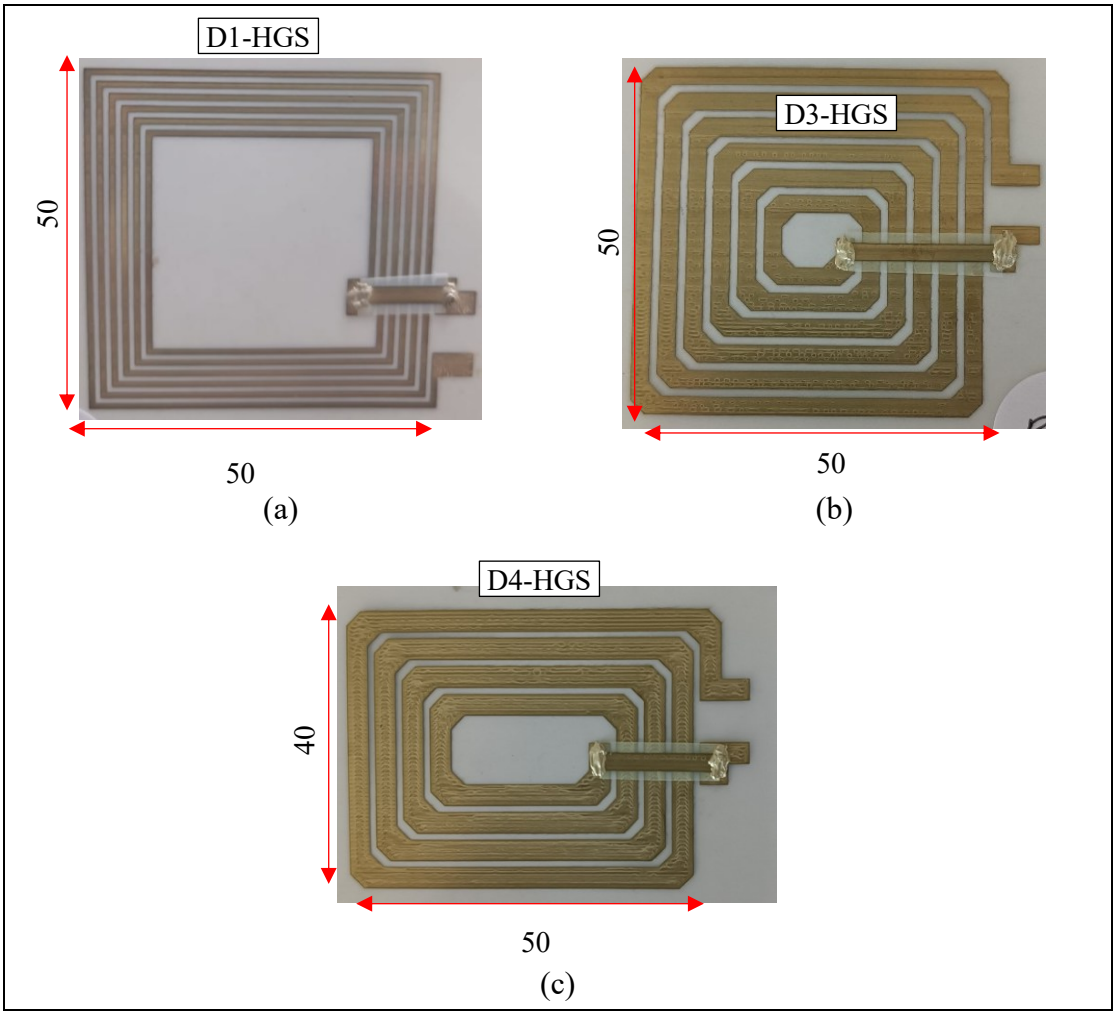


Figure 4.20 Prototype of (a) D1-HGS, (b) D3- HGS and (b) D4- HGS Tag Antenna

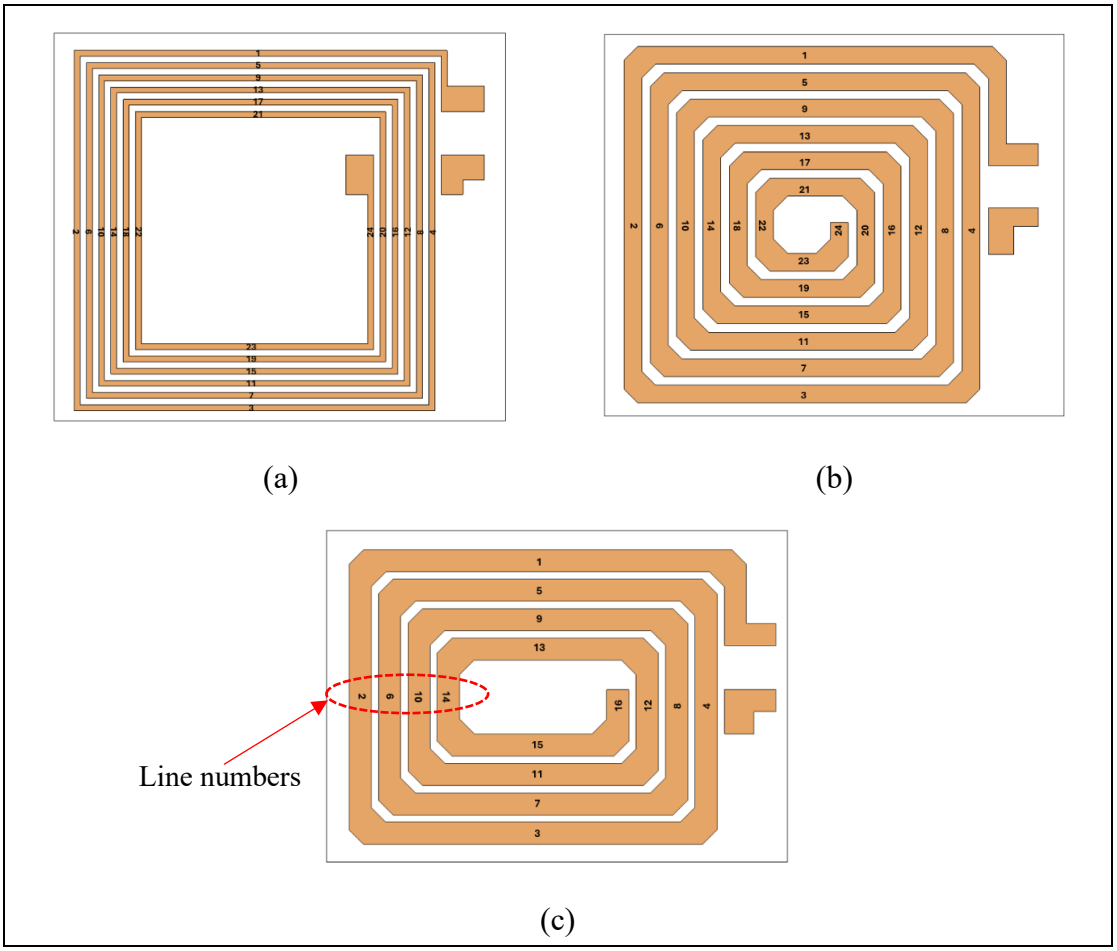


Figure 4.21 The Labelled Line Numbers for (a) D1-HGS, (b) D3- HGS and (b) D4-HGS Tag Antenna Used for Resistance Measurement

Figure 4.22 shows the results of the analysis for the verification of line continuity for the printed coil design of the D1-HGS antenna. The resistance readings show a mean value of 29.88 Ω with a standard deviation (STD) of 3.83 Ω, indicating moderate variability across the 24 lines. Most resistance values fall within the range of (29.88 ± 3.83) Ω, or 26.13 Ω to 33.62 Ω, reflecting reasonable stability in the printed lines. However, there are some outliers, particularly at Lines 1 and 4, which exceed the upper limit of the expected range. These irregularities may be due to inconsistencies in the thickness of the HGS material during deposition. Despite these deviations, the majority of the lines exhibit consistent resistance values, where the readings align closely with the mean. Nevertheless, all the measured resistance values are within the acceptable range for functional conductive lines, which is less than 50 Ω [164].

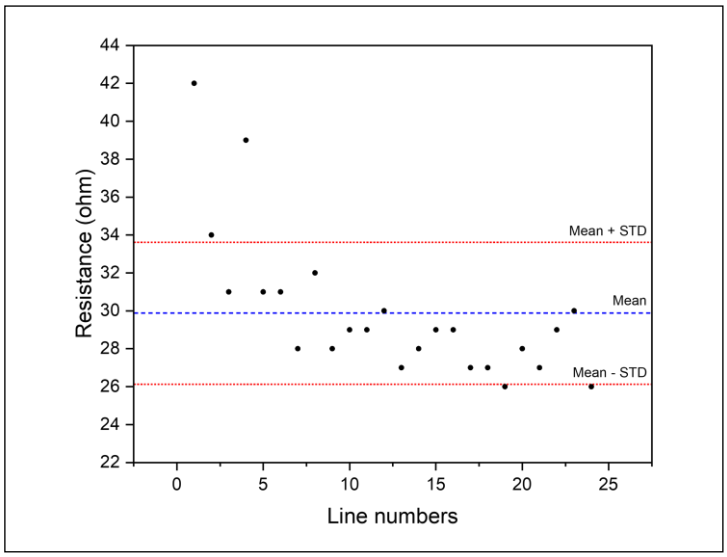


Figure 4.22 Measured Resistance Reading Across the 24 lines for D1-HGS Antenna

For the resistance measurement results of the D3-HGS coil antenna, as depicted in Figure 4.23, the mean value obtained is 21.54 Ω with a very small STD of 1.44 Ω, indicating good consistency and minimal variability across the 24 lines. The majority of the readings fall within the range of (21.54 ± 1.44) Ω, or 20.13 Ω to 22.96 Ω, reflecting stability in the printed lines. Slight deviations occur at Lines 1 and 4 with higher resistance values of 25 Ω, which are above the upper limit of the range. These outliers may be due to minor inconsistencies in the thickness of the hybrid graphene material during deposition, similar to the observation in D1-HGS. The remaining lines show consistent readings closely aligned with the mean. Overall, the resistance measurements for D3-HGS are stable and within acceptable limits, with only minor deviations that do not compromise the functionality of the conductive lines.

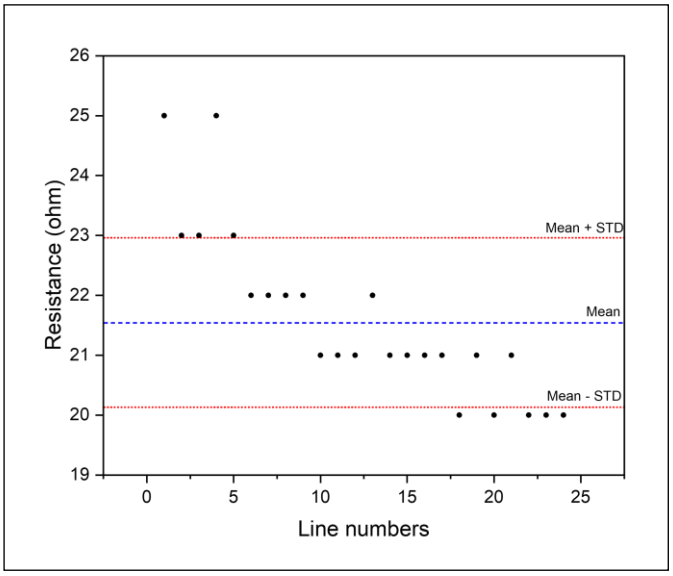


Figure 4.23 Measured Resistance Reading Across the 24 lines for D3-HGS Antenna

Figure 4.24 shows the resistance measurement results of the D4-HGS coil antenna. The resistance readings exhibit a mean value of 21.06 Ω with a very small STD of 1.06 Ω, indicating excellent stability and minimal variability across the 16 lines. The majority of the resistance readings fall within the range of (21.06 ± 1.06) Ω, or 20.03 Ω to 22.09 Ω, reflecting a high level of consistency in the printed lines. Slight variations are observed in Lines 1 and 3, with resistance differences of less than 1 Ω from the upper threshold of the STD range. Overall, the resistance distribution is closely aligned around the mean, with the values maintaining functional reliability. The consistent readings validate the uniformity of the conductive lines and suggest a robust manufacturing process for the D4-HGS design.

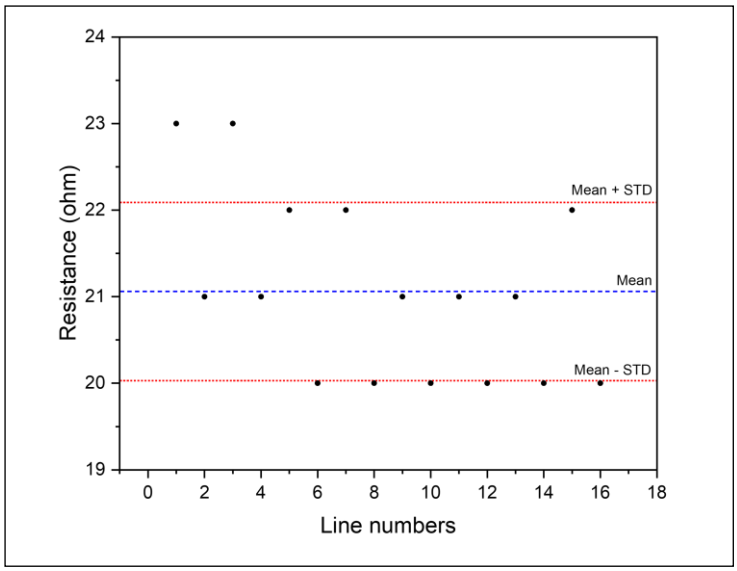


Figure 4.24 Measured Resistance Reading Across the 16 lines for D4-HGS Antenna

4.3.2.2 Simulation and Measurement Result Analysis

The Design 1 (D1) antenna, as shown in Figure 4.25 (a), exhibits good performance when using SC material, with detection capabilities extending up to 3 cm, as detailed in Section 4.3.1.2. However, when the same design is applied with HGS material (D1-HGS), the antenna resistance, R_a, increases significantly from 27.39 Ω to 308.77 Ω at 1 MHz, as shown in Figure 4.25 (b), despite the higher conductivity of HGS material compared to SC material. This is most probably due to the very small thickness of the printed HGS material on the PET substrate. As mentioned in Section 3.5.4.3, the allowable thickness for HGS material printing ranges from 1 to 5 µm, which is much lower than the minimum permissible thickness for SC material, set at 50 µm [146]. Using a much thinner conductive material reduces the cross-sectional area of the conductor. According to Equation (4.1), the cross-sectional area, A, and the resistance of the antenna, R_a are inversely proportional [192]. Therefore, as the conductor thickness decreases, antenna resistance increases.

$$R_a = \rho \frac{l}{A} \tag{4.1}$$

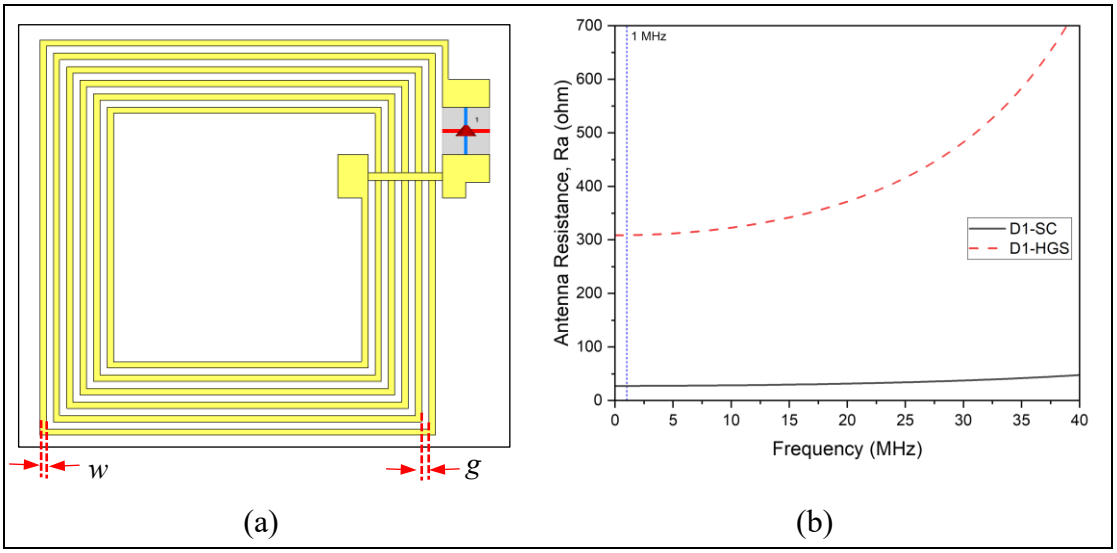


Figure 4.25 Antenna Geometry and Resistance Comparison: (a) Geometric Layout of D1 Antenna, and (b) Comparison of Antenna Resistance (R_a) Versus Frequency for D1-SC and D1-HGS Antennas

To further reduce the antenna resistance, an analysis of the antenna's geometrical parameters was conducted by varying the coil width (w) and the gap between the conductors (g). The overall antenna dimensions were maintained at 50 x 50 mm^2 throughout the analysis, with the thickness of the HGS material, t_c fixed at 1 µm. Figure 4.26 (a) illustrates the correlation between coil width, w, varied from 1 mm to 2.5 mm (i.e., 1, 1.5, 2, and 2.5), and the antenna's inductance and resistance, while g was kept constant at 1.2 mm. The results show that increasing the coil width significantly reduces both inductance and resistance. A broader coil width reduces inductance by expanding the loop area, which disperses the magnetic field lines over a larger area, thereby decreasing the magnetic field density. The resistance also decreases as a wider conductor provides a larger cross-sectional area for current flow, thereby minimizing resistive losses.

Figure 4.26 (b) shows the correlation between g, varied from 1 mm to 1.3 mm (i.e., 1.0, 1.1, 1.2, and 1.3 mm), and the antenna's inductance and the resistance, while w was fixed at 2.5 mm and the number of turns, n remained at 6. The results indicate that increasing the gap between the coils slightly reduces the antenna inductance due to weaker magnetic coupling between adjacent turns, resulting in a decrease in mutual inductance. However, changes in g have minimal effect on resistance, as resistance is primarily determined by the total conductor length and cross-sectional area, which remain constant regardless of the gap variation.

Meanwhile, the Q-factor increases with the increase in coil width, w, as shown in Figure 4.26 (c), due to the significant reduction in antenna resistance. In contrast, increasing the gap, g, slightly reduces the Q-factor, as shown in Figure 4.26 (d), since antenna resistance is minimally affected by the increased spacing between conductors. Therefore, the optimum parameter values obtained from the variation of w and g are 2.5 mm and 1.0 mm, respectively, which contribute to the Design 3 antenna (D3-HGS), as shown in Figure 4.27 (a). Compared to the D1-HGS, the D3-HGS antenna exhibits a significant reduction in antenna resistance by approximately 70% from 308.77 Ω to 71.11 Ω, as illustrated in Figure 4.27 (b). However, this optimization came with a trade-off, as the antenna inductance decreased from 2.34 µH to 1.21 µH, as shown in Figure 4.27 (c). Despite the reduction in inductance, the lower antenna resistance compensates for it, resulting in an approximately 50% increase in antenna Q-factor at 13.56 MHz, compared to the D1-HGS antenna, as shown in Figure 4.27 (d).

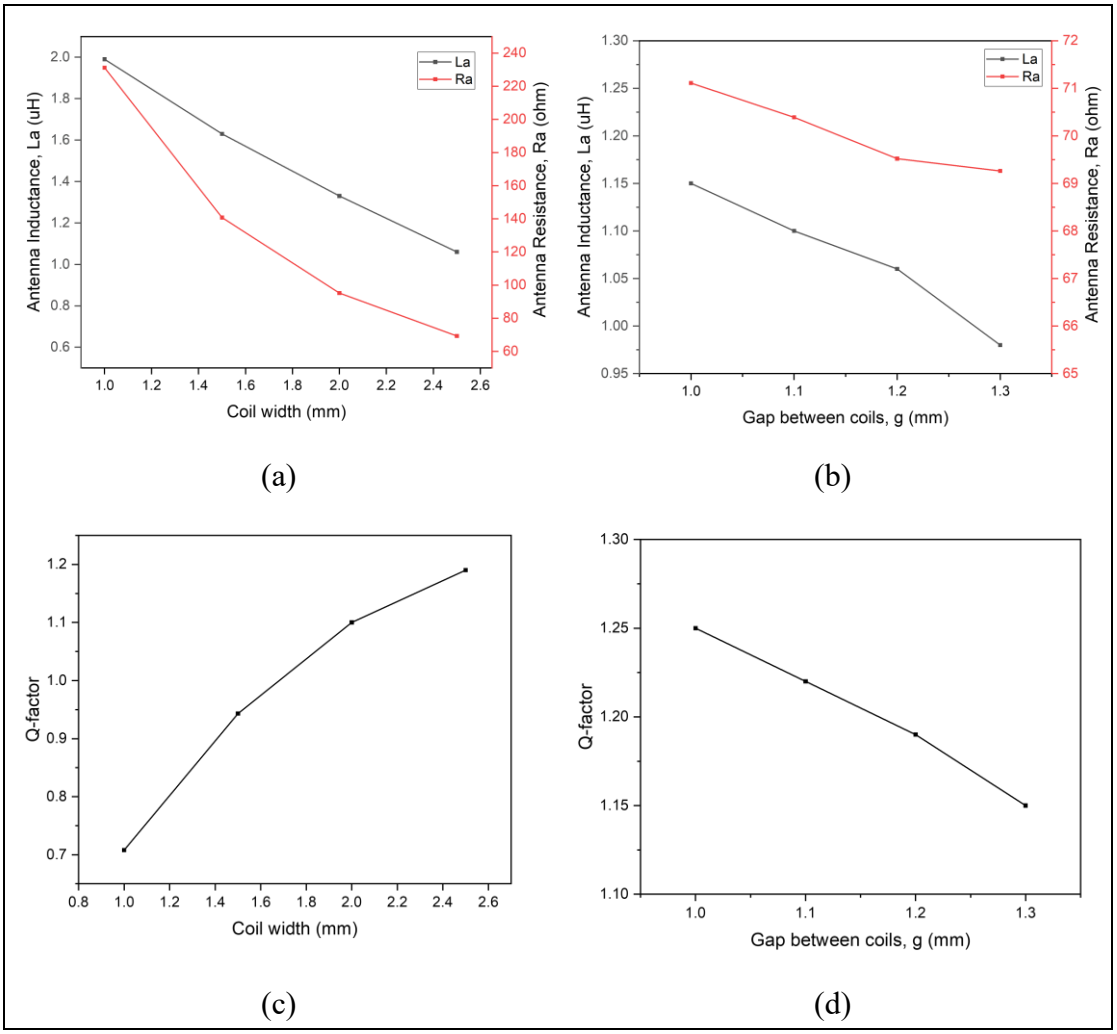


Figure 4.26 Correlation Between Antenna Geometric Parameters and Electrical Performance: (a) Width with L_a and R_a, (b) Gap with L_a and R_a, (c) Width with Q-Factor, and (d) Gap with Q-factor

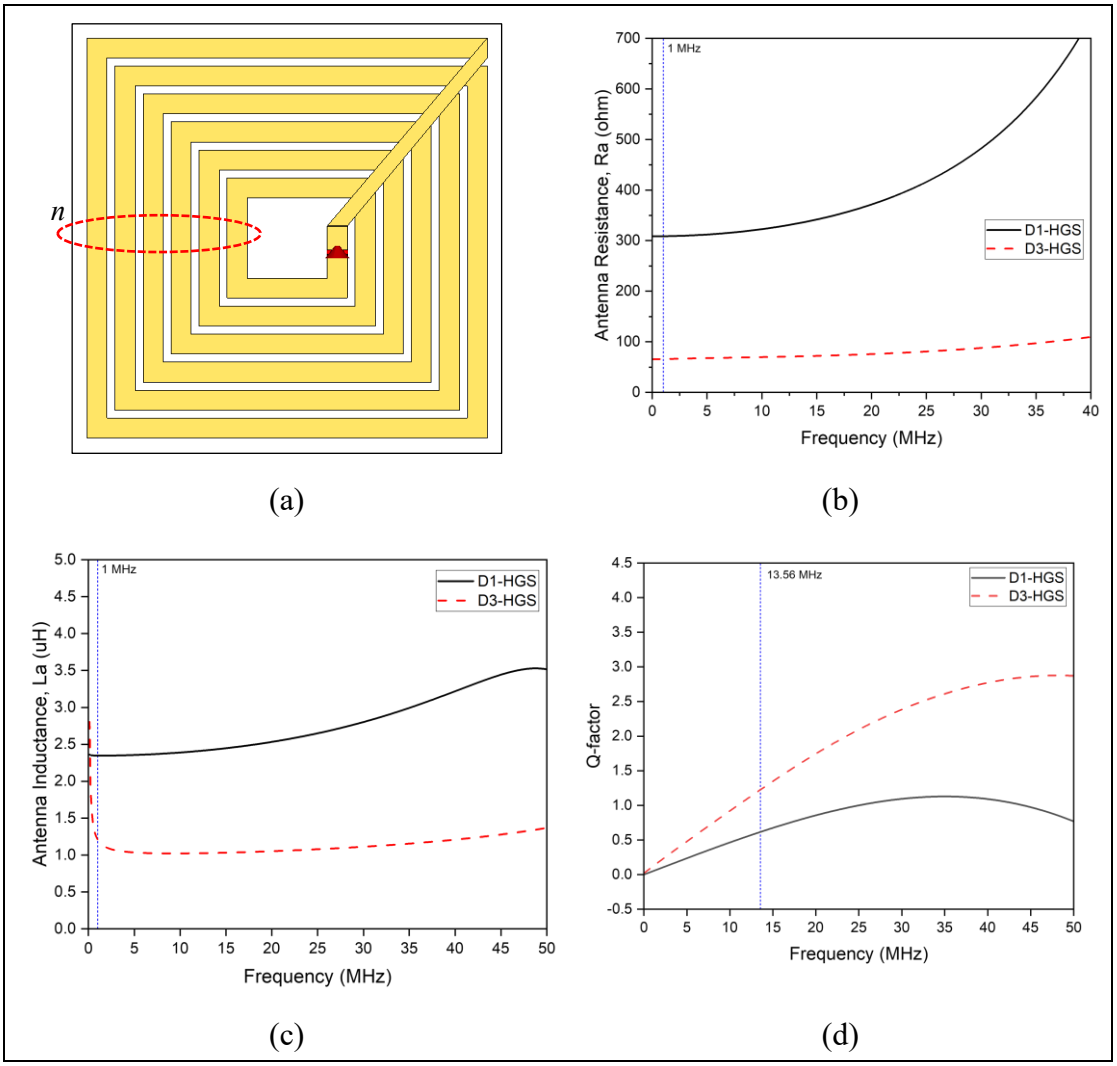


Figure 4.27 Comparison between D1-HGS and D3-HGS Antenna Designs: (a) D3-HGS Antenna Design (b) R_a Versus Frequency, (c) L_a Versus Frequency, and (d) Q-Factor Versus Frequency

Further optimization was carried out to achieve a smaller antenna size and a target resistance of below 50 Ω, as stated in Section 3.2 of Chapter 3, without compromising the antenna Q-factor. To reduce the size of the D3-HGS antenna, the number of turns needed to be decreased to prevent coil overlap. By reducing the antenna size by 20% compared to the D3-HGS, the number of turns, n, was varied from 2 to 4 (i.e., 2, 3, and 4), to evaluate their effect on the antenna's electrical parameters. Figure 4.28 (a) illustrates the correlation between n and the antenna's inductance, resistance, and Q-factor, with w and g fixed at 3 mm and 1 mm, respectively. From the graph, it can be observed that the antenna resistance met the required value of below 50 Ω for all values of n. However, the Q-factor decreased with a smaller number of turns, as shown in Figure 4.28 (b), due to the concurrent reduction in inductance and resistance.

Based on the parameter analysis results, the optimum value configuration was achieved with $n = 4$ and $w = 3$ mm, as the Q-factor remained equivalent to that of the D3-HGS design, with the value of 1.18, while also providing the advantage of a 20% size reduction. This final design is denoted as D4-HGS, with dimensions of 50 × 40 mm^2, as shown in Figure 4.28 (c).

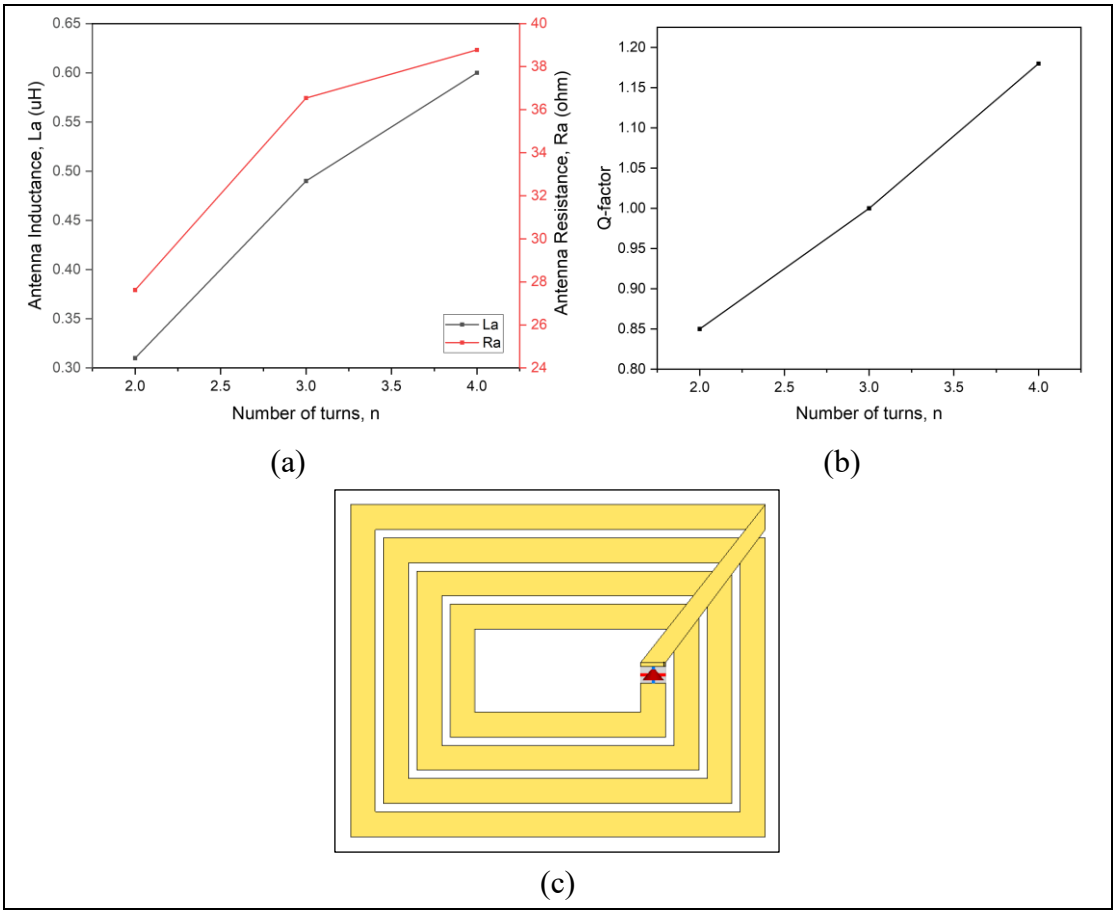


Figure 4.28 Correlation Between the Number of Turns and (a) L_a and R_a, (b) Q-Factor, and (c) Final Antenna Design of D4-HGS

The final optimization process for the antenna design was carried out by implementing a chamfer, c, at each corner of the D3 and D4 antennas, as depicted in Figure 4.29 (a) and (b), respectively. This modification aimed to further reduce antenna resistance, while slightly increasing the Q-factor. The chamfer width used was 2 mm for both antenna designs, and the comparison results are presented in Table 4.8. The results show that the implementation of the chamfer further reduced antenna resistance by approximately 9% to 10% in both designs, along with an increase in antenna inductance. This is due to the smoother current flow and reduced current concentration

at sharp corners, which minimizes resistive losses and slightly increases the effective inductive path length. As a result, the Q-factor increased approximately 3% for both antenna designs.

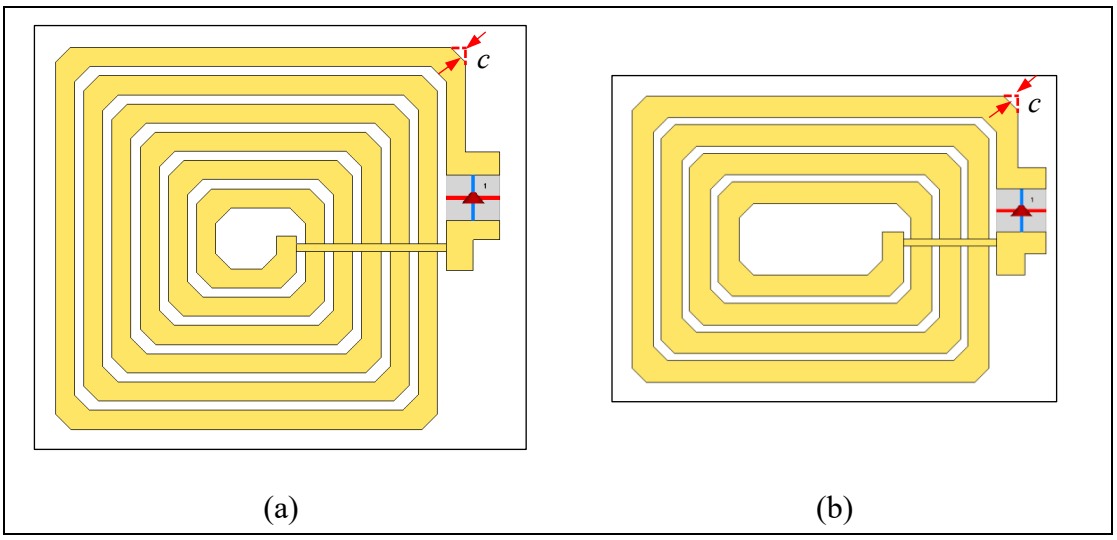


Figure 4.29 Chamfer Implemented in the Design of (a) D3-HGS and (b) D4-HGS

Table 4.8
Comparison of Antenna Electrical Properties for D3-HGS and D4-HGS with and without Chamfer

Antenna Design		**R (ohm)**	**L (µH)**	Q-factor
D3-HGS	without chamfer	71.11	1.05	1.18
	with chamfer	63.74	1.22	1.22
D4 -HGS	without chamfer	38.78	0.6	1.18
	with chamfer	35.15	0.75	1.22

To verify the simulation results, the electrical properties of each antenna design were measured using a VNA as discussed in Section 3.8.1 of Chapter 3. The measured L_a values are generally close to the simulated values for all antenna designs, as presented in Table 4.9. This indicates that the HGS material was printed with sufficient precision and that the physical implementation closely matches the simulated geometry, including factors such as trace width, spacing, and overall coil layout. However, the measured antenna resistance shows significant discrepancies from the simulation for D1-HGS and D3-HGS, in contrast to D4-HGS. Several factors may contribute to these

discrepancies, such as variations in the thickness of the printed HGS layer or microstructural imperfections, including surface roughness of the HGS layer. Additionally, the antenna design for D4-HGS is less complex compared to the others, with fewer turns and wider conductor width, making it less susceptible to fabrication inconsistencies. This is why the simulation assumptions for D4-HGS closely align with real-world fabrication. The Q-factor for D4-HGS is also the highest among the others due to the smallest antenna resistance achieved by the antenna.

Table 4.9
Simulated and Measured Electrical Properties of D1-, D3- and D4-HGS

Parameter	**Design 1 (D1-HGS)**		**Design 3 (D3-HGS)**		**Design 4 (D4-HGS)**	
	Simulation	**Measurement**	**Simulation**	**Measurement**	**Simulation**	**Measurement**
Antenna Inductance, La (μH) @ 1 MHz	2.34	2.51	1.22	1.06	0.75	0.85
Antenna Resistance, Ra (Ω) @ 1 MHz	308.77	210.4	63.74	82.74	35.15	36.16
Antenna Impedance, Zant @ 13.56 MHz	335.36 + j224.83	301.5 + j213.1	71.55 + j88.24	91.88 + j92.74	40.18 + j48.11	64.57 + j86.90
Q-factor @ 13.56 MHz	0.62	0.71	1.22	1	1.22	1.35

Figure 4.30 shows the simulated and measured S_{11} results for all antenna designs with the integration of the PCSC tuning circuit at the antenna port, as previously shown in Figure 4.8. The capacitance values used to tune the antennas to resonate at 13.56 MHz are listed in Table 4.10. A slight variation in the tuning capacitance, C_{tun} during measurement might be attributed to the presence of parasitic capacitance introduced by the conductive epoxy used to connect the bridge of the antenna. This parasitic capacitance reduces the amount of external capacitance required to match the coil inductor antenna. However, the measured tuning capacitance values remain within an acceptable range, as variations due to manufacturing and environmental factors are typically accommodated within ±10% to ±20% tolerances in NFC designs [193]. Additionally, it can be observed that the tuning capacitance is highest for D4-HGS,

followed by D3-HGS and D1-HGS. This trend corresponds to the lower inductance (L_a) value of D4-HGS compared to the other antenna designs, requiring higher capacitance to achieve resonance at 13.56 MHz.

Table 4.10
Simulated and Measured Value of C_{tun}, Which Connected in Parallel to C_{int}

Antenna Design	**Simulation**		**Measurement**	
	C_{tun}	C_{int}	C_{tun}	C_{int}
D1-HGS	17 pF	35 pF	15 pF	35 pF
D3-HGS	95 pF	35 pF	90 pF	35 pF
D4-HGS	150 pF	35 pF	120 pF	35 pF

In Figure 4.30 (b) and (c), it can be observed that the simulated and measured S_{11} results for D3-HGS and D4-HGS, respectively, are closely aligned, with both exhibiting a narrower bandwidth compared to D1-HGS in Figure 4.30 (a). This is due to the higher Q-factor and lower resistance of the D3-HGS and D4-HGS tag antennas, which are directly related to the antenna bandwidth. The broader bandwidth of D1-HGS indicates higher resistive losses and a lower Q-factor, which may reduce the antenna's ability to store energy efficiently.

The S_{11} values for all antenna designs are within an acceptable range for NFC antennas. In the simulation, the values range from -3 dB to -4 dB, while in the measurement, the values are slightly higher, ranging from -2 dB to -3 dB. Based on the measurement setup described in Section 3.8.2 of Chapter 3, the S_{11} values were obtained based on the mutual inductive coupling between the NFC tag antenna and a conventional coil antenna connected to a VNA. Therefore, the reflection coefficient for NFC antennas does not necessarily need to be below -10 dB because the tag antenna does not radiate power but relies on inductive coupling. Reflection coefficient values between -2 dB and -6 dB are typically considered acceptable, as they indicate that at least 40% to 75% of the power is accepted by the tag antenna, which is generally sufficient for passive NFC systems [194].

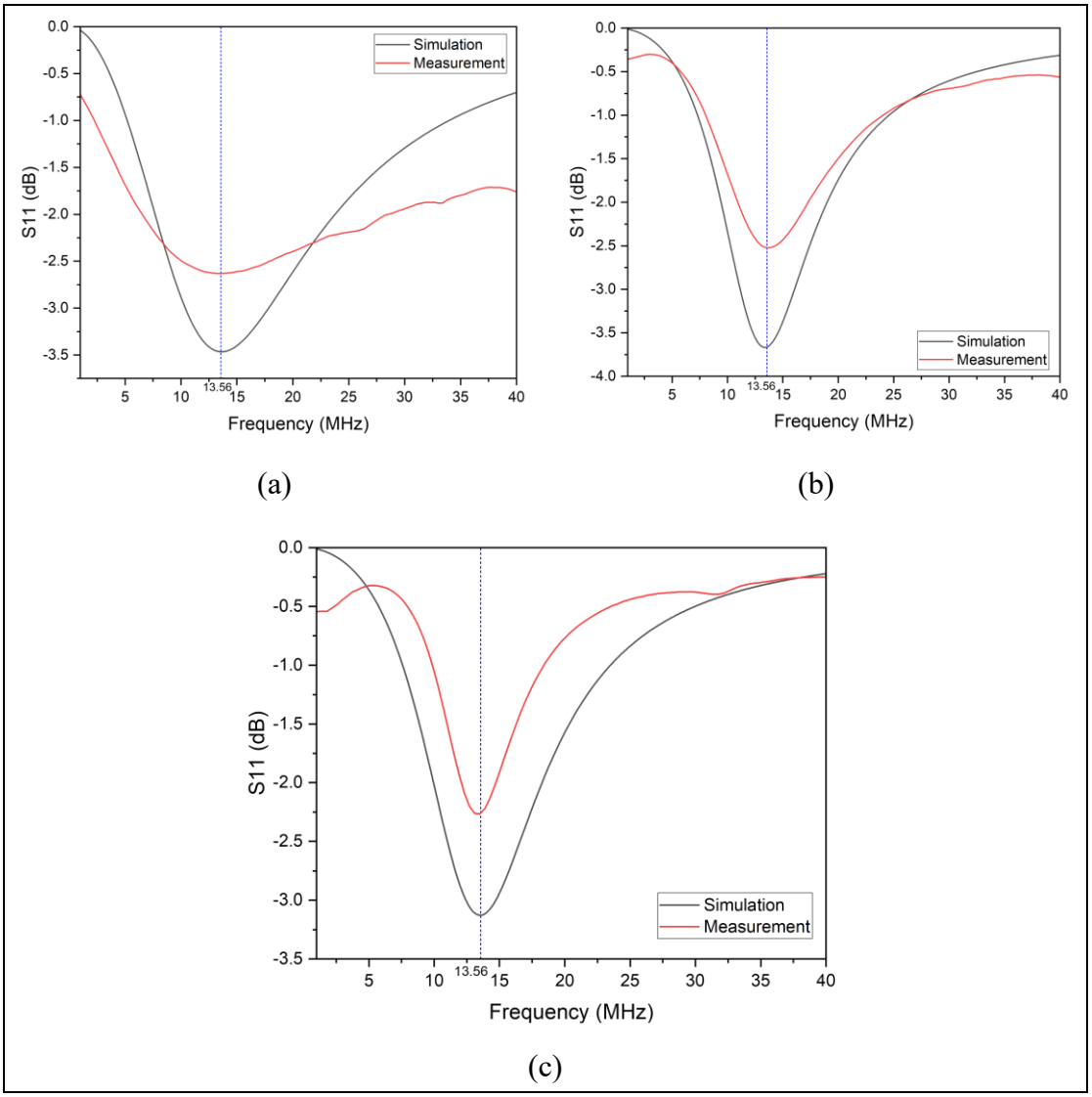


Figure 4.30 Measured and Simulated S11 for (a) D1-HGS, (b) D3-HGS and (c) D4-HGS Tag Antenna

The simulated power transfer efficiency (PTE) of all the antenna designs is depicted in Figure 4.31. It can be observed that D3-HGS achieves the highest PTE, approximately 50%, followed by D4-HGS at around 48%, with D1-HGS having the lowest PTE at approximately 32%. For most passive NFC systems, a PTE of approximately 50% is typically considered acceptable and sufficient for reliable operation [195]. The D3-HGS and D4-HGS tag antennas demonstrate optimized performance for practical NFC applications with acceptable PTE, contributing to longer reading ranges of 3.41 cm and 3.21 cm, respectively, as shown in Figure 4.32. Meanwhile, the D1-HGS, suffers from a shorter reading range of 2.11 cm due to its lower PTE and higher resistance, which reduce the amount of power available for inductive coupling.

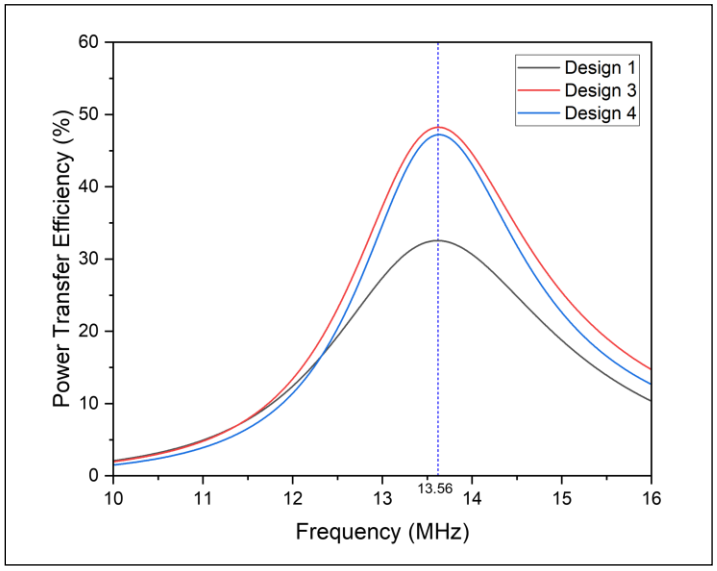


Figure 4.31 Simulation of Power Transfer Efficiency (PTE) for All Antenna Designs

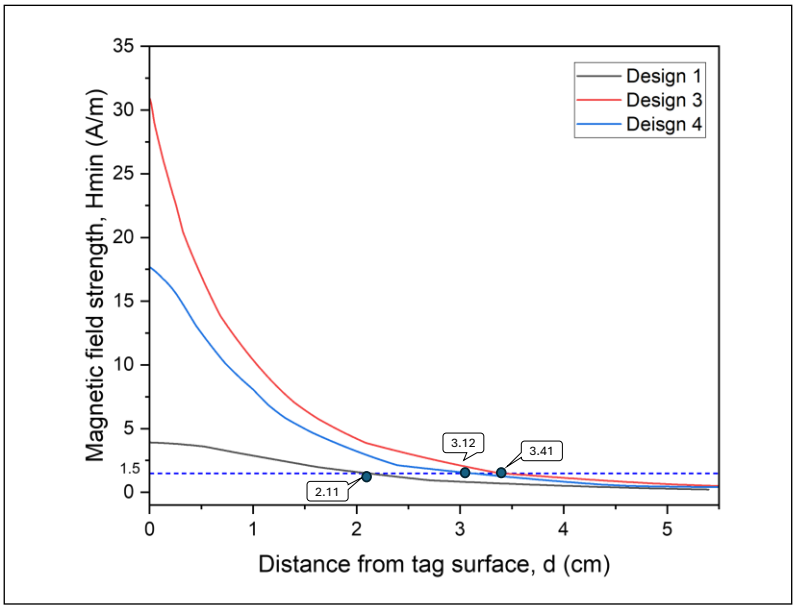
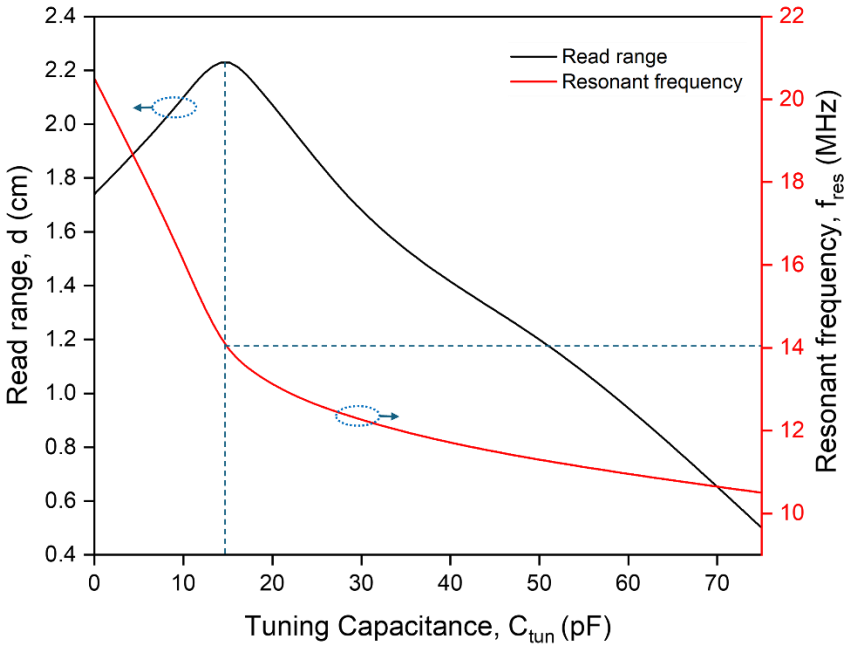


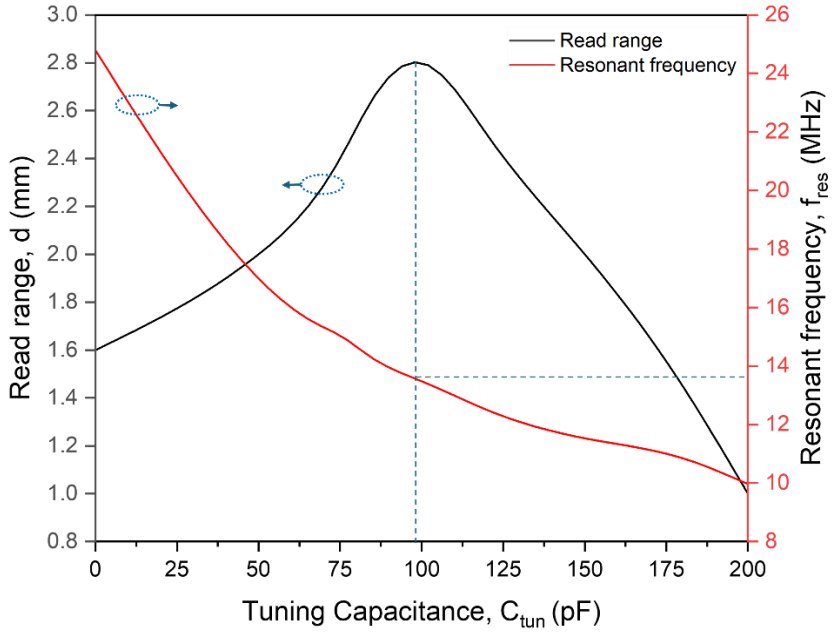
Figure 4.32 Simulation of Reading Range for All Antenna Designs

The tag reading range was also measured for all antenna designs to verify the simulation results. From Figure 4.33, it can be observed that the highest reading range was achieved by D4-HGS (Figure 4.33 (c)) at approximately 3.0 cm, followed by D3-HGS (Figure 4.33 (b)) at 2.8 cm, and lastly D1-HGS (Figure 4.33 (a)) at approximately 2.2 cm. The measured results aligned with the simulation, with percentage differences of 3.8%, 17.9%, and 4.1% for D4-HGS, D3-HGS, and D1-HGS, respectively. The higher percentage difference for D3-HGS is probably due to the higher resistance in the measured tag antenna compared to the simulation, as presented in Table 4.9, which

results in more power being lost as heat rather than generating a magnetic field, thereby reducing the reading range. The trend for antenna resonant frequency, f_{res}, is also similar for all antenna designs, where the frequency shifts to a lower value as the tuning capacitance increase, aligning with Equation (2.21). It can be observed that the tag reading range is maximized when f_{res} is close to the operating frequency of 13.56 MHz, which falls within the range of 12 MHz – 14 MHz.


Read range
Resonant frequency
Read range, d (cm)
Resonant frequency, f_{res} (MHz)
Tuning Capacitance, C_{tun} (pF)

(a)


Read range
Resonant frequency
Read range, d (mm)
Resonant frequency, f_{res} (MHz)
Tuning Capacitance, C_{tun} (pF)

(b)

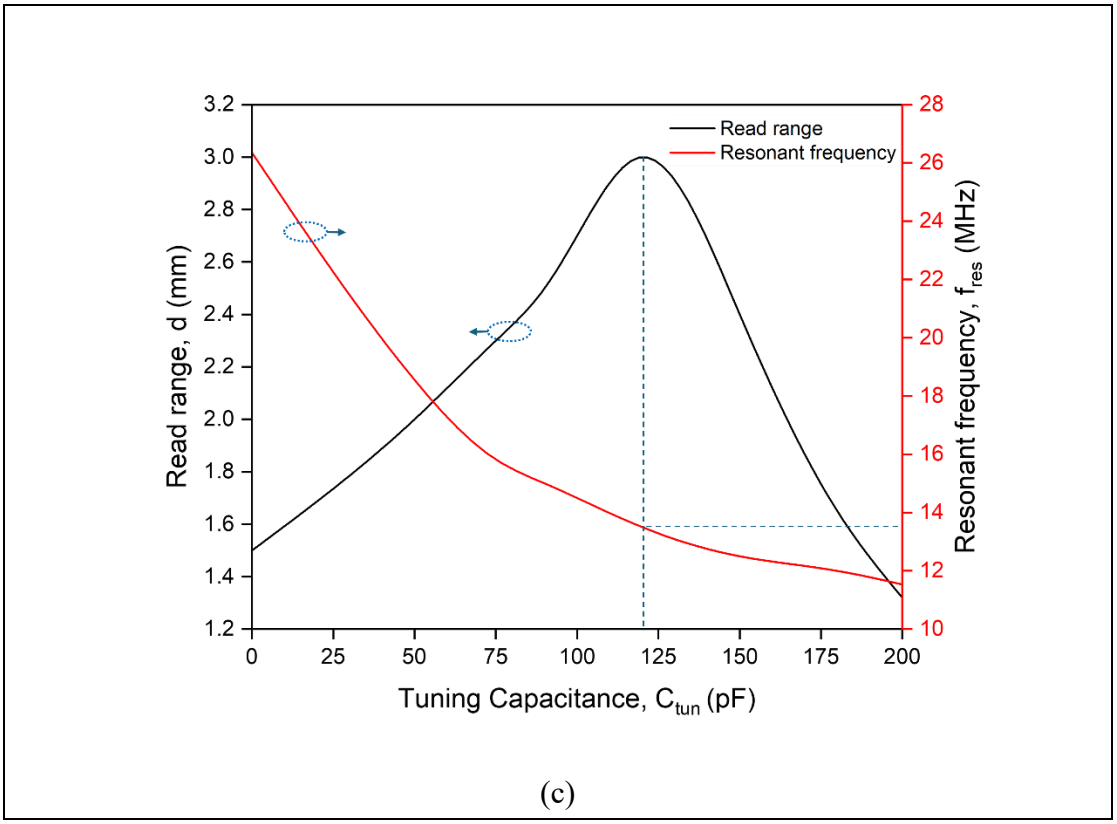


Figure 4.33 Measured Tag Reading Range Along with the Corresponding f_{res} and C_{tun} Values for (a) D1-HGS, (b) D3-HGS and (c) D4-HGS Tag Antenna

The overall results for D1-HGS, D3-HGS, and D4-HGS are summarized in Table 4.11. Based on these results, it can be concluded that the D4-HGS antenna is the optimal design to be used for temperature monitoring in food packaging applications due to its compact size, extended reading range, and lower design complexity. D4-HGS achieves the lowest resistance (36.16 Ω) and highest measured Q-factor (1.35) due to its wider traces (w = 3.0 mm) and fewer turns (n = 4), compensating for the thin printed HGS film. A higher Q-factor enhances the antenna's ability to efficiently store and transfer energy at the desired operating frequency of 13.56 MHz. Furthermore, D4-HGS achieves the longest reading range (3.0 cm) due to its optimized resistance and Q-factor, ensuring maximum magnetic field strength and coupling efficiency. These findings confirm the feasibility of HGS material for compact, high-performance NFC tag application when paired with geometry optimization.

Table 4.11
Summary Results for D1-HGS, D3-HGS, and D4-HGS Antennas

Parameter	D1-HGS	D3-HGS	D4-HGS
Size	50 x 50 cm2	50 x 50 cm2	50 x 40 cm2
Antenna Resistance (Ω)	210.4 Ω (Highest)	91.88 Ω (Moderate)	36.16 Ω (Lowest)
Antenna Inductance (μH)	2.51 μH (Highest)	1.06 μH (Moderate)	0.85 μH (Lowest)
Q-Factor	0.71 (Lowest)	1.0 (Moderate)	1.35 (Highest)
Power Transfer Efficiency	~32% (Lowest)	~50% (High)	~48% (High)
Measured Reading Range (cm)	2.2 cm (Shortest)	2.8 cm (Moderate)	3.0 cm (Longest)
Bandwidth	Broadest (Lower Q -factor)	Narrower (Higher Q -factor)	Narrowest (Highest Q -factor)
Design Complexity	Highest (Narrower width, 6 turns)	Moderate (Wider width, 6 turns)	Lowest (Wider width, 4 turns)

4.3.3 Hybrid Carbon-Graphene (HCG) NFC Tag Antenna

The conductivity of HCG material is the lowest among the other proposed conductive materials, with the conductivity value of 5.84×10^2 S/m, as summarized previously in Table 4.4 in Section 4.2. With this lower conductivity value, it is expected that the tag antenna using this conductive material will exhibit high resistance. Therefore, a coil antenna design with a wide width is required to ensure that the resistance is sufficiently small to minimize power losses and improve the antenna's efficiency.

4.3.3.1 Verification of Printed HCG-based Antenna

For comparison purposes with HGS material, the HCG conductive material has been printed on the optimal design achieved while using HGS material, which is Design

4, denoted as D4-HCG. Figure 4.34 (a) shows the prototype for the D4-HCG tag antenna, printed using the screen printing method as described in Section 3.5.4.2 of Chapter 3. A similar verification process was conducted for the printed SC-based and HGS-based coil antennas to ensure that all the printed lines were well connected and stable. The resistance for each line, labelled as line 1 through line 16, as illustrated in Figure 4.34 (b), was measured and statistically analyzed.

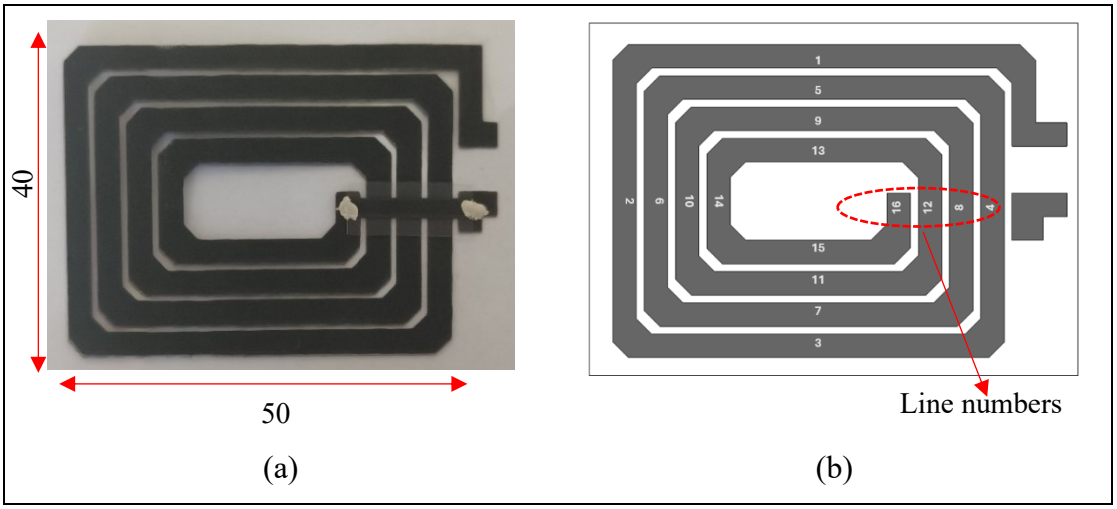


Figure 4.34 D4-HCG Tag Antenna's (a) Prototype and (b) Labelled Line Numbers Used for Resistance Measurement

Figure 4.35 shows the results of the analysis for the verification of line continuity for the printed coil design of the D4-HCG antenna. The resistance measurements reveal a mean value of 533 Ω with an STD of 182.63 Ω, indicating significant variability across the 16 lines. Most resistance values fall within the range of (533 ± 182.63) Ω, or 356.16 Ω to 709.84 Ω, but substantial deviations are observed, particularly at Lines 1 and 14, with resistance values of 905 Ω and 247 Ω, respectively. However, with an average resistance of 533 Ω, the printed lines of the D4-HCG coil design far exceed the acceptable range for functional conductive lines, which is typically less than 50 Ω [164]. Higher resistance leads to increased energy losses, reducing the efficiency of the tag antenna and its ability to transfer power to the NFC chip. Therefore, based on these verification results, it can be concluded that the HCG conductive material is not suitable for NFC applications due to the significantly high resistance of the coil antenna, which prevents the antenna from functioning properly.

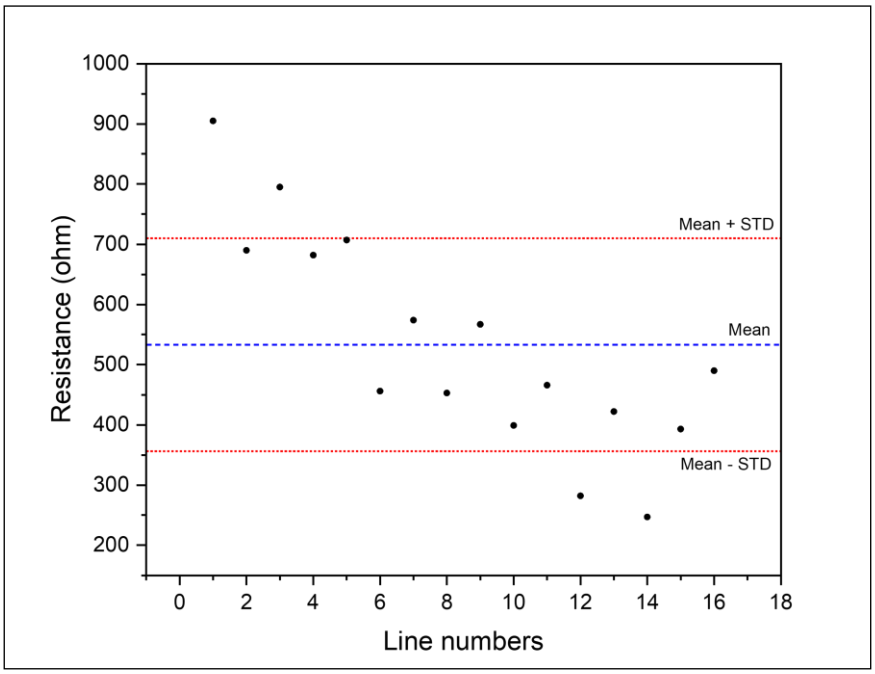


Figure 4.35 Measured Resistance Reading Across the 16 lines for D4-HCG Antenna

4.3.3.2 Simulation and Measurement Result Analysis

To further confirm the non-suitability of HCG material for NFC tag antenna applications, the electrical properties of the D4-HCG, including antenna inductance, L_a, and antenna resistance, R_a, were evaluated through both simulation and measurement. In the simulation, the properties of the HCG material, including a conductivity value of 5.84×10^2 S/m and the thickness of 33 µm, as described previously in Table 4.4 and Table 4.3, respectively, were used in the CST simulation software to simulate the D4-HCG. Figure 4.36 and Figure 4.37 illustrate the simulated L_a and R_a values, respectively, for D4-HCG antenna design across different frequencies. From the results, it can be seen that the R_a value is very high, reaching up to thousands of ohms. Meanwhile, the L_a value shows negative values, indicating that the antenna does not act as an inductor but as a capacitor. This behaviour will prevent the antenna from being inductively coupled with the reader, resulting in the non-detection of the tag. The high resistance of the antenna is due to the extremely low conductivity of the HCG material compared to other materials. According to [17], the suitable conductivity level for antenna modelling is characterized by a sheet resistance lower than 10 Ω/sq. A higher sheet resistance is incompatible with RF applications, where efficient signal transmission and minimal energy loss are crucial.

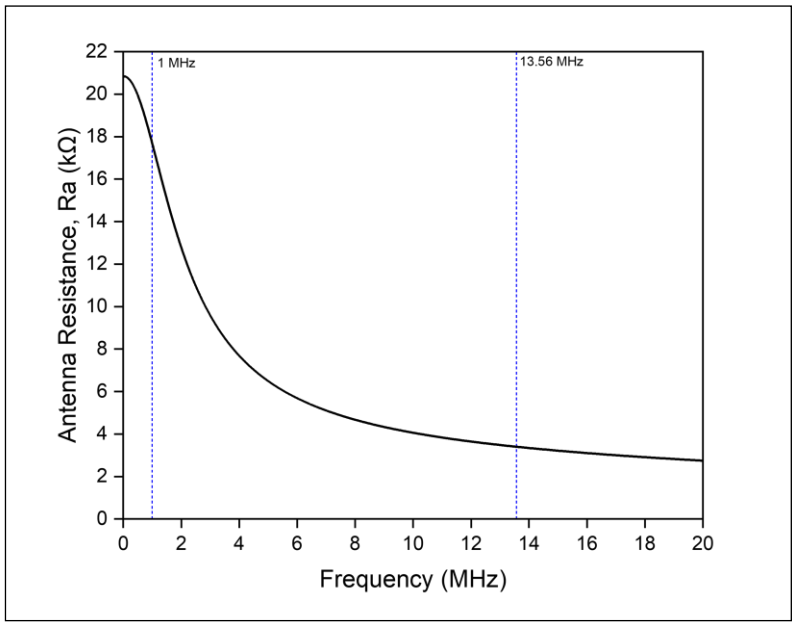


Figure 4.36 Simulated Antenna Resistance, R_a, for D4-HCG

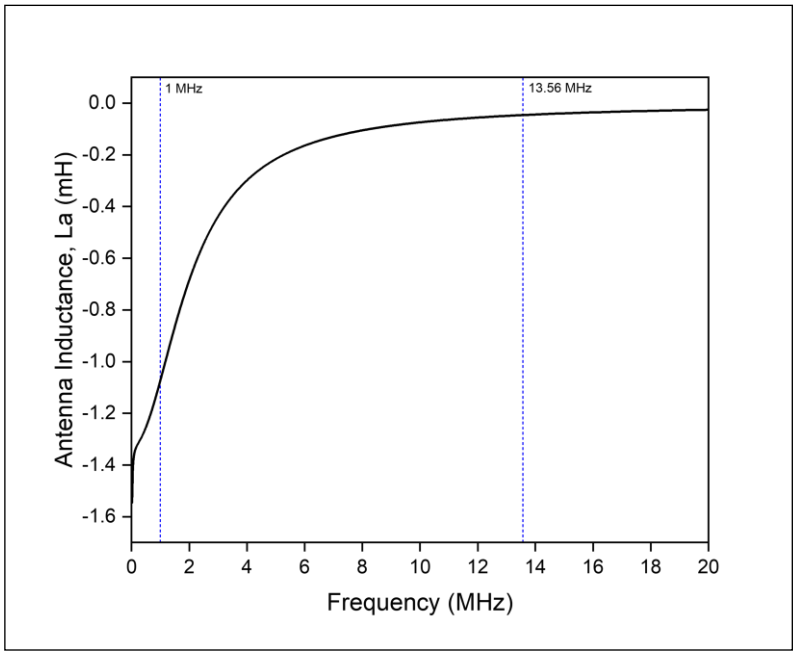


Figure 4.37 Simulated Antenna Inductance, L_a, for D4-HCG

To validate the simulation results, the L_a and R_a values were measured using a VNA, as discussed in Section 3.8.1 of Chapter 3. The measured results are presented in Table 4.12 and compared with the simulation results. From the results, it can be observed that the measured R_a agrees well with the simulation, indicating extremely high resistance. Meanwhile, both the simulated and measured L_a values exhibit negative values of inductance, which indicate that the coil antenna does not function as

an inductor, thus failing to achieve inductive coupling with the reader coil antenna. This failure contributes to the inability of the tag antenna to be detected by the NFC reader, including NFC-enabled smartphones, as no energy is transmitted from the reader to the tag to power the chip due to the unsuccessful coupling between the reader and the tag coil antenna.

Table 4.12
Simulated and Measured Results of L_a and R_a for D4-HGS Antenna

Parameter	Simulation	Measurement
Antenna Resistance, R_a (kΩ) @ 1 MHz	17.52	13.59
Antenna Inductance, L_a (mH) @ 1 MHz	-1.07	-0.49
Antenna Impedance, Z_a (kΩ) @ 13.56 MHz	3.4 – j3.93	5.75 - j2.79
Q-factor @ 13.56 MHz	-1.16	-0.49

4.3.4 Summary of Conductive Material Variation and Antenna Design

Overall, the conductive material and the geometrical parameters of the coil antenna are the primary factors influencing the performance of the NFC tag antenna. The characteristics of the conductive material, including conductivity and thickness, play a crucial role in determining the electrical properties of the antenna, particularly the antenna inductance, L_a and antenna resistance, R_a. These parameters directly affect the antenna's resonance behaviour and power transfer capability, which ultimately determine the achievable reading range.

The SC material serves as the reference material for evaluating the NFC tag antenna's performance, covering all stages from material characterization and printed coil antenna validation to performance analysis. Similar evaluation methods were applied to the HGS and HCG materials to assess their suitability for NFC tag antenna applications. The HGS conductive material was found to be compatible with NFC tag antenna applications, similar to the SC material. However, optimization of the antenna geometrical parameters is required to achieve optimal performance due to the relatively thin printable layer of HGS material. Meanwhile, the HCG material demonstrated undesirable performance for NFC tag applications due to its extremely low

conductivity, which falls outside the acceptable range for antenna modelling and NFC tag operation.

Table 4.13 summarizes the measured results for all antenna designs fabricated using different conductive materials and compares them with the design requirements defined in Table 3.1. The results indicate that most antenna designs fabricated using SC and HGS materials satisfy the required inductance range (300 nH $\leq L_a \leq$3.8 μH) and antenna resistance limit ($\leq$ 50 Ω), enabling successful tag detection with a reading range greater than the minimum requirement of 1 cm. From the comparison, the measured reading range of the optimized D4-HGS antenna is comparable to that of the D1-SC reference antenna, with both achieving a maximum reading range of up to approximately 3 cm. However, the D4-HGS antenna offers the advantage of a more compact size, achieving a 20% reduction in antenna area compared to D1, making it more suitable for applications where space constraints are critical, such as smart food packaging labels.

In comparison with the NFC tag antenna fabricated using multilayer graphene ink reported in [51], the proposed D4-HGS antenna achieves a longer reading range of approximately 0.5 cm, while simultaneously reducing the antenna size by approximately 44%. This demonstrates the effectiveness of the proposed antenna design and material combination.

In contrast, the D4-HCG antenna exhibits extremely low antenna inductance and excessively high antenna resistance, resulting in the failure of the tag antenna to be detected by the NFC reader. Therefore, only the tag antennas fabricated using SC and HGS materials were selected for further performance evaluation. Subsequent analyses focused on the HGS-based antenna, including flexibility testing, environmental sensitivity analysis, and robustness evaluation under different food packaging conditions, as discussed in the following sections.

Table 4.13
Summary of Measurement Results for D1-D4 Tag Antennas with Varying Conductive Materials

Parameter	Design Requirement	D1-SC	D2-SC	D1-HGS	D3-HGS	D4-HGS	D4-HCG
Antenna Inductance (μH)	300 nH ≤ L_a ≤3.8 μH	1.85	1.69	2.51	1.06	0.85	-0.49 x 10^{-3}
Antenna Resistance (Ω)	≤ 50 Ω	33.36	10.22	210.4	82.74	36.16	13.59 x 10^{6}
Read range (cm)	≥ 1 cm	3.3	2.2	2.2	2.8	3.0	0
Size (cm^2)	Ref design: 50 x 50 cm^2	50 x 50	40 x 30	50 x 50	50 x 50	50 x 40	50 x 40

4.4 Robustness Analysis of NFC Tag Antenna

The robustness of the NFC tag antenna has been analysed in terms of its performance under bending effects when attached to curved structures, as well as its sensitivity to various elements, including packaging materials, moisture, and temperature. It is crucial to ensure that the tag antenna remains detectable when attached to different packaging materials and structures, and during exposure to environmental factors such as temperature fluctuations and moisture.

4.4.1 Flexibility of NFC Tag Antenna

This section examines the impact of bending on NFC tag antennas made of SC and HGS conductive materials. D2-SC and D4-HGS antennas have been selected for analysing the bending effect on antenna performance, including resonant frequency, reading range, magnetic field distribution, and power transfer efficiency (PTE). The flexibility of the tag antenna has been assessed by varying the bending radius, ranging from 1.5 cm to 4.5 cm, which corresponds to bending angles of 190.9º to 63.7º, respectively.

The simulated results of the S_{11} for various bending radius are shown in Figure 4.38 (a) for the D2-SC and Figure 4.38 (b) for the D4-HGS antennas. The D2-SC shows a nearly constant resonant frequency across all bending radius, with only a slight

frequency shift of 0.23 MHz from the operating frequency observed at the smallest radius of 1.5 cm. This slight shift is due to the minimal decrease in antenna inductance, L_a, for the D2-SC, as depicted in Figure 4.39. Meanwhile, for the D4-HGS, there is a more noticeable upward shift in the resonant frequency, although it remains less than 1 MHz at the maximum bending angle (r = 1.5 cm). This is due to a more significant decrease in antenna inductance, L_a, which drops by up to 0.55 µH as the bending angle increases, as illustrated in Figure 4.39. The reduction in L_a is caused by deformation of the antenna structure, which alters the current distribution and reduces effective inductive coupling within the conductive traces. Despite the frequency shift, the resonant frequency for both antenna designs remains within the acceptable NFC tag operating range (13.56 MHz < f_{Tag} < 16 MHz) [111].

Additionally, under bending, the S_{11} curve of the D4-HGS antenna becomes sharper and deeper, indicating a higher Q-factor in the bent state. This implies that the antenna stores energy more efficiently than it loses during resonance in a bending condition. The increase in Q-factor can be attributed to the wider conductor width of the D4-HGS design, which provides a larger surface area for current flow, reducing resistive losses and helping to maintain a more uniform current distribution even under mechanical deformation.

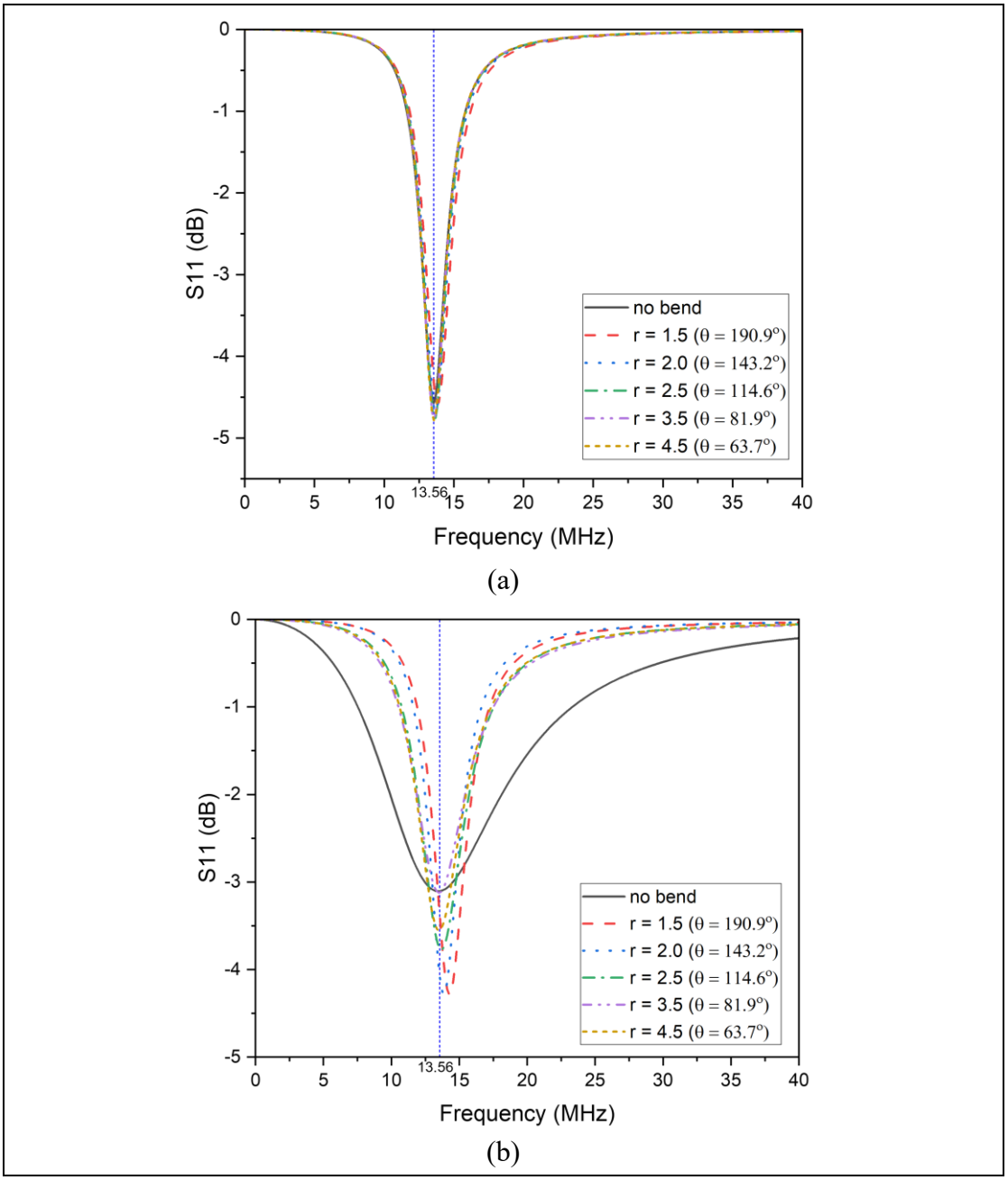


Figure 4.38 Simulation of S_{11} for (a) D2-SC (b) D4-HGS Antennas

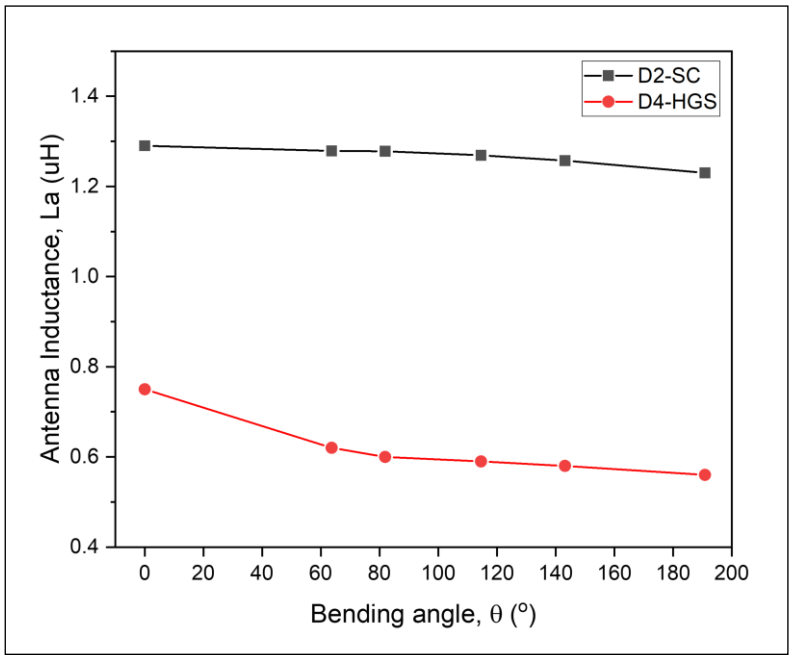


Figure 4.39 Antenna Inductance for (a) D2-SC (b) D4-HGS Antennas

However, bending may contribute to a decrease in coupling efficiency with the reader, as the magnetic field intensity is reduced with an increase in the bending angle, as shown in Figure 4.40 (a) and (b) for the D2-SC and D4-HGS antennas, respectively. The increase in bending angle results in an asymmetrical and non-uniform distribution of the magnetic field, caused by the distortion of the current flow and magnetic field patterns within the antenna structure. Observation of magnetic field intensity is essential to understand how the antenna radiates and couples energy, which directly influences the read range and reliability of the NFC tag [101].

The performance of the tag antenna under bending conditions has also been evaluated through the power transfer efficiency (PTE) between the reader and the bent tag, as depicted in Figure 4.41 (a), with a fixed distance of 1 cm between them. The reader used is the reference Design 1 antenna, made of copper and FR-4 substrate. As shown in Figure 4.41 (b), the PTE for the D2-SC antenna drops significantly from approximately 60% in the unbent condition to 40% at the smallest bending radius of 1.5 cm. This decline is due to the reduction in the effective area of the tag antenna caused by bending, which limits the magnetic field captured by the reader antenna. Consequently, the induced current and voltage are reduced, resulting in decreased PTE as less power is transferred from the NFC reader to the tag. A similar trend is observed for the D4-HGS antenna in Figure 4.411(c), where the PTE decreases from approximately 48% in the flat condition to 20% at the smallest bending radius. Since

PTE is generally correlated with the tag reading range, a similar decreasing trend in reading distance is expected with increased bending angle, and this has been validated through experimental measurements.

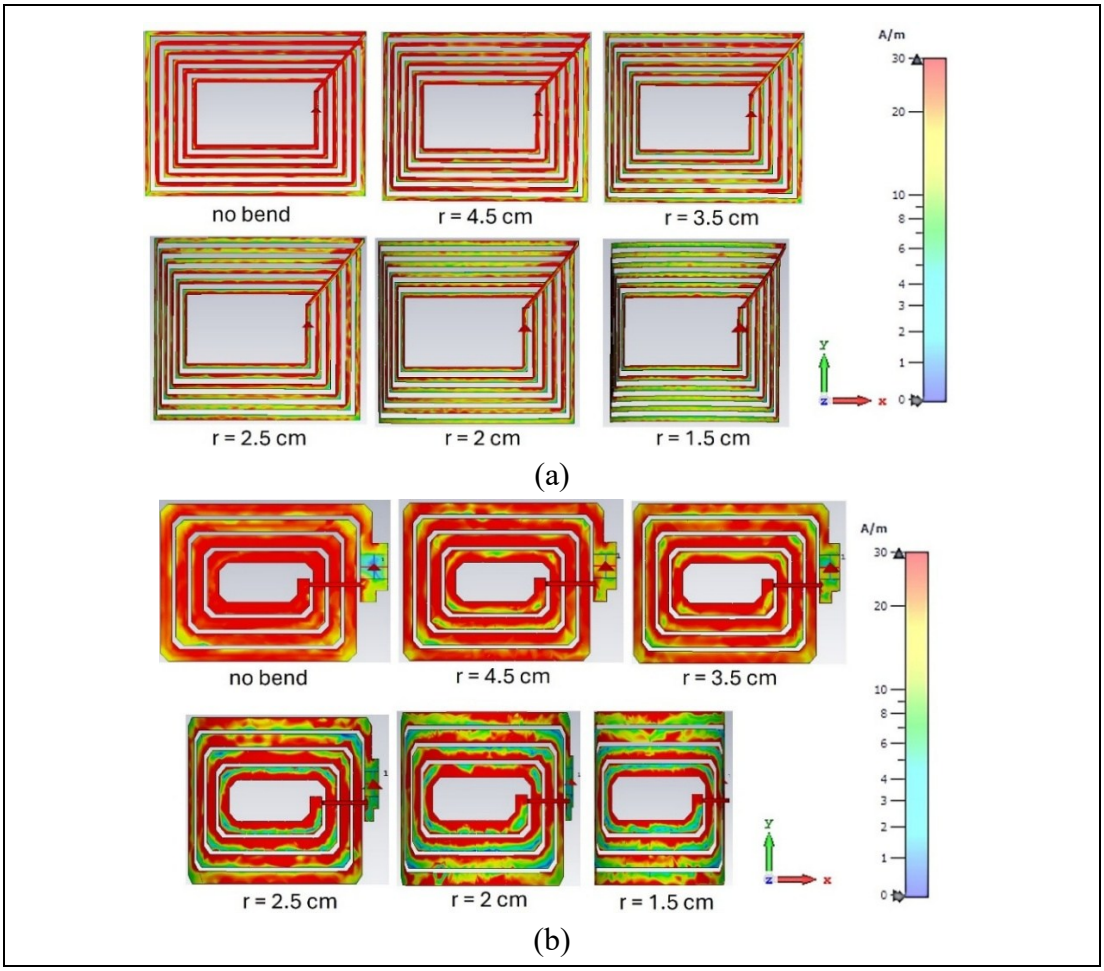


Figure 4.40 Simulation of Magnetic Field Distribution for (a) D2-SC and (b) D4-HGS During Bending

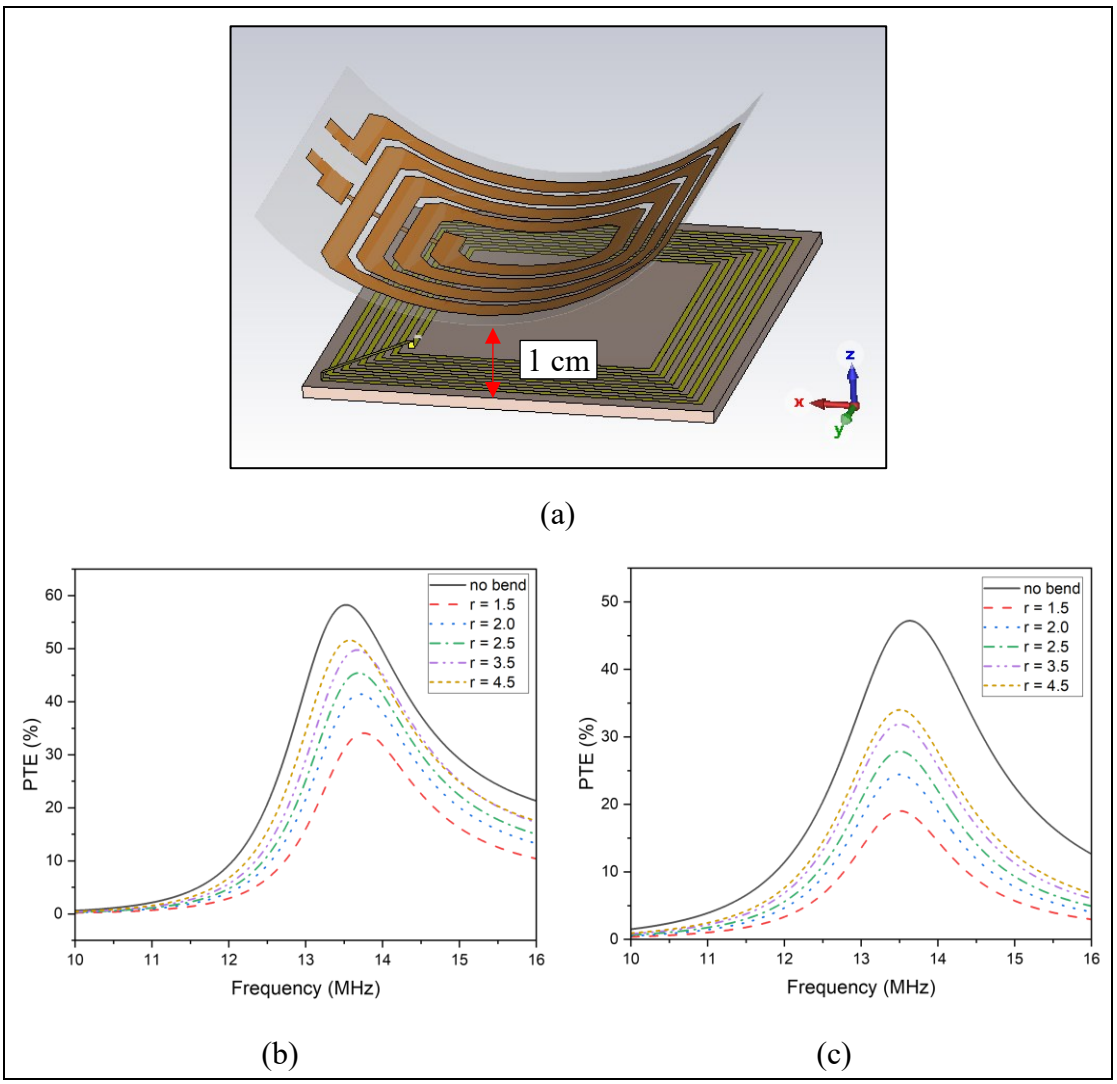


Figure 4.41 (a) Reader and Bending Tag During PTE Simulation and the Simulated PTE Results for (a) D2-SC and (b) D4-HGS Antennas

In the measurement, the tag antenna was attached to cylinders of different sizes made of foam, as depicted in Figure 4.42. The measurements were conducted using the setup described in Section 3.6.1 of Chapter 3. The shift in the antenna's resonant frequency from the operating frequency of 13.56 MHz was observed, and the tag reading range was measured and depicted in Figure 4.43 and Figure 4.44 for D2-SC and D4-HGS, respectively. From the measurement of the D2-SC tag antenna, it is observed that the antenna resonant frequency remains almost the same for different sizes of cylinder foams, which agrees well with the simulated result. However, the tag reading range decreases with a reduction in cylinder radius, as illustrated in Figure 4.43 (b). With the reduction of the cylinder radius from 4.5 cm to 1.5 cm, the tag reading range is reduced from 2 cm to 0.5 cm. The reduction in reading range is aligned with

the reduction in PTE observed from the simulation, as the PTE is proportional to the reading distance from which the reader can detect the tag.

Similar to the D4-HGS tag antenna, the antenna's resonant frequency remains relatively constant across various surface bending of cylinder foams, except for the cylinder foam with r = 1.5 cm (θ = 190.9º), which exhibits a slight frequency shift of approximately 1 MHz to a higher frequency, as depicted in Figure 4.44 (a). Although the resonant frequency is not significantly affected by bending, the tag's reading range decreases from 2.4 cm to 1.3 cm as the bending angle increases from 63.7º to 190.9º, corresponding to a reduction in cylinder radius from 4.5 cm to 1.5 cm, as shown in Figure 4.44 (b). This reduction occurs because a smaller cylinder radius results in a larger bending angle, reducing the antenna's accessible surface area for the reader. Since the surface area is directly proportional to the induced magnetic field, a smaller surface area leads to a lower magnetic field being induced in the tag antenna, thereby reducing the tag reading range. Despite the reduced reading range, it remains within the typical range for NFC communication, which is more than 1 cm. These results demonstrate that the D4-HGS tag antenna is robust for curved surfaces with a maximum angle of 190º, achieving a minimum detection range of 1.3 cm, which is longer than that of the D2-SC antenna.

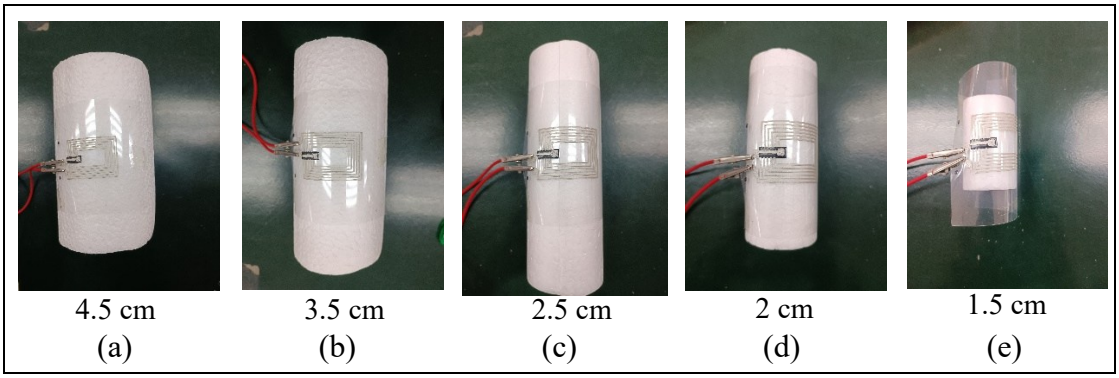


Figure 4.42 D2-SC Antenna Connected to VNA and Attached to Cylinder Foams with Different Radius: (a) 4.5 cm, (b) 3.5cm, (c) 2.5 cm, (d) 2 cm, and (e) 1.5 cm

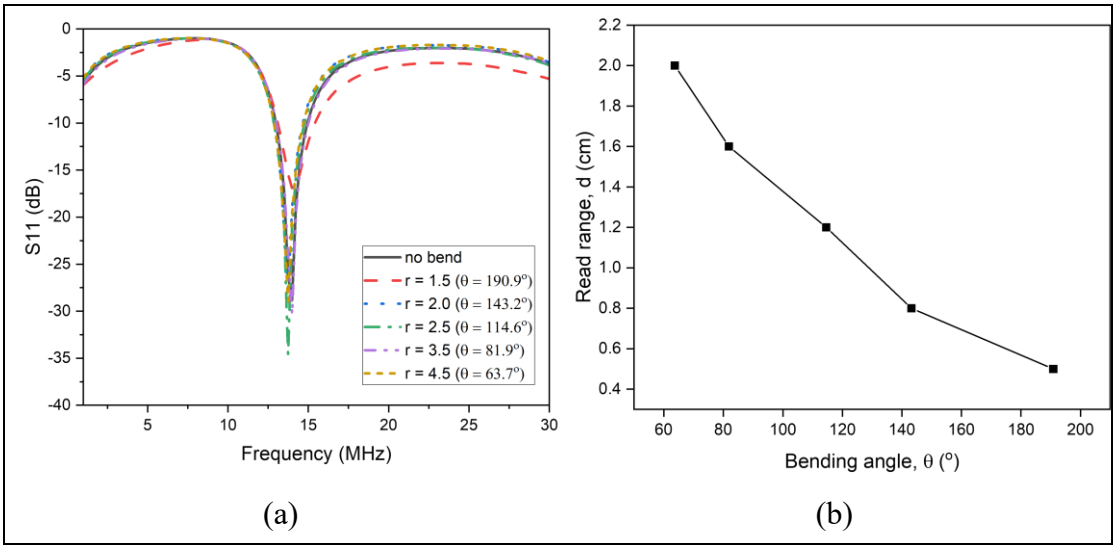


Figure 4.43 Measurement of D2-SC for (a) S_{11} and (b) Reading Range with the Variation of Cylinder Radius, r

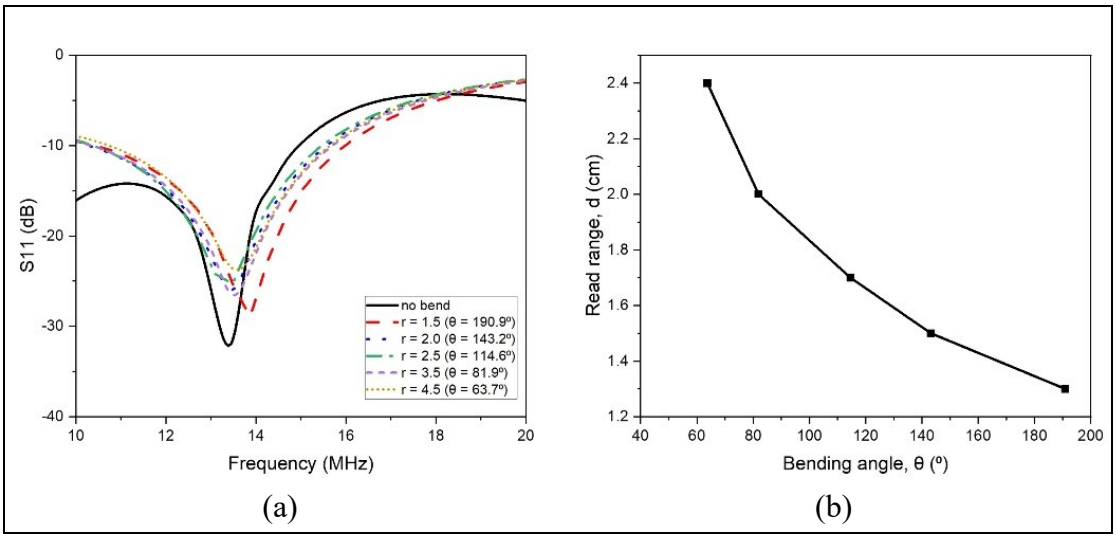


Figure 4.44 Measurement of D4-HGS for (a) S_{11} and (b) Reading Range with the Variation of Cylinder Radius, r

In summary, D2-SC and D4-HGS antennas exhibit stable resonant frequencies under various bending conditions, with frequency shifts remaining within the NFC operating range. Although bending reduces the read range for both designs due to distortion of the magnetic field and a reduction in the effective coupling area, the D4-HGS antenna outperforms the D2-SC, achieving a minimum detection distance of 1.3 cm at the highest bending angle, compared to only 0.5 cm for the D2-SC. This improved performance is attributed to the optimized geometry of the D4-HGS antenna, which includes a wider conductor trace that reduces resistive losses and maintains uniform current distribution under strain, as well as to the superior mechanical and electrical

properties of the HGS material. Unlike the pure SC, the hybrid HGS material combines the high conductivity of silver with the flexibility and mechanical robustness of graphene-based materials. As reported by MIMOS Berhad in [146], a single printed layer (1L) of HGS exhibited a relative resistance change (ΔR) of less than 15% after 5000 bending cycles, with no microcracks detected, indicating strong durability under mechanical strain. This strain tolerance ensures consistent antenna performance during repeated flexing or handling. In contrast, as reported in [24], the pure SC material showed an increase in relative resistance of up to 70% after just 100 bending cycles, with microcracks observed as early as 100 cycles. Therefore, D4-HGS is selected as the final antenna design for subsequent sensitivity evaluation (across various packaging materials, temperature, and moisture conditions), due to its enhanced flexibility, mechanical robustness, and consistent performance under bending, which are essential qualities for reliable NFC-based monitoring applications.

4.4.2 Sensitivity of NFC Tag Antenna

This section examines the sensitivity effects of the NFC tag antenna made of HGS conductive materials when attached to various packaging materials, including plastic, carton box, glass, and metal. Additionally, the sensitivity of the tag to moisture and various storage temperatures has also been investigated and analysed. The D4-HGS tag antenna has been selected for analysing the sensitivity effects on antenna performance, specifically in terms of resonant frequency and reading range.

4.4.2.1 Various Packaging Materials

Table 4.14 shows the electrical properties of each type of commonly used packaging material [196]. It can be observed that the electrical permittivity of carton boxes, plastics such as Polyethylene Terephthalate (PET), and glass falls within the range of 1.7 to 4.8. Meanwhile, aluminium foil has a very high or essentially infinite electrical permittivity as it is a metallic conductor and highly conductive. Figure 4.45 shows the simulated S_{11} result of D4-HGS tag antennas when mounted on different types of packaging materials. From the S_{11} graph, it can be observed that the non-conductive materials, including carton box, PET, and glass, did not significantly impact the resonant frequency of the tag antenna. Only a slight frequency shift of

approximately 0.5 MHz can be observed compared to the tag antenna in free space. However, conductive materials, such as aluminium, significantly shift the antenna resonant frequency by approximately 12 MHz to a higher value. This occurs due to the capacitive coupling that develops between the antenna and the aluminium when they are in close proximity. This capacitive coupling alters the effective inductance and capacitance of the antenna, causing the antenna impedance to become more capacitive and resulting in a shift of the resonant frequency to a higher value.

Table 4.14
Electrical Properties of Various Packaging Materials

Packaging Materials	**Electrical Permittivity (Tan Loss)**	**Conductive**
Carton box	1.78 (0.025)	Non-conductive
Plastic (PET)	3.2 (0.0071)	Non-conductive
Glass (Pyrex)	4.82 (0.0006)	Non-conductive
Aluminium foil	infinite	Highly conductive

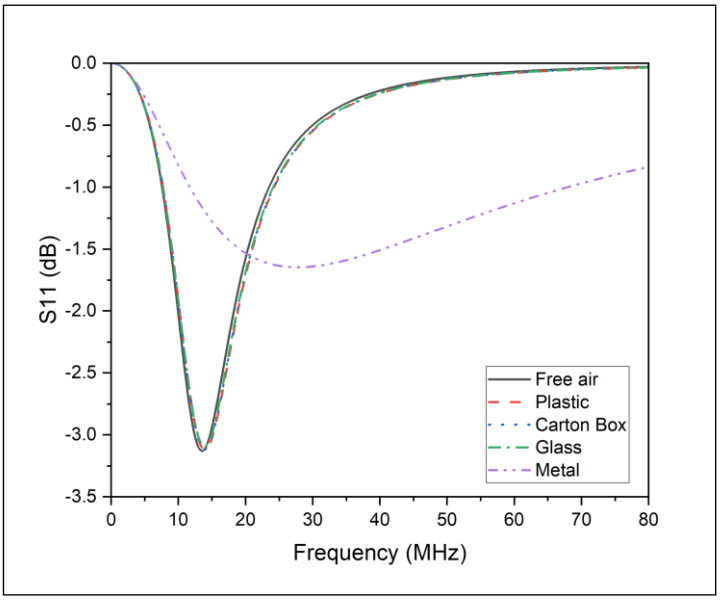


Figure 4.45 Simulation S_{11} for D4-HGS Attached on Different Packaging Materials

The shift of the resonant frequency to a higher value when attached to a metallic surface is aligned with the reduction of the antenna inductance, L_a, as shown in Figure 4.46. From the graph, it can be seen that the L_a is approaching 0 µH when the tag

antenna is attached to the metallic surface. This is due to the induced eddy currents on the metallic surface, which oppose the magnetic field generated by the antenna. These eddy currents disrupt the inductive coupling and significantly reduce the antenna's inductance [197]. Consequently, the resonant frequency increases, and the antenna performance is degraded, making it challenging to maintain proper power transfer efficiency. In contrast, non-metallic surfaces such as plastic, carton box, and glass did not support the formation of eddy currents, due to their non-conductive behaviour, allowing the antenna inductance to remain stable and close to the value in free air.

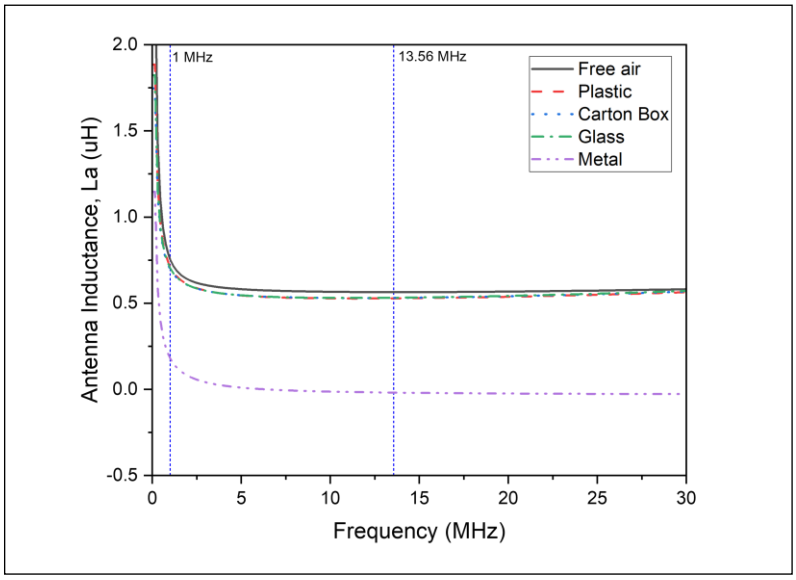


Figure 4.46 Simulated L_a for D4-HGS Attached on Different Packaging Materials

Figure 4.47 shows the simulated tag reading range of the D4-HGS antenna when attached to various materials. Non-conductive materials such as plastic, carton box, and glass exhibit a reading range between 3 and 3.7 cm at a magnetic field strength of 1.5 A/m, which is the minimum threshold required to activate the NFC tag [198]. In contrast, conductive materials like aluminium foil show significantly lower magnetic field strengths compared to other materials, falling below the minimum threshold required to activate the NFC tag. This results in poor coupling efficiency and failed tag detection.

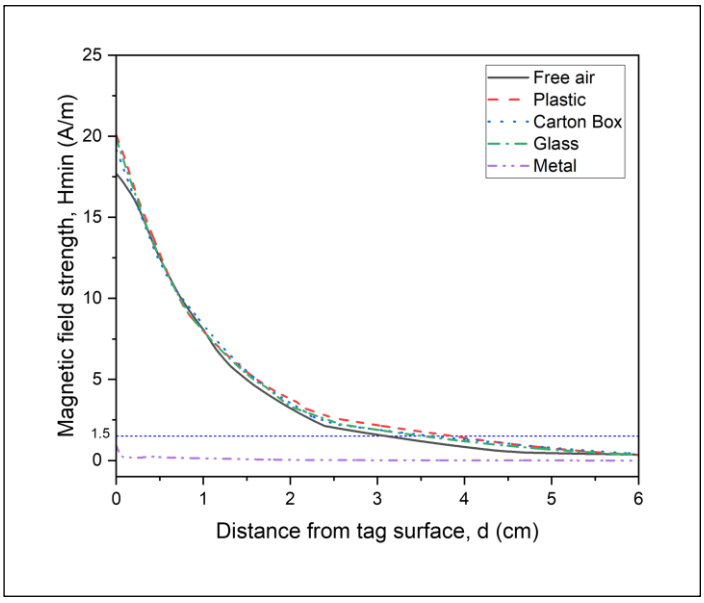


Figure 4.47 Simulated Tag Reading Range for D4-HGS Attached to Different Packaging Materials

To validate the simulated result, the resonant frequency of D4-HGS tag antennas when attached to various packaging materials, as depicted in Figure 4.48, was measured. From the measured S_{11} result illustrated in Figure 4.49, it can be observed that the antenna's resonant frequency is not significantly affected by non-conductive packaging materials, such as carton boxes, PET, and glass, which agrees well with the simulation results. However, the measured S_{11} shows a significant shift in resonant frequency to a higher frequency when the tag was attached to conductive materials such as metal plate due to the developed capacitive coupling between the antenna and the metal plate. This capacitive coupling alters the effective inductance and capacitance of the antenna, causing the antenna impedance to become more capacitive and resulting in a shift of the resonant frequency to a higher value. This measured result agrees well with the simulation results.

The tag reading range has also been measured, showing a constant reading range of 3 cm for the tag antenna attached to all non-conductive packaging materials. In contrast, the tag attached to conductive packaging materials fails to be detected by the reader due to the presence of eddy currents. To mitigate the influence of eddy currents on the tag antenna, an effective magnetic sheet has been proposed for attachment to the back of the tag antenna and is further discussed in Section 4.4.3.

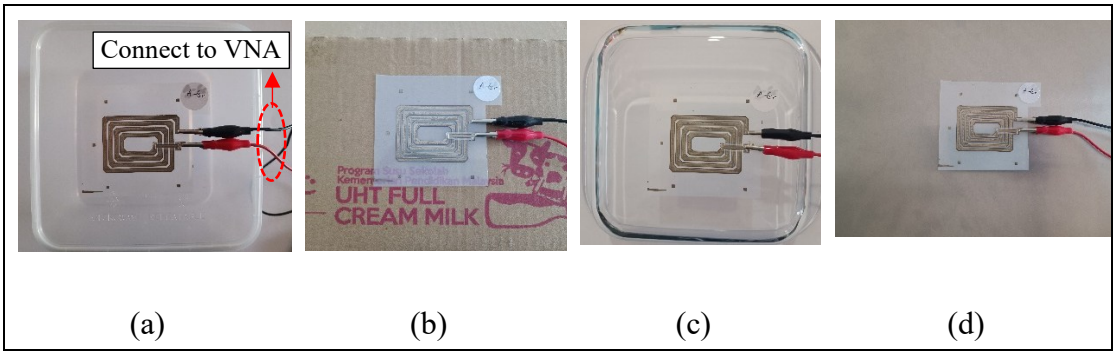


Figure 4.48 D4-HGS Antenna Attached on Different Packaging Materials: (a) Plastic (b) Carton Box (c) Glass and (d) Metal

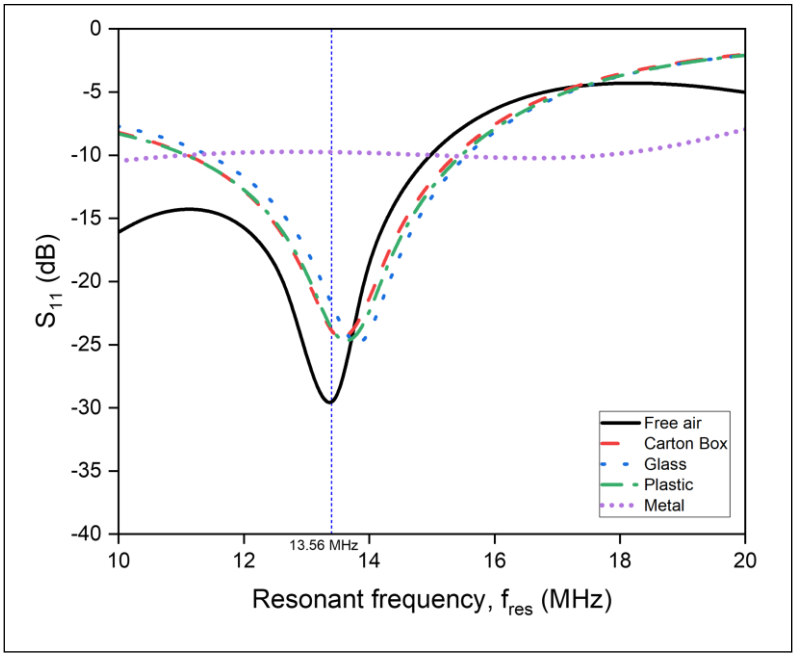


Figure 4.49 Measurement S_{11} for D4-HGS Attached on Different Packaging Materials

4.4.2.2 Moisture

The sensitivity of the NFC tag to a moist environment was investigated and analysed to observe the robustness of the tag antenna. It is important to ensure that the antenna maintains reliable performance when exposed to moisture, as this condition may occur during transportation or storage, particularly inside a refrigerator, where condensation can form. The performance of the Design 4 tag antennas, made of HGS materials, was observed in a dry and wet environment as depicted in Figure 4.50.

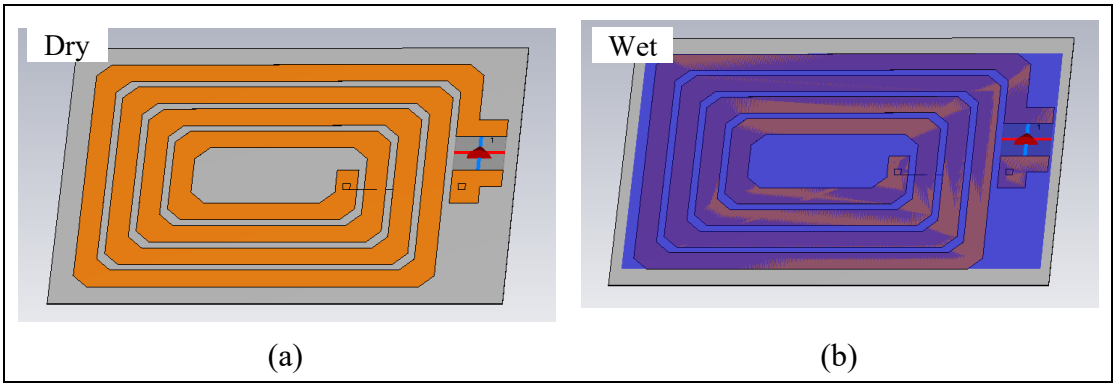


Figure 4.50 D4-HGS Tag Antenna in (a) Dry and (b) Wet Conditions

The results, illustrated in Figure 4.51 (a), demonstrated a shift in frequency to higher values when the tag was in contact with the water layers. Further analysis revealed that when water with a conductivity of 1.59 S/m is present, there is a risk of short-circuiting for the antenna. Such short circuits can create low-resistance paths that connect parts of the antenna, causing changes in its electrical properties, including its inductance (as shown in Figure 4.51 (b)). The antenna inductance is significantly reduced in the wet condition as compared to the dry condition, which undoubtedly affects the inductive coupling of the antenna. The tag reading range observed from the magnetic field strength curve in Figure 4.52 shows a significant reduction of approximately 68% when the tag is exposed to moisture as compared to the dry condition. At 1.5 m/A, the maximum tag reading range achieved is 3.12 cm and 0.7 cm for dry and wet conditions, respectively. This is because water can interfere with the electromagnetic field generated by the NFC tag antenna, which can attenuate the signal and reduce the tag reading range between the tag and the reader.

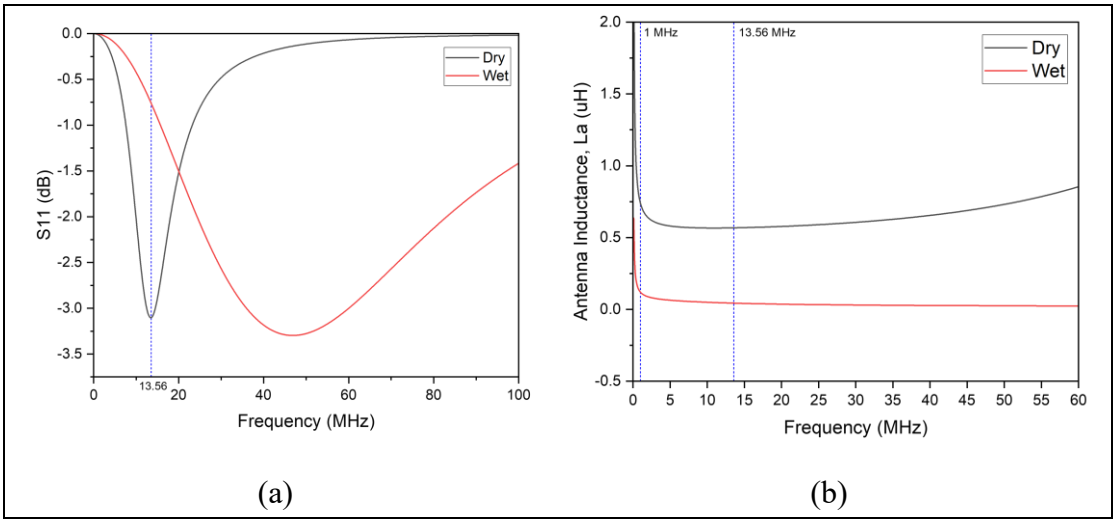


Figure 4.51 The Simulation Results of (a) S_{11} and (b) Antenna Inductance in Dry and Wet Conditions of the D4-HGS Antenna

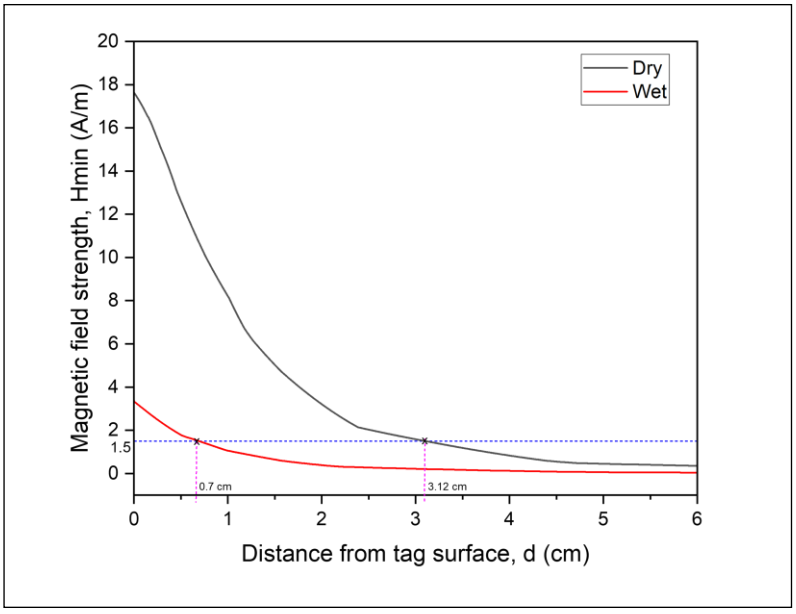


Figure 4.52 The Simulated Tag Reading Range for D4-HGS in Dry and Wet Conditions

The amount of the water layer was also varied to evaluate its influence on the performance of the tag antenna. The water content was varied from 25%, 50%, 80%, and 100% (fully moist), as described in Section 3.6.2. Figure 4.53 (a) shows the change in antenna inductance as the amount of water was varied. It is evident that the larger the amount of water, the lower the antenna inductance, with the inductance of the fully water-covered antenna significantly decreasing by approximately 0.7 µH at a low frequency of 1 MHz compared to the dry antenna.

This decrease might be due to the diamagnetic properties of water, which interact with the magnetic field generated by the NFC tag antenna [199]. The high dielectric constant ($\varepsilon_r \approx 80$) and the slight conductivity of the water layer acts as a lossy dielectric medium, leading to energy dissipation and reducing the antenna's ability to maintain its inductive properties. As the amount of water increases from one size to another, the antenna inductance decreases by 0.1 µH to 0.2 µH.

Furthermore, the capacitive coupling effect between the antenna and the water layer becomes more prominent as the water content increases. This results in detuning of the antenna's resonant frequency, shifting it away from the desired 13.56 MHz operating frequency as depicted in Figure 4.53 (b), which is critical for NFC operation.

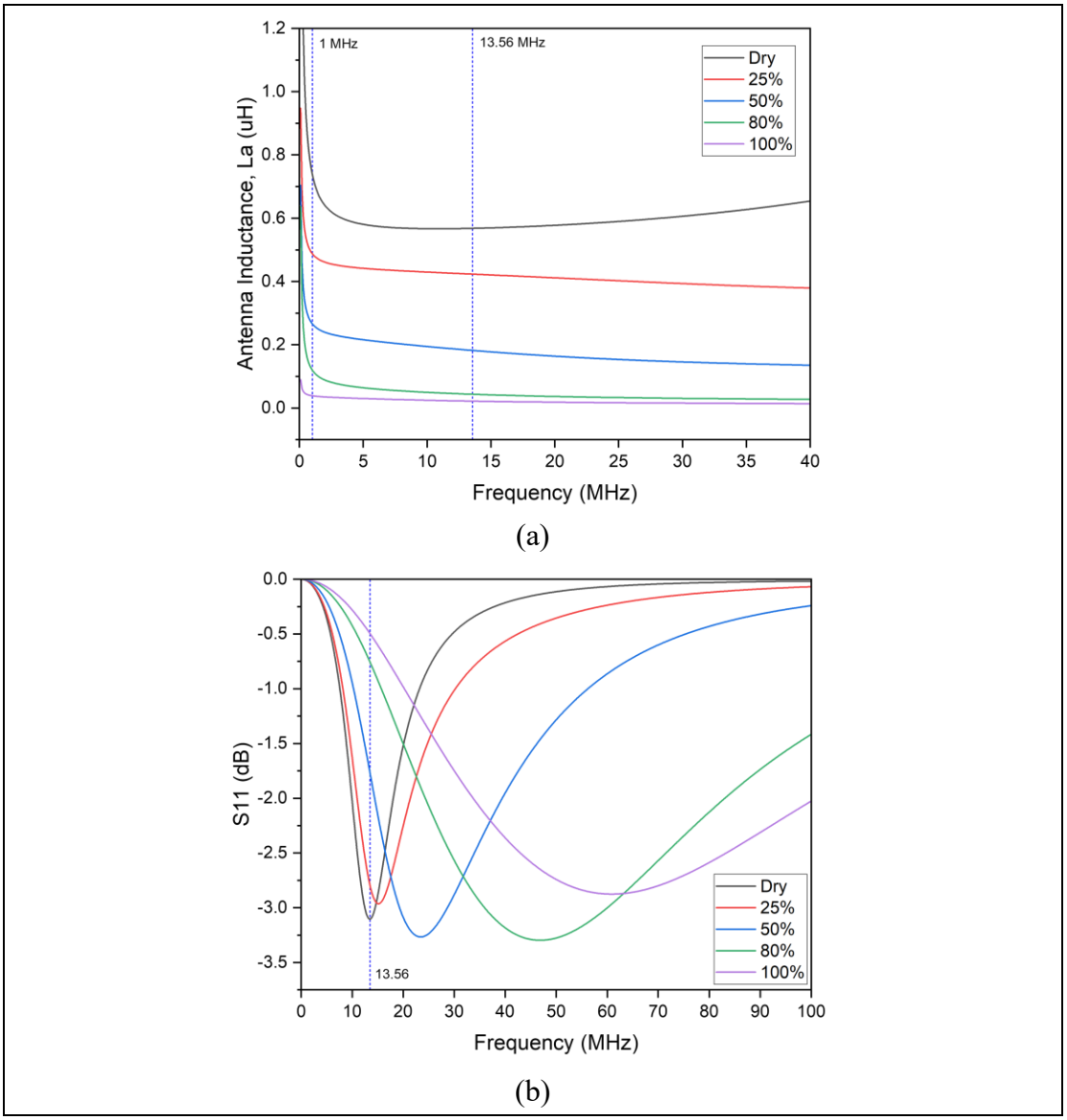


Figure 4.53 The Simulation Results of (a) Antenna Inductance and (b) S_{11} for D4-HGS with Variation of Water Content

Similarly, the tag reading range shown in Figure 4.54 is significantly reduced when the tag antenna is fully covered with water, with the reading range decreasing to 0.7 cm, representing approximately a 78% reduction compared to the tag antenna in dry conditions. When the tag antenna is partially covered with water at 25%, 50% and 80% coverage, the tag reading range at a magnetic field strength of 1.5 A/m is 2.7 cm, 2.0 cm, and 1.2 cm, respectively. The variation in reading range could be due to changes in antenna inductance, which affects the impedance matching of the antenna and the power transfer efficiency between the reader and the tag. Reduced power transfer efficiency affects the tag's ability to receive sufficient power from the reader, thereby decreasing the tag's reading range.

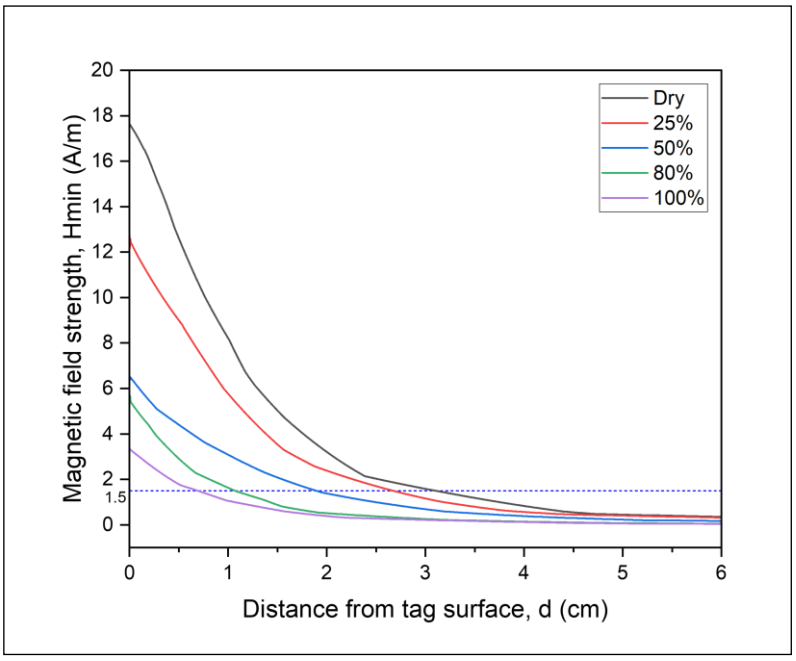


Figure 4.54 The Simulated Tag Reading Range for D4-HGS with Variation of Water Content

Therefore, to overcome this problem, an additional layer of PET was introduced between the antenna's conductive element and the water layer as illustrated in Figure 4.55 (a). This PET layer serves as an insulator, preventing any electrical contact or short-circuiting between the antenna and the water layer. Figure 4.55 (b) displays the S_{11} results for both dry and wet conditions of the antenna with the PET layer. Notably, the resonant frequency in both dry and wet conditions is almost the same, resonating at the operating frequency of 13.56 MHz, with only a slight variation in the S_{11} values of around 1 dB. This observation suggests that the NFC tag antenna, with the PET insulator layer added, maintains its robust performance in the presence of moisture or water, and the insulating PET layer effectively mitigates the risk of short-circuiting.

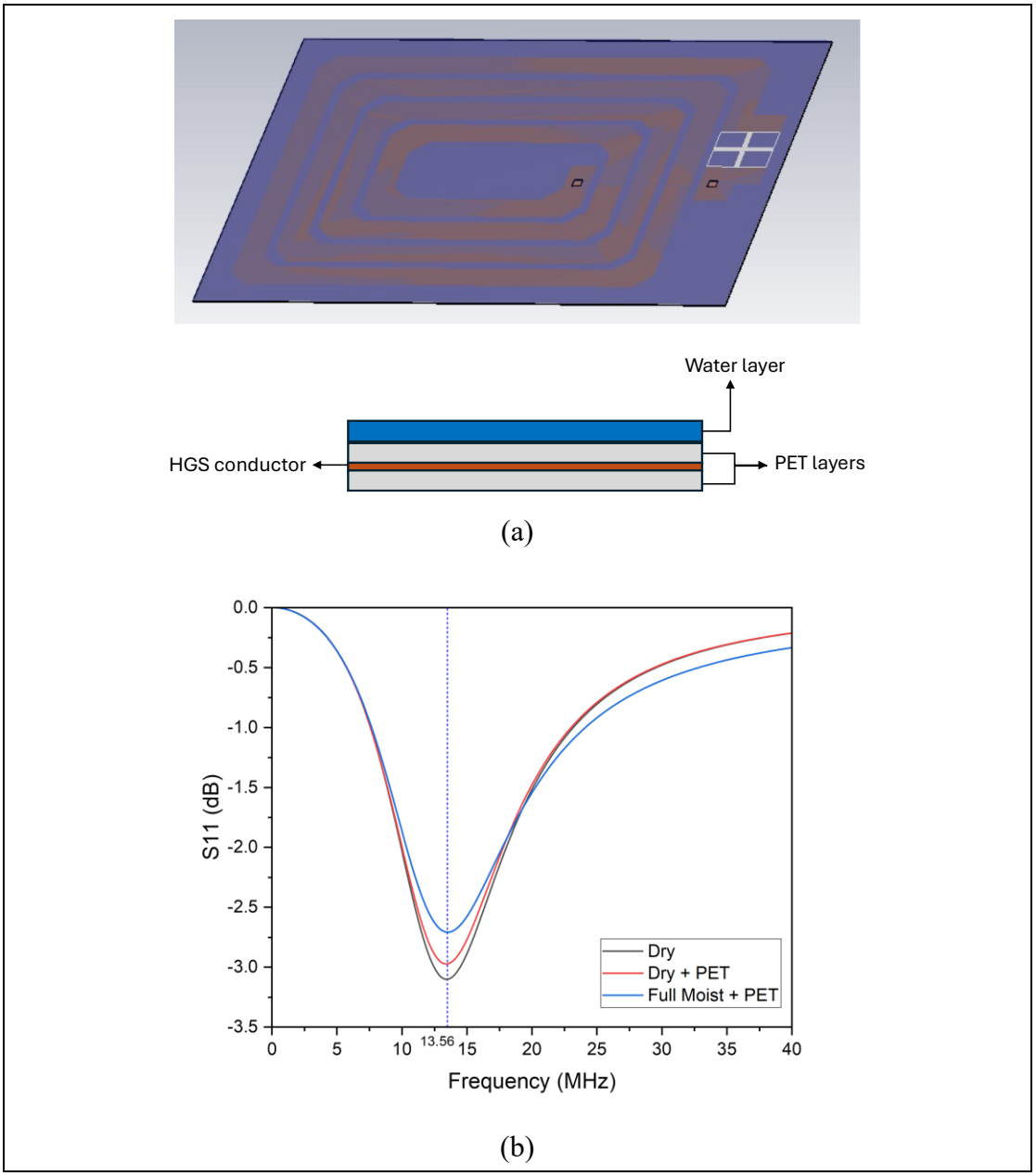


Figure 4.55 (a) Top View and Side View of the PET Layer Introduced Between the Water Layer and Conductive Element (b) S11 Result of Dry and Wet Conditions of The Tag Antenna with the Existence of the PET Layer

The performance of the antenna under both wet and dry conditions with the presence of a PET layer has also been assessed, focusing on antenna inductance and read range. In Figure 4.56 (a), a slight decrease in antenna inductance is observed for the wet condition with the PET layer, approximately 0.2 µH, compared to the dry condition at a low frequency of 1 MHz. This result shows a significant improvement compared to the tag antenna directly exposed to the water layer, where the introduction of a PET layer between the antenna and the water layer minimizes the reduction in

antenna inductance. Furthermore, the maximum tag reading range for wet conditions with the PET layer, as depicted in Figure 4.56 (b), was observed at 2.64 cm, which is approximately 0.5 cm lower than the reading range in dry conditions. The PET insulating layer effectively reduces the impact of water on the antenna's magnetic field distribution. As a result, the reduction in power transfer efficiency is minimized, ensuring that the tag remains functional, though with a slightly reduced reading range.

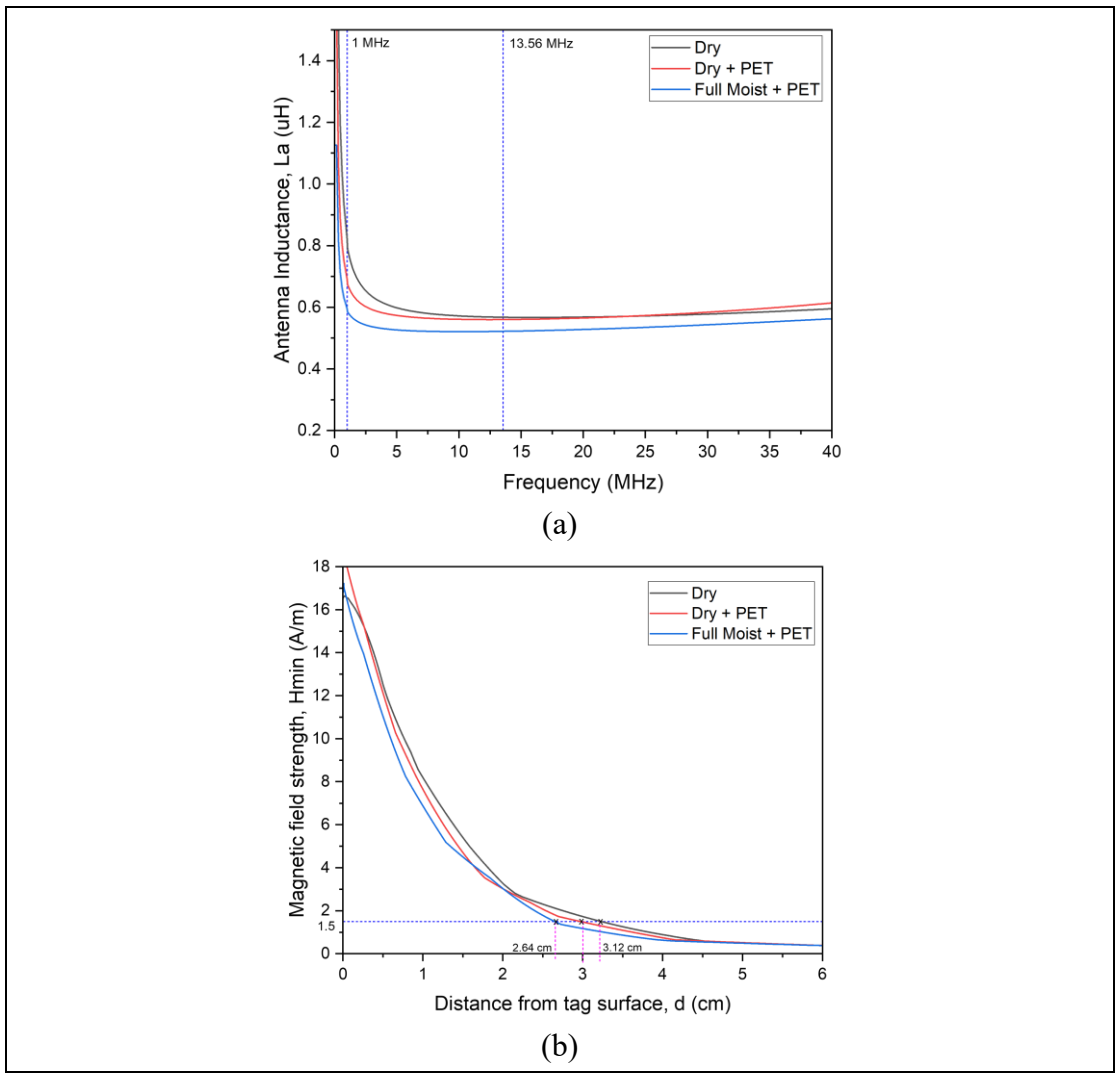
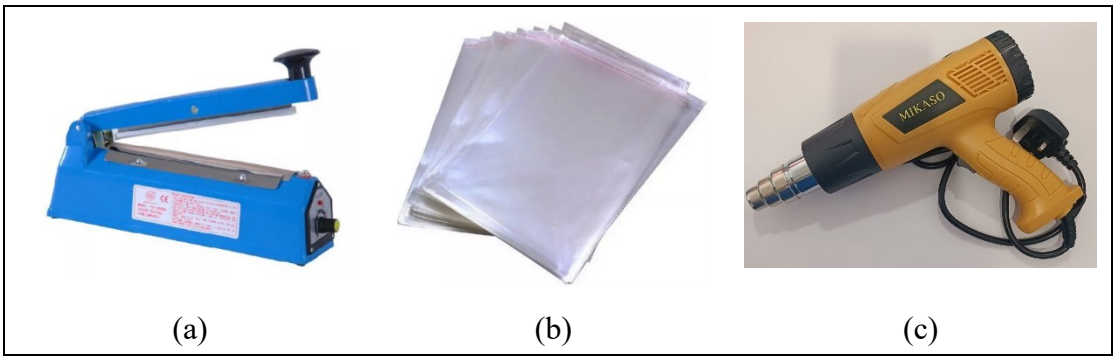


Figure 4.56 Simulation of (a) L_a and (b) Reading Range for Dry and Wet Condition

To validate the simulation results, an antenna prototype with an insulator layer has been fabricated using PET shrink wrap, an impulse sealer, and a blower, as depicted in Figure 4.57. This method, adapted from food packaging techniques used to protect food from damage or dirt, was employed to seal the tag antenna. The tag antenna, connected to the NXP Semiconductor chip (SL2S2102FTB) and capacitors, has been

encapsulated with a PET wrap, as shown in Figure 4.58. A blower was used to shrink the wrap, ensuring the tag antenna was well and tightly covered. The NXP chip is used for this analysis instead of the RF430FRL152H chip from Texas Instruments, as it can be directly connected to the antenna port without requiring a specific circuit layout. However, this chip functions only for reading and writing and cannot be integrated with sensors. For this reason, the NXP chip has been used exclusively to analyze the tag's sensitivity to moisture and also on-metal performance in the next section.



(a) (b) (c)

Figure 4.57 Fabrication Equipment for Antenna Insulation: (a) Impulse Sealer, (b) PET Shrink Wrap and (c) Blower

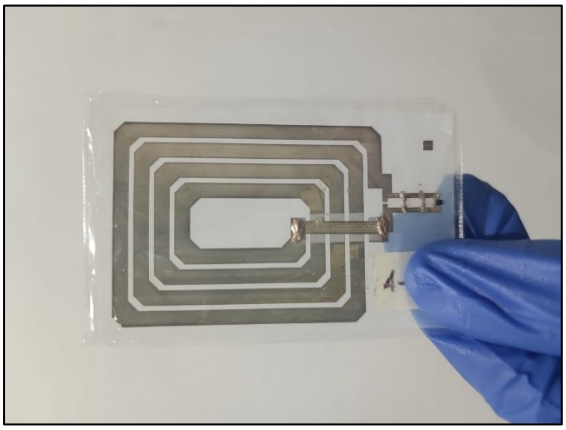


Figure 4.58 D4-HGS Tag Antenna with PET Layer Covered

Measurements of the tag reading range were conducted for the D4-HGS tag antenna in dry conditions, with direct water exposure as illustrated in Figure 4.59, and in both dry and wet conditions with an insulator cover. The comparison of simulated and measured tag reading ranges is presented in Table 4.15. It can be observed that all the measured results align well with the simulated ones, except for the antenna in fully moist conditions, where the measured read range is approximately 1 cm higher than the

simulated range. This discrepancy may result from variations in how water interacts with the antenna in real-world scenarios compared to the simulated environment. Nevertheless, the trend remains consistent between simulation and measurement, with the lowest reading range observed when the antenna was directly in contact with water.

In the presence of PET as an insulator, the performance of the antenna under wet conditions is significantly improved, demonstrating the effectiveness of the insulating material in preserving antenna functionality. Meanwhile, in dry conditions, the presence of an insulator slightly reduces the reading range compared to the bare dry antenna. This slight reduction may be attributed to the added material interfering with the antenna's ability to couple with the reader effectively, but the insulator provides adequate protection without compromising performance significantly.

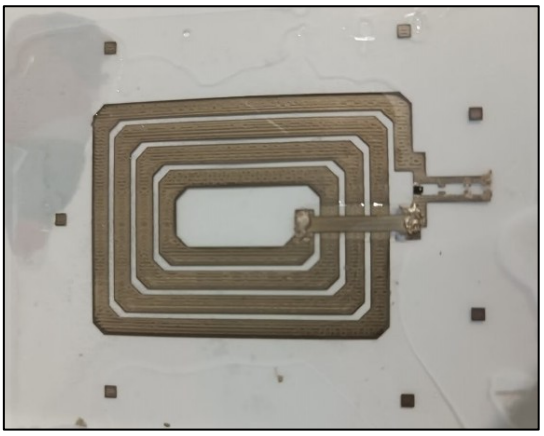


Figure 4.59 Fully Moist D4-HGS Tag Antenna Prototype

Table 4.15
Simulated and Measured Read Range for Antenna in Various Moist Conditions

Antenna Conditions	**Simulated Read Range (cm)**	**Measured Read Range (cm)**
Dry Antenna	3.12	3.03
Wet Antenna (fully moist)	0.7	1.72
Dry Antenna + Insulator	3.0	2.84
Wet Antenna + Insulator	2.64	2.79

4.4.2.3 Temperature

The sensitivity of the NFC tag to temperature differences was investigated and analysed to assess the robustness of the tag antenna. It is essential to ensure that the antenna maintains reliable performance when exposed to varying temperatures, as the tag antenna will be attached to different types of food in a range of temperature conditions, including cold, medium, and hot temperatures. Due to limitations in the simulation for varying environmental temperatures, the evaluation was conducted practically using the method discussed in Section 3.6.2 of Chapter 3.

Figure 4.60 illustrates the correlation between antenna inductance, L_a and antenna resistance, R_a with changes in temperature. The results indicate that as the temperature increases from 25°C to 65°C, both R_a and L_a exhibit consistent and proportional minimal increases. The R_a increases from approximately 37.5 Ω at 25°C to around 40.34 Ω at 65°C, demonstrating a direct relationship between temperature and resistance. Similarly, L_a shows a positive correlation with temperature, increasing from about 0.86 μH at 25°C to approximately 0.95 μH at 65°C.

The increase in R_a with temperature can be attributed to the increased lattice vibrations in the conductor, including silver and graphene. These vibrations impede the flow of electrons, resulting in higher resistivity and decreasing the antenna efficiency [200] [201]. Meanwhile, the minimal increase in L_a (approximately 0.1 μH) with rising temperature could be attributed to the slight increase in the internal inductance of the conductive coil, which is caused by temperature-dependent changes in resistivity. However, this increase remains minimal because the other factors that determine inductance, such as the permeability of the surrounding material and the physical layout of the antenna, including the antenna width, gap, and the number of turns, do not vary significantly with temperature [201]. As a result, the overall temperature-induced variation in inductance is minimal. Nonetheless, the increase in L_a may shift the antenna's resonant frequency to a lower value, potentially reducing the coupling efficiency and the reading range between the NFC tag and the reader. Further analysis regarding temperature variation is discussed in Section 4.5.

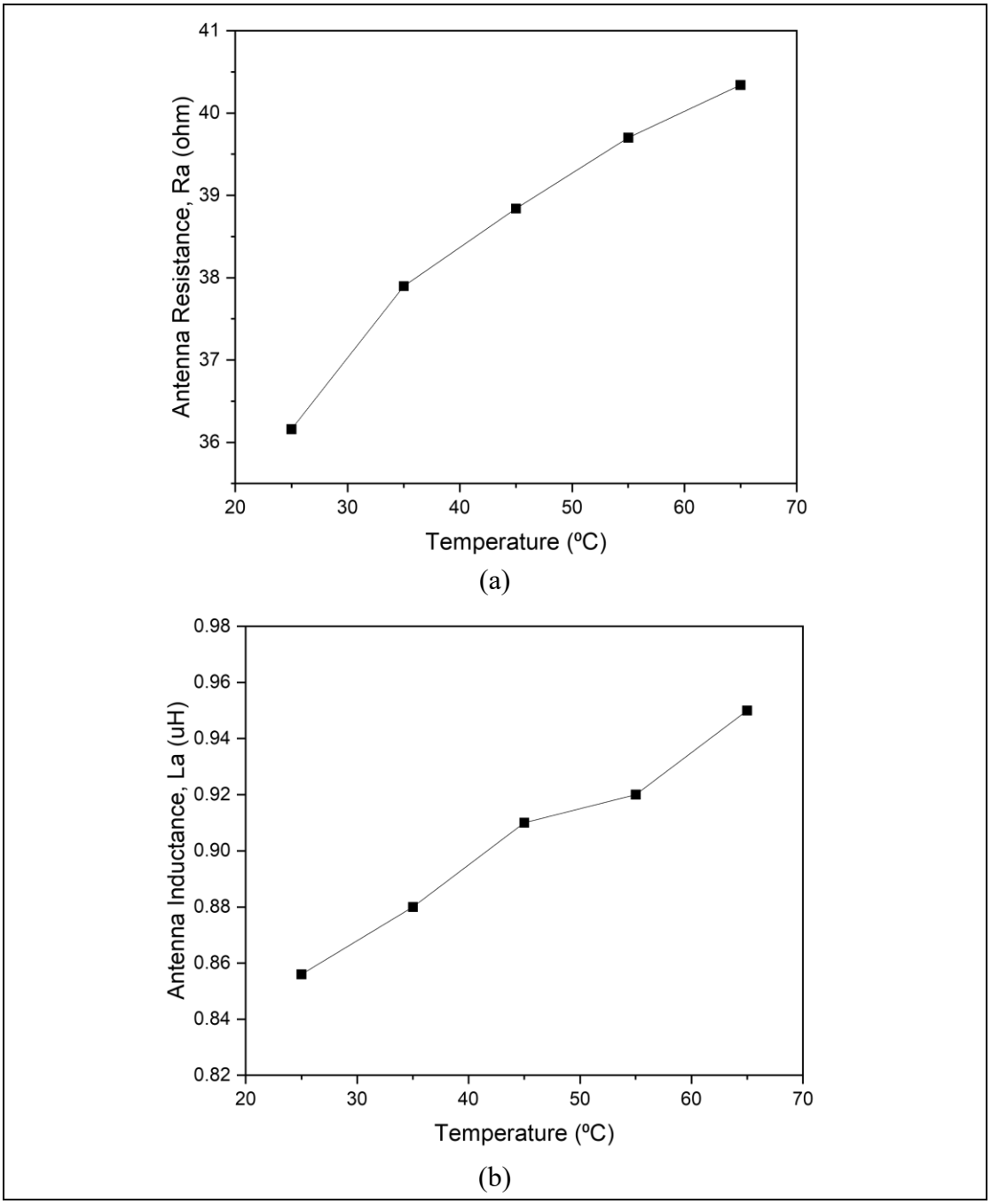


Figure 4.60 The Measured Result of (a) Antenna Resistance and (b) Antenna Inductance with Respect to the Temperature

4.4.3 On Metal HGS NFC Tag Antenna

In Section 4.4.2.1, it was found that the NFC tag antenna is highly sensitive to metal surfaces due to metal interference, specifically eddy currents [202]. When attached to a metal surface, the tag cannot be detected by the reader because the eddy currents generate a magnetic field on the metallic surface that opposes the original

magnetic field created by the reader. This opposition cancels out the magnetic field, preventing the reader from detecting the tag. Therefore, using a shield is the most reliable method to mitigate the impact of metal interference and ensure the reader detects the tag. The selection of the right shielding material depends on factors such as cost, weight, flexibility, ease of manufacture, and the application of the NFC system. Evaluating the trade-offs between these factors is crucial in identifying the most suitable shielding solution for a given NFC tag antenna application.

In this section, the correlation between the magnetic sheet properties and the antenna parameters has been investigated. The performance of the tag with different types of magnetic sheets, including ferrite, amorphous, and nanocrystalline sheets, has also been analyzed. Additionally, the reflection coefficient from the CST simulation has been compared with that from the ADS simulation to verify the circuit model of the proposed tag antenna with the magnetic sheets as discussed in Section 3.7 of Chapter 3. At the end of this section, the magnetic shielding material with optimal performance, suitable for integration with food packaging, has been selected.

4.4.3.1 Correlation Between Magnetic Sheet Parameters and Antenna Properties

The main parameters of the magnetic sheets to consider include thickness, t_m and permeability, μ'. Three types of magnetic sheets, which are ferrite, amorphous, and nanocrystalline sheets, have been compared to observe the effects of varying thickness and permeability on the antenna's properties and performance, including antenna inductance, L_a, antenna resistance, R_a, resonant frequency, f_{res}, and read range. The typical thickness of ferrite and nanocrystalline sheets ranges from 0.1 mm to 0.5 mm and 0.1 mm to 0.18 mm, respectively. Meanwhile, the thickness of the amorphous sheet is significantly lower, typically ranging from 0.02 mm to 0.03 mm. Ferrite sheets have significantly lower permeability at the high frequency of 13.56 MHz compared to nanocrystalline and amorphous sheets, with typical permeability values ranging from 100 to 200, and material loss, μ'', from 1 to 3. In contrast, the typical permeability for amorphous and nanocrystalline sheets used as magnetic shielding at 13.56 MHz is almost similar, ranging from 400 to 600. However, both of these magnetic sheets suffer from high material loss, ranging from 1500 to 1700.

Variations in thickness and permeability for ferrite, amorphous, and nanocrystalline sheets have been simulated with the D4-HGS tag antenna to observe

the effects on antenna performance and electrical properties. During the variation of each magnetic sheet parameter, such as thickness, other parameters, including permeability and material loss, are kept constant. The same approach was applied to the variation of permeability, as listed in Table 4.16. In the simulation, the magnetic sheet is positioned between the NFC tag and the metal plate, as shown in Figure 4.61 (a) and (b).

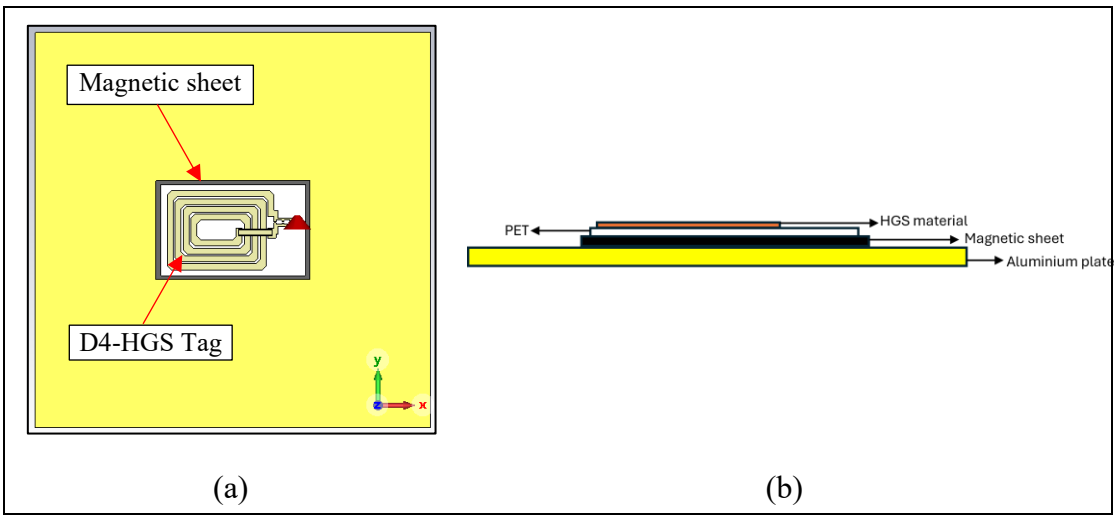


Figure 4.61 (a) Front and (c) Side View of NFC Tag with Magnetic Sheet Affixed to a Metal Plate (200 mm x 200 mm)

Table 4.16
Variation of Thickness and Permeability for Ferrite, Amorphous, and Nanocrystalline Magnetic Sheets

Type of Magnetic Sheet	**Thickness, t_m variation (mm)**	**Constant Parameters**	**Permeability, μ' variation**	**Constant Parameters**
Ferrite	0.1	$\mu' = 150$	100	$t_m = 0.1$ mm
	0.2	$\mu'' = 3$	120	$\mu'' = 3$
	0.3		150	
	0.4		170	
	0.5		200	
Amorphous	0.02	$\mu' = 500$	400	$t_m = 0.02$ mm
	0.03	$\mu'' = 1700$	500	$\mu'' = 1700$
	0.04			
	0.05		600	

Type of Magnetic Sheet	Thickness, t_m variation (mm)	Constant Parameters	Permeability, μ' variation	Constant Parameters
Nanocrystalline	0.10	$\mu' = 600$	400	$t_m = 0.14$ mm
	0.14	$\mu'' = 1500$	500	$\mu'' = 1500$
	0.18		600	

Figure 4.62 illustrates the correlation between the thickness of ferrite sheets, t_f, and L_a, R_a, f_{res} and read range. As the thickness of the ferrite increases from 0.1 mm to 0.5 mm, the L_a rises by approximately 25% as shown in Figure 4.62 (a) due to the increased magnetic path length. The thicker ferrite sheet reduces magnetic field leakage, causing the generated magnetic field to be more tightly constrained within the material. This enhances the magnetic coupling between the reader and the tag, thereby increasing the tag's reading range, as depicted in Figure 4.62 (b). The maximum reading range of 3.0 cm is achieved with a 0.5 mm thick ferrite sheet, representing an increase of approximately 13% compared to the 0.1 mm thick ferrite sheet. The thicker ferrite sheet effectively concentrates and guides the magnetic fields, reducing field leakage and improving coupling between the tag antenna and the NFC reader. However, further increasing the thickness of the ferrite sheet could lead to higher losses due to saturation effects. Once the ferrite sheet reaches saturation, it can no longer effectively enhance inductance or improve the reading range [203].

Meanwhile, the R_a is not significantly affected by the increase in ferrite thickness, as shown in Figure 4.62 (a). The resistance varies by only ±2 Ω as the thickness increases. This is because the ferrite sheet having much lower conductivity compared to the HGS material, does not influence the electrical properties of the antenna conductor material, resulting in minimal impact on the overall resistance of the antenna. The f_{res} is slightly shifted to a lower value, with a maximum shift of 3 MHz, as depicted in Figure 4.62 (c), due to the increase in L_a. However, this shift does not significantly impact the read range, as it is compensated by the improved coupling resulting from the increased thickness of the ferrite sheet.

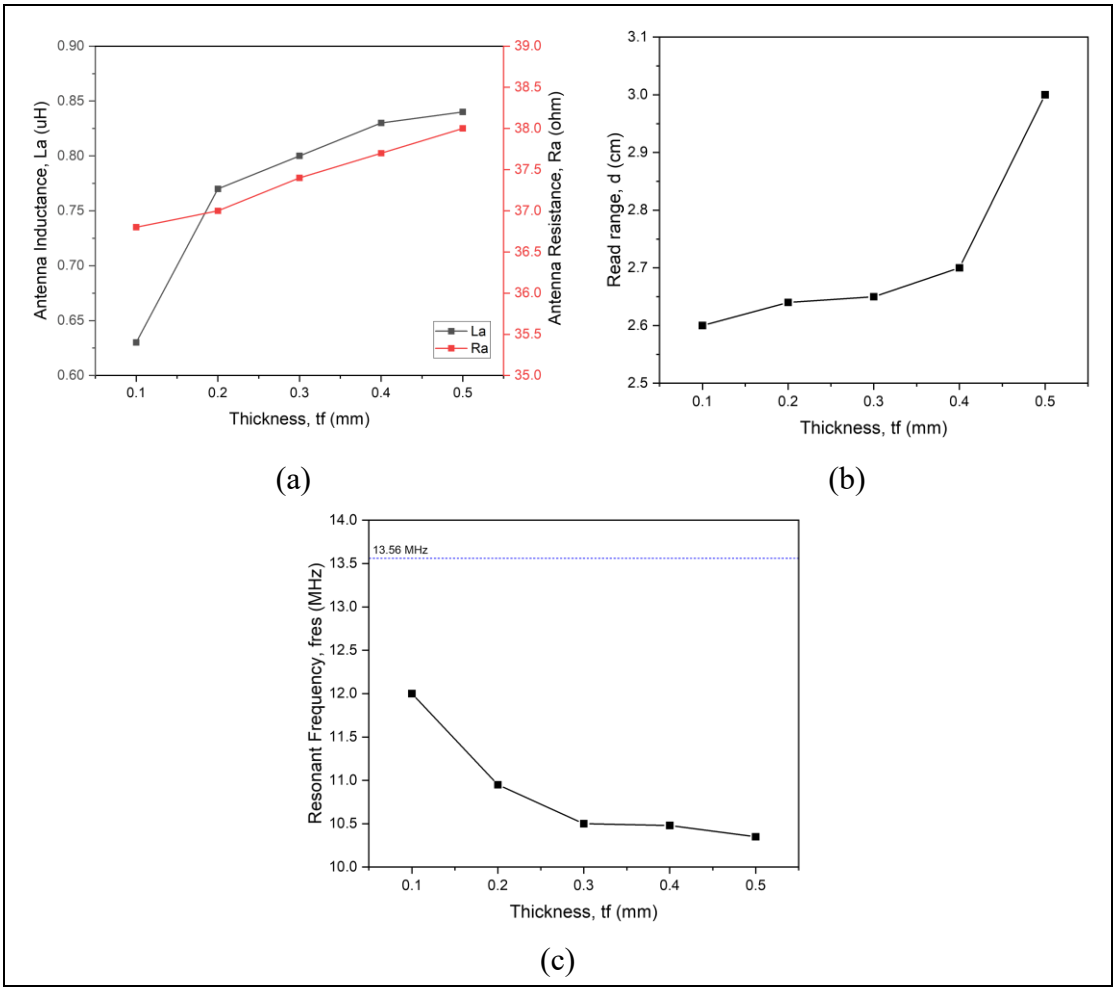


Figure 4.62 Correlation Between the Thickness of Ferrite Sheets with (a) L_a and R_a (b) Read Range and (c) f_{res}.

Conversely, for amorphous and nanocrystalline materials, the increase in the tag reading range is comparatively lower with increasing thickness. This is due to their minimal available thickness, which ranges from 0.02 to 0.05 mm for amorphous and from 0.1 mm to 0.18 mm for nanocrystalline. The maximum tag reading range achieved with the amorphous sheet is 2.45 cm, while for nanocrystalline, the reading range is slightly longer at approximately 2.7 cm, as depicted in Figure 4.63 (a) and (b), respectively. The L_a and R_a for both magnetic materials are also not significantly impacted by variations in thickness, where the change in L_a is only in the range of 0.01 µH to 0.1 µH, as depicted in Figure 4.63 (c) for amorphous and Figure 4.63 (d) for nanocrystalline. This is due to the small thickness variations that do not drastically change the magnetic field concentration capabilities of these materials, thus minimizing the effect on the antenna's electrical properties and reading range. Similarly, the f_{res} remains relatively stable, as shown in Figure 4.63 (e) and (f), since the small thickness

changes in the amorphous and nanocrystalline materials do not significantly alter the antenna inductance.

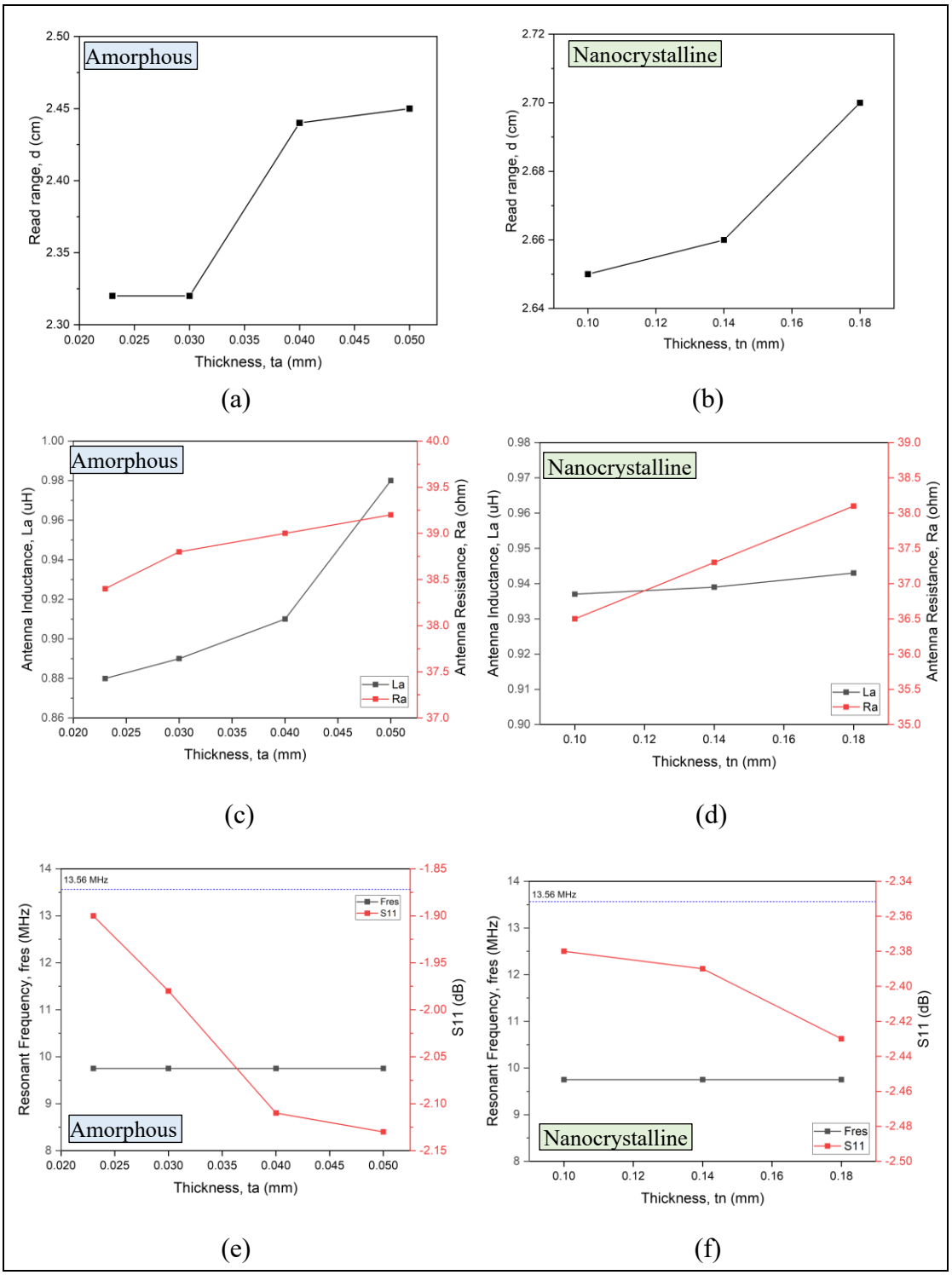


Figure 4.63 Correlation Between the Thickness of Amorphous and Nanocrystalline with (a)(b) Read Range (c)(d) L_a and R_a (e)(f) f_{res}, Respectively

The variation in permeability of the magnetic sheet has also been observed and analysed. The permeability of the ferrite sheet was varied from 100 to 200, which is the typical range for ferrite, while maintaining a fixed thickness of 1 mm. From Figure 4.64 (a), it can be observed that the inductance and resistance of the antenna increase slightly as the permeability value of the ferrite increases. However, a significant increase in tag reading range is observed in Figure 4.64 (b), with an approximately 30% increase in reading range for the tag antenna as the permeability value increases from 100 to 200. This is due to the stronger magnetic field concentration around the antenna when the permeability value is increased, resulting in better coupling between the tag antenna and the reader antenna, and thus increasing the tag reading range. Meanwhile, the antenna's resonant frequency is slightly shifted to a lower frequency, with a maximum shift of 2 MHz, as depicted in Figure 4.64 (c), due to the minimal increase in the antenna inductance.

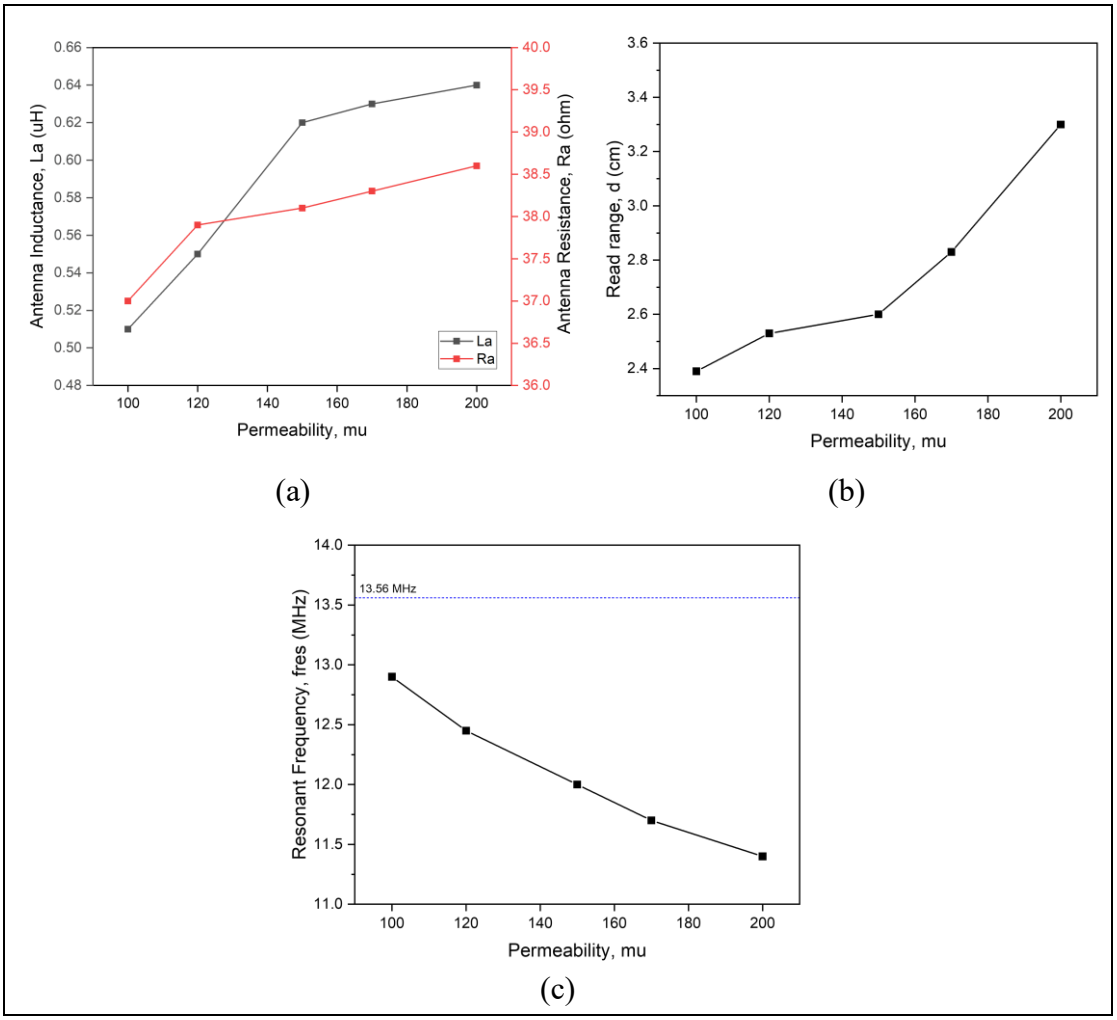
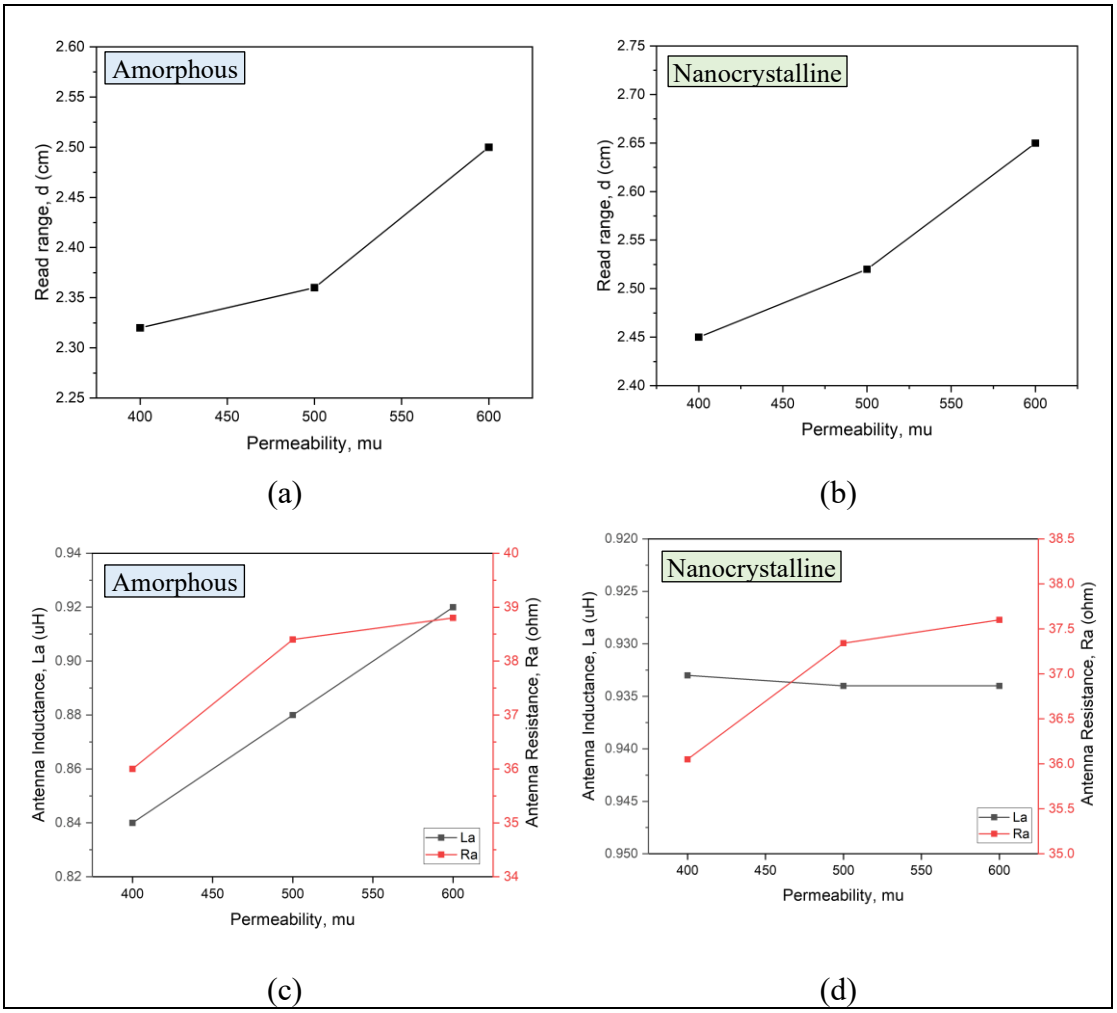


Figure 4.64 Correlation Between the Permeability of Ferrite Sheets with (a) L_a and R_a (b) Read Range and (c) f_{res}.

For the amorphous and nanocrystalline materials, the permeability was varied from 400 to 600, while maintaining a fixed thickness of 0.02 mm and 0.14 mm, respectively. From Figure 4.65 (a), it can be observed that the tag reading range slightly increased from 2.3 cm to 2.5 cm for amorphous and from 2.4 cm to 2.6 cm for nanocrystalline. Similar to the ferrite sheet, the increase in permeability leads to a stronger magnetic field concentration around the NFC tag antenna, thereby enhancing the coupling between the tag antenna and the reader, and resulting in an increased tag reading range. However, the increase in reading range is not as significant as that observed with the ferrite sheet because the higher baseline permeability of amorphous and nanocrystalline sheets has a smaller relative impact on the overall magnetic field concentration compared to the lower baseline permeability of ferrite. Additionally, the higher permeability of amorphous and nanocrystalline sheets might be closer to their

saturation limits, limiting the potential for further significant improvements in magnetic field concentration and reading range.

Meanwhile, the antenna inductance and resistance increased only minimally with the increase in permeability, as depicted in Figure 4.65 (b), since changes in magnetic field concentration do not significantly alter the physical dimensions or properties of the antenna conductor. Similarly, the antenna resonant frequency remains almost constant with an increase in permeability, as shown in Figure 4.65 (c), due to the minimal change in antenna inductance.



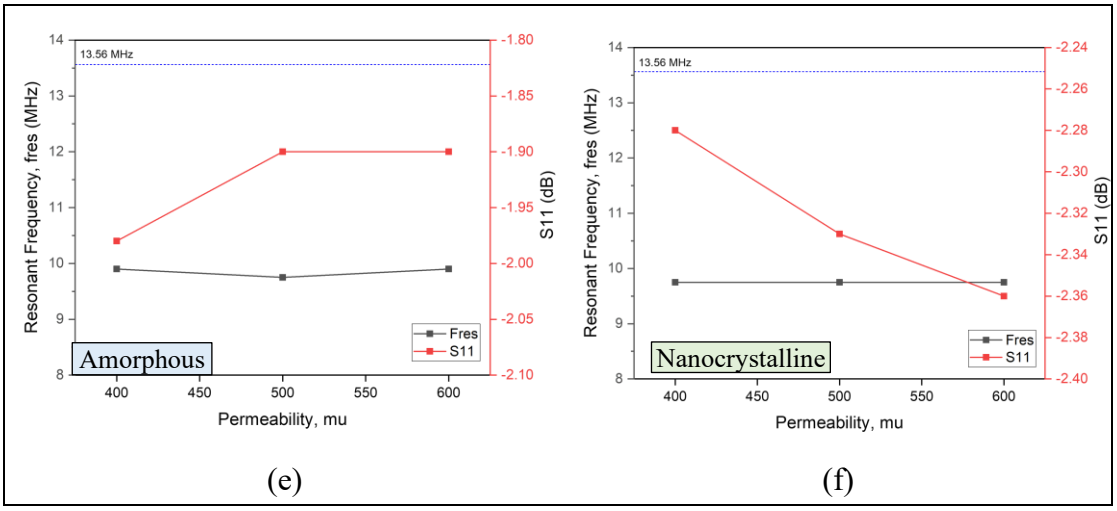


Figure 4.65 Correlation Between The Permeability of Amorphous and Nanocrystalline with (a)(b) Read Range (c)(d) L_a and R_a (e)(f) f_{res}, Respectively

4.4.3.2 Comparative Analysis of Magnetic Shielding

In this section, three types of magnetic shielding; ferrite, amorphous and nanocrystalline sheets, as shown in Figure 4.66, have been selected for further evaluation with the fabricated D4-HGS tag antenna. The selection of magnetic shielding is based on the parameter analysis carried out in section 4.3.3.1, as well as the availability of these materials in the market. The material properties of the selected magnetic sheets, including thickness, permeability, and tangent loss (as referred in Appendix 3), are presented in Table 4.17.

The Flexible Sintered Ferrite Sheet (FSFS) from Wuerth Electronics (WE), with a thickness of 0.24 mm, is chosen, as the optimal ferrite sheet thickness typically ranging from 0.2 mm to 0.3 mm, balancing performance with minimal losses. A much thicker ferrite sheet can lead to higher losses due to saturation effects. Both the amorphous and nanocrystalline sheets are from Vacuumschmelze, with available thicknesses of 0.023 mm and 0.14 mm, respectively. Further performance evaluation, including a comparison between the simulation and measurement of L_a, R_a and tag reading range has been conducted. At the end of this section, the magnetic shielding material with optimal performance, suitable for integration with food packaging at different temperatures, is selected.

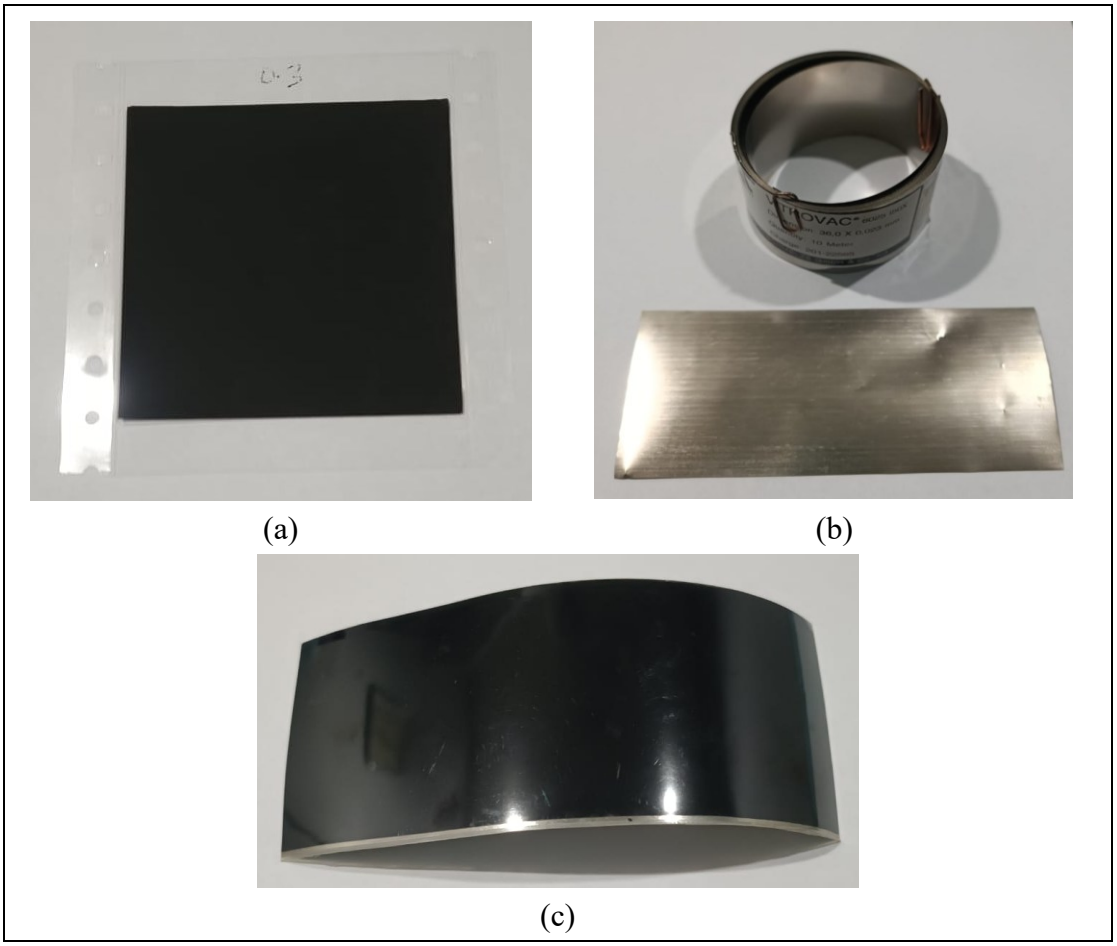


Figure 4.66 Magnetic Sheets: (a) Ferrite (b) Amorphous and (c) Nanocrystalline

Table 4.17
Properties of Magnetic Sheet

Type of Magnetic Sheets	**Product Name**	**Thickness (mm)**	**Permeability (fr = 13.56 MHz)**		**Tangent Loss**
			μ'	**μ''**	
Ferrite	WE - Flexible Sintered Ferrite Sheet (FSFS) 364103	0.24	150	3	0.02
Amorphous	VITROVAC 6025 Amorphous	0.023	500	1700	3.78
Nanocrystalline	VITROPERM 800R Nanocrystalline	0.14	600	1500	2.5

The value of L_a and R_a at a low frequency of 1 MHz were observed through simulation and measurement for all the selected magnetic sheet materials, which were placed between the D4-HGS tag antenna and an aluminium plate with dimensions of

200 mm x 200 mm. The simulation results in Figure 4.67 (a) show that the L_a value increases when it is attached to any of the magnetic sheets and a metal plate, compared to the tag antenna in free space. The highest L_a is achieved with the nanocrystalline material, followed by the amorphous and ferrite sheets. The increase in L_a is due to higher permeability of the magnetic sheet material compared to free space, which alters the magnetic field around the antenna. The nanocrystalline material, having the highest permeability, contributes to a more significant increase in antenna inductance compared to the amorphous and ferrite sheets. Meanwhile, the R_a as shown in Figure 4.67 (b) is only slightly affected by the presence of the magnetic sheet, with a difference of less than 2 Ω for all magnetic sheets compared to the antenna in free space.

The L_a and R_a were measured using a VNA, as described in Section 3.8.1 of Chapter 3. Table 4.18 summarizes the simulated and measured results for L_a and R_a, along with the percentage differences. The results indicate that the simulated and measured values for L_a exhibit similar trends, with slight differences of approximately 30 % for all magnetic sheets. The results show an increase in L_a with the presence of the magnetic sheets compared to the antenna alone. Consistent with the simulation results, the antenna with nanocrystalline magnetic sheets exhibits the highest L_a value, followed by amorphous and ferrite. Meanwhile, the R_a shows minimal variation across the different types of magnetic shielding, and both simulated and measured results align well, with a percentage difference of less than 5%.

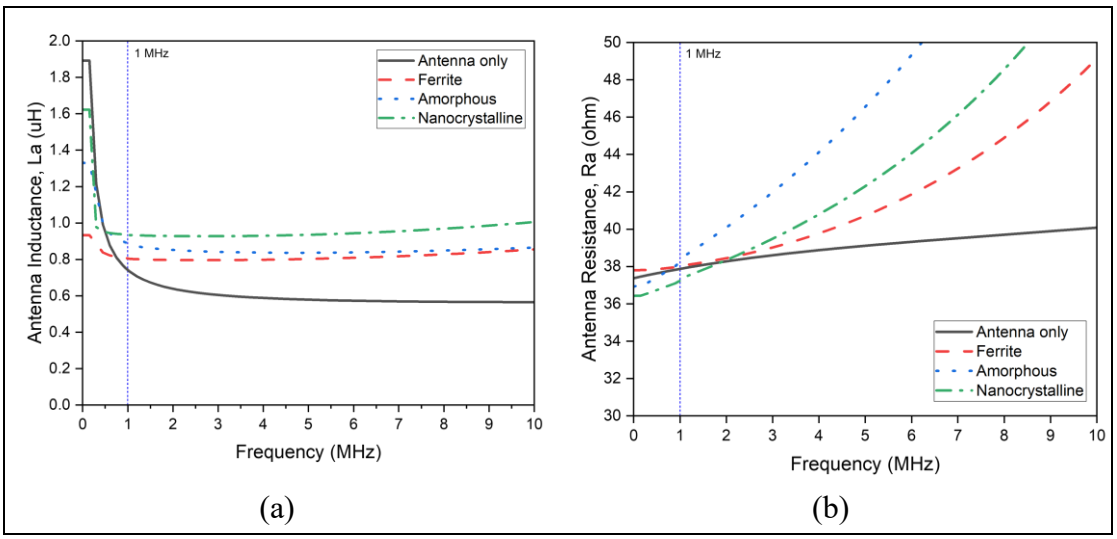


Figure 4.67 (a) Antenna Inductance and (b) S_{11} with Respect to the Frequency for Ferrite and Amorphous Sheet Configuration

Table 4.18
The Simulated and Measured L_a and R_a for D4-HGS Antenna with Different Magnetic Sheets

Parameter	Antenna Inductance, L_a (µH)			Antenna Resistance, R_a (Ω)		
	Simulation	Measurement	Difference (%)	Simulation	Measurement	Difference (%)
Antenna only	0.75	0.85	13.33	37.87	36.16	4.52
Ferrite	0.81	1.07	32.10	37.01	36.82	0.51
Amorphous	0.88	1.14	29.55	38.41	37.52	2.32
Nanocrystalline	0.93	1.22	31.18	37.34	37.04	0.80

Due to the increase in L_a caused by the presence of magnetic shielding, the resonant frequency, f_{res} shifts slightly to a lower value for all types of magnetic sheets, including ferrite, amorphous and nanocrystalline. Figure 4.68 shows the simulated S_{11} results for the D4-HGS tag antenna attached to ferrite, amorphous, and nanocrystalline sheets, along with an aluminium metal sheet, where the observed shifts in f_{res} from the antenna in free air are approximately 2 MHz, 3.2 MHz, and 3.3 MHz, respectively.
A similar trend in S_{11} results is observed in Figure 4.69 for the D4-HGS tag antenna attached to various magnetic sheets, as simulated using the developed equivalent circuit (EC) model in ADS software, as described in Section 3.7 of Chapter 3. Using the properties of the magnetic sheets provided in

Table 4.17, the components of the EC, including L_{mag}, C_{mag}, C_{couple}, C_{met}, R_{met}, and R_{eddy}, were calculated using Equation (3.4) until Equation (3.9) of Chapter 3 and incorporated into the circuit. Other components, such as R_a, L_a and C_a, which refer to the properties of D4-HGS tag antenna in free air, remained the same for all the magnetic sheet evaluations in the EC. Table 4.19 presents all the components used in the circuit.

These similar trends verify that the developed EC can predict the behaviour of different types of magnetic shielding with the tag antenna by considering the properties of the magnetic sheets, such as permeability, thickness, and tangent loss. From the results, it is evident that the higher permeability and very low thickness of the amorphous sheet contribute to a higher value of magnetic sheet inductance, L_{mag}. Consequently, the antenna's resonant frequency shifts significantly to a lower value from the operating frequency of 13.56 MHz. This effect is followed by the

nanocrystalline and ferrite magnetic sheets, which exhibit smaller L_{mag} values compared to the amorphous sheet.

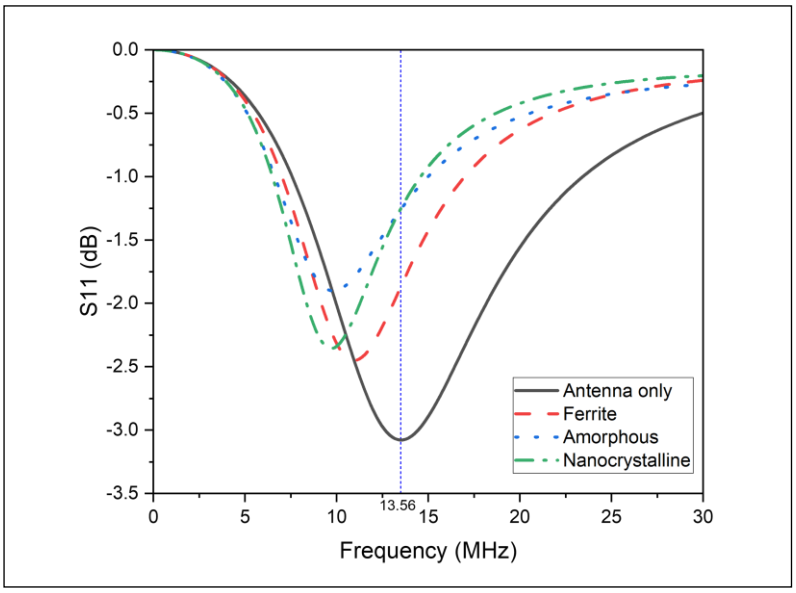


Figure 4.68 Simulated S_{11} Result for D4-HGS Tag Antenna with Magnetic Sheets and Metal Plate Using CST Simulation

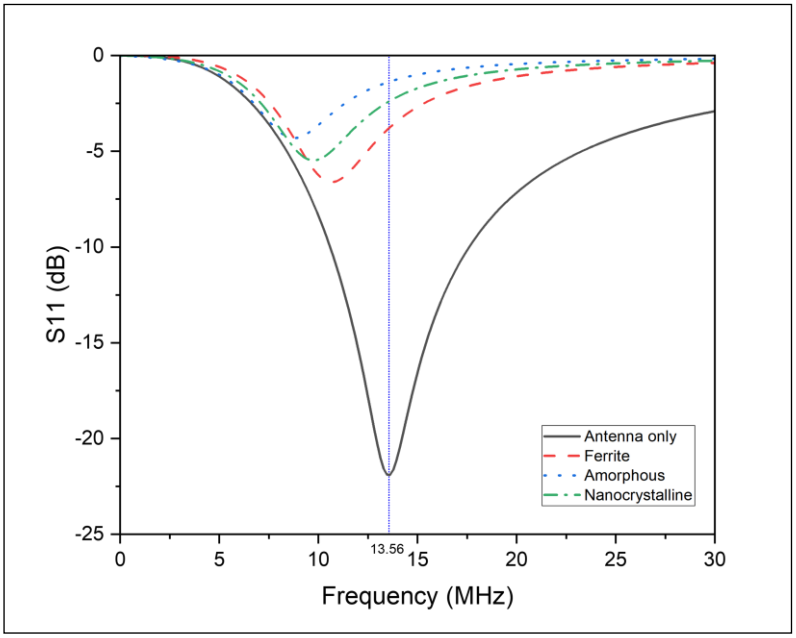


Figure 4.69 Simulated S_{11} Result for D4-HGS Tag Antenna with Magnetic Sheets and Metal Plate Using EC in ADS Simulation

Table 4.19
Electronic Components and Values Used for EC in ADS Simulation

Parameters	Ferrite	Amorphous	Nanocrystalline
L_{mag}	2.49 mH	18.5 mH	4.98 mH
C_{mag}	0.05 nF	0.15 nF	0.1 nF
C_{met}	0.1 nF	0.1 nF	0.1 nF
R_{eddy}	0.376 Ω	0.687 Ω	0.752 Ω
C_{couple}	0.68 nF	0.68 nF	0.68 nF
R_{met}	0.03 mΩ	0.03 mΩ	0.03 mΩ
R_a	37.67 Ω	37.67 Ω	37.67 Ω
L_a	0.75 µH	0.75 µH	0.75 µH
C_a	2.19 pF	2.19 pF	2.19 pF
C_{chip}	35 pF	35 pF	35 pF
C_{tun}	150 pF	150 pF	150 pF

Figure 4.70 illustrates the simulated magnetic field strength as a function of distance from the center of the NFC tag antenna in the z-direction for the antenna in free space and with the selected magnetic sheets and metal plate. From the graphs, it can be seen that at a magnetic field strength of 1.5 m/A, the tag antenna achieves the highest tag reading range in free space, with a range of 3.2 cm. This is followed by the ferrite and nanocrystalline magnetic sheets, which enable NFC tag detection at a similar distance of up to 2.65 cm, surpassing the performance of the amorphous sheet by 0.3 cm.

The tag reading range was then measured using a Xiaomi 11 smartphone with NFC functionality enabled, which was placed on top of the D4-HGS tag antenna attached to ferrite, amorphous and nanocrystalline magnetic sheet along with the aluminium plate, as illustrated in Figure 4.71 (a), (b), and (c), respectively. The results in Table 4.20 indicate that the tag reading ranges achieved for the ferrite, nanocrystalline and amorphous configurations were 2.4 cm, 1.9 cm and 1.5 cm, respectively. Comparing these measurements with the simulation data, the deviations were relatively small for ferrite and nanocrystalline, at 10% and 28%, respectively. However, for the amorphous sheet, the percentage difference between the simulated

and measured read range was quite large, at approximately 35%. This might be due to the higher loss in amorphous material compared to ferrite and nanocrystalline, as referred to Table 4.17, where more energy is dissipated as heat, reducing the effective power available for communication with the reader, which in turn significantly decreases the reading range in practical applications. Nevertheless, the performance of the amorphous sheet as a shielding material is still considered effective and suitable for on-metal NFC tags, as the reading range remains within the acceptable range for NFC communication.

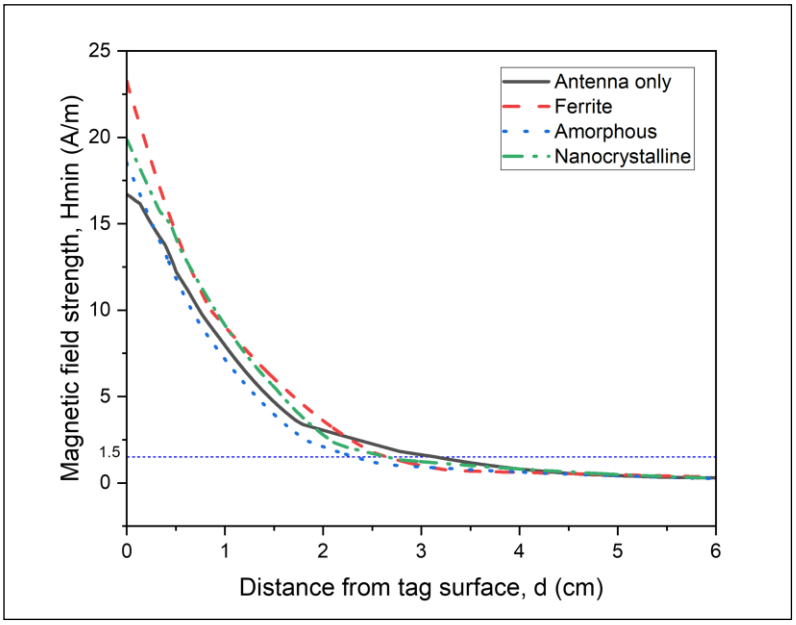


Figure 4.70 Magnetic Field Strength as a Function of the Distance from the Tag Surface (z-axis) for Ferrite and Amorphous Sheet Configuration

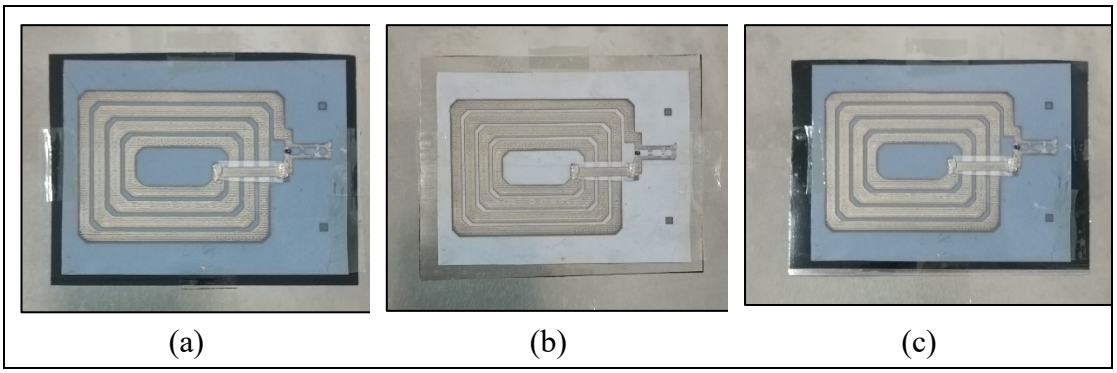


Figure 4.71 D4-HGS Tag Antenna Attached to (a) Ferrite, (b) Amorphous, and (c) Nanocrystalline Magnetic Sheets

Table 4.20
Simulated and Measured Tag Read Range with Various Magnetic Sheets

Parameter	Read range (cm)		
	Simulation	Measurement	Difference (%)
Antenna only	3.2	3.0	6.25
Ferrite	2.65	2.4	10
Nanocrystalline	2.65	1.9	28
Amorphous	2.32	1.5	35

Overall, it can be concluded that all selected magnetic shielding materials effectively enhance the read range of the D4-HGS tag antenna when attached to metal surfaces, typically achieving detection distances between 1 cm and 3 cm. As noted previously, the optimal choice of magnetic sheet depends on the intended application of the NFC tag. For this study, the D4-HGS tag will be attached to food packaging for the purpose of temperature monitoring. Consequently, a magnetic sheet with high flexibility and temperature resistance is required to accommodate various food packaging structures and temperatures. Table 4.21 lists the advantages and disadvantages of each magnetic sheet material in terms of permeability, magnetic loss, read range, temperature stability, flexibility, and cost [204][205].

In terms of thickness, the amorphous sheet has the lowest thickness compared to the others, which provides benefits in terms of flexibility and is particularly advantageous for applications where space is limited, such as food packaging that must remain lightweight and compact. However, its higher tangent loss reduces its shielding performance, thereby shortening the communication distance compared to other materials. Meanwhile, the ferrite sheet, with its greater thickness and lower tangent loss, can concentrate more magnetic flux and minimize eddy currents, contributing to a longer communication range. However, ferrite is less flexible and more brittle, making it prone to cracking and breaking when bent [119]. The nanocrystalline sheet, with its extremely high magnetic permeability, offers highly effective shielding performance, though it faces higher manufacturing complexity and cost, and inevitably becomes brittle during crystallization [206]. Regarding temperature stability, amorphous and nanocrystalline materials exhibit greater thermal stability than ferrites, which is

beneficial for monitoring the temperature of food packaging under various processing and storage conditions, including heating and refrigeration [205].

Considering the advantages and disadvantages of each magnetic shielding material, amorphous material is the most suitable for food temperature monitoring applications, as it offers high flexibility, durability, good thermal stability, and an acceptable reading range. Although amorphous sheets exhibit higher magnetic loss than ferrite, their very high permeability and superior mechanical flexibility provide better flux guidance and reduce magnetic field leakage, resulting in a reading range that remains within the requirements of NFC applications.

Table 4.21
Comparison of Properties and Performance for Various Magnetic Sheets

Property	**Ferrite**	**Amorphous**	**Nanocrystalline**
Thickness	Moderate	Very Low	Low
Magnetic permeability	High	Very high	Very high
Magnetic loss	Low loss	High loss	High loss
Read range (measured)	2.4 cm	1.5 cm	1.9 cm
Temperature stability	Moderate temperature resistance	Good thermal stability	High thermal stability
Flexibility	Rigid and less flexible	Highly flexible	Moderate flexible
Brittleness	Brittle	Not brittle	Generally brittle but can be flexible in thin forms
Cost	Generally lower cost	Moderate cost	High cost

4.5 NFC Tag Antenna for Temperature Monitoring of Food Packaging Application

The D4-HGS antenna was selected for integration with the temperature sensor circuit due to its compact size, compatibility with NFC tag applications, and reliable performance demonstrated during various robustness analysis. In this section, the fabricated D4-HGS antenna, integrated with the temperature sensor circuit, is evaluated in terms of system functionality, reliability under temperature variations, and its real-world application in food packaging temperature monitoring.

4.5.1 Verification of Electrical Connectivity for Temperature Sensor Circuit

The electrical connectivity and functionality of the fabricated D4-HGS tag antenna with a temperature sensor circuit were verified through several tests, including continuity, resistance, and voltage testing. The continuity and resistance tests were conducted simultaneously, measuring the resistance between the Surface Mount Devices (SMD) components and the chip port. A beep sound was heard during the continuity test, indicating a good electrical connection.

Table 4.22 presents the measured resistance results for all connected ports from the RF430FRL152H chip to SMD components, including resistors and capacitors. Each side of the SMD components (1,2) was connected to either the different ports of the chip, ground, or other SMD components, as depicted in the schematic diagram of the chip and the SMD components in Figure 4.72. The measured resistance for SMD components connected to ground exhibited variations in values since ground is distributed across multiple locations in the circuit. The resistance value depends on the distance between the multimeter probes used for measurement, where greater distances result in higher resistance values due to the conductive path length.

For the HGS conductive material, the measured resistance in the range of 10 to 50 Ω is considered acceptable for NFC performance, as it ensures efficient power transfer and minimizes losses. Overall, the measured resistance values fall within the acceptable range, confirming that all components are well-connected and that the printed conductive traces provide sufficient electrical connectivity for reliable operation.

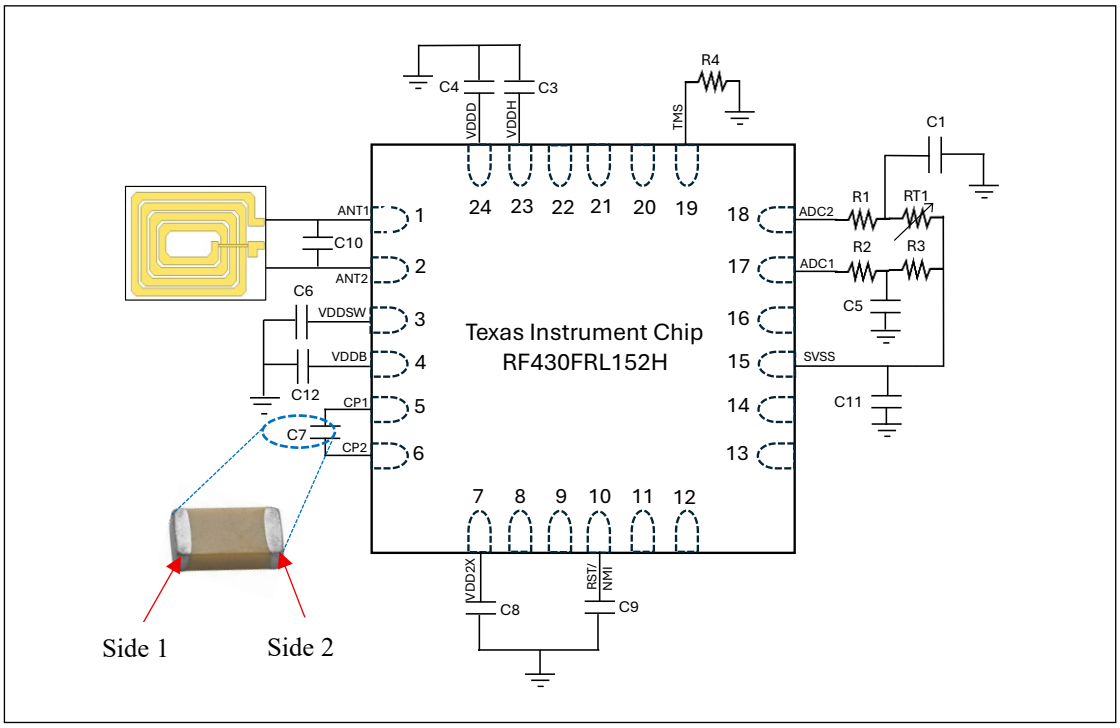


Figure 4.72 Schematic Diagram of RF430FRL152H Chip and Other Components

Table 4.22
Measured Resistance Between SMD Components and NFC Chip Ports

SMD components	**Connected Ports (NFC chip port / other SMD)**		**Resistance [Ω]**	
	Side 1	**Side 2**	**Side 1**	**Side 2**
C10	1	2	3	3
C6	3	Ground	5	5 - 19
C12	4	Ground	3	3 - 19
C7	5	6	3	6
C8	7	Ground	5	3 - 17
C9	10	Ground	5	3 - 16
C11	15	Ground	9	4 - 14
C5	Ground	R2	4	4
R2	17	R3	10	5
R3	R2	15 (SVSS)	3	16
RT1	R1	15 (SVSS)	8	15

SMD components	Connected Ports (NFC chip port / other SMD)		Resistance [Ω]	
	Side 1	Side 2	Side 1	Side 2
R1	18	RT1	4	8
R4	19	Ground	4	6 - 19
C4	24	Ground	3	2 – 16
C3	23	Ground	5	3 – 16
C1	R1	Ground	10	4 – 16

The functionality of the fabricated D4-HGS tag antenna with a temperature sensor circuit was also verified through voltage tests, where the voltage was measured at four different voltage sources: Digital Supply Voltage (VDD), Switched Supply Voltage (VDDSW), Antenna Rectified Voltage (VDDH), and Voltage Doubler Output (VDD2X). During testing, the circuit was powered by bringing an NFC reader, such as an NFC-enabled smartphone, close to the D4-HGS tag antenna. The measured voltage was then compared with the reference voltage from the datasheet [179][143], as well as with the measured voltage from the reference PCB-based tag antenna, which has a similar temperature sensor circuit design, as depicted in Figure 4.73.

From the measured results, it can be observed that the measured voltage of D4-HGS tag aligns well with the reference values from both the datasheet and the PCB at all voltage sources, except for the Voltage Doubler Output (VDD2X), as presented in Table 4.23. The values of VDDH and VDDSW remain stable across all implementations, indicating that the NFC antenna is efficiently rectifying power. Additionally, VDD exhibits stable values in both the D4-HGS and PCB-based antennas, ensuring proper operation of the NFC chip. However, the VDD2X is significantly lower in the D4-HGS tag compared to both the PCB-based reference and the datasheet values. The lower VDD2X in the D4-HGS tag is probably due to the higher resistance of the printed HGS conductive traces compared to copper-based PCB traces, which is primarily caused by the lower conductivity value and lower thickness of the HGS material, leading to increased power dissipation and voltage drops.

Since VDD2X is responsible for boosting the rectified voltage (VDDH) and is used to power circuit components that require higher voltages, such as analog sensors

and active NFC chip components, its lower-than-expected value could impact power transfer efficiency. This may result in the improper functioning of sensor circuits, potentially leading to unstable or inaccurate sensor readings. The impact of VDD2X variations on sensor readings is further analyzed in the subsequent section.

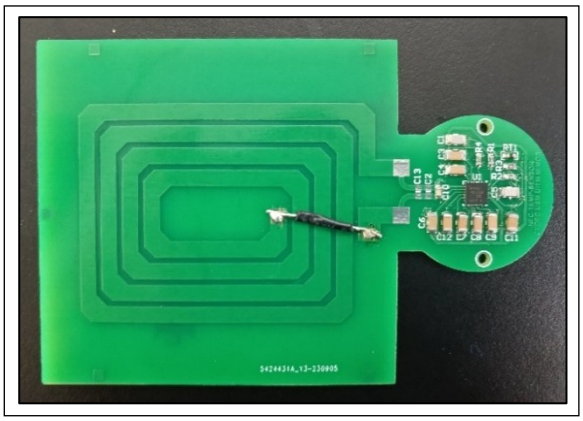


Figure 4.73 PCB-Based Tag Antenna with Temperature Sensor Circuit

Table 4.23
Measured Voltage at Various Voltage Sources for PCB-based and D4-HGS Tag with Temperature Sensor Circuit

Source	Pin	SMD	Measured Voltage [V]		
			Datasheet	PCB	D4-HGS
VDDSW	3	C6	1.5	1.52	1.54
VDD2X	7	C8	2.6 – 2.7	2.34	1.28
VDDH	23	C3	1.8 – 3.6	2.13	2.13
VDD	24	C4	NA	1.15	1.17

4.6 Enhancement of NFC Temperature Monitoring Application

To evaluate the performance of the fabricated D4-HGS tag with the temperature sensor circuit, a commercial mobile application (app) developed by Texas Instruments, as illustrated in Figure 4.74 (a), was used to monitor the temperature of the sensor. The app is designed for metal-based NFC tag temperature monitoring applications. To verify the app's compatibility with the proposed D4-HGS tag antenna and temperature sensor circuit, the temperatures recorded by both the D4-HGS tag and the PCB-based

tag were wirelessly monitored and compared with reference temperatures measured using a Fluke 1523 Reference Thermometer, as depicted in the measurement setup shown in Figure 4.74 (b). The temperature was varied from 25°C to 60°C using a blower, with 12 datasets collected for each antenna design. Each dataset was simultaneously compared with the reference temperature. Figure 4.75 (a) and Figure 4.75 (b) show the correlation between the reference temperature and app-reported temperature for the PCB-based tag antenna, along with the mean temperature difference and respective standard deviation (STD) values. Similar results for the D4-HGS tag antenna are presented in Figure 4.76 (a) and Figure 4.76 (b).

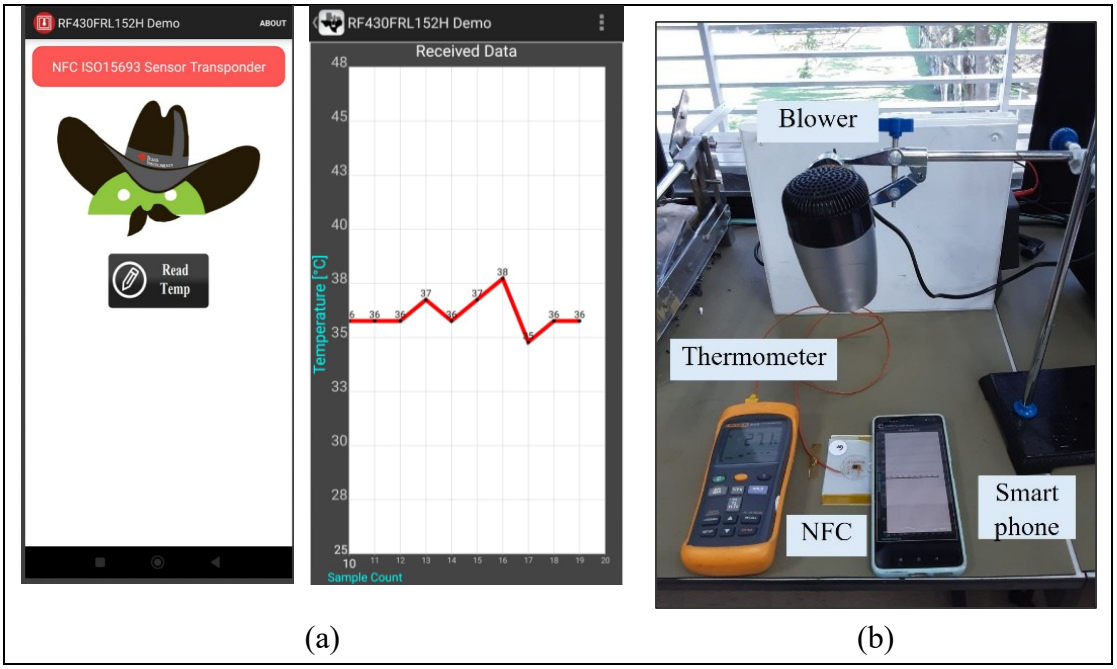


Figure 4.74 (a) Interface of the Temperature Monitoring App Developed by Texas Instruments and (b) the Measurement Setup of Temperature Reading Verification

From the results in Figure 4.75 (a), it can be observed that the linear regression fitted to the data shows a small intercept of 0.38°C, indicating that the PCB-based sensor has a minimal offset, meaning its readings are very close to the actual reference temperature. The mean temperature difference, as shown in Figure 4.75 (b), is minimal at 1.29ºC. Most of the temperature differences are close to the mean, with only a few data points slightly exceeding 2°C. This indicates that the PCB-based tag antenna provides temperature readings that closely match the reference temperature, and the relatively small variation confirms that the sensor functions reliably with the PCB-

based tag antenna. The low standard deviation of 0.85°C indicates that the PCB-based tag provides stable and consistent temperature readings, with most temperature difference values falling within the range of (1.29 ± 0.85) °C, or 0.44°C to 2.14°C.

However, for the D4-HGS tag, the temperature difference is significantly higher than the reference temperature. The intercept of the linear regression in Figure 4.76 (a) exhibits a value of 21.2°C, indicating a systematic error where all readings are offset by approximately 21°C, leading to inaccurate temperature monitoring. The mean temperature difference of 20.41ºC, shown in Figure 4.76 (b), suggests the sensor significantly overestimates temperature readings. Meanwhile, the relatively small STD of 0.8ºC indicates that the sensor provides consistent readings, with most temperature differences falling within the range of 19.60°C to 21.2°C. However, the sensor appears to be inaccurately calibrated for the D4-HGS, probably due to insufficient power transfer caused by the lower VDD2X voltage, as discussed earlier in Section 4.5.1.

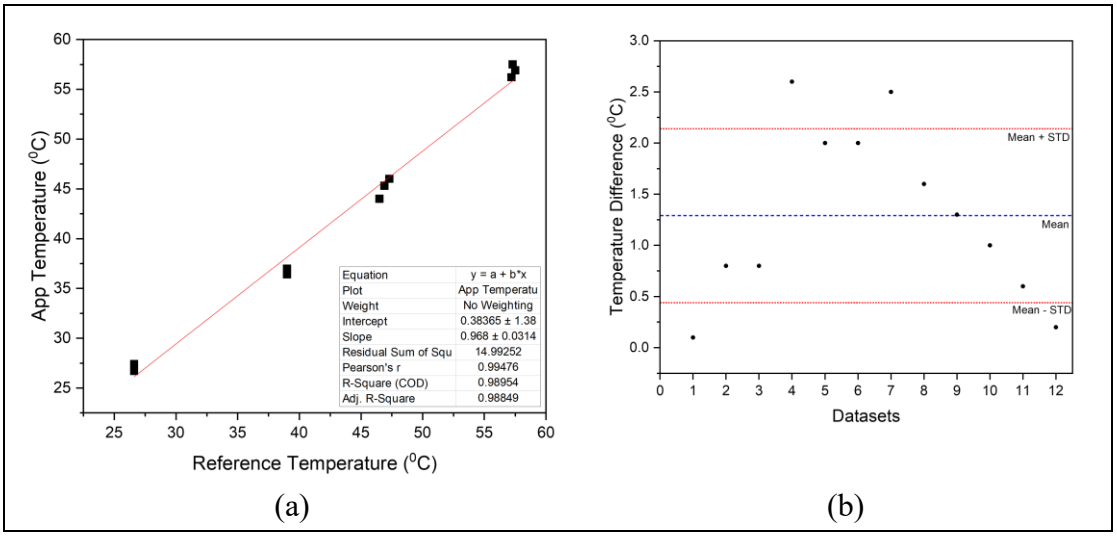


Figure 4.75 (a) Linear Regression Between Reference and App-Recorded Temperatures for the PCB-Based Antenna and (b) Mean Temperature Difference with STD

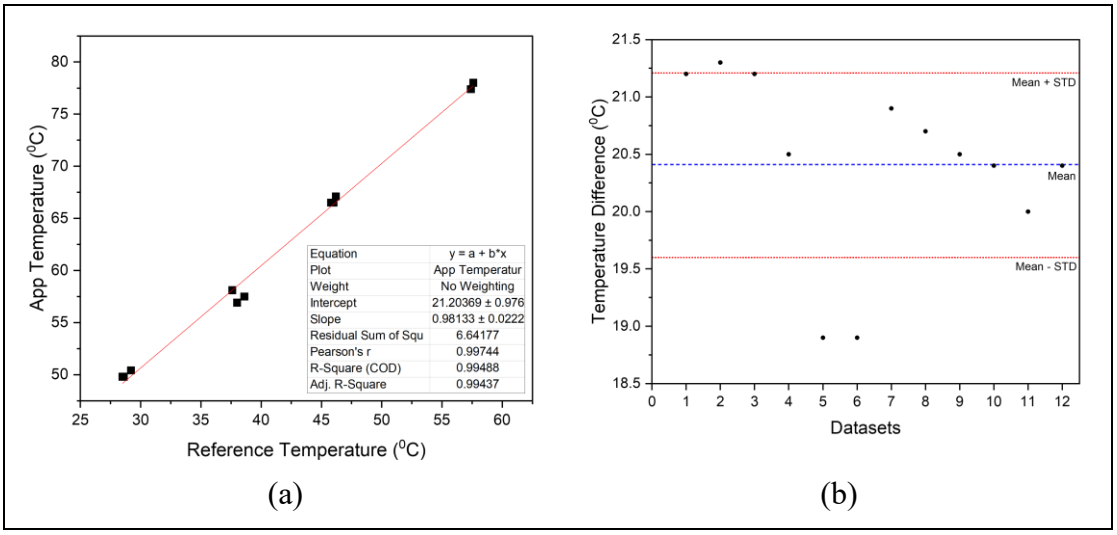


Figure 4.76 (a) Linear Regression Between Reference and App-Recorded Temperatures for the D4-HGS Antenna and (b) Mean Temperature Difference with STD

To address this issue, two possible methods can be considered. The first method involves optimizing the printed HGS conductive traces by increasing the trace width and thickness to reduce the resistance and improve power delivery [185][207]. However, the printed HGS material is limited to a maximum thickness of 5 µm, and increasing the trace width would enlarge the overall circuit dimensions, making the system bulkier. The second suggested method is temperature-specific calibration through data normalization, where a linear regression equation is incorporated into the app's software to normalize the sensor readings for accurate NFC temperature monitoring. This second method is preferable, as it eliminates the need to reprint the D4-HGS tag, which would be time-consuming and costly. Additionally, the software-based temperature calibration approach is more efficient than a hardware modification, as it can be tested multiple times until the desired accuracy is achieved. Therefore, temperature-specific calibration has been implemented to reduce the temperature discrepancy between the reference temperature and the D4-HGS tag temperature.

The calibration of the app temperature was performed by analyzing the reference and app temperatures using linear regression, as depicted in Figure 4.76 (a). The new equation derived from the linear regression, as shown in Equation (4.2), was then incorporated into the temperature app coding in Android Studio, as attached in the Appendix 4. The same temperature measurement was conducted again using the enhanced app. Figure 4.77 (a) and Figure 4.77 (b) show the correlation between the reference temperature and the app temperature using the enhanced app. The linear

regression fitted to the data shows an intercept value of -2.85°C, indicating that the previous overestimation has now shifted to a slight underestimation. Meanwhile, the slope value of 0.93, which is less than 1, indicates that the app underestimates higher temperature values compared to the reference. The temperature difference between the D4-HGS tag antenna and the reference temperature is relatively small, approximately 5.63ºC, showing a significant improvement compared to the previous mean error (~20.5°C before calibration). The STD is moderately low at 2.15°C, meaning most temperature difference values fall within the range of (5.63 ± 2.15)°C, or 3.48°C to 7.78°C. This indicates that the sensor readings are relatively stable, with moderate fluctuation. From these results, it can be concluded that the calibration has improved the temperature readings, but an offset still remains. The mean temperature difference remains beyond the acceptable range of less than 2°C. Further linear regression adjustments are necessary to refine the normalization model for enhanced accuracy of the D4-HGS tag.

Therefore, the second linear regression obtained from the plotted data in Figure 4.77 (a), which exhibits a linear equation as shown in Equation (4.3), was subsequently incorporated after Equation (4.2) in the temperature apps coding in Android Studio, as attached in Appendix 4. The final measurements was conducted using the fully enhanced app, and the measured data is presented in Figure 4.78. The intercept of the linear regression, as depicted in Figure 4.78 (a), shows a minor negative offset of -3.39°C, while the slope is slightly greater than 1, at 1.079°C, indicating that at higher temperatures, the app may slightly overestimate temperature readings. Nevertheless, the temperature readings of the D4-HGS tag are now closer to the reference values, with a small mean deviation of only 1.39°C, as depicted in Figure 4.78 (b). This represents a significant improvement compared to the initial mean error (~20.5°C before calibration) and the first calibration (~5°C mean error). The achieved mean temperature difference is within an acceptable error range for NFC-based temperature sensing. The STD is relatively low at 1.02°C, indicating that the sensor readings are consistent and stable, with most temperature difference values falling within the range of (1.39 ± 1.02)°C, or 0.37°C to 2.41°C. The enhanced app has been successfully calibrated and can be used for D4-HGS tag antenna in real-world deployments.

$$\text{App Temp} = 0.98133\ (\text{Ref temp}) + 21.20369 \tag{4.2}$$

$$\text{App Temp} = 0.93243\ (\text{Ref temp}) - 2.84593 \tag{4.3}$$

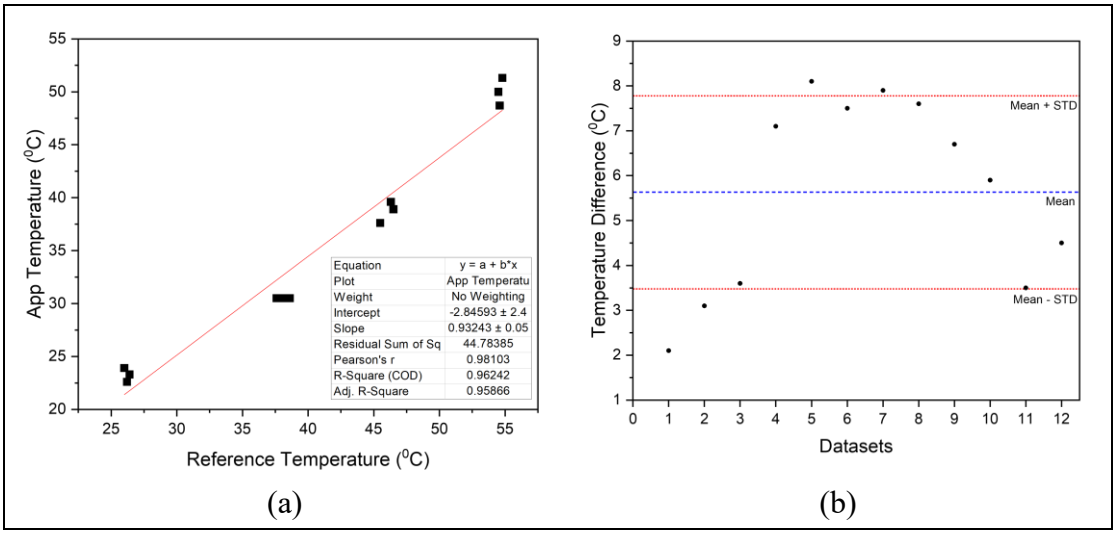


Figure 4.77 (a) Second Linear Regression Between Reference and App-Recorded Temperatures for the D4-HGS Antenna and (b) Mean Temperature Difference with STD

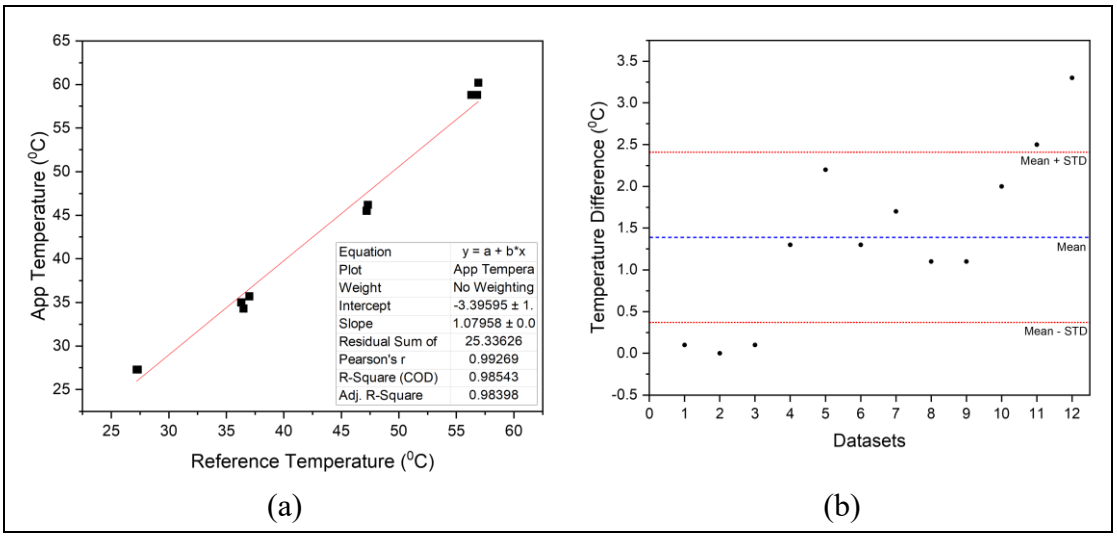


Figure 4.78 (a) Final Linear Regression Between Reference and App-Recorded Temperatures for the D4-HGS Antenna and (b) Mean Temperature Difference with STD

To ensure compatibility with both D4-HGS and PCB-based tag antennas, the mobile app was enhanced by incorporating two temperature reading options: metal-based and carbon-based, as shown in the app interface in Figure 4.79 (a). This

improvement allows users to select the appropriate temperature reading option for their respective tags. The temperature reading process flow is illustrated in Figure 4.79 (b). When the user opens the app, they must first press the “Start Temperature Reading” button. The app then prompts the user to select the tag material type, offering two options: metal-based and carbon-based. If the user selects a metal-based option, the original temperature calculation, as described in Equation (2.34), is executed. However, if the user selects carbon-based, an alternative calculation method incorporating the proposed Equation (4.2) and Equation (4.3) is applied to correct the temperature reading. The complete source code implementing these calculations is provided in Appendix 4.

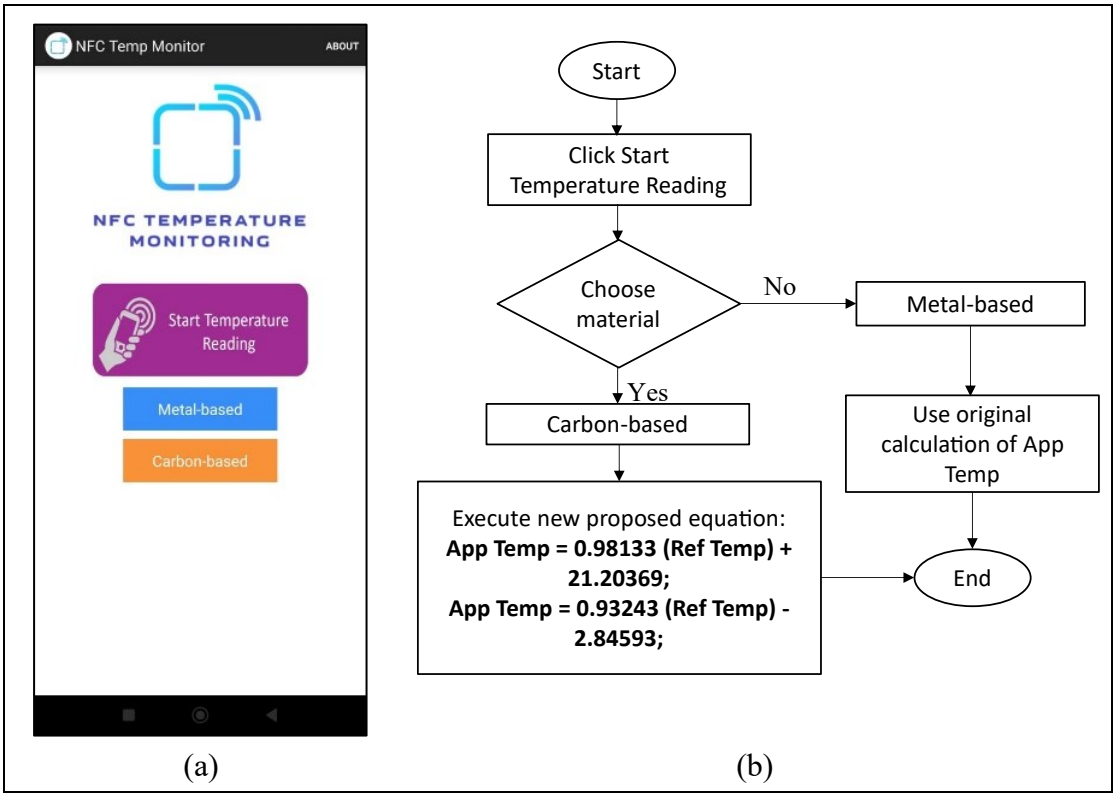


Figure 4.79 (a) The Interface of the Enhanced Mobile App and (b) the Flow of Temperature Reading Through the Enhanced Mobile App

4.6.1 Reliability Test Result of Temperature Monitoring System

The reliability of the fabricated D4-HGS NFC tag integrated with the temperature sensor circuit was evaluated to ensure that the system is both stable and reliable for practical applications. The reliability test was conducted over 30 minutes

across three different temperature ranges: cold, room, and hot, which represent the typical storage and transportation conditions for food products. The measurements were carried out using the setup described in Section 3.9.4 of Chapter 3.

Figure 4.80 presents the measured temperature readings of the D4-HGS tag, which were simultaneously compared with the reference temperature over a 30-minute duration. In the cold temperature range, the reference temperature increases slightly from 4.0°C to 4.9°C, while the tag exhibits minimal variation, ranging from 4.2°C to 4.3°C. The temperature difference between the reference and the tag, as depicted in Figure 4.81, has a mean value of 0.4ºC with a low standard deviation (STD) of 0.19ºC, indicating the sensor's stability and minimal variability over the 30-minute measurement period in low-temperature conditions. Most of the temperature difference values fall within the range of (0.4 ± 0.19)°C, or 0.21°C to 0.59°C, except for the reading between 25 and 30 minutes, where the difference rises to 0.7ºC, slightly exceeding the mean plus 1 STD. This could be attributed to the delayed thermal equilibrium between the tag and its surroundings, which may require more time to stabilize in low-temperature environments.

At room temperature, both the NFC tag and the reference temperatures fluctuate over time, with the tag exhibiting increased deviations after 15 minutes. The reference temperatures vary between 24.8°C and 22.7°C, while the tag deviates significantly, ranging from 26°C to 21.1°C within 30 minutes of measurement. The temperature difference between the reference and the tag, as depicted in Figure 4.82, has a mean value of 0.8ºC with a moderate STD of 0.49ºC, reflecting moderate variability and less stability compared to the cold condition. However, most of the temperature differences fall within the range of (0.8 ± 0.49)ºC, or 0.31°C to 1.29°C, indicating a generally consistent temperature reading trend of the tag relative to the reference thermometer. The lag in the tag's temperature readings compared to the reference after 15 minutes is probably due to the thermal response delay of the HGS material to environmental factors.

In the high-temperature range, both the NFC tag and the reference temperature exhibit an increase from the first 5 minutes to 30 minutes of readings. However, both show an average deviation with a mean difference of 1.44ºC, as depicted in Figure 4.83, which is the highest mean difference among all conditions, indicating reduced accuracy at high temperatures. The slightly higher STD value of 0.56ºC compared to other conditions reflects greater variability in the temperature difference and lower stability

in the NFC tag's thermal response under hot conditions. This is probably due to increased electrical resistance as the temperature rises, as discussed in Section 4.4.2.3, resulting in deviations in temperature readings. Rapid changes in resistance could cause inconsistent NFC signal strength and power transfer efficiency.

Additionally, another factor that may contribute to the deviation is the normalization process in the enhanced temperature monitoring app as described in Section 4.5.2, where the second linear regression shows a slope value greater than 1 (1.079°C). This suggests that at higher temperatures, the app may slightly overestimate temperature readings. Despite the high mean difference compared to other conditions, the measured results of the NFC tag remain acceptable for temperature monitoring in food packaging, where the temperature tolerance is within the range of ±3ºC [208].

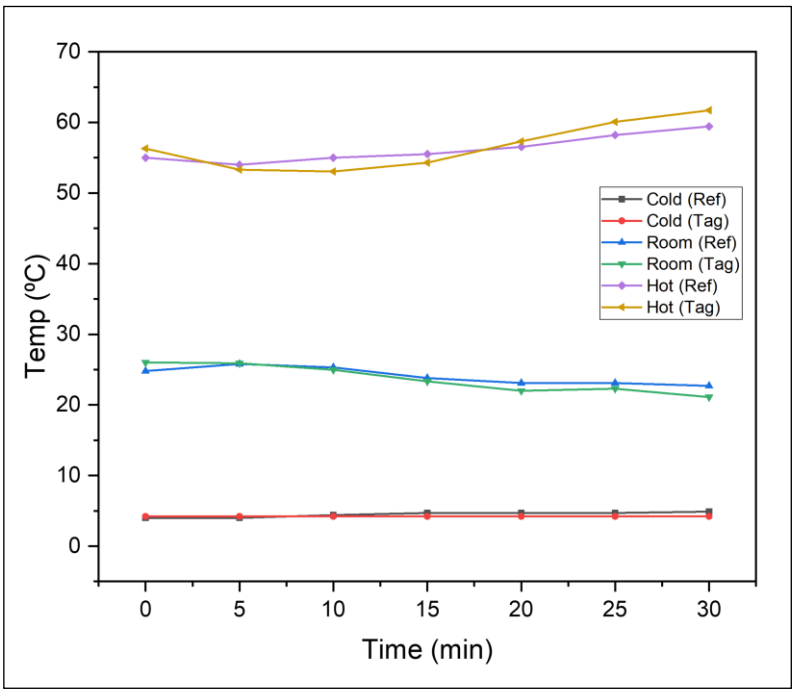


Figure 4.80 Temperature Reading of NFC Tag Sensor and Reference Thermometer

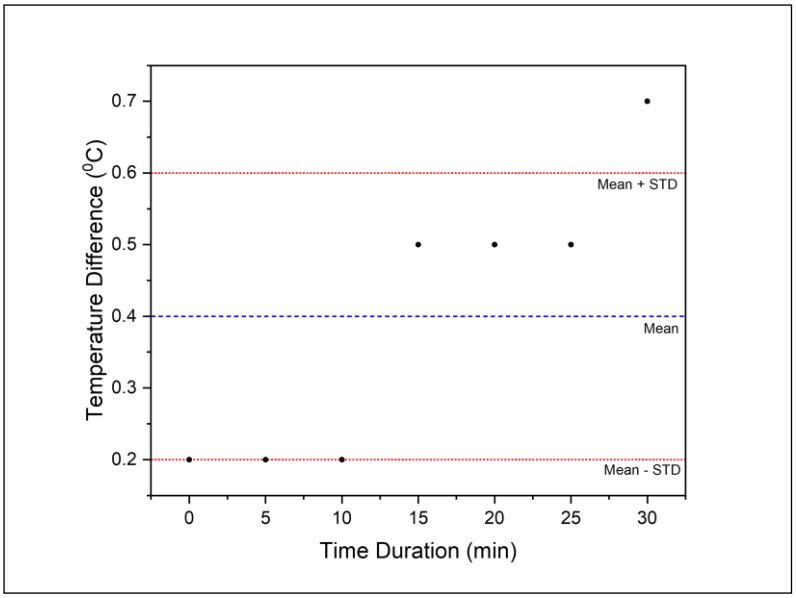


Figure 4.81 Mean Temperature Difference with STD for Cold Condition

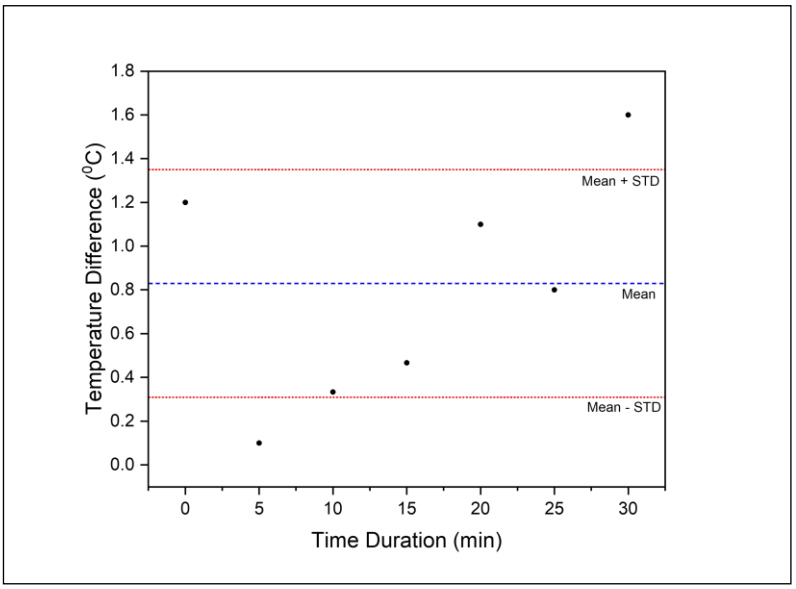


Figure 4.82 Mean Temperature Difference with STD for Room Condition

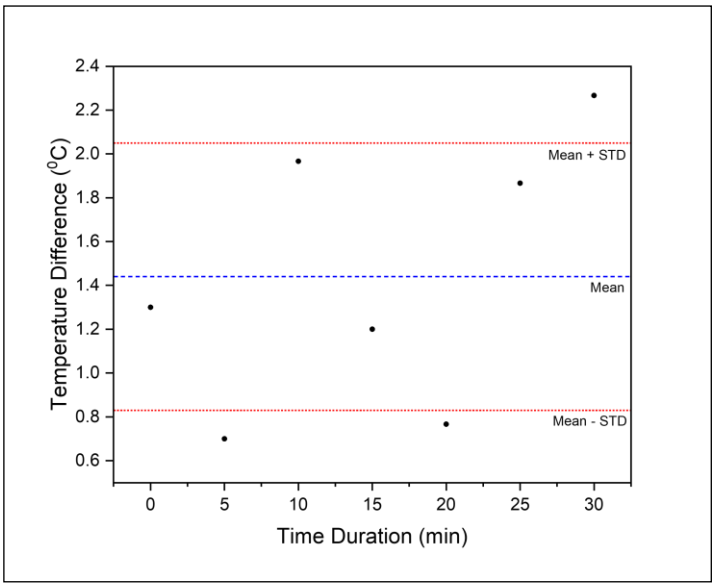


Figure 4.83 Mean Temperature Difference with STD For Hot Condition

4.6.2 Verification of Application for Temperature Monitoring of Food Packaging

To verify the practical applicability of the D4-HGS NFC tag for temperature monitoring in food packaging, the tag was attached to various food products with different storage temperature requirements and packaging structures. The objective of this verification was to assess the tag's detection accuracy, reading range stability, and the impact of packaging materials and food surfaces on NFC performance. The measurements were conducted using the setup described in Section 3.8.3 and Section 3.9.3, with the experiment evaluating key parameters such as tag detection capability, the effect of packaging type (plastic, carton, aluminum foil) on NFC sensitivity, the impact of surface curvature on readability, and the influence of food storage temperature on NFC antenna impedance matching and reading range.

The D4-HGS tag was attached to various types of food, as depicted in Figure 4.84. The packaging types and their corresponding recommended storage temperature are listed in Table 4.24. Based on the measurement, variations in reading range were observed, influenced by factors such as packaging material, the surface structure of the food items, and the temperature of the food packaging under different storage conditions, including cold, room temperature, and hot, as shown in Figure 4.85. The results confirmed that the D4-HGS tag was successfully detected across all food types at their respective storage temperatures, except for lasagna in aluminium foil packaging.

Notably, food items with curved surfaces, such as apples, yoghurt cups, and peanut butter jars, exhibited a slightly reduced reading range, measured between 1.4 cm and 1.6 cm, compared to 2.1 cm for flat plastic-packaged bread items. This reduction occurred due to the lower effective surface area of the NFC tag being exposed to the reader, which weakened the inductive coupling. Despite this limitation, the tag remained detectable, validating its feasibility for curved packaging applications.

The packaging material also played a role in NFC performance. Plastic packaging, used for bread bags, apples, yoghurt containers, and carton boxes, such as those used for pizza, did not have a significant effect on tag detection and allowed for consistent reading range performance. However, the most significant reduction in NFC readability was observed in aluminium foil packaging, particularly in lasagna containers, due to the existence of eddy current, as discussed in Section 4.4.2.1. To mitigate this issue, the most suitable magnetic sheet for food packaging applications, as discussed in Section 4.4.3.2, which is amorphous, was incorporated at the back of the D4-HGS NFC tag, as depicted in Figure 4.86. This addition effectively reduced the eddy current effect, enabling successful tag detection at a reduced but functional read range of 1.2 cm. These results demonstrate that while aluminium packaging presents challenges for NFC applications, strategic design modifications, such as magnetic shielding, can improve detection performance.

Another crucial factor affecting NFC performance was food temperature. The hot delivered pizza, despite having a flat carton box surface, exhibited a lower reading range of 1.7 cm, compared to 2.1 cm for bread at room temperature. This reduction is probably due to the increase in antenna resistance and inductance at high temperatures, resulting in slight frequency shifts and weaker inductive coupling with the reader. This finding aligns with the previous impedance analysis results in Section 4.4.2.3, which demonstrated temperature-dependent resistance and inductance variations affecting NFC performance.

Overall, the D4-HGS NFC tag was successfully detected across all tested food types, confirming its effectiveness for temperature monitoring in food packaging. While variations in reading range and detection efficiency were observed, particularly for curved surfaces, metal packaging, and high-temperature conditions, these remained within acceptable limits. This verification highlights the D4-HGS NFC tag's suitability for real-time monitoring of food packaging temperatures, ensuring compliance with food safety and quality control requirements in supply chain applications.

Table 4.24
Several Types of Food with Various Packaging Types and Storage Temperature

Food	Packaging Type	Storage Temperature [ºC]
Apple	Plastic	0 – 4
Yogurt	Plastic	2 – 6
Peanut butter	Plastic	25 (Room temperature)
Bread	Plastic	25 (Room temperature)
Pizza	Carton box	55 – 70 (hot)
Lasagna	Aluminium foil	55 – 70 (hot)

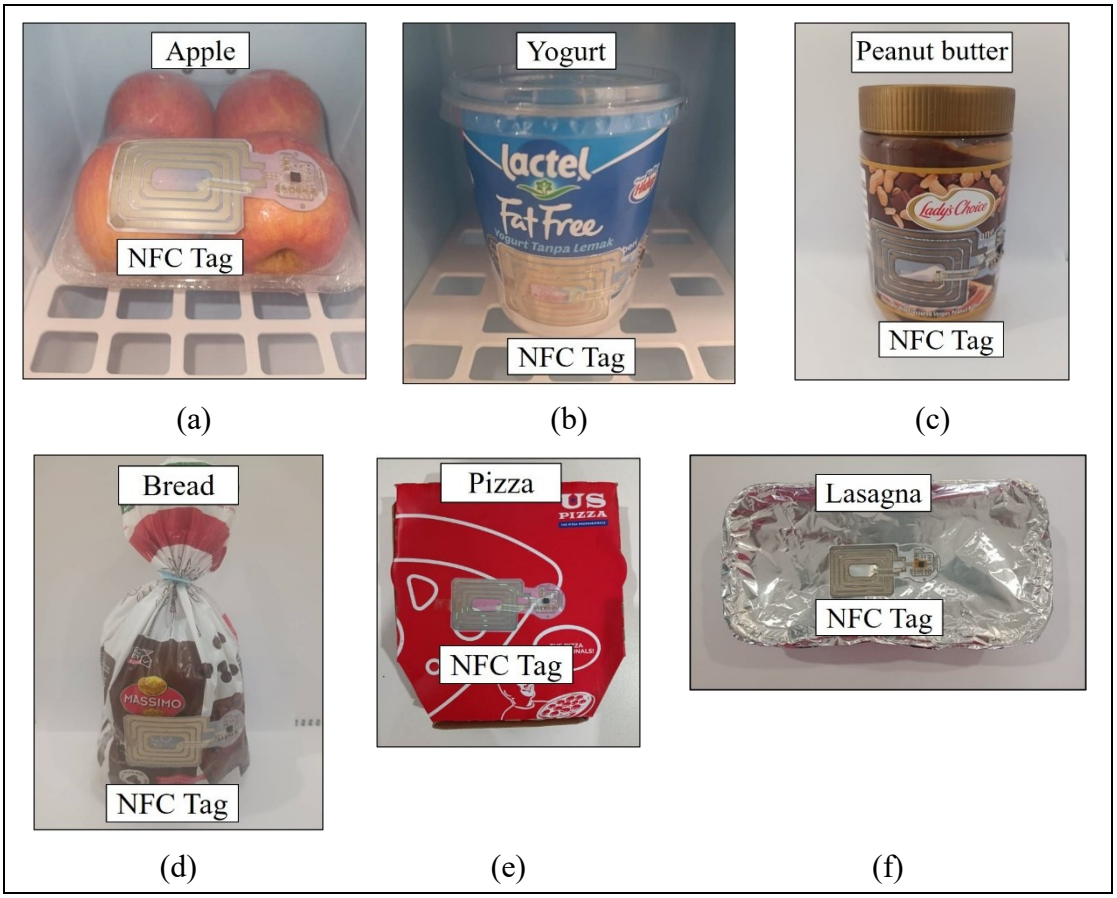


Figure 4.84 NFC Tag Attached to Different Types of Foods: (a) Apple, (b) Yoghurt, (c) Peanut Butter Jar, (d) Bread, (e) Pizza, and (f) Lasagna

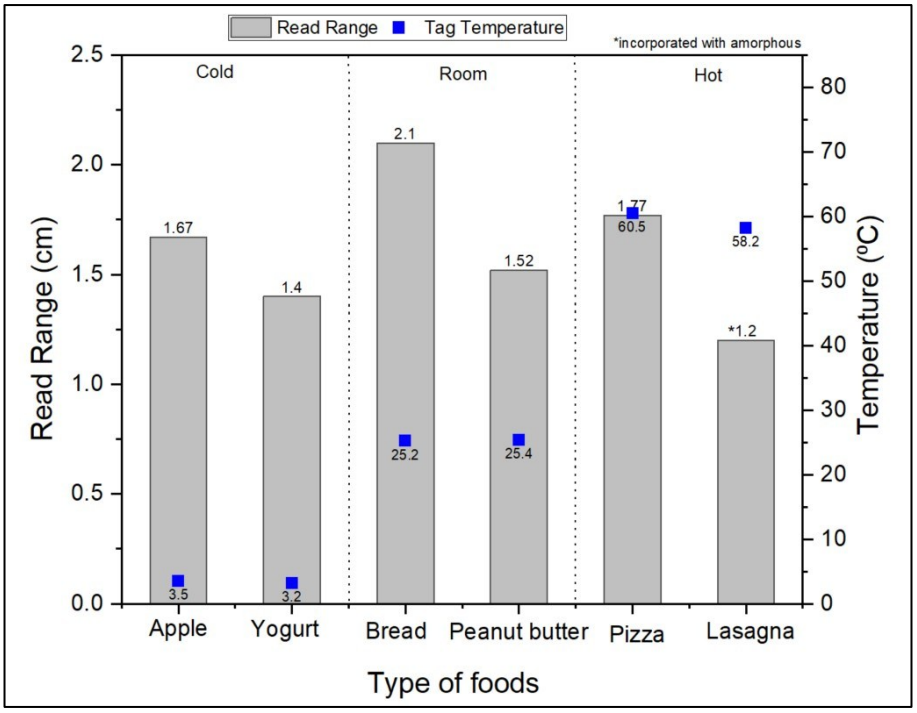


Figure 4.85 The Measured Tag Reading Range and Temperature for Various Types of Foods at Three Temperature Ranges - Cold, Room, and Hot Temperatures

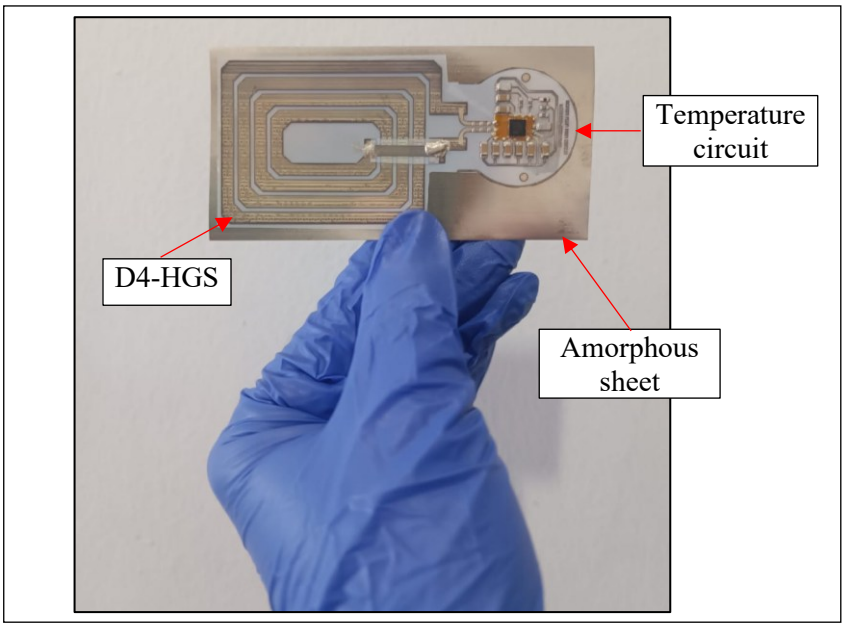


Figure 4.86 D4-HGS NFC Tag with Temperature Sensing Circuit Incorporated with an Amorphous Sheet

4.7 Summary

In this chapter, the performance of the printed NFC tag antenna made from various conductive materials, including SC, HGS, and HCG, was evaluated. The

characteristics of each conductive material were analyzed based on conductivity values, surface morphology, surface roughness, and material thickness. Among these, HGS exhibits the highest conductivity, followed by SC and HCG. The high conductivity of HGS material is attributed to its dense structure and strong attachment of rGO and AgNPs, which facilitates efficient electron transport. However, despite its high conductivity, HGS suffers from extremely low thickness, which contributes to a significantly high antenna resistance.

To address this issue, coil antenna design optimization was conducted through geometrical modifications, including increasing the coil width and reducing the number of turns, which evolved from Design 1 to Design 4 to minimize antenna resistance. Among all designs, the D4-HGS antenna demonstrated the best performance, achieving the highest reading range of 3 cm while also achieving a 20% size reduction compared to the reference Design 1 antenna. Additionally, optimizing the external tuning circuit using Optenni Lab software was a crucial step in achieving an optimum antenna system for operation at 13.56 MHz. Based on the investigation, the PCSC tuning topology was selected as the most optimum configuration to be incorporated into the antenna design in CST simulation, as it minimizes parasitic effects and reduces the complexity of the tuning circuit.

The printed antennas fabricated using different printing methods were also verified through connectivity testing, ensuring the reliability of the printed coil antennas in receiving signals and being inductively coupled with the reader. Based on the measurements, the HCG material exhibited extremely high resistance values, exceeding the acceptable threshold for functional printed conductive lines. This significantly affected the detection performance of the antenna printed with HCG materials. In contrast, antennas printed using SC and HGS materials exhibited reliable resistance values and were successfully detected within a range of 2 cm to 3 cm using an NFC-enabled smartphone as a reader. Therefore, only the antennas printed using SC and HGS materials were selected for robustness analysis.

During the bending analysis, both D2-SC and D4-HGS exhibited minimal frequency shifting as the bending angle increased from 63.7 ° to 190.9 °, corresponding to a reduction in cylinder radius from 4.5 cm to 1.5 cm. However, the measured tag reading range decreased from 2 cm to 0.5 cm for the D2-SC antenna and from 2.4 cm to 1.3 cm for the D4-HGS antenna. This reduction is attributed to the decrease in the magnetic field induced in the tag antenna, as the effective antenna surface area becomes

less accessible due to bending. Nevertheless, the D4-HGS reading range remains within the typical range for NFC communication (greater than 1 cm), indicating that the antenna maintains its robustness under bending conditions.

The D4-HGS tag antennas was also evaluated for other sensitivity effects, including the influence of various packaging materials, moisture, and temperature variations. The sensitivity of the tag to the metal surfaces, such as aluminium foil packaging, was mitigated by introducing a magnetic sheet between the tag antenna and the metal surface. Among the three types of magnetic sheets investigated, the amorphous sheet was identified as the most suitable for integration with the tag antenna in food packaging applications. Despite achieving a lower reading range compared to ferrite and nanocrystalline sheets, the amorphous sheet remains functional within the required NFC operating range. Additionally, it offers high flexibility and good thermal stability, which are essential for reliable attachment in food packaging for temperature monitoring applications.

Finally, the developed NFC tag antenna with the temperature sensor circuit, both fabricated using HGS material, was verified and tested to ensure system functionality and reliability. Further enhancements to the temperature monitoring app were also conducted to improve the accuracy of temperature readings for the D4-HGS tag antenna with the temperature sensor circuit. Temperature-specific calibration was applied using two phases of linear regression to normalize sensor readings for accurate NFC-based temperature monitoring. The reliability of the system was assessed across different temperature ranges, including cold, room, and hot, which represent typical storage and transportation conditions for food products. The system demonstrated reliable performance across all conditions, with the mean temperature difference compared to the reference temperature remaining below 2°C, which is within the acceptable range for food packaging temperature monitoring applications.

The comparison of the proposed D4-HGS tag with recently published graphene-based NFC tags is shown in Table 4.25. The proposed conductive material, hybrid graphene-silver, exhibits the highest conductivity value compared to other graphene-based materials from previous work. Despite its lower printed thickness of 1 μm, the proposed tag achieves performance comparable to other graphene-based NFC tags, particularly in terms of read range and application. Although its reading range is lower than that of [13], it still meets the required range for an NFC tag when detected by a smartphone, typically between 1 cm and 5 cm. The low thickness of printed graphene-

based conductive materials also offers advantages in terms of flexibility, lightweight design, and ease of printing for the NFC tag.

Regarding size, most tags from previous work are bulkier than the proposed tag, which may limit their attachment to specific items. Additionally, the integration of the tag antenna with a flexible temperature monitoring circuit makes it suitable for attachment to conformal structures, unlike the tags in [58] and [59], which have sensor circuits mounted on PCB substrates, reducing their flexibility. Meanwhile, the tags presented in [62] and [13] only integrate with the NFC chip without any available sensors.

Table 4.25
Comparison of the Graphene-Based NFC Tag Antenna with the Proposed Tag

Ref	**Material (substrate)**	**Conductivity (S/m) / thickness**	**Ant Size (mm^2)**	**Read range (cm)**	**Reader**	**Reader spec (output power)**	**NFC Chip (min input power)**	**Application**	**Integrate circuit/ sensor**
This work	Hybrid Graphene Silver (PET)	3.95 x10^6 / 1 µm	50x40	3	Smart-phone Xiaomi 11T	20 dBm - 23 dBm (100 mW-200 mW)	RF430FRL 152H Texas Instrument (2.85 mW)	Temp Monitoring	Yes (Flex)
[62]	Stacked graphene multilayer (G-paper) (PET, PEN, PC, PVC, paper & silk)	4.2x10^5 / 55 µm	75x45	Few cm	ST Micro CR95HF	55 mW - 230mW	NXP ICODE SL2S2002 (40 µW)	Smartcard, wearable bracelet	No
[13]	GO-assembled films (PET)	~10^6 / 25 µm	80x50	7.5	Voyantic Tagformance	-10 dBm to 25 dBm (10 mW to 316 mW)	NXP ICODE SL2S2602 (40 µW)	Wearable bracelet, smart card	No
[58]	Graphene flakes (paper)	3.33 x10^5 / NA	74x53	-	Texas Instrument TRF7970A EVM	20 dBm - 23 dBm (100 mW-200 mW)	RF430FRL 152H Texas Instrument (2.85 mW)	Photosensor	Yes (PCB)
[59]	Graphene laminate (graphene nano flakes)	3.7 x 10^4 / 7.8 µm	65x55	2.5	Texas Instrument TRF7970A EVM	20 dBm - 23 dBm (100 mW-200 mW)	RF430FRL 152H Texas Instrument (2.85 mW)	Temp Monitoring	Yes (PCB)

CHAPTER 5
CONCLUSION AND FUTURE WORK

5.1 Conclusion

This study successfully developed a printed graphene-based NFC tag antenna for food packaging temperature monitoring. It demonstrated the feasibility of the hybrid graphene silver (HGS) conductive ink and compared its electrical and mechanical behaviour with silver conductor (SC) and hybrid carbon graphene (HCG) inks, while establishing practical design and fabrication guidelines. The characterization results revealed that HGS exhibited the highest conductivity (3.95×10^6 S/m), although its very thin printed layer (1 μm) required antenna design optimisation to reduce antenna resistance. Through structural modifications and optimization, including widening the coil trace and reducing the number of turns, the proposed D4-HGS antenna achieved an 88% reduction in series resistance, a 27% increase in reading range, and a 20% reduction in overall size compared to the initial design.

The robustness of the D4-HGS antenna was evaluated based on flexibility, sensitivity to different packaging materials, a moist environment, and temperature variations. During flexibility testing, the D4-HGS tag antenna was bent at various angles, ranging from 63° to 190°, and its performance was assessed in terms of frequency shift and tag reading range. For comparison, a reference SC-based Design 2 antenna (D2-SC) was also tested. Both antenna designs exhibited a similar trend in results, where increasing the bending angle reduced the tag reading range due to a decrease in the antenna's accessible surface, which in turn reduced the induced magnetic field. The D4-HGS antenna showed a 57% reduction in reading range (from 3 cm to 1.3 cm) at a maximum bending angle of 190°, while D2-SC exhibited a 75% reduction (from 2.2 cm to 0.5 cm). Despite this reduction, the D4-HGS antenna maintained a reading range above 1 cm, confirming its robustness for curved surfaces.

Regarding sensitivity to packaging materials, the D4-HGS antenna performed reliably on plastic, glass, and carton box surfaces but was significantly affected by metallic structures, such as aluminium foil. To address this issue, a magnetic sheet was incorporated into the tag antenna design to ensure readability on metallic surfaces. A comparative study of ferrite, amorphous, and nanocrystalline magnetic sheets was

conducted, and amorphous magnetic sheets were identified as the most suitable for temperature monitoring applications due to their high flexibility, durability, and good thermal stability. While the reading range achieved with the amorphous sheet was lower than that of ferrite and nanocrystalline sheets, it was still within the required NFC operational range.

The D4-HGS tag antenna's sensitivity to moisture was also evaluated. Exposure to moisture caused a degradation in reading range, though the tag antenna remained detectable at a short range and did not fully deteriorate as it did when placed on metallic surfaces. To mitigate the effects of moisture, the tag antenna was encapsulated with a PET shrink wrap insulator, which prevented direct contact with water. As a result, the measured reading range improved by approximately 38% compared to the non-encapsulated tag antenna. For temperature sensitivity, it was observed that an increase in temperature influenced the electrical properties of the antenna, leading to a rise in both antenna inductance and resistance.

Furthermore, the D4-HGS tag antenna was also successfully integrated with a flexible temperature sensor circuit fabricated using the same HGS material. The development process, procedures, and guidelines for integrating the D4-HGS tag antenna with the temperature sensor circuit were outlined. A key challenge in this integration was mounting the VQFN-type NFC chip onto the printed HGS circuit, which was resolved using a double-layer chip method. Additionally, the temperature monitoring app was enhanced through temperature-specific calibration method, ensuring accurate temperature readings for both graphene- and metal-based tags. Based on verification with various food products, different packaging materials, and storage temperature, the developed NFC system demonstrated high reliability, with the tag being detected at a minimum distance of 1 cm, even when placed on metallic surfaces with the aid of a magnetic sheet.

Overall, all research objectives were successfully achieved, and the findings confirm that graphene-based printed NFC antennas, when optimally designed and protected, can function as robust, battery-less solutions for temperature monitoring. This research demonstrates strong potential for real-world and industrial implementation in smart food packaging, where the proposed tag enables real-time temperature monitoring throughout storage and distribution. By allowing temperature information to be accessed using standard smartphones, the system supports improved quality assurance across the supply chain. In cold chain logistics, the validated

performance under bending, moisture, temperature variation, and metallic surface conditions confirms its suitability for monitoring perishable goods during transportation and storage. Furthermore, the use of printable graphene-based conductive materials promotes lightweight, flexible, and environmentally friendly smart labels that align with sustainable packaging initiatives and scalable manufacturing practices.

5.2 Research Contributions

This research makes several significant contributions to the field of printed NFC tag antennas for food packaging temperature monitoring applications, particularly in the development, optimization, and validation of graphene-based NFC tag antennas. The key contributions are as follows:

i) Development and Optimization of a Graphene-Based NFC Tag Antenna

This research conducted a systematic evaluation of the newly developed HGS ink as an alternative to metal-based conductive materials for NFC tag applications. By analysing the electrical and structural limitations of HGS, including its low printed thickness and resulting high antenna resistance, this study introduced a geometry optimization approach (increasing coil width and reducing the number of turns). The resulting D4-HGS design achieved an 88% reduction in resistance, a 27% improvement in reading range, and a 20% size reduction compared to the baseline, demonstrating that HGS can be a practical alternative to silver inks when appropriately optimized.

ii) Mitigation of Eddy Current Effects Using Magnetic Sheets

A comparative study of three types of magnetic sheets (ferrite, amorphous, and nanocrystalline) incorporated with a graphene-based NFC tag was conducted, and a validated equivalent circuit (EC) model was introduced to predict tag performance on metal surfaces. This model was designed to analyze the relationship between the physical structure and electrical behaviour of the tag antenna when attached to a metal plate with a magnetic sheet. The model parameters were extracted and cross-verified with CST simulations, showing strong agreement and providing the first structured design-validation workflow for NFC tag tuning on metallic packaging.

iii) Procedure of Fabrication for HGS-based Tag

Previous studies offered limited practical guidance on printing with newly developed HGS material and integrating fine-pitch NFC chips. This research established a step-by-step fabrication and integration guideline, including strategies for improving print quality and overcoming challenges in mounting VQFN-type chips through a double-layer chip method. These guidelines are critical for researchers and manufacturers aiming to adopt hybrid graphene silver inks in antenna fabrication and flexible electronics.

iv) Enhancement of the Temperature Monitoring App

The temperature monitoring app was enhanced to be compatible with both metal-based and graphene-based NFC tag antennas. Initially, temperature readings from the graphene-based tag showed deviations when using Texas Instruments' temperature monitoring app. To resolve this issue, a temperature-specific calibration method was applied to normalize the sensor readings. The calibrated results demonstrated that the temperature readings of the D4-HGS tag closely aligned with reference values, thereby improving monitoring accuracy and demonstrating real-world applicability

5.3 Future Work

While this research has provided significant insights and advancements, several areas could be explored in future studies to enhance the functionality, reliability, and integration of printed graphene-based NFC tag antennas for food temperature monitoring applications:

i) Ink optimization

The performance of the NFC tag antenna is closely related to the electrical conductivity, surface uniformity, and adhesion of the printed ink. In this study, a hybrid graphene-silver (HGS) ink was utilised, demonstrating promising conductivity and flexibility. However, further improvements could be made to reduce the sheet resistance and enhance ink adhesion to the substrate. Future work could focus on optimizing the ink formulation, including the ratio of graphene to silver nanoparticles, as well as

exploring the use of alternative binders and solvents to improve printability and adhesion.

ii) Implementation of stretchable substrates

In this research, only the PET substrate, which is non-stretchable, was used to print the HGS conductive ink due to limitations of the inkjet printer used. Thus, the effect of antenna performance under mechanical deformation, such as stretching, could not be analyzed. For future studies, stretchable substrates such as polyvinyl alcohol (PVA) and thermoplastic polyurethane (TPU) could be used in combination with more suitable printing techniques, such as direct ink writing (DIW). This would enable the evaluation of antenna performance under strain and bending, particularly for integration in flexible and stretchable packaging applications.

iii) Long-Term durability testing

Extended environmental testing can be conducted to assess the long-term reliability of the NFC tag in real-world food packaging conditions, including extreme temperature and humidity cycles. Additionally, chemical resistance testing in the presence of food-related contaminants, such as oils, acids, and cleaning agents, should be performed to validate the tag's robustness and durability for practical food safety monitoring applications.

iv) Multi-sensor integration

To further enhance the functionality of the NFC tag antenna for food safety applications, additional sensing capabilities could be integrated alongside temperature monitoring. For example, pH sensors and gas sensors (e.g., for detecting ammonia, or CO_2) could be incorporated to monitor food freshness and spoilage. These multi-sensor tags would provide a more comprehensive assessment of food quality, enable early detection of spoilage and decomposition, and enhance consumer safety. The integration of multiple sensors would require careful consideration of circuit design, power management, and data handling, which can be addressed in future work.

REFERENCES

[1] W. H. Organization, “WHO: Food safety.” Accessed: Dec. 02, 2024. [Online]. Available: https://www.who.int/news-room/fact-sheets/detail/food-safety

[2] P. Müller and M. Schmid, “Intelligent Packaging in the Food Sector: A Brief Overview,” *Foods*, vol. 8, no. 1, p. 16, Jan. 2019, doi: 10.3390/foods8010016.

[3] P. Escobedo, M. Bhattacharjee, Fatemeh Nikbakhtnasrabadi, and Ravinder Dahiya, “Flexible Strain and Temperature Sensing NFC Tag for Smart Food Packaging Applications,” *IEEE Sens. J.*, vol. 21, no. 23, pp. 26406–26414, 2021, doi: 10.1109/JSEN.2021.3100876.

[4] National Research Council (US) Subcommittee on Microbiological Criteria, *An Evaluation of the Role of Microbiological Criteria for Foods and Food Ingredients*. National Academy Press, 1985.

[5] T. B. Nguyen, T. H. Nguyen, and W. Y. Chung, “Battery-free and noninvasive estimation of food ph and co2 concentration for food monitoring based on pressure measurement,” *Sensors (Switzerland)*, vol. 20, no. 20, pp. 1–12, 2020, doi: 10.3390/s20205853.

[6] T. B. Nguyen, T. H. Nguyen, and W. Y. Chung, “Battery-free and noninvasive estimation of food ph and co2 concentration for food monitoring based on pressure measurement,” *Sensors (Switzerland)*, vol. 20, no. 20, pp. 1–12, 2020, doi: 10.3390/s20205853.

[7] S. Kapse, P. Kedia, A. Kumar, S. Kausley, P. Pal, and B. Rai, “A non-invasive method for detection of freshness of packaged milk,” *J. Food Eng.*, vol. 346, p. 111424, 2023, doi: 10.1016/j.jfoodeng.2023.111424.

[8] D. Pigini and M. Conti, “NFC-Based Traceability in the Food Chain,” *Sustainability*, vol. 9, no. 10, p. 1910, Oct. 2017, doi: 10.3390/su9101910.

[9] B. B. Maskey *et al.*, “A Smart Food Label Utilizing Roll-to-Roll Gravure Printed NFC Antenna and Thermistor to Replace Existing ‘Use-By’ Date System,” *IEEE Sens. J.*, vol. 20, no. 4, pp. 2106–2116, 2020, doi: 10.1109/JSEN.2019.2948752.

[10] V. Le, E. Mackensen, Patrick Moser, and Ulrich Lemmer, “A Comparison of Printed Flexible RFID / NFC Antennas for a Microelectronic Measurement System,” in *2019 IEEE International Conference on RFID Technology and Applications (RFID-TA)*, 2019, pp. 49–54.

[11] W. Pachler, J. Grosinger, B. Wolfgang, G. Holweg, K. Popovic, and A. Bl, “A Silver Inkjet Printed Ferrite NFC Antenna,” in *2014 Loughborough Antennas and Propagation Conference (LAPC)*, 2014, pp. 10–11.

[12] J. Machiels, A. Verma, R. Appeltans, M. Buntinx, E. Ferraris, and W. Deferme, “Printed Electronics (PE) As An enabling Technology to Realize Flexible Mass Customized Smart Applications,” *Procedia CIRP*, vol. 96, pp. 115–120, 2020, doi: 10.1016/j.procir.2021.01.062.

[13] S. Li and R. Song, “Wearable near-field communication bracelet based on highly conductive graphene-assembled films,” *International Journal of RF and Microwave Computer Aided Engineering*, no. July 2020, pp. 9–11, 2020, doi: 10.1002/mmce.22479.

[14] A. Lamminen *et al.*, “Graphene-Flakes Printed Wideband Elliptical Dipole Antenna for Low-Cost Wireless Communications Applications,” *IEEE Antennas Wirel. Propag. Lett.*, vol. 16, no. March, pp. 1883–1886, 2017, doi: 10.1109/LAWP.2017.2684907.

[15] A. M. Díez-Pascual and A. Rahdar, “Graphene-Based Polymer Composites for Flexible Electronic Applications,” *Micromachines (Basel).*, vol. 13, no. 7, p. 1123, Jul. 2022, doi: 10.3390/mi13071123.

[16] Y. Z. N. Htwe and M. Mariatti, “Printed graphene and hybrid conductive inks for flexible, stretchable, and wearable electronics: Progress, opportunities, and challenges,” *Journal of Science: Advanced Materials and Devices*, vol. 7, no. 2, p. 100435, Jun. 2022, doi: 10.1016/j.jsamd.2022.100435.

[17] M. Zolfagharloo-Koohi and M. Neshat, “Antenna efficiency in graphene-based THz photoconductive antennas,” *22nd Iranian Conference on Electrical Engineering, ICEE 2014*, no. Icee, pp. 1587–1590, 2014, doi: 10.1109/IranianCEE.2014.6999789.

[18] M. Tamagnone, J. S. Gómez-Díaz, J. R. Mosig, and J. Perruisseau-Carrier, “Analysis and design of terahertz antennas based on plasmonic resonant graphene sheets,” *J. Appl. Phys.*, vol. 112, no. 11, 2012, doi: 10.1063/1.4768840.

[19] P. Kopyt *et al.*, “Graphene-Based Dipole Antenna for a UHF RFID Tag,” *IEEE Trans. Antennas Propag.*, vol. 64, no. 7, pp. 2862–2868, 2016, doi: 10.1109/TAP.2016.2565696.

[20] X. Huang, T. Leng, X. Zhang, J. C. Chen, and K. H. Chang, “Binder-free highly conductive graphene laminate for low cost printed radio frequency applications,”

Appl. Phys. Lett., vol. 203105, no. May, pp. 19–23, 2015, doi: 10.1063/1.4919935.

[21] M. Akbari *et al.*, "Fabrication and Characterization of Graphene Antenna for Low - Cost and Environmentally Friendly RFID tags," *IEEE Wireless and Propagation Letters*, vol. 1, no. c, pp. 10–13, 2015, doi: 10.1109/LAWP.2015.2498944.

[22] R. Busquets, *Emerging Nanotechnologies in Food Science*. Elsevier, 2017.

[23] W. Yang, X. Cheng, Z. Guo, Q. Sun, J. Wang, and C. Wang, "Design, fabrication and applications of flexible RFID antennas based on printed electronic materials and technologies," *J. Mater. Chem. C Mater.*, vol. 11, no. 2, pp. 406–425, Nov. 2023, doi: 10.1039/D2TC03736J.

[24] L. P. Padhye *et al.*, "Silver contamination and its toxicity and risk management in terrestrial and aquatic ecosystems," *Science of The Total Environment*, vol. 871, p. 161926, May 2023, doi: 10.1016/J.SCITOTENV.2023.161926.

[25] L. Mo *et al.*, "Nano-Silver Ink of High Conductivity and Low Sintering Temperature for Paper Electronics," *Nanoscale Res. Lett.*, vol. 14, no. 1, pp. 1–11, Jun. 2019, doi: 10.1186/S11671-019-3011-1/FIGURES/11.

[26] M. Boada, A. Lazaro, R. Villarino, and D. Girbau, "Battery-Less NFC Sensor for pH Monitoring," *IEEE Access*, vol. 7, pp. 33226–33239, 2019, doi: 10.1109/ACCESS.2019.2904109.

[27] A. Lazaro, M. Boada, R. Villarino, and D. Girbau, "Feasibility Study on the Reading of Energy-Harvested Implanted NFC Tags Using Mobile Phones and Commercial NFC IC," in *2020 IEEE MTT-S International Microwave Biomedical Conference (IMBioC)*, IEEE, Dec. 2020, pp. 1–3. doi: 10.1109/IMBIoC47321.2020.9385033.

[28] S. Kang, M. Song, J. Kim, and J. W. Lee, "Near-Field Communication in Biomedical Applications," pp. 1–17, 2021.

[29] M. Stoppa and A. Chiolerio, "Wearable Electronics and Smart Textiles: A Critical Review," pp. 11957–11992, 2014, doi: 10.3390/s140711957.

[30] M. Bhattacharyya, W. Gruenwald, D. Jansen, L. Reindl, and J. Aghassi-Hagmann, "An Ultra-Low-Power RFID/NFC Frontend IC Using 0.18 μm CMOS Technology for Passive Tag Applications," *Sensors*, vol. 18, no. 5, p. 1452, May 2018, doi: 10.3390/s18051452.

[31] P. Lathiya and J. Wang, “Near-Field Communications (NFC) for Wireless Power Transfer (WPT): An Overview,” in *Wireless Power Transfer – Recent Development, Applications and New Perspectives*, IntechOpen, 2021. doi: 10.5772/intechopen.96345.

[32] E. P. Putra, Fifilia, and H. Juwitasary, “Trend of NFC Technology for payment transaction,” *Telkomnika (Telecommunication Computing Electronics and Control)*, vol. 16, no. 2, pp. 795–802, Apr. 2018, doi: 10.12928/TELKOMNIKA.v16i2.8441.

[33] A. R. Solution, “Active vs. Passive RFID.” [Online]. Available: http://atlasrfid.com/auto-id-education/active-vs-passive-rfid/

[34] M. Ward, R. Van Kranenburg, W. Marsterson, and A. Hopkinson, “RFID : Frequency , standards , adoption and innovation,” *JISC Technology and Standard Watch*, no. May, 2006.

[35] M. Kaur, M. Sandhu, N. Mohan, and P. S. Sandhu, “RFID Technology Principles , Advantages , Limitations & Its Applications,” *International Journal of Computer and Electrical Engineering*, vol. 3, no. 1, pp. 151–157, 2011.

[36] International Organization for Standardization, “ISO/IEC 18092: International Standard -Telecommunications and information exchange between systems - Near Field Communication Interface and Protocol 1 (NFCIP-1),” Dec. 2023.

[37] International Organization for Standardization, “ISO/IEC 14443: Identification cards – Contactless integrated circuit cards – Proximity cards’. ,” 2016.

[38] International Organization for Standardization, “ISO/IEC 15693: Identification cards — Contactless integrated circuit cards — Vicinity cards’,” 2010.

[39] Ekta Desai; and Mary Grace Shajan, “A Review on Operating Modes of Near Field Communication,” *International Journal of Engineering and Advanced Technology (IJEAT)*, vol. 2, no. 2, 2012, [Online]. Available: http://www.techspot.com/guides/385-everything-about-nfc/

[40] J. I. Cairo, J. Bonache, F. Paredes, and F. Martin, “Reconfigurable System for Wireless Power Transfer (WPT) and Near Field Communications (NFC),” *IEEE Journal of Radio Frequency Identification*, vol. 1, no. 4, pp. 253–259, Dec. 2017, doi: 10.1109/JRFID.2018.2801120.

[41] T. V. Prabhakar, U. Mysore, U. Saini, K. J. Vinoy, and B. Amruthur, “NFC for Pervasive Healthcare Monitoring,” *Proceedings of the IEEE International*

Conference on VLSI Design, vol. 2015-Febru, no. February, pp. 75–80, 2015, doi: 10.1109/VLSID.2015.18.

[42] A. Lazaro, M. Boada, R. Villarino, and D. Girbau, "Study on the Reading of Energy-Harvested Implanted NFC Tags Using Mobile Phones," *IEEE Access*, vol. 8, pp. 2200–2221, 2020, doi: 10.1109/ACCESS.2019.2962570.

[43] F. Tounsi *et al.*, "Variation Range of Different Inductor Topologies with Shields for RF and Inductive Sensing Applications," *Sensors*, vol. 22, no. 9, May 2022, doi: 10.3390/s22093514.

[44] N. Ibrahim, J. O. Akindoyo, and M. Mariatti, "Recent development in silver-based ink for flexible electronics," 2022, doi: 10.1016/j.jsamd.2021.09.002.

[45] J. Wiklund *et al.*, "A Review on Printed Electronics: Fabrication Methods, Inks, Substrates, Applications and Environmental Impacts," *Journal of Manufacturing and Materials Processing*, vol. 5, no. 3, p. 89, Aug. 2021, doi: 10.3390/jmmp5030089.

[46] G. Tomaszewski, P. Jankowski-Mihułowicz, J. Potencki, A. Pietrikova, and P. Lukacs, "Inkjet-printed HF antenna made on PET substrate," *Microelectronics Reliability*, vol. 129, Feb. 2022, doi: 10.1016/j.microrel.2021.114473.

[47] G. K. F. Serres *et al.*, "Eco-Friendly Metamaterial Antenna for 2.4GHz WLAN Applications," in *2020 14th European Conference on Antennas and Propagation (EuCAP)*, IEEE, Mar. 2020, pp. 1–5. doi: 10.23919/EuCAP48036.2020.9135785.

[48] Y. Kim, Byoungyoon Lee, Seungnam Yang, Inho Byun, Inbum Jeong, and S. M. Cho, "Use of copper ink for fabricating conductive electrodes and RFID antenna tags by screen printing.pdf," *Current Applied Physics*, pp. 440–478, 2012.

[49] V. Van Tran, S. Lee, D. Lee, and T.-H. Le, "Recent Developments and Implementations of Conductive Polymer-Based Flexible Devices in Sensing Applications," 2022, doi: 10.3390/polym14183730.

[50] M. Yadav, D. K. Singh, V. Ganesan, and R. Ramaraj, "Functionalization of carbon-based materials for the electrochemical sensing applications," *Versatile Solicitations of Materials Science in Diverse Science Fields*, pp. 193–215, Jun. 2021.

[51] U. Kamran, Y.-J. Heo, J. Lee, and S.-J. Park, "Functionalized Carbon Materials for Electronic Devices: A Review," *Micromachines (Basel).*, vol. 10, no. 4, p. 234, Apr. 2019, doi: 10.3390/mi10040234.

[52] M. Tamagnone, J. S. Gómez-Díaz, J. R. Mosig, and J. Perruisseau-Carrier, “Analysis and design of terahertz antennas based on plasmonic resonant graphene sheets,” *J. Appl. Phys.*, vol. 112, no. 11, 2012, doi: 10.1063/1.4768840.

[53] M. Zolfagharloo-Koohi and M. Neshat, “Antenna efficiency in graphene-based THz photoconductive antennas,” *22nd Iranian Conference on Electrical Engineering, ICEE 2014*, no. Icee, pp. 1587–1590, 2014, doi: 10.1109/IranianCEE.2014.6999789.

[54] K. Y. Shin, J. Y. Hong, and J. Jang, “Micropatterning of graphene sheets by inkjet printing and its wideband dipole-antenna application,” *Advanced Materials*, vol. 23, no. 18, pp. 2113–2118, 2011, doi: 10.1002/adma.201100345.

[55] M. Akbari, L. Sydanheimo, Y. Rahmat-Sami, J. Virkki, and L. Ukkonen, “Implementation and performance evaluation of graphene-based passive UHF RFID textile tags,” *2016 URSI International Symposium on Electromagnetic Theory, EMTS 2016*, pp. 447–449, 2016, doi: 10.1109/URSI-EMTS.2016.7571422.

[56] B. Zhang *et al.*, “Passive UHF RFID tags made with graphene assembly film-based antennas,” *Carbon N. Y.*, vol. 178, pp. 803–809, 2021, doi: 10.1016/j.carbon.2021.02.096.

[57] K Jaakkola *et al.*, “Screen-printed and spray coated graphene-based RFID transponders,” *2d Mater.*, no. March, 2020, doi: 10.48550/arXiv.1906.01089.

[58] T. Leng *et al.*, “Printed graphene/WS2 battery-free wireless photosensor on papers,” *2d Mater.*, vol. 7, no. 2, 2020, doi: 10.1088/2053-1583/ab602f.

[59] K. Pan *et al.*, “Sustainable production of highly conductive multilayer graphene ink for wireless connectivity and IoT applications,” *Nat. Commun.*, vol. 9, no. 1, p. 5197, Dec. 2018, doi: 10.1038/s41467-018-07632-w.

[60] T. Delipinar, E. A. Ozek, C. E. Kaya, S. Tanyeli, and M. K. Yapici, “Flexible Graphene Textile RFID Tags Based on Spray, Dispense and Contact Printing,” in *FLEPS 2020 - IEEE International Conference on Flexible and Printable Sensors and Systems*, Institute of Electrical and Electronics Engineers Inc., Aug. 2020. doi: 10.1109/FLEPS49123.2020.9239557.

[61] E. A. Ozek, S. Tanyeli, and M. K. Yapici, “Flexible Graphene Textile Temperature Sensing RFID Coils Based on Spray Printing,” *IEEE Sens. J.*, vol. 21, no. 23, pp. 26382–26388, 2021, doi: 10.1109/JSEN.2021.3075902.

[62] A. Scidà *et al.*, “Application of graphene-based fl exible antennas in consumer electronic devices,” *Materials Today*, vol. 21, no. 3, 2018, doi: 10.1016/j.mattod.2018.01.007.

[63] T. S. Tran, N. K. Dutta, and N. R. Choudhury, “Graphene inks for printed flexible electronics: Graphene dispersions, ink formulations, printing techniques and applications,” *Adv. Colloid Interface Sci.*, vol. 261, pp. 41–61, Nov. 2018, doi: 10.1016/J.CIS.2018.09.003.

[64] J. Liu, Y. Wang, X. Li, J. Wang, and Y. Zhao, “Graphene-Based Wearable Temperature Sensors: A Review,” *Nanomaterials*, vol. 13, no. 16, p. 2339, Aug. 2023, doi: 10.3390/nano13162339.

[65] John Compas, “Wearable Circuits,” Wearable Technology Srping 2019.

[66] R. Katragadda and P. A. N. Rao, “Bending Conditions, Conductive Materials, and Fabrication of Wearable Textile Antennas: Review,” *Smart Innovation, Systems and Technologies*, vol. 313, pp. 547–555, 2023, doi: 10.1007/978-981-19-8669-7_48.

[67] K. Lomakin *et al.*, “Impact of Surface Roughness on 3D Printed SLS Horn Antennas,” in *12th European Conference on Antennas and Propagation (EuCAP 2018)*, Institution of Engineering and Technology, 2018, pp. 876 (4 pp.)-876 (4 pp.). doi: 10.1049/cp.2018.1235.

[68] A. S. B. Mohammed *et al.*, “Mathematical model on the effects of conductor thickness on the centre frequency at 28 GHz for the performance of microstrip patch antenna using air substrate for 5G application,” 2021, doi: 10.1016/j.aej.2021.04.050.

[69] L. Sun, S. S. Park, D. Sheberla, and M. Dinc, “Measuring and Reporting Electrical Conductivity in Metal-Organic Frameworks: Cd2(TTFTB) as a Case Study,” *J. Am. Chem. Soc.*, vol. 138, no. 44, Oct. 2016, doi: https://doi.org/10.1021/jacs.6b09345.

[70] P. Arenas and C. Arturo, “Construction and implementation of a 4-probe measuring system to determinate the temperature dependent sheet resistance of thin films,” 2017.

[71] ASTM International, “F1711 − 96 Standard Practice for Measuring Sheet Resistance of Thin Film Conductors for Flat Panel Display Manufacturing Using a Four-Point Probe Method,” May 01, 2016, *ASTM International, West Conshohocken, PA*. doi: 10.1520/F1711-96R16.

[72] J. Cejkova, V. Prokopec, S. Brazdova, A. Kokaislova, P. Matejka, and F. Stepanek, “Characterization of copper SERS-active substrates prepared by electrochemical deposition,” *Appl. Surf. Sci.*, vol. 255, no. 18, pp. 7864–7870, Jun. 2009, doi: 10.1016/J.APSUSC.2009.04.152.

[73] G. H. Kim, E. A. Shin, J. Y. Jung, J. Y. Lee, and C. K. Lee, “Effect of Spray Parameters on Electrical Characteristics of Printed Layer by Morphological Study,” *Processes*, vol. 10, no. 5, p. 999, May 2022, doi: 10.3390/pr10050999.

[74] G. Demeneghi, P. Gradl, J. R. Mayeur, and K. Hazeli, “Size effect characteristics and influences on fatigue behavior of laser powder bed fusion of thin wall GRCop-42 copper alloy,” *Heliyon*, vol. 10, no. 7, Apr. 2024, doi: 10.1016/j.heliyon.2024.e28679.

[75] Y. Shi, “Design and Fabrication of Fabric Near Field Antenna for Wearable Applications,” University of Manchester, 2017.

[76] H. Jeong *et al.*, “NFC-enabled, tattoo-like stretchable biosensor manufactured by ‘cut-and-paste’ method,” *Proceedings of the Annual International Conference of the IEEE Engineering in Medicine and Biology Society, EMBS*, pp. 4094–4097, 2017, doi: 10.1109/EMBC.2017.8037756.

[77] S. W. Han *et al.*, “Fatigue Behavior of Thin Cu Foils for Flexible Printed Circuit Board,” *Solid State Phenomena*, vol. 124–126, pp. 1369–1372, Jun. 2007, doi: 10.4028/WWW.SCIENTIFIC.NET/SSP.124-126.1369.

[78] Y. Ouroua, S. Abdi, and I. Bachirbey, “Rupture by impact-induced fatigue of a copper foil strip embedded in a multifunctional composite material,” *J. Compos. Mater.*, vol. 55, no. 19, pp. 2631–2643, Aug. 2021, doi: 10.1177/0021998321994327.

[79] K. Hong, J. Cho, and G. Shin, “Stretchable, Multi-Layered Stack Antenna for Smart/Wearable Electronic Applications,” *Materials*, vol. 15, no. 9, p. 3275, May 2022, doi: 10.3390/ma15093275.

[80] A. Lazaro, M. Boada, R. Villarino, and D. Girbau, “Color measurement and analysis of fruit with a battery-less NFC sensor,” *Sensors (Switzerland)*, vol. 19, no. 7, 2019, doi: 10.3390/s19071741.

[81] J. T. Reeder *et al.*, “Waterproof, electronics-enabled, epidermal microfluidic devices for sweat collection, biomarker analysis, and thermography in aquatic settings,” *Sci. Adv.*, vol. 5, no. 1, Jan. 2019, doi: 10.1126/sciadv.aau6356.

[82] C. M. Awuah, P. Danuor, J. I. Moon, and Y. B. Jung, “Novel coil design and analysis for high-power wireless power transfer with enhanced Q-factor,” *Sci. Rep.*, vol. 13, no. 1, Dec. 2023, doi: 10.1038/s41598-023-31389-y.

[83] D. Paret, *Antenna Designs for NFC Devices*. 2016. doi: 10.1002/9781119145301.

[84] Voltera, “Voltera Conductor 2 (1000388),” Jul. 2020.

[85] Dycotec Materials, “DM-GRA-9100S.” [Online]. Available: www.dycotecmaterials.com

[86] Infineon, “Antenna design guide for NLM001x,” 2020.

[87] S. Kolev, “Designing a NFC system,” in *2021 56th International Scientific Conference on Information, Communication and Energy Systems and Technologies, ICEST 2021 - Proceedings*, IEEE, 2021, pp. 111–113. doi: 10.1109/ICEST52640.2021.9483482.

[88] Avery Dennison, “AD Block Lite,” 2021.

[89] Eccel Technology Ltd, “External RFID antenna 13.56 MHz,” Mar. 2020.

[90] K. F. Warnick, R. B. Gottula, S. Shrestha, and J. Smith, “Optimizing power transfer efficiency and bandwidth for near field communication systems,” *IEEE Trans. Antennas Propag.*, vol. 61, no. 2, pp. 927–933, 2013, doi: 10.1109/TAP.2012.2220325.

[91] Nordic Semiconductor, “nRF52832 NFC Antenna Tuning,” 2018.

[92] STMicroelectronics, “AN2866 Application note: How to design a 13.56 MHz customized antenna for ST25 NFC/RFID Tags,” Aug. 2021.

[93] NXP Semiconductor, “AN13219 PN7160 antenna design and matching guide,” 2022.

[94] Microchip, “Antenna Circuit Design for RFID Applications,” 2003. [Online]. Available: http://ww1.microchip.com/downloads/en/AppNotes/00710c.pdf

[95] J. Q. Zhu, Y. L. Ban, C. Y. D. Sim, and G. Wu, “NFC antenna with nonuniform meandering line and partial coverage ferrite sheet for metal cover smartphone applications,” *IEEE Trans. Antennas Propag.*, vol. 65, no. 6, pp. 2827–2835, 2017, doi: 10.1109/TAP.2017.2690532.

[96] J. Mujal *et al.*, “Inkjet printed antennas for NFC systems,” in *2010 17th IEEE International Conference on Electronics, Circuits and Systems*, IEEE, Dec. 2010, pp. 1220–1223. doi: 10.1109/ICECS.2010.5724738.

[97] Jordi Mujal, E. Ramon, and E. Diaz, “Inkjet Printed Antennas for NFC systems,” in *2010 17th IEEE International Conference on Electronics, Circuits, and Systems (ICECS)*, 2010, pp. 1220–1223.

[98] J. Grosinger, “Robustly Operating: Passive Near-Field Communication Systems in Metal Environments,” *IEEE Microw. Mag.*, vol. 24, no. 4, pp. 30–39, Apr. 2023, doi: 10.1109/MMM.2022.3233508.

[99] Moongee Cho, “Coil Antenna Design for Transmitter and Receiver for Bioelectronics,” University of Illinois at Urbana-Champaign, Urbana, Illinois, 2017.

[100] M. B. Navarro, “Battery-Less Near Field Communications (NFC) Sensors For Internet of Things (IoT) Applications,” Universitat Rovira I Virgili, 2020.

[101] B. Zhan, D. Su, S. Liu, and F. Liu, “Wearable near-field communication antennas with magnetic composite films,” *AIP Adv.*, vol. 7, no. 6, Jun. 2017, doi: 10.1063/1.4991332.

[102] NXP Semiconductors, “AN13219 PN7160 antenna design and matching guide,” Feb. 2024.

[103] P. Escobedo *et al.*, “Smart facemask for wireless CO2 monitoring,” *Nature Communications 2022 13:1*, vol. 13, no. 1, pp. 1–12, Jan. 2022, doi: 10.1038/s41467-021-27733-3.

[104] K. Finkenzeller, *RFID Handbook: Fundamentals and Applications in Contactless Smart Cards and Identification*, 3rd ed. Wiley, 2010.

[105] M. H. Misran, S. K. A. Rahim, A. A. Eteng, and G. A. E. Vandenbosch, “Assessment of Kapton-based flexible antenna for near field wireless energy transfer,” *Appl. Comput. Electromagn. Soc. J.*, vol. 32, no. 1, pp. 31–36, 2017.

[106] D. Kupreyev, K. Dautov, M. Hashmi, and M. A. Chaudhary, “High-Performance Planar Hexagonal Coil-Type Wireless Power Transfer System,” *2020 IEEE MTT-S Latin America Microwave Conference, LAMC 2020*, 2020, doi: 10.1109/LAMC50424.2021.9602805.

[107] H. Chen *et al.*, “Advances in graphene-based flexible and wearable strain sensors,” *Chemical Engineering Journal*, vol. 464, p. 142576, May 2023, doi: 10.1016/j.cej.2023.142576.

[108] Z. Xie, R. Avila, Y. Huang, and J. A. Rogers, “Flexible and Stretchable Antennas for Biointegrated Electronics,” *Advanced Materials*, vol. 32, no. 15, pp. 1–16, 2020, doi: 10.1002/adma.201902767.

[109] Y. Jiang, K. Pan, T. Leng, and Z. Hu, “Smart Textile Integrated Wireless Powered near Field Communication Body Temperature and Sweat Sensing System,” *IEEE J. Electromagn. RF Microw. Med. Biol.*, vol. 4, no. 3, pp. 164–170, 2020, doi: 10.1109/JERM.2019.2929676.

[110] S. Mukherjee, D. Kundu, and A. Khan, “Mitigation of Metal Body Proximity Effect in Magnetically Coupled HF RFID Systems,” *IEEE Journal of Radio Frequency Identification*, vol. 8, pp. 421–430, 2024, doi: 10.1109/JRFID.2024.3368882.

[111] J. Grosinger, “Robustly Operating: Passive Near-Field Communication Systems in Metal Environments,” *IEEE Microw. Mag.*, vol. 24, no. 4, pp. 30–39, Apr. 2023, doi: 10.1109/MMM.2022.3233508.

[112] B. Lee, B. Kim, F. J. Harackiewicz, S. Member, B. Mun, and H. Lee, “NFC Antenna Design for Low-Permeability Ferromagnetic Material,” *IEEE Antennas Wirel. Propag. Lett.*, vol. 13, pp. 59–62, 2014.

[113] V. Solera, A. Alcarria, P. A. Martinez, J. Victoria, R. Herraiz, and J. Torres, “Optimization of the Magnetic Shielding Selection for NFC Systems,” in *2023 International Symposium on Electromagnetic Compatibility – EMC Europe*, IEEE, Sep. 2023, pp. 1–5. doi: 10.1109/EMCEurope57790.2023.10274198.

[114] A.-I. Petrariu, V. Popa, V.-G. Gaitan, and I. Finis, “Test results for HF RFID Antenna system tuning in metal environment,” in *Proceedings of the 13th International Carpathian Control Conference (ICCC)*, IEEE, May 2012, pp. 543–546. doi: 10.1109/CarpathianCC.2012.6228704.

[115] L. J. Görtschacher, F. Amtmann, U. Muehlmann, E. Merlin, P. Priller, and J. Grosinger, “Passive HF RFID Repeater for Communicating with Tags in Metal Housings,” *IEEE Antennas Wirel. Propag. Lett.*, vol. 19, no. 9, pp. 1625–1629, Sep. 2020, doi: 10.1109/LAWP.2020.3012202.

[116] H. Saghlatoon, R. Mirzavand, M. M. Honari, and P. Mousavi, “Investigation on Passive Booster for Improving Magnetic Coupling of Metal Mounted Proximity Range HF RFIDs,” *IEEE Trans. Microw. Theory Tech.*, vol. 65, no. 9, pp. 3401–3408, Sep. 2017, doi: 10.1109/TMTT.2017.2676095.

[117] M. Xiong, X. Wei, Y. Huang, Z. Luo, and H. Dai, “Research on Novel Flexible High-Saturation Nanocrystalline Cores for Wireless Charging Systems of Electric Vehicles,” *IEEE Transactions on Industrial Electronics*, vol. 68, no. 9, pp. 8310–8320, Sep. 2021, doi: 10.1109/TIE.2020.3016259.

[118] A. Chrobak, A. Kaleta, P. Kwapuliński, M. Kubisztal, and G. Haneczok, “Magnetic Shielding Effectiveness of Iron-Based Amorphous Alloys and Nanocrystalline Composites,” *IEEE Trans. Magn.*, vol. 48, no. 4, 2012, doi: 10.1109/TMAG.2011.2172587.

[119] Y. Liu, J. Yang, F. Cao, X. Zhang, and S. Zheng, “Enhancement of Magnetic Shielding Based on Low-Noise Materials, Magnetization Control, and Active Compensation: A Review,” *Materials*, vol. 17, no. 22, p. 5469, Nov. 2024, doi: 10.3390/ma17225469.

[120] T. Björninen, L. Sydänheimo, J. Voutilainen, and L. Ukkonen, “Characterization of HF RFID tags exposed to moisture based on threshold power measurement,” in *Progress in Electromagnetics Research Symposium*, Stockholm, Sweden, Aug. 2013.

[121] M. Toivonen, T. Bjorninen, L. Sydanheimo, L. Ukkonen, and Y. Rahmat-Samii, “Impact of moisture and washing on the performance of embroidered UHF RFID tags,” *IEEE Antennas Wirel. Propag. Lett.*, vol. 12, pp. 1590–1593, 2013, doi: 10.1109/LAWP.2013.2293334.

[122] M. Lucia Scarpello, I. Kazani, C. Hertleer, H. Rogier, S. Member, and D. Vande Ginste, “Stability and Efficiency of Screen-Printed Wearable and Washable Antennas,” *IEEE Antennas Wirel. Propag. Lett.*, vol. 11, 2012, doi: 10.1109/LAWP.2012.2207941.

[123] Y. Wang *et al.*, “Effect of Temperature on Electromagnetic Performance of Active Phased Array Antenna,” *Electronics (Basel).*, vol. 9, no. 8, p. 1211, Jul. 2020, doi: 10.3390/electronics9081211.

[124] S. L. Merilampi, J. Virkki, L. Ukkonen, and L. Sydänheimo, “Testing the effects of temperature and humidity on printed passive UHF RFID tags on paper substrate,” *International Journal of Electronics*, vol. 101, no. 5, pp. 711–730, May 2014, doi: 10.1080/00207217.2013.794491.

[125] S. Maurya, “Effect of Temperature Variation on Microstrip Patch Antenna and Temperature Compensation Technique,” *International Journal of Wireless Communications and Mobile Computing*, vol. 1, no. 1, p. 35, 2013, doi: 10.11648/j.wcmc.20130101.16.

[126] T.-H. Kim, L. Mapa, D. Ramamurthy, and F. Goni, “Investigating the Effect of Temperature in RFID Technology,” in *2017 ASEE Annual Conference & Exposition Proceedings*, ASEE Conferences. doi: 10.18260/1-2--28589.

[127] A. Rollo and M. G. Gnoni, “Performance Analysis of Rfid Applications in Cold Chain Management,” in *Business Performance Measurement and Management*, Berlin, Heidelberg: Springer Berlin Heidelberg, 2010, pp. 61–71. doi: 10.1007/978-3-642-04800-5_4.

[128] J. J. Park and M. Taya, “Design of Micro-Temperature Sensor Array With Thin Film Thermocouples,” *J. Electron. Packag.*, vol. 127, no. 3, pp. 286–289, Sep. 2005, doi: 10.1115/1.1997157.

[129] T. H. Kim and S. J. Kim, “Development of a micro-thermal flow sensor with thin-film thermocouples,” *Journal of Micromechanics and Microengineering*, vol. 16, no. 11, p. 2502, Oct. 2006, doi: 10.1088/0960-1317/16/11/035.

[130] L.-H. Wang, Z. Pan, H. Jiang, H.-L. Lai, Q.-P. Ran, and P. A. R. Abu, “A Low-Power Passive UHF Tag With High-Precision Temperature Sensor for Human Body Application,” *IEEE Access*, vol. 10, pp. 77068–77080, 2022, doi: 10.1109/ACCESS.2022.3193155.

[131] C. Occhiuzzi, S. Parrella, and G. Marrocco, “Flexible Dual chip on-skin RFID Sensor for Body Temperature Monitoring,” in *2020 IEEE International Conference on Flexible and Printable Sensors and Systems (FLEPS)*, IEEE, Aug. 2020, pp. 1–4. doi: 10.1109/FLEPS49123.2020.9239531.

[132] S. Wickramasinghe, J. Jayasinghe, and M. Senadeera, “Compact battery-free UHF RFID tag for temperature measurement in poultry egg incubators,” in *2023 IEEE 17th International Conference on Industrial and Information Systems (ICIIS)*, IEEE, Aug. 2023, pp. 1–6. doi: 10.1109/ICIIS58898.2023.10253604.

[133] M. Le Breton, R. Bhattacharyya, and M. Cassel, “Challenges of Using RFID for Outdoor Environmental Monitoring,” *Wireless Identification and Sensing Systems for Harsh and Severe Environments*, pp. 91–131, Jan. 2024, doi: 10.1002/9781394169108.CH4.

[134] B. B. Maskey *et al.*, “A Smart Food Label Utilizing Roll-to-Roll Gravure Printed NFC Antenna and Thermistor to Replace Existing ‘Use-By’ Date System,” *IEEE Sens. J.*, vol. 20, no. 4, pp. 2106–2116, 2020, doi: 10.1109/JSEN.2019.2948752.

[135] J. Choi, I. Visagie, Y. Chen, R. Abbel, and K. Parker, “NFC-Enabled Dual-Channel Flexible Printed Sensor Tag,” *Sensors*, vol. 23, no. 15, p. 6765, Jul. 2023, doi: 10.3390/s23156765.

[136] A. Lazaro, R. Villarino, and D. Girbau, “A survey of NFC sensors based on energy harvesting for IoT applications,” *Sensors (Switzerland)*, vol. 18, no. 11, 2018, doi: 10.3390/s18113746.

[137] J. M. Vicente, E. Avila-Navarro, C. G. Juan, N. Garcia-Aracil, and J. Maria Sabater-Navarro, *Design of a Wearable Bio-Patch for Monitoring Patient’s Temperature*. 2016. doi: 10.0/Linux-x86_64.

[138] A. Nag *et al.*, “Graphene-based wearable temperature sensors: A review,” *Mater. Des.*, vol. 221, p. 110971, Sep. 2022, doi: 10.1016/j.matdes.2022.110971.

[139] A. Nag, A. Mitra, and S. C. Mukhopadhyay, “Graphene and its sensor-based applications: A review,” *Sens. Actuators A Phys.*, vol. 270, pp. 177–194, Feb. 2018, doi: 10.1016/J.SNA.2017.12.028.

[140] Z. Wan *et al.*, “Battery-free flexible wireless temperature sensing for food storage,” *FlatChem*, vol. 47, p. 100709, 2024, doi: 10.1016/j.flatc.2024.100709.

[141] C. Buchberger and K. Aslanidis, “RF430FRL15xH NFC and ISO / IEC 15693 Sensor Transponder Practical Antenna Design,” Jul. 2015.

[142] Texas Instruments, “RF430FRL15xH Firmware User ’ s Guide,” 2014. [Online]. Available: http://www.ti.com/lit/ug/slau603b/slau603b.pdf

[143] Texas Instrument, “Frequently Asked Questions for RF430FRL15xH Devices,” Jul. 2017. [Online]. Available: www.ti.com

[144] Seritag, “NFC Tag Scan Distance Explained.” Accessed: Sep. 07, 2025. [Online]. Available: https://seritag.com/learn/using-nfc/nfc-tag-scan-distance-explained

[145] N. Abdul Rashid, N. D. S. Zambri, A. S. Abd Aziz, M. H. S. Mohd Jaafar, and S. Sulaiman, “Characterization of Hybrid Reduced Graphene Oxide - Silver Nanoparticles Conductive Ink for Flexible Electronics Applications,” in *Proceedings of the 4th International Symposium on Advanced Materials and Nanotechnology 2020, (i-SAMN2020)*, 2020.

[146] N. H. Ismail, N. Abdul Rashid, S. M. H. Syed Mohd Jaafar, S. F. Kamarudin, and H. W. Lee, “Electrical and mechanical performance of Inkjet-printed flexible electrodes based on reduced graphene oxide/silver nanoparticles,” *Journal of Materials Science: Materials in Electronics*, vol. 35, no. 7, Mar. 2024, doi: 10.1007/s10854-024-12273-5.

[147] S. Pei and H. M. Cheng, “The reduction of graphene oxide,” *Carbon N. Y.*, vol. 50, no. 9, pp. 3210–3228, 2012, doi: 10.1016/j.carbon.2011.11.010.

[148] G. Kaur, A. Singh, D. Mittal, A. Kaur, P. Panday, and E. Sidhu, “Performance Analysis of Conductive Patch Materials for the Design and Fabrication of Microstrip Patch Antennas,” in *2017 Progress In Electromagnetics Research Symposium (PIERS)*, St Petersburg, Russia, May 2017, pp. 1–7.

[149] M. Naftaly *et al.*, “Sheet resistance measurements of conductive thin films: A comparison of techniques,” *Electronics (Switzerland)*, vol. 10, no. 8, Apr. 2021, doi: 10.3390/electronics10080960.

[150] Y. Bin Kwon, J. H. Kang, C. S. Han, D. W. Kim, and C. W. Park, “The Effect of Particle Size and Surface Roughness of Spray-Dried Bosentan Microparticles on Aerodynamic Performance for Dry Powder Inhalation,” *Pharmaceutics*, vol. 12, no. 8, p. 765, Aug. 2020, doi: 10.3390/PHARMACEUTICS12080765.

[151] C. Wang *et al.*, “New Advances in Antenna Design toward Wearable Devices Based on Nanomaterials,” *Biosensors (Basel).*, vol. 14, no. 1, p. 35, Jan. 2024, doi: 10.3390/BIOS14010035.

[152] J. M. Stankiewicz, “Analysis of the Influence of the Skin Effect on the Efficiency and Power of the Receiver in the Periodic WPT System,” *Energies 2023, Vol. 16, Page 2009*, vol. 16, no. 4, p. 2009, Feb. 2023, doi: 10.3390/EN16042009.

[153] N. Instruments, “Resistivity Measuring Systems NH Instruments,” 2022. [Online]. Available: www.nh-instruments.de

[154] ST Microelectronic, “AN2972 Application note Application note How to design an antenna for dynamic NFC tags,” 2019.

[155] Z. Cao *et al.*, “Near-field communication sensors,” *Sensors (Switzerland)*, vol. 19, no. 18, 2019, doi: 10.3390/s19183947.

[156] A. R. Hossain, M. S. I. Sagar, A. A. Mertvyy, P. K. Sekhar, and T. Karacolak, “Inkjet Printed Flexible Dual-Band Dual-Sense Circularly Polarized Patch Antenna,” *IEEE Access*, vol. 12, pp. 55424–55433, 2024, doi: 10.1109/ACCESS.2024.3389706.

[157] M. Hussain, H. Zahra, S. M. Abbas, and Y. Zhu, “Flexible Dielectric Materials: Potential and Applications in Antennas and RF Sensors,” *Adv. Electron. Mater.*, vol. 10, no. 11, p. 2400240, Nov. 2024, doi: 10.1002/AELM.202400240.

[158] Christian Merz, “Impedance Matching for Near Field Communication Applications,” *Wuerth Elektronik*, Dec. 10, 2020. Accessed: Jun. 10, 2024. [Online]. Available: www.we-online.comANP084a//2020-12-10//2

[159] Y. Qin, X. Ouyang, Y. Lv, W. Liu, Q. Liu, and S. Wang, “A Review of Carbon-Based Conductive Inks and Their Printing Technologies for Integrated Circuits,” *Coatings*, vol. 13, no. 10, p. 1769, Oct. 2023, doi: 10.3390/coatings13101769.

[160] Z. Hou, H. Lu, Y. Li, L. Yang, and Y. Gao, “Direct Ink Writing of Materials for Electronics-Related Applications: A Mini Review,” *Front. Mater.*, vol. 8, p. 647229, Apr. 2021, doi: 10.3389/FMATS.2021.647229/BIBTEX.

[161] K. Zub, S. Hoeppener, U. S. Schubert, K. Zub, S. Hoeppener, and U. S. Schubert, “Inkjet Printing and 3D Printing Strategies for Biosensing, Analytical, and Diagnostic Applications,” *Advanced Materials*, vol. 34, no. 31, p. 2105015, Aug. 2022, doi: 10.1002/ADMA.202105015.

[162] Y.-X. ; Lin, K.-Y. ; Ko, and F.-P. ; Lai, “Inkjet-Printed Reflectarray Antenna Integrating Feed andAperture on a Flexible Substrate Using Origami Techniques,” *Electronics (Basel).*, 2024, doi: 10.3390/electronics13132505.

[163] K. Saito, T. Nakamura, K. Kamezawa, R. Ikeda, Y. Hashimoto, and B. Shizuki, “Japanese patterns as NFC antennas for interactive urushi-ware,” in *TEI 2020 - Proceedings of the 14th International Conference on Tangible, Embedded, and Embodied Interaction*, Association for Computing Machinery, Inc, Feb. 2020, pp. 443–451. doi: 10.1145/3374920.3374952.

[164] D. Büttner and K. Krüger, “Improving Performance of Laser-Printed Conductive Silver Lines,” in *IMAPS/ACerS 8th International CICMT Conference and Exhibition (2012)* |, Erfurt, Germany, Apr. 2012. [Online]. Available: http://meridian.allenpress.com/imaps-conferences/article-pdf/2012/CICMT/000377/2360942/cicmt-2012-wa46.pdf

[165] T. Leng *et al.*, “Screen-Printed Graphite Nanoplate Conductive Ink for Machine Learning Enabled Wireless Radiofrequency- Identification Sensors,” *ACS Appl. Nano Mater.*, 2019, doi: 10.1021/acsanm.9b01034.

[166] I. Ortego, N. Sanchez, J. Garcia, F. Casado, D. Valderas, and J. I. Sancho, “Inkjet printed planar coil antenna analysis for NFC technology applications,” *Int. J. Antennas Propag.*, vol. 2012, 2012, doi: 10.1155/2012/486565.

[167] M. Kisic, B. Dakic, M. Damnjanovic, A. Menicanin, N. Blaz, and L. Zivanov, “Design and simulation of 13.56 MHz RFID tag in ink-jet printing technology,” in *Proceedings of the International Spring Seminar on Electronics Technology*, 2013. doi: 10.1109/ISSE.2013.6648254.

[168] T. Žurbi and D. Gregor-Svetec, “NFC Tag Awareness and Its Visual Implementation on Food Packaging: Case Study in Slovenia,” *Applied Sciences*, vol. 14, no. 21, p. 9933, Oct. 2024, doi: 10.3390/app14219933.

[169] J. Zuo *et al.*, “RFID-based sensing in smart packaging for food applications: A review,” Dec. 01, 2022, *Elsevier B.V.* doi: 10.1016/j.fufo.2022.100198.

[170] Martin Heritier, “Adapting an NFC Antenna to its Environment,” *Swiss Technology Inside Smart Sapphire* , Jan. 22, 2025.

[171] J. Victoria, P. A. Martinez, A. Suarez, A. Alcarria, S. Mirasol, and J. Torres, “Design approach for high efficiency NFC systems with magnetic shielding materials,” in *Proceedings of the 2020 International Symposium on Electromagnetic Compatibility - EMC EUROPE, EMC EUROPE 2020*, Institute of Electrical and Electronics Engineers Inc., Sep. 2020. doi: 10.1109/EMCEUROPE48519.2020.9245861.

[172] D. Paret, *Antenna Designs for NFC Devices*. 2016. doi: 10.1002/9781119145301.

[173] S. Alagiasundaram, K.-Y. Lee, E.-H. Lim, P.-S. Chee, and F.-L. Bong, “Planar Inverted Antenna with Embedded Patch Excitor for On-metal Tag Design,” *IEEE Journal of Radio Frequency Identification*, pp. 1–1, Jun. 2023, doi: 10.1109/jrfid.2023.3286486.

[174] L.O. Hoeft and J.S. Hofstra, “Experimental and Theoretical Analysis of the Magnetic Field Attenuation of Enclosures,” *IEEE Transactions on Electromagnetic Compatibility* , vol. 30, no. 3, pp. 326–340, 1988, doi: 10.1109/15.3312.

[175] Nordic Semiconductor, “nRF52832 NFC Antenna Tuning,” 2018.

[176] Kifle. Y, J. J. Wikner, J. Zotterman, A. Jalili, and S. Farnebo, “NFC Powered Implantable Temperature Sensor,” in *2016 International Symposium on Integrated Circuits (ISIC)*, IEEE, Dec. 2016, pp. 1–4. doi: 10.1109/ISICIR.2016.7829739.

[177] M. Boada, A. Lazaro, R. Villarino, and D. Girbau, “Read range study of energy-harvested implanted NFC sensors with commercial NFC ICs and smartphones,” *2021 34th General Assembly and Scientific Symposium of the International Union of Radio Science, URSI GASS 2021*, no. September, pp. 1–4, 2021, doi: 10.23919/URSIGASS51995.2021.9560195.

[178] M. E. Rahman, M. Abdelatti, M. S. Sodhi, and K. Mankodiya, “Design and Performance Analysis of a Chemically- Etched Flexible NFC Tag Antenna,” *Electrical Engineering and Systems Science*, pp. 11–14, Oct. 2022, doi: https://doi.org/10.48550/arXiv.2210.12327.

[179] Texas Instruments, “RF430FRL15xH NFC ISO 15693 Sensor Transponder,” 2014.

[180] J. Perelaer *et al.*, “Printed electronics: The challenges involved in printing devices, interconnects, and contacts based on inorganic materials,” *J. Mater. Chem.*, vol. 20, no. 39, pp. 8446–8453, Oct. 2010, doi: 10.1039/c0jm00264j.

[181] R. Xing, *The Application of Coefficient of Variation Estimation in Reliability Study of Existing Structure*.

[182] G. Atkinson and A. M. Nevill, “Statistical methods for assessing measurement error (reliability) in variables relevant to sports medicine,” *Sports Medicine*, vol. 26, no. 4, pp. 217–238, 1998, doi: 10.2165/00007256-199826040-00002.

[183] W. Li, A. Meredov, and A. Shamim, “Silver Nanowire based Flexible, Transparent, Wideband Antenna for 5G Band Application,” in *2019 IEEE International Symposium on Antennas and Propagation and USNC-URSI Radio Science Meeting*, IEEE, Jul. 2019, pp. 275–276. doi: 10.1109/APUSNCURSINRSM.2019.8888371.

[184] A. S. Abd Aziz, S. Z. Rejal, N. Abdulrashid, S. Sulaiman, S. M. H. Syed Mohd Jaafar, and H. Wah Lee, “Reliability Test of Inkjet-Printable Silver Conductive Ink,” in *Key Engineering Materials*, vol. 945, Trans Tech Publications Ltd, 2023, pp. 35–40. doi: 10.4028/p-cp1337.

[185] I. Ortego, N. Sanchez, J. Garcia, F. Casado, D. Valderas, and J. I. Sancho, “Inkjet Printed Planar Coil Antenna Analysis for NFC Technology Applications,” *Int. J. Antennas Propag.*, vol. 2012, pp. 1–6, 2012, doi: 10.1155/2012/486565.

[186] G. G. Buchmeier, A. Takacs, D. Dragomirescu, J. Alarcon Ramos, and A. Fortes Montilla, “Optimized NFC Circuit and Coil Design for Wireless Power Transfer with 2D Free-Positioning and Low Load Sensibility,” *Sensors*, vol. 21, no. 23, p. 8074, Dec. 2021, doi: 10.3390/s21238074.

[187] T. Instruments, “RF430FRL152HEVM User’s Guide,” Jul. 2018. [Online]. Available: www.ti.com

[188] O. Mourad, P. Le Thuc, R. Staraj, and P. Iliev, “System modeling of the RFID contactless inductive coupling using 13.56 MHz loop antennas,” *8th European*

Conference on Antennas and Propagation, EuCAP 2014, pp. 2034–2038, 2014, doi: 10.1109/EUCAP.2014.6902206.

[189] M. Mabrouk, M. Dhaouadi, T. P. Vuong, A. C. De Souza, and A. Ghazel, "A Broadband UHF Tag Antenna for Near-Field and Far-Field RFID Communications," *Radioengineering*, vol. 23, no. 4, Dec. 2014.

[190] Y. Zhao, H. Li, S. Naderiparizi, A. Parks, and J. R. Smith, "Low-cost wireless power efficiency optimization of the NFC tag through switchable receiver antenna," *Wireless Power Transfer*, vol. 5, no. 2, pp. 87–96, Sep. 2018, doi: 10.1017/WPT.2018.1.

[191] M. Chakraborty, R. Mukherjee, and R. Dahiya, "Reliability Analysis of Screen-printed Tags with Low-power Electronics on Flexible Substrates," in *2022 IEEE International Conference on Flexible and Printable Sensors and Systems (FLEPS)*, IEEE, Jul. 2022, pp. 1–4. doi: 10.1109/FLEPS53764.2022.9781484.

[192] C. M. Awuah, P. Danuor, J. I. Moon, and Y. B. Jung, "Novel coil design and analysis for high-power wireless power transfer with enhanced Q-factor," *Sci. Rep.*, vol. 13, no. 1, Dec. 2023, doi: 10.1038/s41598-023-31389-y.

[193] STMicroelectronics, "Automatic antenna tuning (AAT) for ST25R3916/16B and ST25R3920/20B devices," May 2022. [Online]. Available: www.st.com

[194] Klaus Finkenzeller, *RFID Handbook: Fundamentals and Applications in Contactless Smart Cards, Radio Frequency Identification and Near-Field Communication*, 3rd ed. Wiley, 2010.

[195] P. Sittithai, K. Phaebua, T. Lertwiriyaprapa, and P. Akkaraekthalin, "Magnetic Field Shaping Technique for HF-RFID and NFC Systems," *Radioengineering*, vol. 27, no. 1, pp. 121–128, Apr. 2019, doi: 10.13164/re.2019.0121.

[196] Z. Khonsari, T. Bjorninen, M. M. Tentzeris, L. Sydanheimo, and L. Ukkonen, "2.4 GHz inkjet-printed RF energy harvester on bulk cardboard substrate," in *IEEE Radio and Wireless Symposium, RWS*, IEEE Computer Society, Jun. 2015, pp. 153–155. doi: 10.1109/RWS.2015.7129721.

[197] C. P. Dick, C. Polak, and E. Waffenschmidt, "Proposal of a figure of merit for the characterization of soft-magnetic shielding material used in inductive wireless power transmission systems," *IEEE J. Emerg. Sel. Top. Power Electron.*, vol. 3, no. 1, pp. 272–279, Mar. 2015, doi: 10.1109/JESTPE.2014.2320694.

[198] J. Victoria, A. Suarez, P. A. Martinez, A. Alcarria, A. Gerfer, and J. Torres, “Improving the Efficiency of NFC Systems through Optimizing the Sintered Ferrite Sheet Thickness Selection,” *IEEE Trans. Electromagn. Compat.*, vol. 62, no. 4, pp. 1504–1514, Aug. 2020, doi: 10.1109/TEMC.2020.3003800.

[199] R. Mghaiouini, A. Elmalouky, N. Benzbiria, R. El Moznine, M. Monkade, and A. El Bouari, “The influence of the electromagnetic field on the electric properties of water,” *Mediterranean Journal of Chemistry*, vol. 10, no. 5, p. 507, May 2020, doi: 10.13171/mjc10502005181406rm.

[200] Y. G. Rabobason, B. Ravelo, and N. Benjelloun, “Thermal empirical effect on the Kapton-based passive microstrip circuit,” in *2016 URSI Asia-Pacific Radio Science Conference (URSI AP-RASC)*, IEEE, Aug. 2016, pp. 1911–1914. doi: 10.1109/URSIAP-RASC.2016.7601215.

[201] G. E. Ponchak, J. L. Jordan, and M. C. Scardelletti, “Temperature dependence of thin film spiral inductors on Alumina over a temperature range of 25 to 475° C,” *Proceedings - Electronic Components and Technology Conference*, pp. 713–719, 2010, doi: 10.1109/ECTC.2010.5490775.

[202] J. Victoria *et al.*, “Study of a Novel High Permeability Ferrite Sheet Intended for Near Field Communication Systems,” in *2019 IEEE International Symposium on Electromagnetic Compatibility, Signal & Power Integrity (EMC+SIPI)*, IEEE, Jul. 2019, pp. 78–83. doi: 10.1109/ISEMC.2019.8825260.

[203] A. Yadav and T. K. Bera, “Ferrite shielding thickness and its effect on electromagnetic parameters in wireless power transfer for electric vehicles (EVs),” *Journal of Engineering and Applied Science*, vol. 70, no. 1, p. 132, Dec. 2023, doi: 10.1186/s44147-023-00298-2.

[204] D. Ding, J. You, X. Cui, Y. Xue, X. Tan, and G. Zhai, “Application of Amorphous and Nanocrystalline Soft Magnetic Materials in Balanced-Force-Type Electromagnetic Relay,” *Micromachines (Basel).*, vol. 15, no. 3, p. 368, Mar. 2024, doi: 10.3390/mi15030368.

[205] Y. Liu *et al.*, “Study on the Magnetic Noise Characteristics of Amorphous and Nanocrystalline Inner Magnetic Shield Layers of SERF Co-Magnetometer,” *Materials*, vol. 15, no. 22, p. 8267, Nov. 2022, doi: 10.3390/MA15228267.

[206] W. Wang *et al.*, “Low-Loss Soft Magnetic Materials and Their Application in Power Conversion: Progress and Perspective,” *Energies (Basel).*, vol. 18, no. 3, p. 482, Jan. 2025, doi: 10.3390/en18030482.

[207] N. M. Faudzi *et al.*, “Characterization of Carbon-based NFC Tag Antenna Design,” *Proceedings - 2022 RFM IEEE International RF and Microwave Conference, RFM 2022*, 2022, doi: 10.1109/RFM56185.2022.10065256.

[208] J. Lundén, V. Vanhanen, T. Myllymäki, E. Laamanen, K. Kotilainen, and K. Hemminki, “Temperature control efficacy of retail refrigeration equipment,” *Food Control*, vol. 45, pp. 109–114, Nov. 2014, doi: 10.1016/J.FOODCONT.2014.04.041.

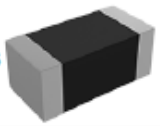
APPENDICES

APPENDIX 1

NTC Thermistor

Chip Temp. Sensing NTC Thermistor – SDNT Series

Operating Temp. : -55℃~+125℃



FEATURES

- SMD type suitable for high density mounting
- Series of B constant for various applications
- Excellent solder ability

APPLICATIONS

- Telecommunication equipments such as cellular phone, automobile phone, etc.
- Office automation such as printer, facsimile, word processor, etc.
- Battery, CPU temperature protection.

PRODUCT IDENTIFICATION

SDNT	1005	X	103	F	3380	F	T	F
①	②	③	④	⑤	⑥	⑦	⑧	⑨

①

Type	
SDNT	Chip NTC Thermistor

②

External Dimensions (L×W) (mm)	
0603 [0201]	0.6×0.3
1005 [0402]	1.0×0.5
1608 [0603]	1.6×0.8
2012 [0805]	2.0×1.25

③

Internal Code
X
C

④

Zero-power Resistance	
Example	Nominal Value
472	4.7kΩ
103	10kΩ

⑤

Tolerance of Resistance	
F	±1%
H	±3%
J	±5%
K	±10%

⑥

B Constant (25-50℃)	
Example	Nominal Value
3380	3380K
4250	4250K

⑦

Tolerance of B Constant	
F	±1%
H	±3%

⑧

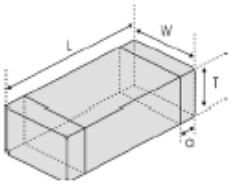
Packing	
T	Tape & Reel

⑨

Hazardous Substance Free Products
F

SHAPE AND DIMENSIONS

Unit: mm [inch]



Type	L	W	T	a
SDNT0603 [0201]	0.6±0.05 [.024±.002]	0.3±0.05 [.012±.002]	0.3±0.05 [.012±.002]	0.15±0.05 [.006±.002]
SDNT1005 [0402]	1.0±0.15 [.039±.006]	0.5±0.15 [.020±.006]	0.5±0.15 [.020±.006]	0.25±0.1 [.010±.004]
SDNT1608 [0603]	1.6±0.15 [.063±.006]	0.8±0.15 [.031±.006]	0.8±0.15 [.031±.006]	0.3±0.2 [.012±.008]
SDNT2012 [0805]	2.0±0.2 [.079±.008]	1.25±0.2 [.049±.008]	0.85±0.2 [.033±.008]	0.5±0.3 [.020±.012]

Sunlord Specifications subject to change without notice. Please check our website for latest information. Revised 2021/05/15

Sunlord Industrial Park, Dafuyuan Industrial Zone, Guanlan, Shenzhen, China 518110 Tel: 0086-755-29832333 Fax: 0086-755-82269029 E-Mail: sunlord@sunlordinc.com

SPECIFICATIONS

SDNT1608 TYPE

Part Number	Resistance at 25℃	B Constant (25-50℃)	Max. Permissive Operating Current (25℃)	Thermal Time Constant	Dissipation Factor	Rated Electric Power
Units	kΩ	K	mA	sec	mW/℃	mW
Symbol	R25	B25/50	Imax	t	C	P
SDNT1608X333□4050◎TF	33	4050	0.17	<5 sec.	1.0	100
SDNT1608X473□4050◎TF	47	4050	0.14			
SDNT1608X473□4150◎TF	47	4150	0.14			
SDNT1608X503□4150◎TF	50	4150	0.13			
SDNT1608X683□4150◎TF	68	4150	0.12			
SDNT1608X104□3950◎TF	100	3950	0.1			
SDNT1608X104□4250◎TF	100	4250	0.1			
SDNT1608X124□4250◎TF	120	4250	0.1			
SDNT1608X154□4250◎TF	150	4250	0.08			
SDNT1608X224□4300◎TF	220	4300	0.06			

SDNT2012 TYPE

Part Number	Resistance at 25℃	B Constant (25-50℃)	Max. Permissive Operating Current (25℃)	Thermal Time Constant	Dissipation Factor	Rated Electric Power
Units	kΩ	K	mA	sec	mW/℃	mW
Symbol	R25	B25/50	Imax	t	C	P
SDNT2012X472□3950◎TF	4.7	3950	0.65	<5 sec.	2.0	200
SDNT2012X502□3950◎TF	5	3950	0.6			
SDNT2012X103□3450◎TF	10	3450	0.4			
SDNT2012X103□3950◎TF	10	3950	0.44			
SDNT2012X223□4050◎TF	22	4050	0.31			
SDNT2012X333□4050◎TF	33	4050	0.24			
SDNT2012X473□4050◎TF	47	4050	0.2			
SDNT2012X473□4150◎TF	47	4150	0.2			
SDNT2012X503□4150◎TF	50	4150	0.18			
SDNT2012X104□3950◎TF	100	3950	0.14			
SDNT2012X104□4250◎TF	100	4250	0.14			
SDNT2012X154□4250◎TF	150	4250	0.11			
SDNT2012X224□4300◎TF	220	4300	0.08			

※□: Please specify the resistance tolerance code (F=±1%, H=±3%, J=±5%, K=±10%).
※◎: Please specify the B value tolerance code (F=±1%, H=±3%).
And products with other electrical characteristics can be provided upon customer's request. Please contact your local sales.

Sunlord Industrial Park, Dafuyuan Industrial Zone, Guanlan, Shenzhen, China 518110 Tel: 0086-755-29893999 Fax: 0086-755-82290000 E-Mail: sunlord@sunlordinc.com

APPENDIX 2

Voltera Conductor 2

Rev. Date 2020-07-22 **CONDUCTOR 2**

Voltera Conductor 2 (1000388)

Description

Voltera Conductor2 ink is our second-generation ink that allows for higher conductivity, adhesion strength, and more robust riveting.

Application Notes

Curing

For best results, follow recommendation in Table 4.

For curing on the V-One, use automatic bake cycle. Invert the substrate on the baking ledges of the clamps. For a box oven, cure right-side up at 190°C.

Soldering

Use SMD291 flux. For best results, burnish before soldering for 20[s] with supplied abrasive burnishing pad.

180°C – excellent solderability and rework.

Recommended Substrates

- Fibreglass-epoxy or epoxy laminates (FR4, FR1), bare or soldermask-coated
- Glass (untreated, no coating)

Design recommendations

For circuit board applications with the standard 250µm nozzle, consider these design recommendations:

- Minimum IC pin-to-pin pitch: 0.65 [mm]
- Minimum 2-terminal package: 0402 (imperial)
- Minimum tracewidth: 8 mil/ 200 [µm] (recommend 10mil)

Safety and Handling

See MSDS for safety, handling, and disposal information.

Table 1: Physical & Electrical Properties (Post-cure)

Test	Value
Sheet Resistance: (50µm film thickness)	2.05 [mΩ/sq]
Resistivity (4-point-probe):	1.265×10^{-7} [Ω.m]
Typical cured film thickness:	50 [um]
Film shrinkage, post-cure:	N/A
*Bend radius at fracture:	N/A
Adhesion (crosshatch tape test):	No transfer

*Test fracture on 5mil polyimide

Table 2: Composition Properties

Test	Value
Density:	3.35 [g/mL]
Clean-up solvent:	Isopropyl Alcohol (99%)

Table 3: Printing Properties (Printed on FR4)

Test	Value
Trace spread after print:	< 20%
Recommended Nozzle ID:	150 – 225 [µm]
Typical Line Width:	6-10 [mil] 150-250 [um]
** Typical Print Height:	50 – 100 [µm]
** Typical Feedrate:	300 – 500 [mm/min]
** Typical Kick:	0.35 [mm]

** V-One specific settings

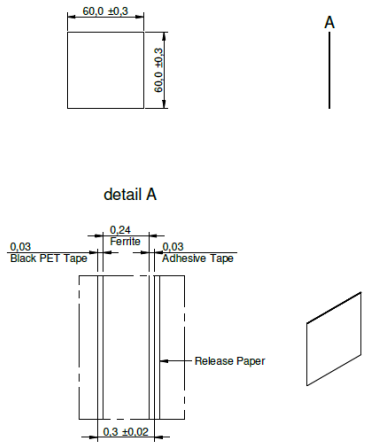
Table 4: Processing Parameters

Test	Value
Curing:	30 [min], 210°C
Compatible solder:	$SnBiAg_1$ $SnBiAg_{0.4}$ $Sn_{62}Pb_{36}Ag_2$
Typical Print Height:	50 – 100 [µm]
Typical shelf life:	6 months, unopened
Storage:	4 – 10°C, sealed container.

APPENDIX 3

Flexible Sintered Ferrite Sheet

Dimensions: [mm]



Electrical Properties:

Properties		Value	Unit	Tol.
Complex Permeability	μ' @ 1 MHz	150		typ.
Complex Permeability	μ' @ 13.56 MHz	150		typ.
Complex Permeability	μ'' @ 1 MHz	3		max.
Complex Permeability	μ'' @ 13.56 MHz	3		max.
Adhesive Thickness		0.03	mm	max.
Surface Resistance [1]	R_S	1	GΩ	min.
Insulation Resistance [2]	R_{ISO}	1	GΩ	min.
Peel Adhesion over Steel		6	N/ cm	min.

[1] Measured over the PET surface. Method ASTM D257-07
[2] Measured between the top PET layer and the bottom Adhesive later. Method ASTM D257-07

Certification:

RoHS Approval	Compliant [2011/65/EU&2015/863]
REACh Approval	Conform or declared [(EC)1907/2006]
Halogen Free	Conform [JEDEC JS709B]
Halogen Free	Conform [IEC 61249-2-21]

General Information:

Operating Temperature	-40 up to +85 °C
Storage Conditions (in original packaging)	< 40 °C ; < 75 % RH
Moisture Sensitivity Level (MSL)	1

WÜRTH ELEKTRONIK MORE THAN YOU EXPECT

Würth Elektronik eiSos GmbH & Co. KG
EMC & Inductive Solutions
Max-Eyth-Str. 1
74638 Waldenburg
Germany
Tel. +49 (0) 79 42 945 - 0
www.we-online.com
eiSos@we-online.com

CHECKED	REVISION	DATE (YYYY-MM-DD)	GENERAL TOLERANCE	PROJECTION METHOD
JoV	001.001	2021-11-23	DIN ISO 2768-1m	

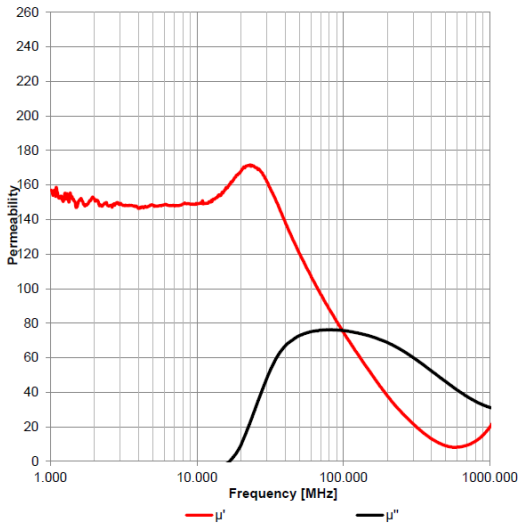
DESCRIPTION: **WE-FSFS Flexible Sintered Ferrite Sheet**

ORDER CODE: **364103**

BUSINESS UNIT	STATUS	PAGE
eiSos	Valid	1/4

This electronic component has been designed and developed for usage in general electronic equipment only. This product is not authorized for use in equipment where a higher safety standard and reliability standard is especially required or where a failure of the product is reasonably expected to cause severe personal injury or death, unless the parties have executed an agreement specifically governing such use. Moreover Würth Elektronik eiSos GmbH & Co KG products are neither designed nor intended for use in areas such as military, aerospace, aviation, nuclear control, submarine, transportation (automotive control, train control, ship control), transportation signal, disaster prevention, medical, public information network etc. Würth Elektronik eiSos GmbH & Co KG must be informed about the intent of such usage before the design-in stage. In addition, sufficient reliability evaluation checks for safety must be performed on every electronic component which is used in electrical circuits that require high safety and reliability functions or performance.

Permeability vs. Frequency:



WÜRTH ELEKTRONIK MORE THAN YOU EXPECT

Würth Elektronik eiSos GmbH & Co. KG
EMC & Inductive Solutions
Max-Eyth-Str. 1
74638 Waldenburg
Germany
Tel. +49 (0) 79 42 945 - 0
www.we-online.com
eiSos@we-online.com

CHECKED	REVISION	DATE (YYYY-MM-DD)	GENERAL TOLERANCE	PROJECTION METHOD
JoV	001.001	2021-11-23	DIN ISO 2768-1m	

DESCRIPTION: **WE-FSFS Flexible Sintered Ferrite Sheet**

ORDER CODE: **364103**

BUSINESS UNIT	STATUS	PAGE
eiSos	Valid	2/4

This electronic component has been designed and developed for usage in general electronic equipment only. This product is not authorized for use in equipment where a higher safety standard and reliability standard is especially required or where a failure of the product is reasonably expected to cause severe personal injury or death, unless the parties have executed an agreement specifically governing such use. Moreover Würth Elektronik eiSos GmbH & Co KG products are neither designed nor intended for use in areas such as military, aerospace, aviation, nuclear control, submarine, transportation (automotive control, train control, ship control), transportation signal, disaster prevention, medical, public information network etc. Würth Elektronik eiSos GmbH & Co KG must be informed about the intent of such usage before the design-in stage. In addition, sufficient reliability evaluation checks for safety must be performed on every electronic component which is used in electrical circuits that require high safety and reliability functions or performance.

Shielding Foils from VITROVAC® 6025 I50X

Magnetic Properties (typical)

Saturation induction	B_s	[T]	0.55	RT
Curie temperature	T_c	[°C]	225	
Saturation magnetostriction	$\lvert\lambda_s\rvert$	ppm	< 0.2	RT
Coercitivity	H_c	[A/m]	< 4	20 A/m; 60 Hz
Initial permeability	μ_2		> 10000	0.2 A/m, stat.
Maximum permeability	μ_{max}		> 100000	static
Remanence	B_r/B_s		~ 0.7	static

Mechanical, Physical and Chemical Properties (typical)

Composition			$Co_{69}\ Fe_4\ Mo_3\ (Nb\ Si\ B)_{Rest}$	
Density	ρ	[g/cm³]	7.86	
Strip thickness	d	[µm]	19 - 25	Via weight per length
Specific electrical resistivity	ρ_{el}	[Ωm]	1.35×10^{-6}	RT
Thermal expansion coefficient	α	[K⁻¹]	12×10^{-6}	20 - 100 °C
Crystallization temperature	T_x	[°C]	530	Heating rate 10 K/min
Young's module	E	[GPa]	~160	
Vickers hardness	HV_{02}	[kp/mm²]	~1000	

SEKELS GmbH
Dieselstrasse 6
61239 Ober-Mörlen
Germany

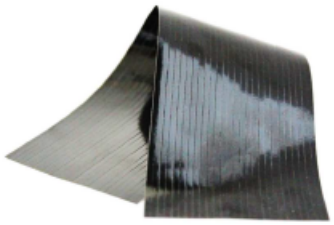
Tel.: +49 6002 9379-0
Fax: +49 6002 9379-79
mail@sekels.de
www.sekels.de

All statements, information and data given herein are believed to be accurate and reliable, but are presented without guarantee, warranty or responsibility of any kind, expressed or implied on our part. Published by SEKELS GmbH, Germany. All rights reserved.

Issue 2019 - 3

VITROLAM®

Thin and flexible shielding material designed for wireless power transfer applications (e.g. smart phones, tablets, ...)



Patent pending.

Composition:

Layered composite foil with VITROPERM®

Application Requirement:

☑ Power Transfer Efficiency (@ 110 ...205 kHz): high efficiency of typ. 70% and more
☑ Magnetic Shielding: protection of electronic components & battery from inductive heating

Features:

- 2 or 4 layers of nanocrystalline VITROPERM® 800 R
- Thin: 0,10mm (2 layers) to 0,18 mm (4 layers) incl. PET foils and adhesives
- Flexible and easy to use ribbon sheet with black PET protection tape
- Excellent power transfer efficiency
- Outstanding shielding performance → lowest temperature rise
- High temperature stability → no performance degradation due to temperature rise

Magnetic properties of VITROPERM® 800 R

Property	Value	Unit
Saturation polarisation (20°C)	1,23	T
Permeability (@ 100 kHz, 3 mA/cm)	min. 12.000	
Static coercivity	typ. 1,5	A/m
Curie temperature	600	°C

Physical properties of VITROPERM® 800 R

Property	Value	Unit
Thickness (CAT) per layer	0,018	mm
Electrical conductivity @ 100 kHz	0,35	10^6 $(\Omega\ m)^{-1}$
Heat conductivity:	approx. 12	W/(K m)

APPENDIX 4

Temperature App Coding (Android Studio)

```
public static void processData(byte[] result) {
    mProgressDialog.dismiss();
    String dataFromTag = FlomioNdefHelper.mBytesToHexString(result);

    long refValue = Long.parseLong(dataFromTag.substring(6,
8).concat(dataFromTag.substring(4, 6)), 16); //ADC1 data
    long thermValue = Long.parseLong(dataFromTag.substring(10,
12).concat(dataFromTag.substring(8, 10)), 16); //ADC2 data
    Log.d(LOG_TAG, "thermValue = '" + thermValue + "'");

    float tempConv = (float) (((((((double) thermValue) * 0.9d) /
16384.0d) / 2.0d) / 2.4E-6d) * 8738.13d) / ((double) refValue));
    //tempConv = Rt value, 2.4uA is a typical output current

    Log.d(LOG_TAG, "tempConv = '" + tempConv + "'");

    float tempConv2 = (float) ((3950.0d / (Math.log10(((double)
tempConv) / (Math.exp((-3950.0d) / 298.15d) * 100000.0d)) /
Math.log10(2.718d))) - 273.15d);

    Log.d(LOG_TAG, "tempConv = '" + tempConv2 + "'");

    if (unit) {
       tempConv2 = ((9.0f * tempConv2) / 5.0f) + 32.0f;  // metal-
based in fahrenheit
       Log.d(LOG_TAG, "tempConv = '" + tempConv2 + "'");
    }

    Log.d(LOG_TAG, "The actual temperature is " + tempConv2);

    float tempConv3 = ((float) Math.round(2.0f * tempConv2)) / 2.0f;
//metal-based in celcius


    // extra calculation for carbon-based
    //tempConv3 = (tempConv3 - 21.20369) / 0.98133;
    //tempConv3 = (tempConv3 + 2.84593) / 0.93243;

    if (Objects.equals(type, "carbon"))
    {
       tempConv3 = (float) ((tempConv3 - 21.20369) / 0.98133);
//calibration carbon-based
       tempConv3 = (float) ((tempConv3 + 2.84593) / 0.93243);
//calibration carbon-based

    } else

       String formatted = String.format("%.1f", tempConv3); // final
result displayed on screen
```

AUTHOR'S PROFILE



Najwa Mohd Faudzi was born on 9th November 1987 in Kelantan, Malaysia. After completing her A-Levels at the International Education Centre (INTEC) in Shah Alam, she pursued her studies in Osnabrück, Germany. In 2012, she received her B.Sc. degree in Electrical Engineering from Hochschule Osnabrück, Germany. Due to her high research interest, she continued her Master's studies in Electrical Engineering at the Faculty of Electrical Engineering, Universiti Teknologi MARA (UiTM) from 2012 to 2015. During her Master studies, she has been fully sponsored by the Ministry of Higher Education and UiTM under Young Lecturer Scheme. In 2020, she pursued her Ph.D. degree in Electrical Engineering at Universiti Teknologi MARA Cawangan Pulau Pinang. During her Ph.D study, she has published five conference papers and three journals on various topics related to tag antennas. She is a member of IEEE Malaysia and a Professional Technologist recognized by Malaysia Board of Technologists (MBOT). She is currently a lecturer at Universiti Teknologi MARA Cawangan Pulau Pinang. Her research interests include RFID systems, near-field communication, antenna designs, microwave technologies, and wearable and flexible antennas.

LIST OF PUBLICATION:

Journal

N. M. Faudzi, A. R. Razali, A. A. Manaf, N. H. A. Rahman, S. Sulaiman, A. S. A. Aziz, N. A. Rashid, A. A. A. Aziz, Revolutionising Military Identification and Communication with NFC Antenna Technology, FRONTIER, Vol. 4, 2023.

N. M. Faudzi, A. R. Razali, A. A. Manaf, N. H. A. Rahman, S. Sulaiman, A. S. A. Aziz, N. A. Rashid, A. A. A. Aziz, Analysis of Flexible Silver-printed NFC Tag Antenna on Miniaturization and Bending Effect, ESTEEM Academic Journal, Vol. 19, pp. 54-67, 2023.

N. M. Faudzi, A. R. Razali, A. A. Manaf, N. H. A. Rahman, A. A. A. Aziz, S. M. Hafiz, S. Sulaiman, N. A. Rashid, A. Ibrahim and A. M. Mozi, Flexible Hybrid Graphene-Based NFC Tag Antenna for Temperature Monitoring Application, Indonesian Journal of Electrical Engineering and Computer Science (IJEECS), Vol. 38, pp. 227-242, 2025.

A. Ibrahim, A. R. Razali, M. Jusoh, **N. M. Faudzi**, and A. M. Mozi, Bending Effects on Polyvinyl Alcohol Thin Film for Flexible Wearable Antenna Substrate, Pertanika Journal of Science and Technology, Vol. 32, pp. 2055 - 2067, 2024.

Conference Proceeding

N. M. Faudzi, A. R. Razali, A. A. Manaf, N. H. A. Rahman, A. A. A. Aziz, A. Ibrahim, and A. M. Mozi, Characterization of Carbon-based NFC Tag Antenna Design, 2022 IEEE International RF and Microwave Conference (RFM), 2022.

N. M. Faudzi, A. A. A. Aziz, A. R. Razali, N. H. A. Rahman, A. A. Manaf, A. Ibrahim, and A. M. Mozi, Moisture Impact Analysis on NFC Tag Antennas, 2023 6th International Conference on Applied Computational Intelligence in Information Systems (ACIIS), 2023.

N. M. Faudzi, A. A. A. Aziz, A. R. Razali, N. H. A. Rahman, A. A. Manaf, A. Ibrahim, and A. M. Mozi, Comparative Study of Ferrite and Amorphous Shielding Materials for NFC Tag Antenna on Metal, 2023 IEEE International Symposium On Antenna and Propagation (ISAP), 2023.

N. M. Faudzi, A. R. Razali, A. A. Manaf, N. H. A. Rahman, A. A. A. Aziz, A. Ibrahim, A. M. Mozi, S. M. Hafiz, S. Sulaiman and N. A. Rashid, Characterization of Graphene-based Flexible One-Side-Coil NFC Tag for Temperature Sensing, 2024 IEEE Sensors, 2024.

N. M. Faudzi, A. R. Razali, N. H. A. Rahman, A. A. Manaf, A. A. A. Aziz, A. A. Bakar, A. Ibrahim, A. M. Mozi and S. M. Hafiz, Analysis of Printed Graphene-Based NFC Tag Antenna in Moist Environment, 2025 IEEE International RF and Microwave Conference (RFM), 2025. (Presented)

A. Ibrahim, A. R. Razali, M. Jusoh, **N. M. Faudzi**, and A. M. Mozi, SAR Evaluation of 5G Antenna Using Polyvinyl Alcohol Thin Film Substrate, 2022 IEEE International RF and Microwave Conference (RFM), 2022.

A. M. Mozi, Z. Zulkarnil, A. R. Razali, A. A. Bakar, N. H. A. Rahman, S. N. Azemi, **N. M. Faudzi** and A. Ibrahim, Sensitivity Study of Slotted Radiator Antenna-Based Sensor for Sweat Monitoring, 2022 IEEE International RF and Microwave Conference (RFM), 2022.

A. Ibrahim, A. R. Razali, M. Jusoh, **N. M. Faudzi**, and A. M. Mozi, Gain Enhancement for Wearable 5G Antenna on PVA thin film substrate, 2023 IEEE International Symposium On Antenna and Propagation (ISAP), 2023.

A. M. Mozi, A. R. Razali, N. H. A. Rahman, S. N. Azemi, **N. M. Faudzi** and A. Ibrahim, Design of Antenna-Based Sensor for Sweat Sensing, 2024 IEEE Symposium on Wireless Technology & Applications (ISWTA), 2024.

A. M. Mozi, A. R. Razali, N. H. A. Rahman, S. N. Azemi, **N. M. Faudzi** and A. Ibrahim, Sensitivity Study of a Coplanar Waveguide Antenna-Based Sensor for Hydration Monitoring, 2024 IEEE 7th International Conference on Electrical, Electronics and System Engineering (ICEESE), 2024.